



The
University
Of
Sheffield.

**Monitoring Trace Gases in the Biological Sciences and
Petrochemistry by Photoacoustic and Raman Spectroscopy**

Saeed Dammas Alahmari

*A thesis submitted in partial fulfilment of the requirements for the degree of
Doctor of Philosophy*

The University of Sheffield

Faculty of Science

Department of Chemistry

September 2019

Acknowledgements

First of all, I would like to thank to my god, the Most Beneficent, the Most Merciful, for all his guidance while I was completing this PhD thesis.

I would especially like to thank my thesis advisor, Dr. Michael Hippler. His knowledge and assistance during the course of this study was greatly influential in making this research a success. I want to thank him for taking me into his research laboratory, providing me with an excellent atmosphere for doing research and for his excellent guidance, caring, and patience throughout my time at the University of Sheffield.

In Dr Michael Hippler's group, I would like to thank Dr Thomas Smith for his practical help, Dr. Mark Stringer for his advice, and PhD student George D Metcalfe for help and encouragement. I would like to thank the Ministry of Education of Saudi Arabia for funding. Thanks to fellow PhD students Alex Auty and George Farrow for welcoming me into the office and helping me.

And finally, many thanks to my parents, my wife, my daughters and my brothers who endured this long process with me, always offering support and love as I strive to become a better person in general.

Abstract

Photoacoustic spectroscopy (PAS) and Cavity-Enhanced Raman Spectroscopy (CERS) can detect headspace gases above a microbiological culture in a closed system. PAS and CERS have a detection limit of few ppm per volume. These techniques were used to investigate the aerobic respiration of *Escherichia coli* (*E. coli*). Both techniques are able to monitor O₂ and CO₂ and its isotopomers with excellent sensitivity and time resolution to characterise bacterial growth and metabolism. CO₂ can be detected using CERS and a differential Helmholtz Resonator (DHR) because it has Raman and IR active vibrations. However, homonuclear diatomic molecules, such as O₂, have only symmetric stretching vibrations that are Raman active but not IR active. In PAS, O₂ can be detected by exciting a formally forbidden electronic absorption band in the red, the $b\ ^1\Sigma_g^+ (\nu = 0) \leftarrow X\ ^3\Sigma_g^- (\nu = 0)$ band (the “A band”) near 760 nm.

Identification of different growth phases and changes in the aerobic metabolic activity of *E. coli* was possible by taking simultaneous measurements of O₂ consumption and CO₂ production using CERS and DHR in PAS, including optical density (OD) measurements. We demonstrate how ¹³C isotopic labelling of sugars combined with spectroscopic detection allows the study of bacterial mixed sugar metabolism, to establish whether sugars are sequentially or simultaneously metabolised. For *E. coli*, we have characterised the shift from glucose to lactose metabolism without a classic diauxic lag phase.

DHR and CERS are shown to be cost-effective and highly selective analytical tools in the biosciences and in biotechnology, complementing and superseding existing, conventional techniques. They also provide new capabilities for mechanistic investigations in biochemistry and show a great deal of promise for use in stable isotope bioassays.

Finally, PAS in a differential Helmholtz resonator has been employed with near-IR detection of CO₂ and H₂S in natural gas, in static and flow cell measurements. The set-up has also been used for simultaneous *in situ* monitoring of O₂, CO₂ and H₂S in the cysteine metabolism of microbes (*E.coli*), and for the analysis of CO₂ and H₂S impurities in natural gas.

Abbreviations

ATP	Adenosine Triphosphate
ADP	Adenosine Diphosphate
CCD	Charge-Coupled Device
CH1	Channel 1
CH2	Channel 2
CERS	Cavity Enhanced Raman Spectroscopy
cw	Continuous Wave
DFB	Distributed Feedback
DHR	Differential Helmholtz Resonator
<i>E. Coli</i>	<i>Escherichia Coli</i>
ECDL	External Cavity Diode Laser
FWHM	Full Width at Half Maximum
Hz	Hertz
InGaAs	Indium Gallium arsenide
KHz	Kilohertz
K	Kelvin
LOD	Limit of Detection
LB	Lysogeny Broth
mbar	Millibar
mV	Millivolt
mW	MilliWatt
μ	Micro

MIR	Mid-Infrared
NAD	Nicotinamide Adenine Dinucleotide
NIR	Near Infrared
NG	Natural Gas
OD	Optical Density
PAS	Photoacoustic Spectroscopy
ppb	Part-per-billion
ppm	Part-per-million
PD	Photodiode
p	Pressure
2YT	Two Times Yeast Tryptone
Q	Quality Factor
V	Volt
W	Watt

Table of Contents

Acknowledgements	3
Abstract	4
Abbreviations	5
Table of Contents	7
Chapter 1. Introduction	13
1.1. Approaches to Gas Analysis.....	13
1.1.1. Photoacoustic Spectroscopy (PA).....	14
1.1.2. Cavity-Enhanced Raman Spectroscopy (CERS)	14
1.2. The bacterium <i>Escherichia Coli</i> (<i>E. Coli</i>)	15
1.2.1. Aerobic Respiration of <i>E. coli</i>	16
1.2.2. Production of Hydrogen Sulfide by <i>E. coli</i>	18
1.3. Literature Review of Hydrogen Sulfide in Natural Gas and Air	20
1.4. State of the Art of the Detection of CO ₂ , H ₂ S, O ₂	21
1.5. Aims and Thesis Structure	25
Chapter 2. Overview of Spectroscopic Techniques	27
2.1. Introduction	27
2.2. Photoacoustic Spectroscopy.....	27
2.2.1. Description of the Photoacoustic Effect in Gases.....	28
2.2.2. Standard PAS.....	29
2.2.3. Resonant Cell Design.....	31
2.2.4. Helmholtz Resonator (HR).....	32
2.2.5. The Differential Helmholtz Resonator (DHR).....	33

2.3. Cavity-Enhanced Raman Spectroscopy (CERS).....	34
Chapter 3. Theory of Vibrational and Rotational Spectroscopy.....	37
3.1. Introduction.....	37
3.2. Kinetics of Radiation Transitions	37
3.2.1. Einstein Coefficients.....	37
3.3. Beer-Lambert Absorption Law.....	40
3.4. Vibrational Spectroscopy and Selection Rules for Diatomic and Polyatomic Molecules...41	
3.5. Harmonic and Anharmonic Oscillator	45
3.6. Rotational Motion.....	47
3.7. Raman spectroscopy.....	48
Chapter 4. Construction and Characterisation of Differential Helmholtz Resonator (DHR)	
Enhanced Resonant Photoacoustic Spectroscopy (RPAS)	51
Abstract	51
4.1. Introduction	52
4.1.1. External Cavity Diode Laser (ECDL).....	52
4.1.2. Distributed Feed-Back (DFB) Laser.....	54
4.1.3. Lock-In Amplifier	55
4.2. Aims	55
4.3. Experimental	56
4.3.1. The Set-Up of the ECDL system	56
4.3.2. The Set-Up of the DFB laser system	57
4.3.3. General Set-Up for the system	58
4.3.4. Determination of the Resonance Frequency of the DHR	65

4.3.5. Theoretical Absorption Cross Sections of O ₂ in the Red and CO ₂ in the Near-IR	70
4.3.6. Preparation of Gas Mixtures	71
4.4. Results and Discussions	73
4.4.1. External Cavity Diode Laser (ECDL) Characterisation	73
4.4.2. Calibration Spectrum of Carbon Dioxide (CO ₂) with HITRAN Data Base	74
4.4.3. Hydrogen Sulfide (H ₂ S) Measurements Using ECDL	75
4.4.4. Calibration Spectrum of Carbon Dioxide (CO ₂) with HITRAN Data Base by using the DFB laser system	77
4.4.5. Hydrogen Sulfide (H ₂ S) Measurements in Air/ N ₂ Using a DFB laser at 1.57 μm	82
4.4.6. Photoacoustic Detection of Molecular Oxygen Near 764 nm	84
4.4.7. Demonstrating the Distinction of ¹² CO ₂ and ¹³ CO ₂ Isotopomers in Preparation of Biology Experiments	86
4.5. Conclusions	88
Chapter 5. Trace Gas Analysis in the Biosciences and Petrochemistry	89
5.1. Cavity Enhanced Raman and Helmholtz Resonator Photoacoustic Spectroscopy to Monitor the Mixed Sugar Metabolism of <i>E. coli</i>	89
5.1.1. Introduction	89
5.1.1.1. Spectroscopic Detection of Headspace Gases	90
5.1.1.2. Growth phases of <i>E. Coli</i>	92
5.1.1.3. Glucose-Lactose Diauxie in <i>E. Coli</i>	93
5.1.2. Aims	94
5.1.3. Experimental	95

5.1.3.1. General setup of Cavity Enhanced Raman Spectroscopy (CERS) with Optical Feedback	95
5.1.3.2. Starter Culture Preparation	98
5.1.3.2.1. Description of Growth Media	98
5.1.3.2.2. <i>E. coli</i> Starter Cultures	99
5.1.3.3. Sample Preparation	99
5.1.3.3.1. Sample Preparation Using M9 Minimal Medium	99
5.1.3.3.2. Sample Preparation Using LB Rich Medium	99
5.1.3.4. Monitoring Aerobic Respiration of <i>E. coli</i> by Using CERS and DHR Separately.....	100
5.1.3.4.1. CERS Measurements	100
5.1.3.4.2. DHR Measurements	103
5.1.3.5. pH, OD ₆₀₀ and Biomass Measurements	106
5.1.4. Results and Discussion	107
5.1.4.1. Measuring the different phases of <i>E. coli</i> growth in Rich LB Medium Using OD ₆₀₀ Measurements and Monitoring of the Headspace Gases	107
5.1.4.2. Measuring the Different Phases of <i>E. coli</i> Growth in M9 Medium (Minimal Medium) Supplemented with Glucose by Monitoring of the Headspace Gases and OD ₆₀₀	111
5.1.4.3. Measuring the Different Phases of <i>E. coli</i> Growth in M9 Medium Supplemented with Mixed Sugars without Isotopic labelling by Monitoring of the Headspace Gases and OD ₆₀₀	116
5.1.4.4. Measuring the Different Phases of <i>E. coli</i> growth in M9 Medium Supplemented with a Mixture of Sugars with Isotopic Labelling by Monitoring of the Headspace Gases	122

5.2 Trace Gas Analysis of CO₂, H₂S and O₂ by Near-IR and Red Diode Laser Photoacoustic Spectroscopy in a Differential Helmholtz Resonator: Applications in the Biosciences (L-Cysteine metabolism) and Natural Gas analysis (Petrochemistry)	126
5.2.1 Aims	126
5.2.2. Experimental	127
5.2.2.1. Preparation of a Glass Balloon of Defined Gas Mixtures of H ₂ S in NG, and CO ₂ in NG to be Used for Calibrations	127
5.2.2.2. Monitoring H ₂ S Production from L-Cysteine in 2YT Medium of LB	127
5.2.2.2.1. 2YT Growth Medium Preparation	127
5.2.2.2.2. Sample Preparation Using L-Cysteine Hydrochloride Monohydrate.....	127
5.2.2.3. Biological Measurements Using DHR	129
5.2.2.4. pH and Final OD ₆₀₀ Measurements	129
5.2.3. Results and Discussions	130
5.2.3.1. Detection of H ₂ S and CO ₂ Impurities in Natural Gas Samples	130
5.2.3.2. Monitoring O ₂ , CO ₂ and H ₂ S During the Metabolism of L-cysteine by <i>E. coli</i>	132
5.2.4. Conclusions	137
Chapter 6. General Conclusions and Future Work	139
References	143

Appendix	150
1. Growth-Limiting Conditions of <i>E.coli</i> using CERS	150
2. Dissolved O ₂ and CO ₂ in the Solution	151
3. Carbonate Equilibria	152
4. A Noise Equivalent Normalized Absorption Coefficient for CO ₂ in PAS	154
5. A Noise Equivalent Normalized Absorption Coefficient for O ₂ in PAS	154
6. Calculating the Detection Limit of O ₂ in an Aqueous Solution	155
7. Growth-Limiting Conditions of <i>E coli</i> Using PAS	155
8. Calculating the Amount of Dissolved CO ₂ in the Solution When Using PAS System	156
9. The Constant used for the Dissociation of Carbonic Acid H ₂ CO ₃ to the Bicarbonate Ion HCO ₃ ⁻	157
10. The Constant used for the Dissociation of H ₂ S to HS ⁻	157

Reprints of two publications

Chapter 1. Introduction

Trace gas detection is essential in many areas of fundamental and applied research, including environmental monitoring, industrial process control and biological applications. The safety and health of industrial activity is of great scientific interest and of great public concern. A model sensor should have high selectivity and sensitivity. It should also have high accuracy and precision. The sensor should be capable of identifying and distinguishing chemicals of interest. Important properties of a sensor include a wide dynamic range, easy handling, high reliability, durability, and compact size. It should be capable of multi-component analysis at a reasonable price.

There are many toxic materials which are caused by industrial activity. The presence of toxic pollutants may be due to materials being stored or used, and industrial work being performed. Natural processes may also produce toxic materials. Carbon dioxide, as a greenhouse gas and as a product of the metabolism of microbes, and hydrogen sulfide, as a very toxic industrial gas and as a signaling molecule for microbes, are two relevant gases, especially in confined spaces. Monitoring of trace gases released by microbes is also very relevant and has been studied in the Hippler group before.

1.1. Approaches to Gas Analysis

Detection of trace gas can be performed with a variety of approaches, which can be characterized as either spectroscopic or non-spectroscopic techniques. Important non-spectroscopic techniques include gas chromatography, chemiluminescence or mass spectrometry. Gas chromatography requires the preparation and the elicitation of the gas sample resulting in a long response time and it is not suitable for continuous measurements. Chemiluminescence is based on a chemical reaction of the gaseous sample, thus modifying the composition of the initial gas and it suffers from interferences and a lack of selectivity. Infrared spectroscopy (IR) is a technique to detect gas traces. Infrared spectroscopy offers many advantages in comparison to the above-mentioned techniques. For example, short response time, continuous and real-time trace gas detection from the part-per-million (ppm) down to the part-per-billion (ppb) per volume range are possible with this technique. Optical absorption is possible for CO₂ and H₂S using strong fundamental vibrational bands in the mid-IR, or much weaker overtones and combination bands in the near-IR. This forms the focus of this project. Although weaker, near-IR absorption offers the advantages of much more convenient optics

and light sources in the near-IR. Molecular oxygen (O₂) does not have an IR-active vibration; although Raman detection of its fundamental is possible, Raman scattering is a rather weak process and special Raman enhancement techniques are required to detect gases at the ppm level, for example by stimulated Raman photoacoustic spectroscopy (PARS)¹ or the recently introduced technique of cavity-enhanced Raman spectroscopy (CERS).^{2,3,4}

1.1.1. Photoacoustic Spectroscopy (PA)

Spectroscopic measurements which depend on optical absorption are most widely used in gas detection because they are simple, cheap, and can be done *in situ*. Photoacoustic spectroscopy (PA) is one such technique. This method is indirect but allows for highly sensitive measurements of molecular absorption of gases. In addition, there are other optical techniques for gas analysis such as Raman scattering which is used in this project. Raman scattering depends on light scattering, which causes shifts in the wavelength of a photon (Raman shifts).^{2,5}

In photoacoustic spectroscopy, internal excitation of molecules by optical absorption is converted to heat release and resultant pressure increase by collisions. The transformation from optical energy to heat is by molecular absorption of photons followed by non-radiative relaxation of the excited state by collisional relaxation. If the excitations are modulated periodically, acoustic waves are induced which can be picked up by microphones. This is indirect, but a very sensitive way of detecting optical absorption. By detecting in an acoustic resonator and modulating at an acoustic resonance frequency, building-up of acoustic standing waves further increases sensitivity in resonant photoacoustic spectroscopy.^{6,7} This is described in more detail in chapter 2.

1.1.2. Cavity-Enhanced Raman Spectroscopy (CERS)

Typically, at atmospheric pressures, large, high power laser systems are required in order to analyse trace gases using Raman spectroscopy, making it difficult to use Raman detection in analytical methods. Very powerful lasers are needed in order to achieve strong Raman signals; this helps to increase the number of Raman scattered photons. Stronger signals can also be obtained by using a range of stimulated Raman techniques. There are several methods which can increase the sensitivity, such as, PARS (photoacoustic stimulated Raman spectroscopy), CARS (coherent anti-Stokes Raman spectroscopy) and fiber-enhanced or cavity enhanced Raman spectroscopy.^{1,3,8,9}

Cavity-enhanced Raman spectroscopy (CERS) is a new technique, recently developed in the Hippler group.^{2,5,10,11} This technique has uses in gas sensing applications such as analysis of natural gas and for a number of isotopic labelling studies using ¹⁴N and ¹³C isotopes. CERS has high spectral resolution therefore it is very selective, and high sensitivity allowing for trace gas detection in multicomponent analysis. CERS is the focus of Chapter 5, with the details of operation presented there.

In short, CERS is a method where the light passes through an optical cavity which has highly reflective mirrors ($R > 99.9\%$). The mirrors are aligned such that a single optical mode (i.e., a standing wave) is supported in the cavity. This is called an optical resonance. Light intensity will build up inside the cavity with the path length reaching distances up to kilometres. This power build up is advantageous for CERS as an application of Raman spectroscopy. The signal measured after the cavity in CERS is strongly dependent on the light intensity before the passing through of the cavity. Therefore, a continuous-wave (cw) laser is used, as this provides a stable output power achieving a cavity resonance equilibrium. For cavity enhanced laser spectroscopy and gas sensing, cw lasers are most suitable. They require low power feeding, have a low cost, support a large number of wavelengths, and offer high spectral resolution because of the narrow width of laser line obtained by controlled optical feedback. The CERS method only supports certain light wavelengths because only one mode will be excited in the cavity, so there should either the laser wavelength or the length of the cavity be modified in order to fit a multiple of the wavelength within the optical cavity (cavity mode). This is described in more details in chapter 2.

1.2. The bacterium *Escherichia Coli* (*E. Coli*)

Part of the gram negative family of bacteria, *E Coli* appears as approximately 1 μm long rods. The rods will extend during the course of the cell cycle, before dividing.¹² *E Coli* has many mobile strains, having many flagella which help in cell movement to nutrients source. It contains a single circular chromosome as shown in Figure 1.1. *E. coli*, like other gram-negative bacteria, has two membranes made up of lipids, an inner membrane and an outer membrane which includes the whole cell volume. *E. Coli* is considered as a typical, prototype representative of bacterial systems. Therefore, it has been extensively studied in the past.

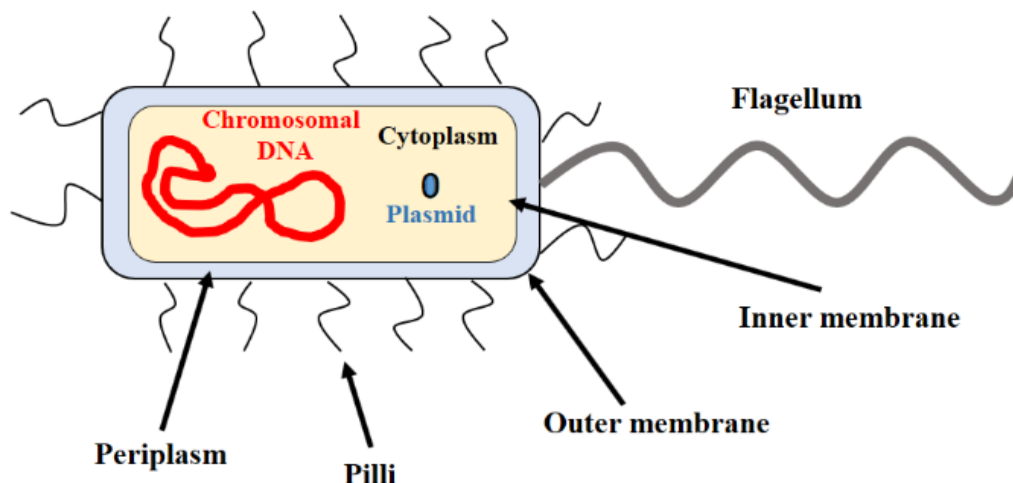


Figure 1.1. Basic *E.coli* cellular structure showing the important structural features.

1.2.1. Aerobic Respiration of *E. coli*

E. coli is generally used as a model organism as it can grow and reproduce very fast. *E. coli* is considered to be better understood than any other primitive organism. It was selected for use in demonstration of spectroscopic detection in the biosciences,⁵ and for monitoring of its aerobic respiration.¹³ The aerobic respiration of *E. coli* and subsequent O₂ consumption and CO₂ production can be monitored by spectroscopic techniques.



Equation 1 represents the reaction of aerobic respiration of converting glucose into energy. In the presence of O₂, *E. coli* will undergo aerobic respiration to produce adenosine triphosphate (ATP). On the other hand, when O₂ is not present it can convert by anaerobic fermentation or anaerobic respiration. ATP contains three phosphate groups and acts as a cellular battery. The energy is stored in the chemical bond between the second and third phosphate groups. When this bond is broken, energy is released, with the production of adenosine diphosphate (ADP).¹⁴ Therefore, cellular respiration regenerates ATP from the phosphorylation of ADP. CO₂ is produced from the metabolism of glucose which has three main components: glycolysis, the pentose phosphate pathway, and the tricarboxylic acid (TCA) cycle.^{12,15}

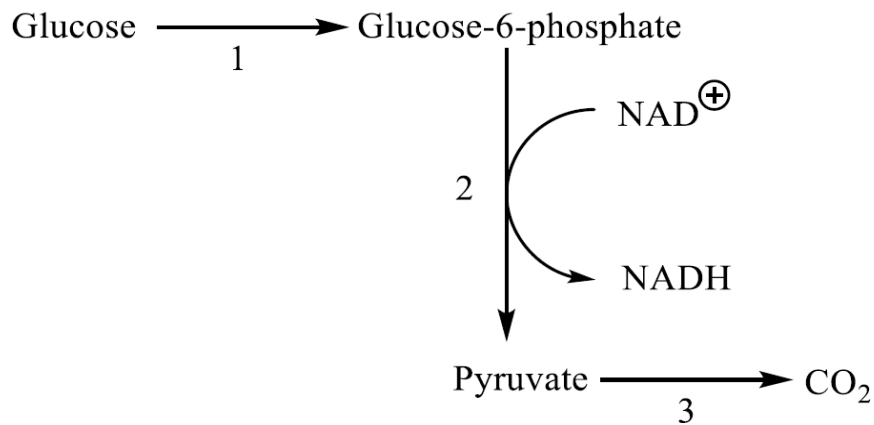


Figure 1.2. Schematic of the process of glucose oxidation to CO_2 : (1) glucose transport, (2) glycolysis, (3) pyruvate conversion to CO_2 in the TCA cycle.

Figure 1.2. shows a schematic of the process of glucose oxidation to CO_2 . In the first step glucose is transported to the inside of the cell; this is by a phosphotransferase system converting glucose to intracellular glucose-6-phosphate.¹⁶ The second step represents glycolysis which is an anaerobic pathway with a chain of several reversible steps that ends at pyruvate formation. Each stage of glycolysis produces different metabolites. The metabolites are used as starting materials for biosynthesis or for conversion to pyruvate. ATP is generated by specific steps of glycolysis from ADP as well as from reduction of nicotinamide adenine dinucleotide (NAD) from its oxidised form (NAD^+) to its reduced form (NADH). Finally, the third step represents pyruvate conversion to CO_2 in the TCA cycle; this is done via initial decarboxylation to the acetyl coenzyme, followed by an oxidation step to CO_2 .¹⁵

NADH generated in glycolysis works as the electron donor for aerobic respiration as shown in Figure 1.3. In the cytoplasmic membrane NADH is reduced to NAD^+ ; the protons being pumped from the cytoplasm to the periplasm. NADH dehydrogenase is active in both aerobic and anaerobic respiration. The reduction of NADH transfers electrons to Q (Quinone) in the cytoplasmic membrane. Cytochrome *bo* oxidase (reductase) reduces O_2 to H_2O by coupling with the oxidation of QH_2 . On the other hand, these protons are used to drive ATP synthase to produce ATP as shown in Figure 1.3.^{17,18}

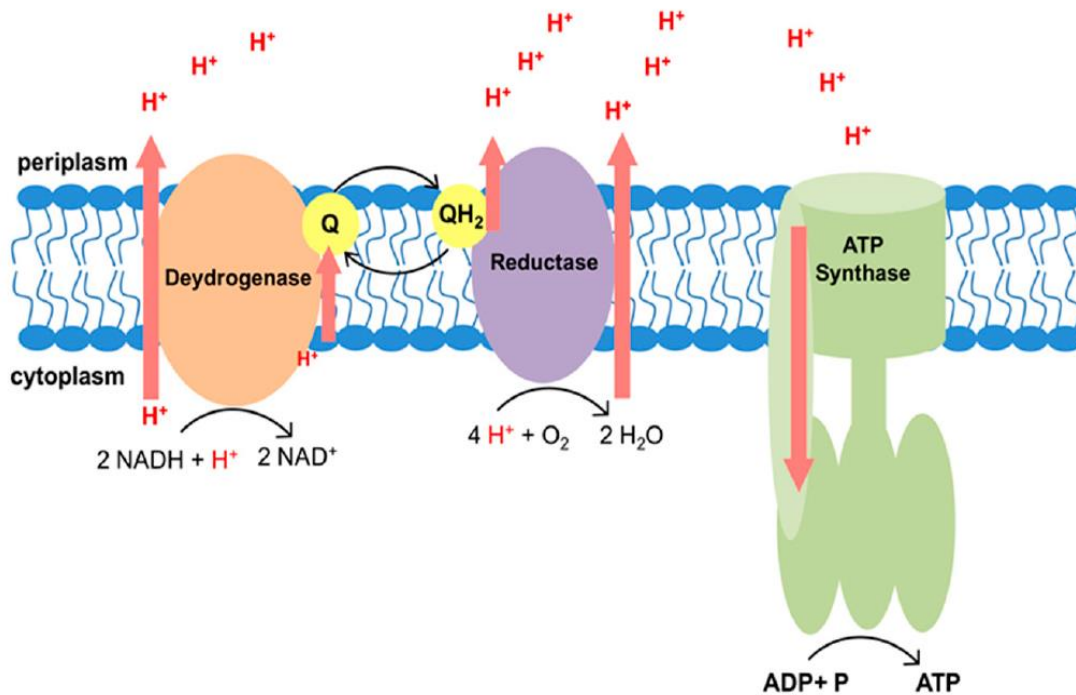


Figure 1.3. The reduction of O_2 to H_2O by cytochrome *bo* oxidase with NADH acting as an electron donor, where Q represents quinone and QH_2 represents ubiquinol, ref [18].

1.2.2. Production of Hydrogen Sulfide by *E. coli*

H_2S is a relevant gas in biochemistry and microbiology, with an important role as a signalling molecule as well as a cytoprotectant.^{19,20,21} It has been recently reported that H_2S helps defend a number of bacteria against antibiotics, including *Escherichia Coli* (*E. coli*).²¹ Understanding the mechanisms of its production by microbes may therefore be very relevant to develop new strategies to protect and enhance the potency of existing antibiotics. H_2S helps some type of bacteria to protect them against antibiotics, including *E. coli*.²¹ Hydrogen sulfide plays a protective role for increasing the potency of existing antibiotics in microbes. Although bacteria are known to produce the gas during the metabolism of sulfur compounds, the biochemistry associated with these processes is not yet fully understood.

H_2S is generated during dissolution of the sulfur-containing amino acid L-cysteine. This happens in many organisms, including *E. coli*. Cysteine desulfhydrases are enzymes which convert cysteine to pyruvate, a source of energy and a key intermediate in the production of ATP.^{21,22} This process releases one equivalent of ammonia and hydrogen sulfide.²² The amount

of ammonia and hydrogen sulfide produced during this process depend on the microbes. There are a number of different enzymes which can catalyse this reaction. In *E. coli*, all of the enzymes MalY, MetC, TnaA, CysK, and CysM can act as cysteine desulfhydrases, as shown in Figure 1.4. These enzymes also catalyse other reactions.^{23,24}

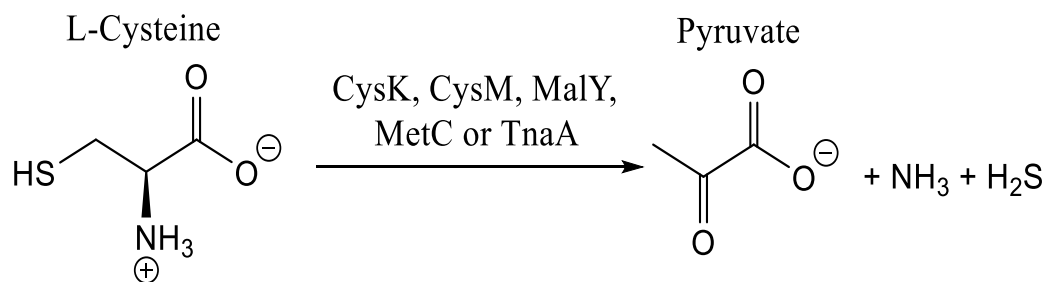


Figure 1.4. Conversion of cysteine to pyruvate by cysteine desulfhydrases, from ref [23,24].

In an alternative way to produce H₂S from cysteine, a two-step mechanism produces pyruvate by the intermediate 3-mercaptopyruvate, as shown in Figure 1.5. In the first step, the transaminase aspartate amino transferase (AspC) transfers the amino group of L-cysteine to oxoglutarate to give L-glutamate and 3-mercaptopyruvate. In the second step, the S-C bond is cleaved by 3-mercaptopyruvate sulfurtransferase (3MST) to give pyruvate and hydrogen sulfide.²⁵ Often, this second route is considered to be the major source of H₂S production in *E. coli*.²¹

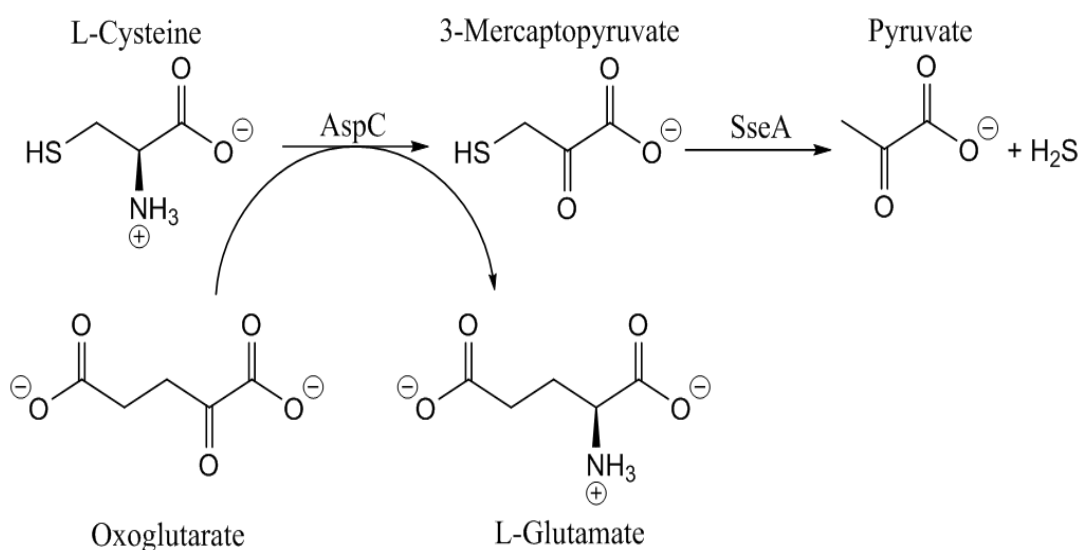


Figure 1.5. Conversion of L-cysteine to pyruvate via 3-mercaptopyruvate, from ref [25].

1.3. Literature Review of Hydrogen Sulfide in Natural Gas and Air

Multicomponent analysis of trace gases is an important topic in biochemistry and in petrochemistry for example for the analysis of natural gas. Natural gas (NG) contains different trace gas compounds, some of them toxic, with different concentrations, where the concentrations are depending on the source of NG.²

NG typically contains a mixture of hydrocarbon gases, and may include traces of H₂S, N₂, H₂ and CO₂. Methane is typically the main component with concentrations from 70 to 90%, ethane, propane, butane have typical concentrations between 0 to 20%, N₂ 0 to 5%, CO₂ 0 to 10%, H₂S 0 to 5%, H₂O vapor 0 to 2% and O₂ 0 to 0.02%. H₂S is also a trace gas with associated biological processes in sulfate-reducing bacteria.^{26,27}

H₂S is a particularly relevant trace gas due to its toxicity. H₂S is very harmful and has a bad smell. It may cause unconsciousness and even death as a result of respiratory paralysis and suffocation when exposed to high concentration levels. It is comparable in toxicity to carbon monoxide.²⁸ It has an immediately dangerous to life or health limit (IDLH) of 100 ppmv in air.²⁹ It is therefore important to be able to monitor H₂S with great sensitivity and selectivity as a toxic industrial and environmental compound. This is particularly relevant in petrochemistry since H₂S is a common minor component in natural gas (sour gas), but due to its high toxicity, it has to be removed at source before the gas can be fed to gas supply lines.^{19,20,21}

NG often contains some amounts of H₂S, this gas is then called sour gas.^{26,27} NG often comes from wells with some amount of H₂S and CO₂.³⁰ H₂S is considered problematic because it is toxic and together with water vapor it has an extremely bad effect on equipment. Furthermore, sulfur dioxide (SO₂) is the product of the combustion of H₂S which may harm the environment. Similar considerations apply to biogas. Industry thus developed a lot of purification techniques to reduce concentrations to allowable H₂S and H₂O vapor concentrations for use in commercialized natural gas.³¹ In many industrial processes, H₂S is also often released as a toxic industrial compound, therefore its concentration needs to be closely monitored.³²

There are several techniques for measuring the concentration of H₂S at ppm level, including pulsed UV fluorescence,³³ lead-acetate tape,³⁴ flame photometry,³⁵ and potentiometry.³⁶

However, there are issues with all of these individual techniques and because of that, they are not fully accepted by the NG industry for the reliable detection of H₂S.²⁶ The main issue is that these techniques suffer from uncontrolled variations in sensitivity on long-time scales.²⁶ Solid state electrochemical and chemisorbing sensors are also widely used, where a change in physical properties on adsorption of analyte gas molecules is detected, or acoustic sensors which measure changes in acoustic properties of gas mixtures.³⁷ Although detection limits in the ppm range can be achieved, these sensors often suffer from several disadvantages. Chemisorbing sensors, for example, are often affected by ageing and poisoning of the sensor surfaces, from long response and settlement times, and from interferences due to limited selectivity. Acoustic sensors have a response that depends on temperature, and the method lacks selectivity. The lead-acetate tape test is only a qualitative technique that is not suitable for quantitative analysis.

Spectroscopic detection has therefore distinct advantages. PA techniques have good long-term stability when the measured component is buffered in a relatively simple carrier gas with a fixed composition.^{26,38} The main aim of this project here was to improve a PA system to measuring trace gases in a mixture, using the intrinsic high sensitivity and long-term stability of PA. Most spectroscopic techniques are based on the detection of the molecular absorption spectrum in the infrared (IR) spectral region.^{26,27,39,40}

1.4. State of the Art of the Detection of CO₂, H₂S, O₂

Gas composition is another process parameter frequently monitored online in bioreactors. CO₂ is the main anthropogenic greenhouse gas with a current ambient level of 410 ppmv in air.⁴¹ It is also a main product of the metabolism of organisms. The ability of an analytical technique to distinguish isotopes will allow isotope labelling experiments to determine sources and sinks of CO₂. In the urea breath test for *Helicobacter pylori* (*H. pylori*), for example, patients swallow ¹³C-labelled urea. ¹³CO₂ detected in the exhaled breath indicates *H. pylori* infection in the stomach, since only this bacterium can digest urea efficiently to release ammonia and carbon dioxide. CO₂ detection is particularly relevant to study the metabolism and activity of bacteria. Monitoring of molecular oxygen (O₂) complements such metabolism studies. O₂ detection is also very relevant in biotechnology, for example to ensure that there is no oxygen in a bioreactor in anaerobic fermentation processes. O₂ and CO₂ are two key gases to consider.⁴² O₂ availability is a key parameter for aerobic bioprocesses as well as anaerobic systems that are sensitive to disruption by O₂, such as production of biohydrogen. CO₂ is a key

by-product of both aerobic respiration and fermentation and can be monitored to closely follow these processes. Dissolved gases can be monitored by gas sensitive electrode-based sensors, some of which have the advantage of not consuming the analyte. However, most sensors are invasive as they must be submerged in the microbial culture and often have a limited lifespan under operating conditions of the bioreactor due to poisoning. Online, solution-based sensors create challenges such as the requirement for including an additional port on the bioreactor, increased risk of contamination and challenges associated with sterilisation and the need to frequently calibrate the sensor, which is often impossible without process contamination. Disadvantages also include interferences with other components, ageing, temperature dependence, and long response and settlement times. The measurement of partial pressures in the effluent headspace gases can give a good approximation of dissolved gases *via* Henry's law and eliminates the need to use invasive devices. Gas chromatography (GC) and mass spectrometry (MS) are two common methods of gas phase analysis. High sensitivity O₂ measurements are performed by taking gas samples for analyses of O₂ by using GC in combination with mass spectrometry (GCMS) to determine O₂/N₂ ratios.⁴¹ Both these techniques require sampling, are expensive, require frequent calibration, they are slow and have limitations, including difficulties detecting certain components. Also, chromatographic techniques rely upon the spatial separation of the compounds that are being quantified, and so are only of use on a non-continual basis.¹⁴

In trace gas analysis, spectroscopic detection has distinct advantages due to its quantitative nature, its sensitivity and selectivity due to the very characteristic spectroscopic signature of different molecules. Spectroscopic methods for gas phase analysis offer numerous benefits including high precision and accuracy, no sampling is necessary and it has the ability to perform non-invasive real-time measurements. Detection by optical absorption is possible for CO₂ and H₂S using strong fundamental vibrational bands in the mid-IR, or much weaker overtones and combination bands in the near-IR. Although weaker, near-IR absorption offers the advantages of much more convenient optics and light sources in the near-IR. Molecular oxygen (O₂) does not have an IR-active vibration; although Raman detection of its fundamental is possible, Raman scattering is a rather weak process and special Raman enhancement techniques are required to detect gases at the ppmv level, for example by stimulated Raman photoacoustic spectroscopy (PARS)¹ or the recently introduced technique of cavity-enhanced Raman spectroscopy (CERS)^{2,3,9} O₂ can be detected by a formally forbidden electronic absorption band in the red, the $b^1\Sigma_g^+ (\nu = 0) \leftarrow X^3\Sigma_g^- (\nu = 0)$ band (the "A band") near 760 nm; although weak,

the absorption cross sections are comparable to near-IR overtone and combination band absorptions of CO₂ and H₂S. For efficient detection beyond the limitations of conventional, Beer-Lambert type absorption, absorption pathlengths should be as long as possible, as in the extreme case of cavity ringdown spectroscopy which achieves km effective pathlengths^{43,44,45,46,47} or detection should be coupled with a background-free scheme as in photoacoustic spectroscopy,^{6,7,48,49,50,13,51} or a combination of both as in the recently introduced technique of cavity-enhanced resonant photoacoustic spectroscopy, CERPAS.^{10,52}

Detection in the near-IR has the advantage of low-cost light sources and detectors; the sensitivity, however, suffers due to low absorption cross-sections. In addition, relevant homonuclear molecules including O₂ cannot be observed by IR-absorption due to unfavourable selection rules. Molecular O₂ has two main absorption bands in its UV-vis spectrum, one deep in the UV at 145 nm and the other at 760 nm.^{15,16} O₂ detection at 145 nm faces interferences by water vapour and CO₂ and the weak absorption lines at 760 nm typically provide detection limits that are of little practical use.

In photoacoustic spectroscopy, internal excitation of molecules by optical absorption is converted to heat release and pressure increase by collisions; if the excitations are modulated periodically, acoustic waves are induced which can be picked up by microphones. This is indirect, but a very sensitive detection of optical absorption. By detecting in an acoustic resonator and modulating at an acoustic resonance frequency, building-up of acoustic standing waves further increases sensitivity in resonant photoacoustic spectroscopy.^{6,7} Highest sensitivities are achieved with CERPAS^{10,52} or with excitation of the acoustic modes of a quartz tuning fork (quartz enhanced or cantilever enhanced photoacoustic spectroscopy).^{51,53} With the quartz tuning fork and a 30 mW DFB laser, a noise-equivalent detection limit of 20 ppm for O₂ was achieved before, corresponding to a noise-equivalent normalized detection limit of $4.8 \times 10^{-9} \text{ cm}^{-1} \text{ W Hz}^{-1/2}$, which is the detection limit normalized to the absorption cross section, the laser power and integration time.⁵¹ Also, the setup for the quartz enhanced or cantilever enhanced photoacoustic spectroscopy has been applied to detect CO₂, based on a recently demonstrated cantilever technique.⁵³ For detection of CO₂ at 1572 nm wavelength, the noise-equivalent normalized detection limit of $1.4 \times 10^{-10} \text{ cm}^{-1} \text{ W Hz}^{-1/2}$ was achieved. A much simpler approach to photoacoustic spectroscopy of CO₂ and O₂ is employing a special acoustic resonator which effectively amplifies signal and reduces noise in a differential Helmholtz resonator (DHR).^{49,13,54,55}

A cantilever-enhanced photoacoustic spectroscopy (CEPAS) setup, using a detector in combination with a telecom NIR L-band laser source, was used as a sensitive method for the detection of different pressure levels of H₂S. A detection limit (3σ) of 8 ppmv was achieved with an averaging time of 50 s for the H₂S absorption near 1.6 μm .³² Also, H₂S concentrations of several ppb have been detected by employing an integrated cavity output spectroscopy approach (ICOS).^{26,56} Quartz-enhanced photoacoustic (QEPAS) was used before for gas sensing H₂S detection. The system architecture is based on a custom quartz tuning fork (QTF) optoacoustic transducer with a novel geometry and a quantum cascade laser (QCL) as light source.²⁷ The detection limit of the measurement is 30 ppm with integration time 3 s and 13 ppm for a 30 s integration time. An industry-tailored H₂S sensor has been developed with very high selectivity requirements achieved by employing a dual-channel longitudinal-type PA resonator cell with capacitive microphones; it used a telecommunication-type diode laser with a wavelength of 1574.5 nm and an output optical power of 40mW. The detection limit for H₂S in NG was reported as 0.5 ppmv.²⁶

FT-IR or diode laser near-IR spectroscopy is widely used in analytical chemistry, but it can be quite difficult to detect some molecules such as diatomic homonuclear molecules like O₂ or N₂. Detection of these homonuclear diatomic molecules would be useful for monitoring NG and trace gases in the environment where these gases can be minor components, or for the monitoring of the purity of biofuels or hydrogen gas produced by biotechnology or alternative energies.² Due to different selection rules, Raman spectroscopy can monitor all relevant components, including these diatomic homonuclear molecules.^{2,57,58} Raman detection of NG typically requires high power lasers and high sample pressures in order to achieve suitable sensitivity.^{58,59} The resonance enhancement of CERS, however, is suitable with the use of low cost diode lasers for monitoring of NG mixtures, including monitoring H₂, H₂S, N₂, CO₂, and alkanes.^{2,60}

1.5. Aims and Thesis Structure

This project is interested in the application of advanced spectroscopic techniques to study gases in biology and biochemistry, and to analyse natural gas for components such as O₂, CO₂ and H₂S. The ability to detect these gases by spectroscopic techniques is of increasing importance due to their references in the biosciences and in trace gas analysis. There are many different analytical techniques that have different disadvantages such as the difficulty in detection of gases *in situ*, or limited selectivity or sensitivity. Therefore, detection methods capable of selective detection of biologically relevant gases *in situ* are very relevant, and the development of such methods is important.

We also introduced first applications, including time-dependent monitoring of the bacterial growth and aerobic metabolism of microbes (*E. coli*, supplemented with ¹²C and ¹³C labeled sugars), and detection of H₂S impurities in natural gas.

This thesis is structured as follows:

Chapter 1

The aims of this chapter are a full literature review of the detection of CO₂, O₂ and H₂S by various spectroscopic and non- spectroscopic techniques. In addition, a literature review of production of CO₂, and H₂S by microbes is provided.

Chapter 2

The aims of this chapter are to provide an overview of spectroscopic techniques which are used in this research. A full and detailed description of the photoacoustic spectroscopy in an acoustic differential Helmholtz resonator (DHR) and Cavity Enhanced Raman spectroscopy (CERS) is given.

Chapter 3

The aim of this chapter is to introduce the relevant theory, principles and selection rules behind molecular vibrational and rotational spectroscopic techniques (Raman and IR spectroscopies).

Chapter 4

This chapter describes a new home-built system, photoacoustic spectroscopy in an acoustic differential Helmholtz resonator (DHR). In this chapter, the characterisations of this system, including; detection limit, sensitivity, laser power, and wavelength tuneability is explained.

Chapter 5

The aims of this chapter are to demonstrate two techniques for the monitoring of the headspace gases coming from microorganisms by using Cavity Enhanced Raman spectroscopy (CERS) and Photoacoustic spectroscopy where a differential Helmholtz resonator (DHR) is used. The simultaneous measurements of O₂ consumption and CO₂ production by *E. coli* can be achieved using CERS and DHR in photoacoustic spectroscopy. *E. coli* growth in a medium supplemented with sugars will allow detection of changes in the metabolic activity. Spectroscopy can distinguish between isotopomers: the experiment with mixed sugars to feed *E. coli* will demonstrate that spectroscopic headspace gas detection can be used to investigate metabolic preferences. The carbon source metabolism of aerobic *E. coli* will be investigated using a mix of two labelled sugars such as ¹³C-glucose and ¹²C-lactose. Therefore, ¹³CO₂ from glucose is expected to be produced preferentially to ¹²CO₂ from lactose, before a potential diauxic shift to lactose metabolism.

This chapter also describes using photoacoustic spectroscopy in a differential Helmholtz resonator to detection trace gas CO₂, O₂ and H₂S in natural gas and in the cysteine metabolism of microbes (*E. coli*). A DFB diode laser near 1.57 μm is used for CO₂ and H₂S detection, and O₂ detection near 760 nm. The set-up has been used for simultaneous *in situ* monitoring of O₂, CO₂ and H₂S.

The thesis then finishes with **Chapter 6**, conclusions and future work, and the **Appendix**.

Chapter 2. Overview of Spectroscopic Techniques

2.1. Introduction

The reliable, sensitive and selective detection of trace gas levels is very relevant for environmental monitoring, industrial process control and biological applications. CO₂, O₂ and H₂S are particularly relevant. The work presented in this thesis aims to work with, and make improvements to, vibrational gas-phase spectroscopies in the monitoring of gas metabolism by microbes and multicomponent analysis of natural gas. Two complementary approaches to optical gas detection are presented: photoacoustic spectroscopy (PA) in a differential Helmholtz resonator (DHR) and Cavity-Enhanced Raman spectroscopy (CERS).

2.2. Photoacoustic Spectroscopy

The photoacoustic effect, also called optoacoustic effect, was discovered in 1880 by Alexander Graham Bell first in solids and then in gases.⁶¹ He found that thin discs emitted sound when exposed to a rapidly intermittent beam of sunlight. Sunlight was collimated by a mirror and associated optics in order that the light which is reflected by the mirror could be collected by the remotely placed receiver which consisted of a parabolic mirror at which focus a cell of selenium was incorporated into a conventional telephone loop, as shown in Figure 2.1.⁶²

Until *ca.* 1970, this technique was only used in some special cases to determine the absorption of a gas as a function of the wavelength, but due to the lack of suitable light sources (lasers), photoacoustic spectroscopy (PAS) did not provide significant advantages compared to conventional absorption spectroscopy. In 1938, M. L. Viengerov used PAS to analyse gases, but the results were limited due to the microphone's sensitivity and the effects of unwanted light.⁶¹ Between 1978 and 1980, multiple wavelength PAS was developed, particularly PA Fourier transform infrared spectroscopy.⁶³ Since the 1980s, PAS has become a valuable analytical technique with developments in lasers, low noise electronics, very high sensitivity microphones, computerised data handling and analysis.^{61,64}

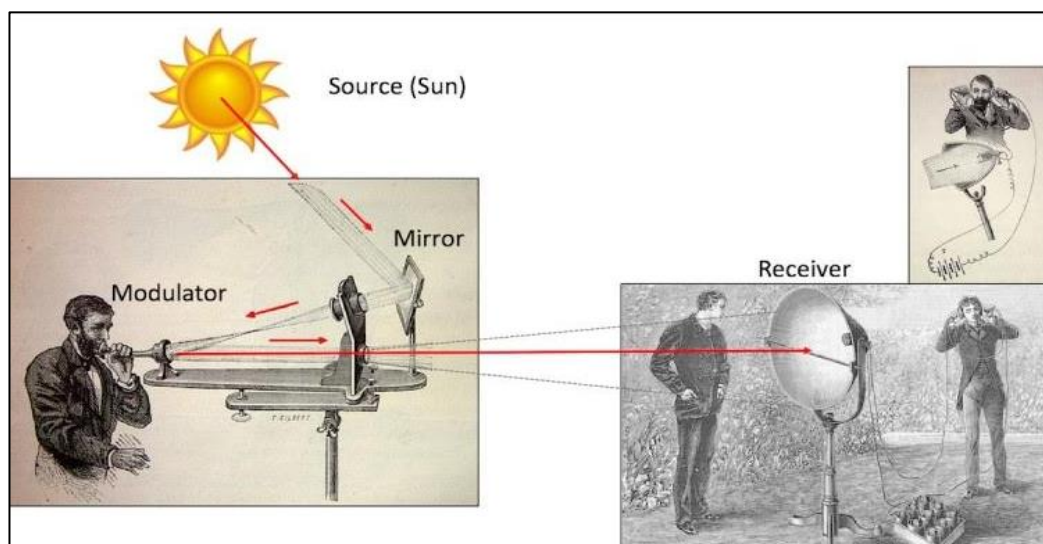


Figure 2.1. Principle of Bell's Photophone, ref [65].

Photoacoustic spectroscopy is a widely used method, with many different applications, such as; environmental pollutants monitoring, medical diagnostics, industrial process control, life sciences, and detection of gas leaks in hazardous work environment.^{54,13,66,67} Each of these applications requires high sensitivity, high selectivity, short response time and small mobile instruments, which makes photoacoustic spectroscopy a good candidate to meet these needs.⁶² PAS is considered one of the most advanced spectroscopic techniques for measuring trace gases with low concentrations fewer than ppm.^{68,69} In the following, a description of the principle is given.

2.2.1. Description of the Photoacoustic Effect in Gases

The photoacoustic effect results in the generation of sound when an absorbing material is illuminated with modulated or pulsed light. The effect of the PA can be divided in the following steps:

- Molecules absorb light to get excited.
- Excited molecules vibrate and collide which generates heat.
- Heating of the sample material following the absorption of the photon via relaxation through collisions between molecules.
- The localised heat causes gases to expand and contract which creates an acoustic wave by the periodic pressure change, if excitation occurs periodically.
- Detection of the acoustic signal in the PA cell using a microphone.

Generally, when photons are absorbed by the material, internal energy levels (rotational,

vibrational, and electronic) within the sample are excited. The excited molecules will collide with other molecules, resulting in the change of the absorbed internal energy into heat. Emission of radiation and chemical reactions do not play an important role, because vibrational levels have such a long excited-state lifetime that only collisional deactivation is relevant at pressures that are commonly used in PAS. Also, in general the energy of an absorbed photon is too small to induce chemical reactions, so in practice, the absorbed energy is completely released thermally where a pressure is built-up within a gas cell. The transfer rate of this wave is determined in the material by the speed of sound. Local transient heating and expansion generates thermal and acoustic waves if excitation occurs periodically. This sound is then detected using a sensitive microphone.⁷⁰ The process is shown schematically in Figure 2.2.

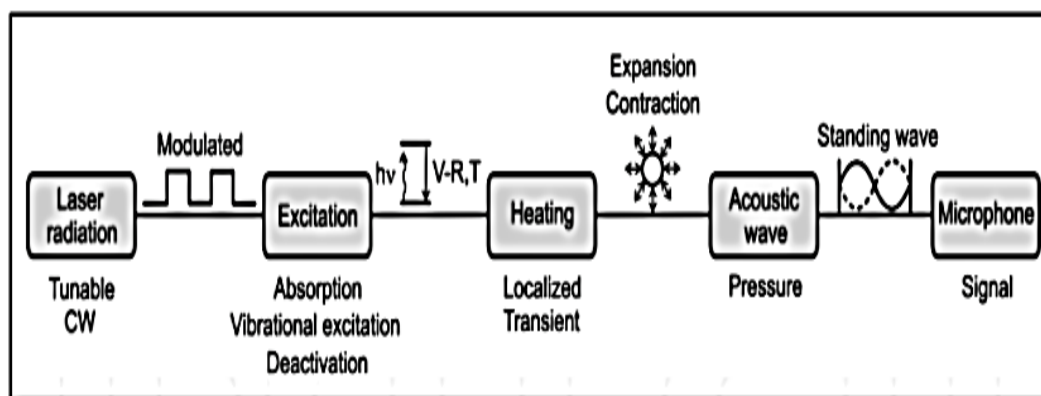


Figure 2.2. Schematic of the physical mechanism of photoacoustic signal generation, ref [71].

The main advantage of the PAS technique is that it is essentially background free, that means no signal is produced in the absence of the absorbing gas species. Using a sensitive microphone, detection limits in the low ppm to ppb per volume range are routinely achieved, *in situ* and in real time. As a further advantage, the size of the PA cell is small, so only a small sample size is needed.^{54,67,72}

2.2.2. Standard PAS

Standard PAS uses a modulated laser beam in an acoustic resonator filled with a weakly absorbing gas.⁷ The acoustic resonator allows an acoustic standing wave to build up which increases the signal.

The PA signal measured by the microphone (S) is given by Equation 2:

$$S = C \cdot P \cdot \alpha \quad \text{Equation 2}$$

where C is the cell constant, dependent on cell dimension and modulation frequency, P the optical power output of the laser. α is the coefficient of absorption which is related to the gas concentration (c , the molecules' number density) and absorption cross section (σ) by Equation 3.

$$\alpha = c \cdot \sigma \quad \text{Equation 3}$$

The constant of the cell depends on the cell geometry, the beam profile, the response of the microphone and the nature of the acoustic mode excited.⁷³

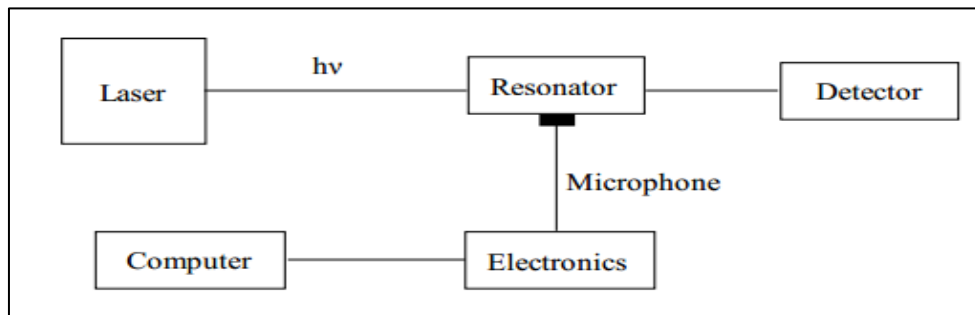


Figure 2.3. Typical setup of PA, ref [73].

A typical PAS setup consists of a beam source, the PA cell, a modulator, signal acquisition equipment and processing equipment. A schematic diagram is shown in Figure 2.3. The modulated laser beam is passed through the PA cell, which is filled with gaseous sample, to excite acoustic modes which are radial and longitudinal, thus generating acoustic waves. The acoustic waves are then picked up by a microphone and amplified by a lock-in amplifier. Once the signal has been amplified, it is sent to the computer in order to record the spectrum. In the acoustic mode of the resonator, the absorbed laser power is accumulated for Q oscillation periods, where Q is the quality factor, usually in the range of 10–300.⁷³ The quality factor Q is a key parameter that takes into account the accumulated sound energy and losses in the PA system. The quality factor Q of the acoustic resonance is defined in Equation 4:

$$Q = \frac{f_0}{\Delta f} \quad \text{Equation 4}$$

where f_0 is the resonance frequency of the resonator and Δf is the half width of the resonance peak. The half width Δf is measured between the points where the amplitude is $1/\sqrt{2}$ value of the amplitude of the peak. A high Q factor means that the resonant PA system has a higher resonance amplitude.^{7,73} In this project, a somewhat special acoustic resonator is used, a differential Helmholtz resonator which is described in detail later.

2.2.3. Resonant Cell Design

A photoacoustic cell can be operated in two different ways, either at an acoustic resonance frequency specific to the PA resonator or in non-resonant mode. In the non-resonant mode, the acoustic resonance frequency of the PA resonator is much higher than the modulation frequency. In this case, an acoustic wave is generated that has a wavelength larger than that of the dimensions of the cell. Therefore, standing acoustic waves cannot be generated and acoustic enhancement is impossible.⁷⁴

The PA signal is proportional to the absorption path length, and it is inversely proportional to the cell volume and the modulation frequency, therefore small cell volumes ($<10 \text{ cm}^3$) and low modulation frequencies ($<100 \text{ Hz}$) give higher PA signal levels.⁷ It is desirable to keep the volume of the sample as small as possible to reduce the amount of sample gas needed, which reduces the system size. On the other hand, longer absorption path length leads to a larger signal and better signal-to-noise-ratio (SNR). Noise levels are of importance in the measurements of trace gases at ultralow gas concentrations. Noise levels determine the final detection limits. In PA, the detection limit is normally defined by multiples of the signal to noise ratio (SNR).⁷ In resonant mode, an acoustic standing wave can build up. A resonant cell commonly consists of a resonator, microphone, and buffer volumes. The basic and most common type is the open-tube cylindrical resonator. It is basically an organ pipe resonator. Typically, there are three modes of different acoustic resonance which are longitudinal, azimuthal and radial modes, as shown in Figure 2.4.

The acoustic resonance modes depend on the cell structure. There are three types of acoustic resonators which have found common use in photoacoustic detection: one-dimensional cylindrical resonators, Helmholtz Resonators, and cavity resonators.^{54,69}

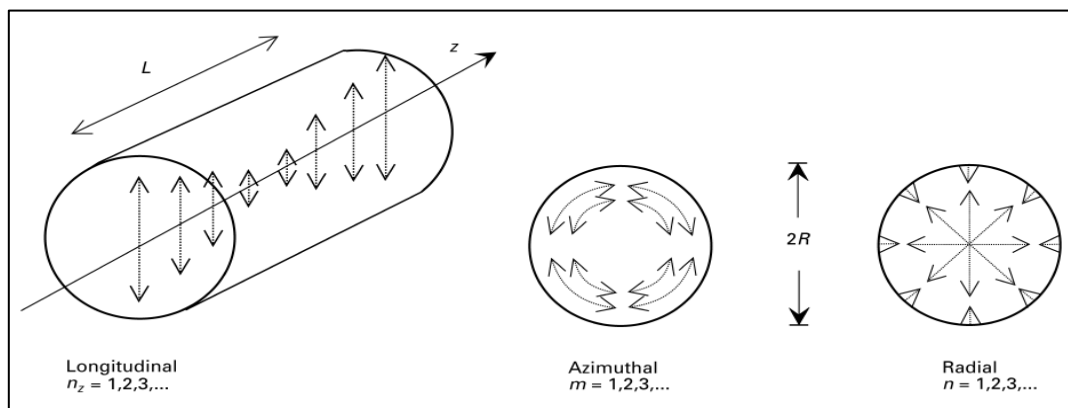


Figure 2.4. The longitudinal, azimuthal and radial acoustic modes in a cylindrical resonator are shown in this scheme, ref [70]

2.2.4. Helmholtz Resonator (HR)

A Helmholtz Resonator (HR) typically consists of two volumes V_1 and V_2 connected together by a thin capillary.^{13,54} Figure 2.5 shows different kinds of Helmholtz Resonators. The most common HR type is a differential Helmholtz resonator (DHR) with two compartments connected by a capillary. A DHR is basically similar to a harmonic oscillator. The mass of air occupying the capillary tube between the two identical chambers behaves as the weight in a common harmonic oscillator. At the resonance frequency in the cell, the laser light is absorbed by molecules inside one compartment, the gas inside this chamber will expand and therefore resulting in the compression of the gas in the other chamber via the capillary connection acting as a piston. In this way, acoustic pressure is generated by periodic oscillation of the piston with periodic expansion and pressing of air. The acoustic waves in the two compartments are identical but have a 180° phase difference. One can estimate the resonance frequency f_0 of such a resonator by Equations 5 and 6.^{75,76}

$$f_0 = \frac{\mu}{2\pi} \sqrt{\frac{A}{V_{eff} l}} \quad \text{Equation 5}$$

$$V_{eff} = \frac{1}{\frac{1}{V_1} + \frac{1}{V_2}} \quad \text{Equation 6}$$

where μ , A , V and l are the sound speed, the capillary cross section, the volume in the two chambers and the length of the capillary, respectively. Compared to other resonators, the DHR has some advantages like small volumes of sample with low resonance frequency and the possibility to enhance the SNR by using differential microphone detection schemes⁷⁶

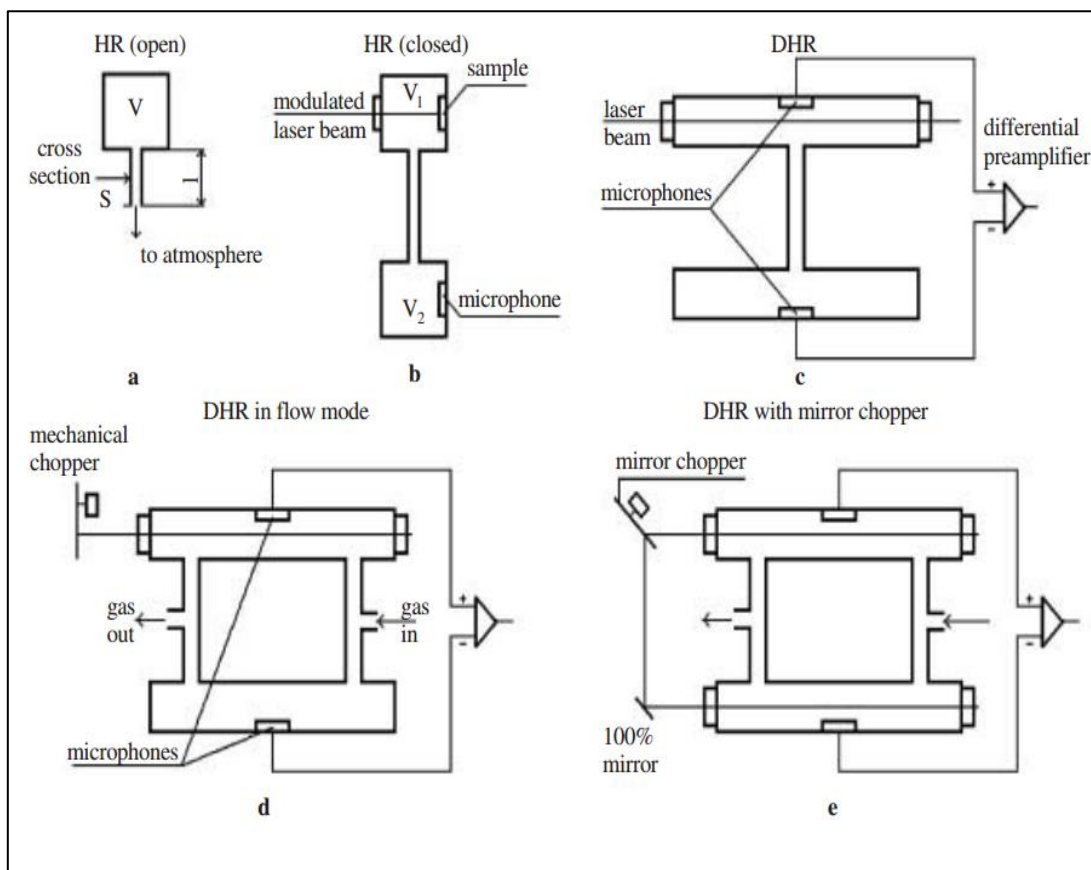


Figure 2.5. Several designs of Helmholtz Resonator acoustic cell: (a) (HR) open to the atmosphere; (b) (HR) with 2 chambers to separate sample and detection chambers for solid samples; (c) Differential HR (DHR) which gives doubling of the acoustic signals and also noise cancellation; (d) DHR with 2 capillaries for gas flow mode and 2 chambers; (e) DHR with mirror chopper and additional amplification of acoustic signals. Ref [75].

2.2.5. The Differential Helmholtz Resonator (DHR)

The Differential Helmholtz Resonator (DHR) design is the most popular HR used in trace gas analysis.^{13,54} The DHR can amplify the signal amplitude and significantly improve the external noise cancellation at the same time.^{13,48,49,54} A schematic of the resonator which is used in the present project is shown in Figure 2.6. A DHR typically has a smaller cell volume and lower resonance frequency when compared to basic PA cells. DHRs measure the difference of the signals which are picked up by the two microphones from both chambers. Since photoacoustic signals have a 180° phase difference in the chambers, taking the difference signal of the microphone response doubles the PA signal. However, the gas flow in and out of the DHR is symmetrical, thus the gas flows through the two chambers under same conditions (flow rate, flow noise i.e.). This case generates an in-phase gas flow noise (acoustic noise) in both

chambers, and the gas flow noise thus cancels out by the differential detection. The same applies to external noise which will affect both chambers in the same way, with the same amplitude and phase. By this joint effect, doubling of signal and noise cancellation, the DHR has a high SNR.

There are several advantages of using DHR; they include high sensitivity of microphones, high signal-to-noise (S/N) ratio, trace gas detection, flow measurements are possible, it can operate in noisy environments, low cost and the simplicity of the design.

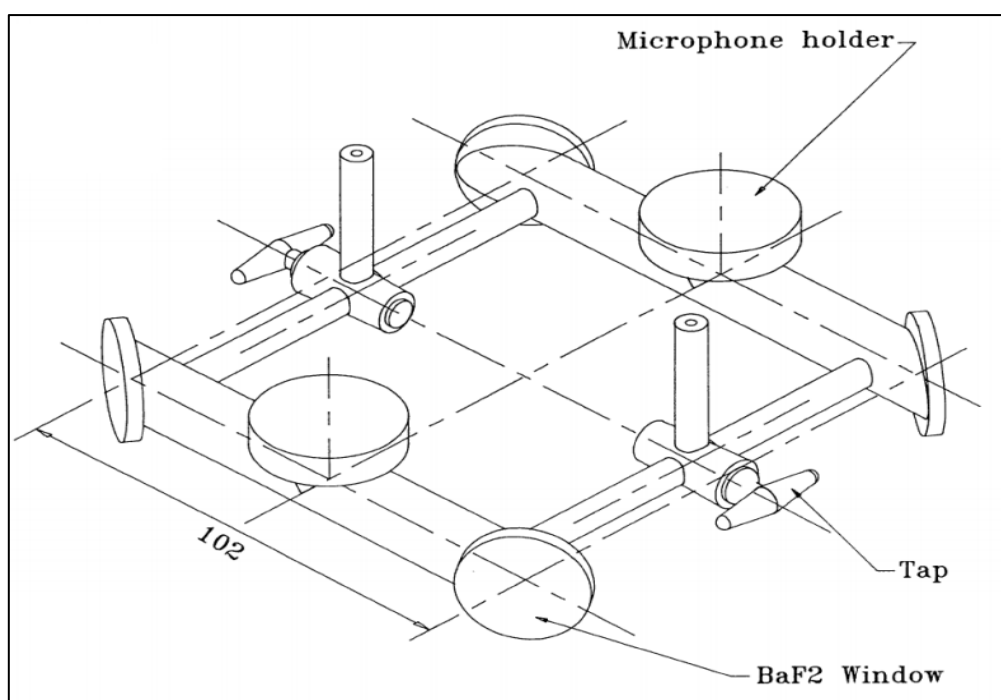


Figure 2.6. Differential Helmholtz Resonator (DHR), ref [76].

2.3. Cavity-Enhanced Raman Spectroscopy (CERS)

Cavity-enhanced Raman spectroscopy (CERS) is a new technique, recently developed in the Hippler group.^{2,5,10,11} This technique has uses in gas sensing applications such as analysis of natural gas and for a number of isotopic labelling studies using ^{14}N and ^{13}C isotopes. CERS is very selective due to high spectral resolution, and its high sensitivity allows trace gas detection in multicomponent analyses. The technique takes advantage of the build-up of laser power inside an external optical cavity which consists of two highly reflective mirrors ($R > 99.99\%$) arranged to be parallel in a linear geometry as shown in Figure 2.7. If the laser frequency is stabilised with this cavity's resonance frequency, light can be efficiently coupled

into the cavity and power build up can occur by numerous orders of magnitude.^{10,77,78,79} This power build-up within an optical cavity can be used to enhance the efficiency of spontaneous Raman spectroscopy (cavity-enhanced Raman spectroscopy, CERS).⁸⁰ Continuous wave (cw) diode lasers are particularly suitable for CERS and gas sensing; generally cw lasers have a very small footprint, low power consumption, low cost, wide wavelength range (from the MIR to near-UV) and the laser wavelength can be tuned through changes in temperature or by feedback from an optical element such as a diffraction grating.

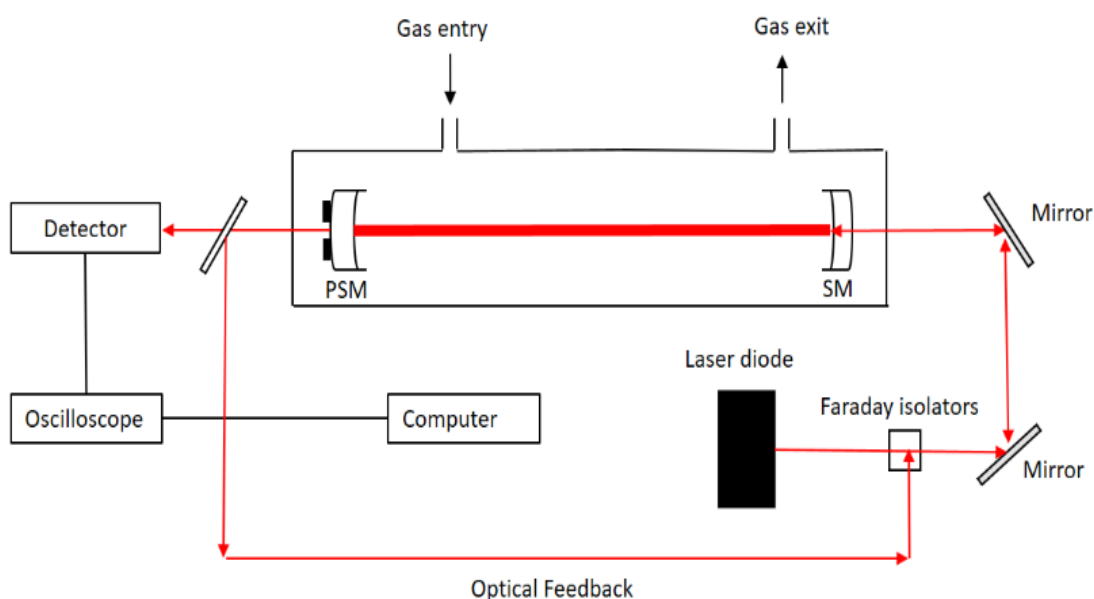


Figure 2.7. Typical setup of CERS, where SM and PSM are concave highly reflective mirrors.

In 2012, Salter, Chu and Hippler³ introduced a novel approach where a standard 635 nm diode laser (without an antireflection (AR) coating) is coupled into an external linear optical cavity. The laser is stabilised to the cavity by optical feedback from light exiting the cavity. This allows better feedback control with single mode operation and avoids direct back-reflections to the source,³ as shown in Figure 2.7. Build-up of the light power by three orders of magnitude occurs. Raman light is collected in a forward scattering collection geometry (more details in chapter 5).

The principle of cavity enhancement, including the effect of mirror reflectivity within the region of Raman emission, is discussed in many publications by the Dr Hippler group, and the apparatus performance was characterised by recording Raman spectra of H₂, air, CH₄, NG and benzene vapour. It was shown that CERS is a powerful technique for selective, sensitive, and quantitative gas phase analysis.

Chapter 3. Theory of Vibrational and Rotational Spectroscopy

3.1. Introduction

Infrared and Raman spectroscopy are techniques that induce transitions between the vibrational states of molecules. IR radiation absorption by a molecule causes transitions between two vibrational states of the molecule. IR and Raman spectroscopy have different selection rules for which energy level transitions are allowed and can be detected. IR spectroscopy requires a change in electric dipole moment for a vibrational transition to be IR active, such as the asymmetric stretching vibration of CO_2 . Raman spectroscopy requires a change in polarizability for a vibrational transition to be Raman active, such as the symmetric stretching vibration of homonuclear diatomic molecules. In this chapter, the theory, quantum mechanics, and the selection rules for IR and Raman spectroscopy are introduced. The material discussed here is adapted from several sources, including Dr Michael Hippler's lecture course on Advanced Spectroscopy, J. Michael Hollas' text book 'Modern Spectroscopy' and Peter Atkins' textbook 'Physical Chemistry'.^{81,82}

3.2. Kinetics of Radiation Transitions

3.2.1. Einstein Coefficients

In 1916, Albert Einstein suggested that there are three processes occurring in the interaction of light with matter. The three processes are referred to as spontaneous and stimulated emission, and absorption, as shown in Figure 3.1. With each is associated an Einstein coefficient which is a measure of the probability of that particular process occurring.

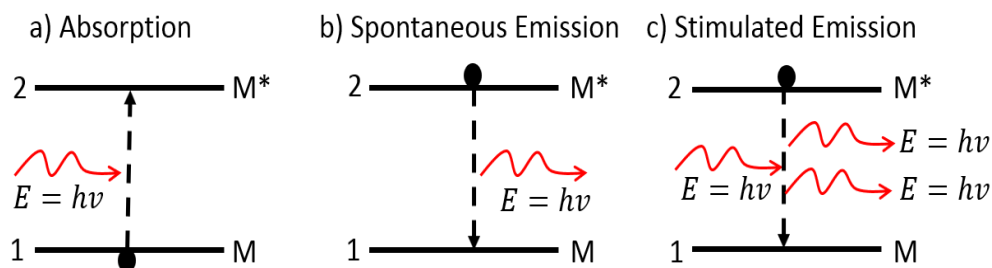


Figure 3.1. The three primary processes of interaction of light with matter.

a) Absorption

Absorption is the process by which an atom or molecule absorbs the photon, that is causing a jump from a lower energy level to a higher energy level, as shown in Figure 3.1. The process is described by the Einstein coefficient B_{12} as in Equation 7

$$-\frac{d[M]}{dt} = B_{12} [M]\rho(\nu) \quad \text{Equation 7}$$

where $[M]$ is concentration of molecules in state 1, $(\frac{1}{m^3})$, ρ is the photon energy per volume per frequency interval $(\frac{J}{m^3s^{-1}})$, and B_{12} is the Einstein coefficient for absorption $1 \rightarrow 2$, $(\frac{m}{kg})$.

b) Spontaneous Emission

In spontaneous emission, the atom or molecule decays "spontaneously", without any outside influence, from a higher energy level to a lower one, as shown in Figure 3.1. The process is described by the Einstein coefficient A as in Equation 8

$$+\frac{d[M]}{dt} = A [M^*] \quad \text{Equation 8}$$

where A is the Einstein coefficient for spontaneous emission (s^{-1}).

c) Stimulated Emission

In stimulated emission, an atom or molecule is induced to jump from a higher energy level to a lower one by the presence of electromagnetic radiation at the frequency of the transition, as shown in Figure 3.1. The process is described by the Einstein coefficient B_{21} as in Equation 9

$$+\frac{d[M]}{dt} = B_{21} [M^*]\rho(\nu) \quad \text{Equation 9}$$

where B_{21} is the Einstein coefficient for the transition $2 \rightarrow 1$.

Analysis using the Einstein's coefficients and the Equations 7 to 9 applying to thermal equilibrium under certain conditions can obtain relations between these coefficients. Assuming the detailed balance is achieved between the spontaneous emission, the absorption and the stimulated emission, Equation 10 is obtained at equilibrium.

$$\frac{d[M]}{dt} = 0 = A[M^*] + B_{21}[M^*] + B_{21}[M^*]\rho(\nu) - B_{12}[M]\rho(\nu) \quad \text{Equation 10}$$

1) Suppose $T \rightarrow \infty$: $\rightarrow \rho \rightarrow \infty$: $B_{21}[M^*]\rho - B_{12}[M]\rho = 0$ $A[M^*]$ is negligible

$$\rightarrow [M^*] = [M] : B_{21} = B_{12} \equiv B$$

This shows that the Einstein coefficients for absorption and stimulated emission are the same.

2) Suppose to have T . Use $B_{21} = B_{12} = B$ in (10), use $\rho(\nu) =$ Planck's blackbody expression in (10). Further, use the Boltzmann distribution as in Equation 11

$$\frac{[M^*]}{[M]} = e^{-\Delta E/kT} \quad \text{Equation 11}$$

And finally use $\Delta E = h\nu$ (photon energy) in (10). After some manipulation, this will give

$$\frac{A}{B} = \frac{8\pi}{C^3} h\nu^3 \quad \text{Equation 12}$$

This shows that all Einstein coefficients are related. Quantum theory further shows that A can be calculated *ab initio* by Equation 13

$$A = \frac{64\pi^4\nu^3}{3hc^3(4\pi\epsilon_0)} \int \Psi_1 \bar{\mu} \Psi_2 dV \quad \text{Equation 13}$$

The wave functions Ψ_1 and Ψ_2 of the combining states are related to the Einstein coefficients through the transition moment R_{12} , a quantity given by Equation 14.

$$R_{12} = \int \Psi_1 \bar{\mu} \Psi_2 dV \quad \text{Equation 14}$$

where $\bar{\mu}$ is the transition moment operator, usually the electric dipole moment operator as shown in Equation 15

$$\bar{\mu} = \sum_i q_i \vec{r}_i \quad \text{Equation 15}$$

3.3. Beer-Lambert Absorption Law

For efficient detection beyond the limitations of conventional, Beer-Lambert type absorption, absorption pathlengths should be as long as possible, as in the extreme case of cavity ringdown spectroscopy which achieves km effective pathlengths.^{43,44,45,46,47} Conventional optical absorption spectroscopy methods are based on the Beer-Lambert law as defined by Equation 16 and 17. According to this law, the attenuation of light is proportional to the concentration of the absorbing sample $[c]$, the path length (L) of absorption, the material specific absorption cross-section (σ) and the molar absorptivity (ϵ). Absorbance is defined, using the natural logarithm as in Equation 18, or using the decadic logarithm as in Equation 19.

$$-\frac{dI}{dx} = \sigma \cdot [c] \cdot L \quad \text{Equation 16}$$

$$I = I_0 \cdot e^{-\sigma[c] \cdot L} \quad \text{Equation 17}$$

$$A = \sigma \cdot [c] \cdot L = \ln\left(\frac{I_0}{I}\right) \quad \text{Equation 18}$$

or alternatively, using the decadic logarithm,

$$A = \epsilon \cdot [c] \cdot L = \lg\left(\frac{I_0}{I}\right) \quad \text{Equation 19}$$

There is a relation between the absorption cross section σ and the Einstein coefficient of absorption B , as shown in Equations 20,21.

$$-\frac{dI}{dx} = B \cdot g(\nu) \cdot [c] \cdot g(\nu) \quad dr \quad \text{Equation 20}$$

where $g(\nu)$ is line shape function of the absorption line.

Comparison with the Beer-Lambert Equation shows

$$\sigma(\nu) = B \cdot g(\nu) \cdot \frac{h}{c} \cdot \nu$$

and after integration over the absorption line, Equation 21 is finally obtained showing the relationship between the absorption cross-section σ and the Einstein coefficient B .

$$\int \frac{1}{\nu} \sigma(\nu) d\nu = B \frac{h}{c} \quad \text{Equation 21}$$

where $\int \frac{1}{\nu} \sigma(\nu) d\nu$ is the integrated absorption line strength.

3.4. Vibrational Spectroscopy and Selection Rules for Diatomic and Polyatomic Molecules

Gases have absorption bands in the IR, visible and UV regions. IR absorption bands are due to vibrational-rotational excitations. They are highly specific and very useful for analytical applications. UV and visible absorption bands are mainly electronic transitions. These bands are less useful for analytical applications since they are usually very broad and have large overlaps with absorption bands from components of the atmosphere.

The vibrational energy levels of a bound molecule have specific values; arbitrary values cannot be taken. The energy provided by a photon absorption or energy lost by emission is given by the Planck-Einstein Equation 22. The difference in energy between two states after photon transition can be expressed as in Equation 23.

$$E = h\nu = \frac{hc}{\lambda} = hc\tilde{\nu} \quad \text{Equation 22}$$

$$\Delta E = h\nu = \frac{hc}{\lambda} = hc\tilde{\nu} \quad \text{Equation 23}$$

In this equation, E is the photon energy, ΔE is the difference in energy between the two states, h is Planck's constant, λ is wavelength, ν is frequency, $\tilde{\nu}$ is wavenumber and c is the speed of light in vacuum.

The absolute energies of vibrational states can be expressed in wavenumber units by the vibrational terms $G(\nu)$ as given by Equation 24 (harmonic oscillator approximation), where ν is the vibrational quantum number 0,1,2.... The difference between $G(0)$, the vibrational ground state, and $G(1)$, the first excited vibrational state, is equal to $\tilde{\nu}$. Therefore, in a fundamental transition (transition from the ground state to the first excited state) the

wavenumber of the absorption photon is equal to $\tilde{\nu}$, where $\tilde{\nu}$ is the wavenumber of the vibration as given in Equation 25,

$$G(v) = \left(v + \frac{1}{2}\right) \tilde{\nu} \quad \text{Equation 24}$$

$$\tilde{\nu} = \frac{1}{2\pi c} \left(\frac{k}{\mu}\right)^{\frac{1}{2}}, \quad \text{with} \quad \mu_{\text{Reduced}} = \frac{m_1 m_2}{m_1 + m_2} \quad \text{Equation 25}$$

where k is the bond force constant, μ_{Reduced} is the reduced mass, m_1 and m_2 are the two vibrating masses (in a diatomic molecule) and c is the speed of light in vacuum.

As shown before in Equation 13, the strength and whether a transition is allowed (selection rule) depends on the transition moment between the two states with vibrational wave functions Ψ'_v and Ψ''_v respectively is given by Equation 26

$$R_v = \int \Psi'_v{}^* \mu \Psi''_v dx \quad \text{Equation 26}$$

where $(x = r - r_e)$ is the internuclear displacement of distance from the equilibrium. $R_v = 0$ (transition not allowed) if the electric dipole moment μ is always zero as for a homonuclear diatomic molecules, therefore all pure vibrational transitions are forbidden in this case. For a heteronuclear diatomic molecule which has polarity, μ is non-zero and varies with x . This variation can be expressed as a Taylor series expansion as in Equation 27

$$\mu = \mu_e + \left(\frac{d\mu}{dx}\right)_e x + \frac{1}{2} \left(\frac{d^2\mu}{dx^2}\right)_e x^2 + \dots \quad \text{Equation 27}$$

where 'e' refers to the equilibrium configuration. The transition moment (R_v) of Equation (26) then becomes as in Equation 28

$$R_v = \mu_e \int \Psi'_v{}^* \Psi''_v dx + \left(\frac{d\mu}{dx}\right)_e \int \Psi'_v{}^* x \Psi''_v dx + \dots \quad \text{Equation 28}$$

Ψ'_v and Ψ''_v are eigenfunctions of the Hamiltonian. The Hamiltonian for quantum mechanical for a one-dimensional harmonic oscillator is given by Equation 29.

$$H = -\frac{\hbar^2}{2\mu} \frac{d^2}{dx^2} + \frac{1}{2} kx^2 \quad \text{Equation 29}$$

where Ψ'_v and Ψ''_v are orthogonal functions with

$$\int \Psi'_v{}^* \Psi''_v dx = 0 \quad \text{Equation 30}$$

Therefore the first term in Equation 28 vanishes which leaves Equation 31

$$R_v = \left(\frac{d\mu}{dx} \right)_e \int \Psi'_v{}^* x \Psi''_v dx + \dots \quad \text{Equation 31}$$

The first term in this series is non-zero only if $\Delta v = \pm 1$, which constitutes the vibrational selection rule for the harmonic oscillator.

For the Hamilton operator/Schrödinger equation of polyatomic molecules, we need the potential energy V . To simplify things, the harmonic approximation for each bond can be used. But it is still nearly impossible to solve the Schrödinger equation, because: if \vec{r}_1 are the usual Cartesian coordinates of atom 1, \vec{r}_2 of atom 2, etc, then the Hamiltonian with V depends on all these coordinates, $V(\vec{r}_1, \vec{r}_2, \dots, \vec{r}_N)$:

$$H = \sum_{i=1}^N \frac{1}{2} m_i \dot{\vec{r}}_i^2 + V(\vec{r}_1, \vec{r}_2, \dots, \vec{r}_N) \quad \text{Equation 32}$$

where $\sum_{i=1}^N \frac{1}{2} m_i \dot{\vec{r}}_i^2$ is the kinetic energy operator; $\dot{\vec{r}}_i$ is a velocity (the dot is an abbreviation for the time derivative).

To solve this problem and reduce the complexity, certain combinations of coordinates are introduced, so that in this new set of coordinates no cross-products occur, and the new coordinates are independent. Mathematically, this is a kind of a coordinate transformation; it is accomplished by a matrix diagonalization. These new coordinates \vec{Q} are called “normal coordinates”. In total, $3N-6$ normal coordinates are needed for non-linear molecules, to describe all vibrational modes in the Hamiltonian by Equation 33.

$$H = \sum_{i=1}^{3N-6} \frac{1}{2} m_i \dot{Q}_i^2 + \sum_{i=1}^{3N-6} \frac{1}{2} \lambda_i Q_i^2 \quad \text{Equation 33}$$

Where the Hamilton operator is now the sum of independent (separated) harmonic oscillators. The corresponding harmonic oscillations are called “normal mode vibrations”. In a normal mode vibration, all atoms move coherently in phase with the same normal mode frequency, but different normal modes have different frequencies. The vibrational degrees of freedom for a

non-linear molecule is $3N-6$ and for a linear molecule is $3N-5$, where N means the number of atoms in the molecule.

IR absorption and Raman scattering have different selection rules for which energy level transitions are allowed and can be detected. Some formally forbidden transitions are strictly forbidden and other transitions are still weakly allowed, thus the strength of such an absorption band is low, but they can be observed with a sensitive device. For an allowed transition in IR absorption, a change in electric dipole moment is required for a vibrational transition to be IR active, such as in the asymmetric stretching vibration of CO_2 where one oxygen is momentarily nearer to the central carbon than the other, as shown in Figure 3.2. Raman spectroscopy requires a change in polarizability for a vibrational transition to be Raman active, such as in the symmetric stretching vibration of CO_2 where both C=O distances are always the same thus the electric dipole moment is equal to zero, as shown in Figure 3.2 which means that this vibration is not IR active. In addition, in CO_2 there are two bending modes, they have the same frequency but are alternately perpendicular to each other in space so that the atoms of oxygen are no longer directly opposite to each other, this causing a change in electric dipole moment, making this IR active as shown in Figure 3.2.

Homonuclear diatomic molecules, such as N_2 , O_2 and H_2 , only have one vibration that can only be observed by Raman spectroscopy. These modes are IR inactive meaning IR absorption is forbidden as the electric dipole moment equals zero (no polarity). Raman spectroscopy is subject to different selection rules and can give information on the excited vibrational states of homonuclear diatomic molecules.

Heteronuclear diatomic molecules (CO , NO ...etc) have a permanent electric dipole moment and the vibration will change the electric dipole moment therefore making these IR active, in addition to being Raman active.

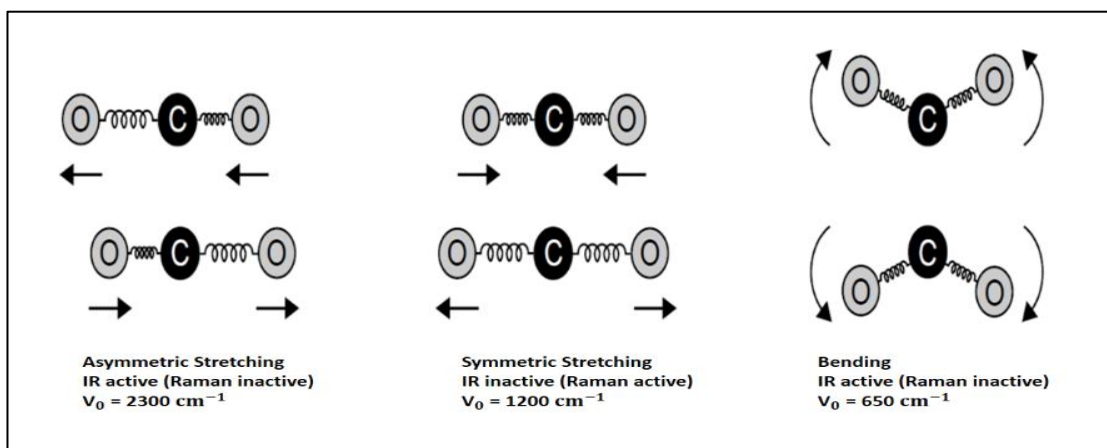


Figure 3.2. CO₂ vibrational modes and fundamental frequencies expressed as value of a wavenumber, ref [83].

Usually the vibrational quantum number changes by one unit ($\Delta v = \pm 1$) in a strong IR absorption (fundamental transition). This means that IR absorption is typically observed at the fundamental frequency (ν_0) for most molecules within the energy range of 250 – 4000 cm^{-1} . However, anharmonicity causes higher overtone transitions ($\Delta v = \pm 2, 3, 4 \dots$) to occur, but these bands are usually weaker than the fundamental bands.

3.5. Harmonic and Anharmonic Oscillator

The quantum harmonic oscillator is an approximation of the lowest vibrational transitions of molecules and can be used to describe small oscillations, such as a transition that occurs for $\Delta v = \pm 1$. It uses a parabolic potential to describe the bond. This potential energy does not apply for energies which are close to dissociation energy. Molecular dissociation is not accounted for by the parabolic potential as shown in Figure 3.3 for the harmonic oscillation. The vibrational behaviour is unsuccessfully described in higher modes because the internuclear separation is distorted away from the equilibrium length of the bond. Thus, an anharmonic oscillator needs to be considered for high excitation.

The potential energy of a molecular curve can be estimated by a parabola near the bottom of the well. The parabolic approximation (harmonic approximation) is poor at high excitation energies and does not apply near the dissociation limit. An asymmetric potential curve, for example the Morse oscillator, is a better approximation. The Morse potential is provided as in Equation 34. It is also shown in Figure 3.3.⁸²

$$V(r) = D_e (1 - e^{-\alpha(r-r_e)})^2, \quad \text{with} \quad \alpha = \sqrt{\frac{k}{2D_e}} \quad \text{Equation 34}$$

where $V(r)$ is the vibrational potential energy, D_e is well depth of the potential energy, r is the internuclear separation, k is the constant of the bond force, and r_e is the equilibrium internuclear separation. The dissociation energy for the Morse potential is given by Equation 35.⁸²

$$D_0 = D_e - E_0 \quad \text{Equation 35}$$

The Morse potential can be introduced into the Schrödinger equation and solved, giving allowed energy levels as in Equation 36.

$$G(v) = \left(v + \frac{1}{2}\right) \tilde{\nu} - \left(v + \frac{1}{2}\right)^2 x_e \tilde{\nu}, \quad \text{with} \quad x_e = \frac{\tilde{\nu}}{4D_e} \quad \text{Equation 36}$$

where x_e is the anharmonicity constant, v is the vibrational quantum number of the Morse oscillator, which is $v = 0, 1, 2, 3, \dots$, and $\tilde{\nu}$ is the fundamental vibrational wavenumber, and D_e the depth of the potential energy, as shown in Figure 3.3.⁸²

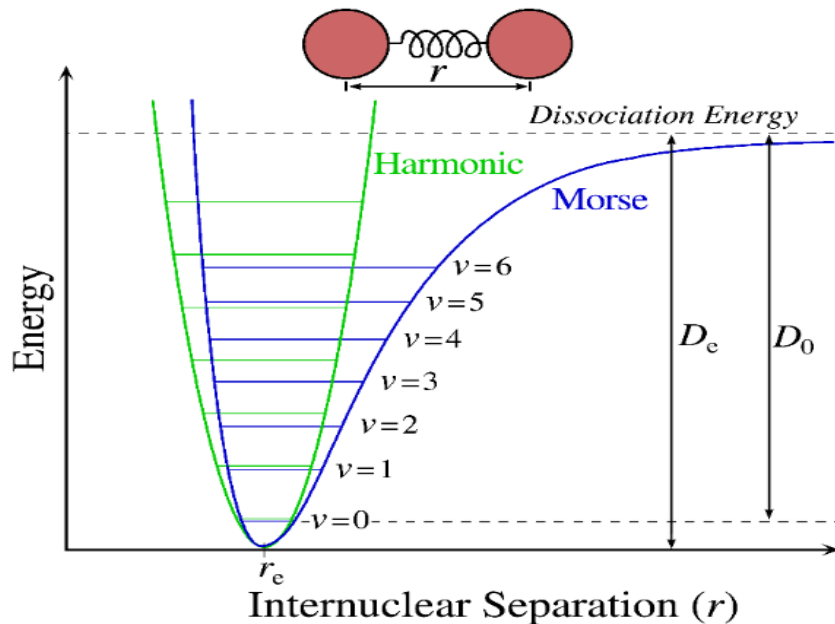


Figure 3.3. Comparison of the Morse potential energy curves and harmonic oscillation for a diatomic molecule, ref [82].

3.6. Rotational Motion

Usually with the vibrational transition, also transitions appear between different rotational states, which gives a fine structure of the rovibrational spectrum as shown in Figure 3.4. Both the vibrational and rotational states of the molecules may change. At room temperature, typically, only the ground vibrational state will be populated, with several rotational levels being populated.

In the simplest case of linear molecules, these fine structures are observed as two branches, *P* and *R*, of narrow lines which are located to either side of the vibrational fundamental frequency centre. In special cases, also a central *Q* branch may appear. The separation and the energy of vibrational states is considerably higher than rotational states.

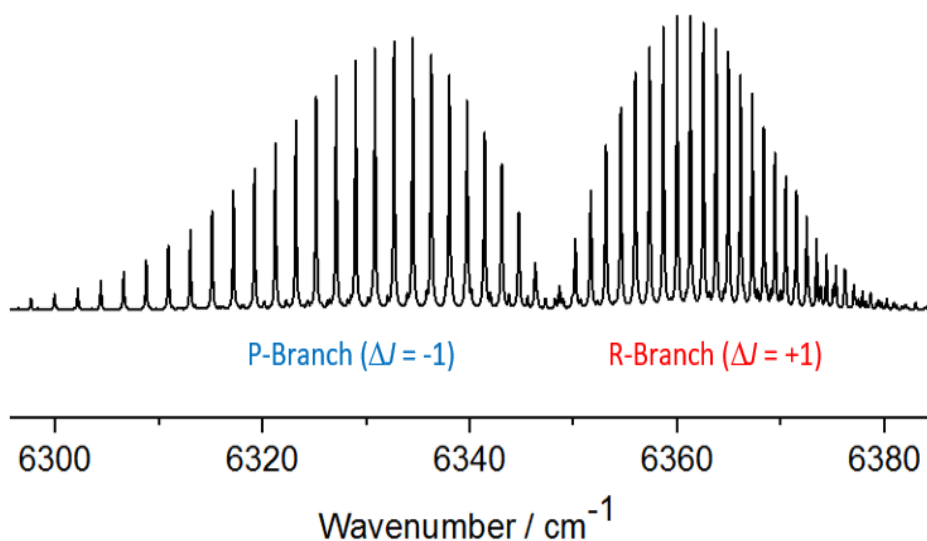


Figure 3.4. Overtone and combination absorption bands of carbon dioxide (CO₂) from the HITRAN 2012 database.⁸⁴ R-branch ($\Delta J = +1$) and P-branch ($\Delta J = -1$) structures are showing by the rotational lines.

Each rotational state has a rotational quantum number J . The rotational term value $F(J)$ can be expressed in Equation 37.

$$F_v(J) = B_v J (J + 1), \text{ with } J = 0, 1, 2, 3, \dots \quad \text{Equation 37}$$

where $F_v(J)$ is the rotational term value with the rotational quantum number J in the vibrational state with quantum number v , and B_v the rotational constant in the vibrational state with quantum number v . The separation between adjacent levels is given in Equation 38.

$$2BJ = F(J) - F(J - 1) \quad \text{Equation 38}$$

In linear molecules, only transitions are allowed with a change $\Delta v = \pm 1$ and $\Delta J = \pm 1$. In the special case of a molecule which has non-zero electronic or vibrational angular momentum like NO, $\Delta J = 0$ is also allowed. The rotational selection rule gives a *P*-branch when $\Delta J = -1$ and an *R*-branch when $\Delta J = +1$ and, if allowed, a *Q*-branch with $\Delta J = 0$. Each branch line is labeled $R(J)$ or $P(J)$, where J means the value of the lower state. For example, the $P(1)$ line is a transition from $J = 1$ to $J = 0$. *Q*-branches are located in the centre at the fundamental vibrational wavenumber and shows as a narrow band, whereas *P* and *R*-branches are typically much broader.

The selection rules for rotational transitions in Raman spectroscopy are $\Delta J = 0, \pm 2$ giving, *S*, *Q*, and *O* branches, where in an *O* branch $\Delta J = -2$, *Q* branch $\Delta J = 0$, and *S* branch $\Delta J = +2$. Usually, all *Q* branch lines build up to one sharp, strong feature which can be used to detect the molecule.

3.7. Raman spectroscopy

The Raman scattering of light by materials was predicted first in 1923 by Adolf Smekal.⁸⁵ The first experimental Raman scattering was discovered in 1928 by Sir Chandrasekhara Venkata Raman.⁸⁶ Raman was awarded the 1930 Nobel Prize in Physics for this discovery. It can be used as a spectroscopic technique to detect molecules.

In general, a UV, visible or NIR laser is used in Raman spectroscopy. It is passed through the sample which causes scattering of the light, followed by collection of scattered light by a monochromator. Through absorption and re-emission, scattering of electromagnetic radiation can occur. There are two types of scattering. Elastic, 'Rayleigh' scattering does not change the state of the molecule after the return from the excited state, with no change in energy. Inelastic scattering results in the change of state of the molecule after the return from the excited state. The Raman effect is the generation of inelastic scattering of light in vibrating and rotating molecules which have changing polarizability. Rayleigh scattering is the main contributor of scattered light. The low probability Raman scattering has two components, a Stokes and an anti-Stokes shift on which Raman spectroscopy is based.

If the excitation light makes a transition to a virtual energy level followed by relaxation to a rovibrational state of higher energy, it is called a Stokes shift. If the relaxation is to a rovibrational state lower in energy, it is called an anti-Stokes shift, as shown in Figure 3.5. The Raman wavenumber (Raman shift) in cm^{-1} is the difference between excitation wavenumber and the final wavenumber, the difference is equal to a rovibrational excitation of the molecule. Figure 3.5 shows a schematic of Raman shifts.

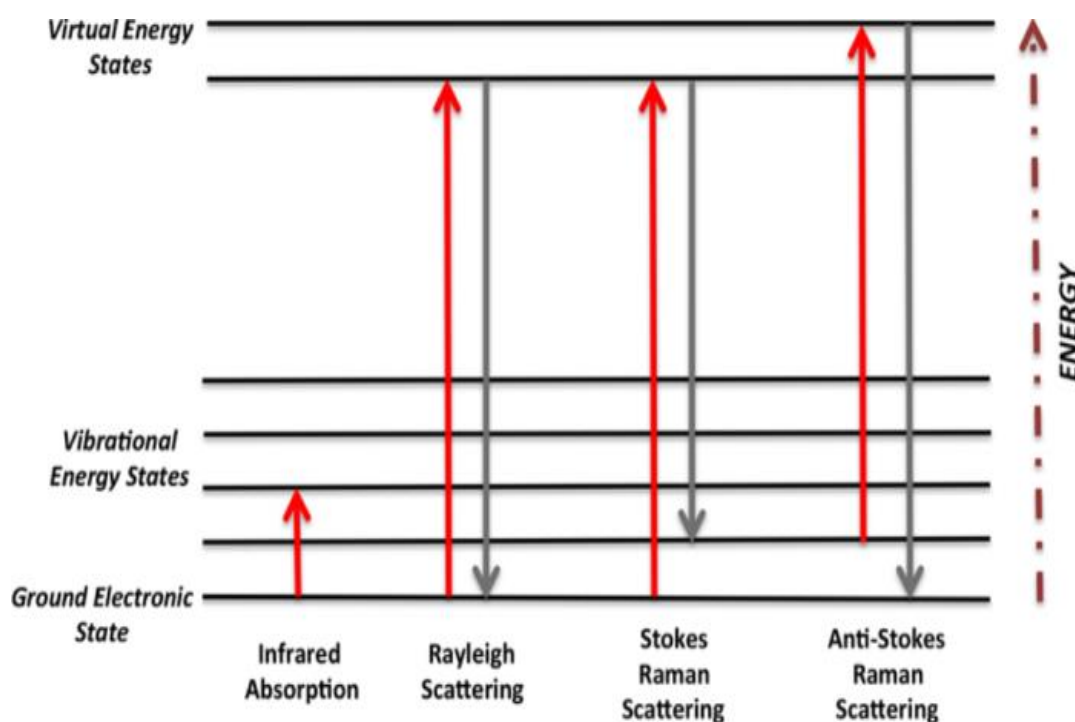


Figure 3.5. Schematics of a Rayleigh, a Stokes, and an anti-Stokes shift.

Raman spectroscopy can be used with samples in solid, liquid and gas phases like IR spectroscopy. It requires strong excitation light sources as the scattering is a weak process. Usually the process is a two-photon process, with excitation *via* a very short lived ($\tau < \text{fs}$) virtual state, which is in fact electronic states broadened by the short interaction time.

In general, Raman spectroscopy has had limited use in trace gas analytical applications because of the inherently weak signal intensities. Usually, infrared absorption signals are much higher, but unfavourable selection rules mean it is difficult or impossible for IR spectroscopy to detect homonuclear diatomic molecules. The changes in rotational energy depend on the selection rules occurring together with vibrational transitions, as given before.

IR spectroscopy requires a change in electric dipole moment for a vibrational transition to be IR active such as the asymmetric stretching vibration of CO_2 . Raman spectroscopy requires a change in polarizability for a vibrational transition to be Raman active such as the

symmetric stretching vibration of homonuclear diatomic molecules such as N₂, O₂, and hydrogen, H₂. To be an allowed vibrational transition in Raman spectroscopy, there must be a change in polarizability that is associated with the vibrational mode.

There are different selection rules between Raman and IR spectroscopy. If a molecule is centrosymmetric such as N₂, CO₂, H₂, or O₂, the selection rules mean that a vibration is either IR or Raman active. However, if a molecule is non-centrosymmetric such as HCl, CO, H₂O, or N₂O, the selection rules mean that a vibration can be either IR or Raman active, or both.

Strong Raman signals can be obtained by symmetric vibrations which in contrast give weak IR signals. The advantage of Raman spectroscopy is that it can detect homonuclear diatomic molecules which is very useful for gas sensing, such as the monitoring of hydrogen or oxygen and their isotopomers.⁵ With asymmetric vibrations, the opposite situation is usually found, with strong IR signals and weak Raman signals.

Figure 3.5. shows an energy level diagram distinguishing between the underlying principles of IR and Raman spectroscopy.⁸⁷ IR spectroscopy is a direct absorption technique involving a sample being irradiated with IR light. The photons of IR light are absorbed if they match the energy gap between rotational-vibrational energy levels in the sample. As IR spectroscopy is a direct absorption technique, it follows the Beer-Lambert law as shown in Equations 16 - 19. Raman spectroscopy is an indirect technique as the sample is irradiated with monochromatic light to excite the sample from the ground state to a high virtual energy state. Since the scattered Raman light contains many energy components, it has to be analysed in a monochromator to obtain a spectrum.

Gas phase samples have much lower densities when compared to the solid and liquid phases. Trace gas analysis requires enhancing the sensitivity of IR and Raman spectroscopy. This is particularly relevant for Raman spectroscopy. Raman spectroscopy is an inherent low sensitivity technique due to Rayleigh scattering occurring more often than Stokes scattering, so it is difficult to use for trace gas detection. Most excitations to the virtual energy level result in Rayleigh scattering to the vibrational ground state which reproduces the excitation photon. Special enhancement techniques are required for Raman trace gas analysis.

Chapter 4

Construction and Characterisation of Differential Helmholtz Resonator (DHR) Enhanced Resonant Photoacoustic Spectroscopy (RPAS)

Abstract

Photoacoustic spectroscopy in a differential Helmholtz resonator has been employed with near-IR and red diode lasers for the detection of CO₂, H₂S and O₂ in 1 bar of air/N₂, in static and flow cell measurements. With the red DFB diode laser, O₂ can be detected at 764.3 nm with a noise equivalent detection limit of 0.60 mbar (600 ppmv) in 1 bar of air (35 mW laser, 1 s integration), corresponding to a normalized absorption coefficient $\alpha = 2.2 \times 10^{-8} \text{ cm}^{-1} \text{ W s}^{1/2}$. Within the tuning range of the near-IR DFB diode laser (6357 – 6378 cm⁻¹), CO₂ and H₂S absorption features can be accessed, with a noise equivalent detection limit of 0.160 mbar (160 ppmv) CO₂ in 1 bar N₂ (30 mW laser, 1 s integration), corresponding to a normalized absorption coefficient $\alpha = 8.3 \times 10^{-9} \text{ cm}^{-1} \text{ W s}^{1/2}$. Due to stronger absorptions, the noise equivalent detection limit of H₂S in 1 bar N₂ is 0.022 mbar (22 ppmv) at 1 s integration time. Similar detection limits apply to trace impurities in 1 bar natural gas. Possible interferences due to weak water and methane absorptions have been discussed and shown to be either negligible or easy to correct. The set-up and the calibrations for O₂, ¹²CO₂, ¹³CO₂ and H₂S have been characterised to understand the system very well before starting with any applications.

This chapter forms part of a scientific publication [ref. 89]. The initial work was done in collaboration with an MChem student (Xiu-Wen Kang). A reprint of the full article can be found in the Appendix.

“Diode Laser Photoacoustic Spectroscopy of CO₂, H₂S and O₂ in Differential Helmholtz Resonator for Trace Gas Analysis in the Biosciences and Petrochemistry”, by Saeed Alahmari, Xiu-Wen Kang, and Michael Hippler, *Analytical & Bioanalytical Chemistry*, 411, 2019, 3777-3787. Selected as ‘paper in forefront’ by the journal.

4.1. Introduction

Photoacoustic detection is one of the most sensitive optical absorption techniques, but it suffers from ambient acoustic noise and flow noise introduced by sampling gases; this ultimately limits detection limits. A DHR has the advantage that the symmetrical resonator composed of two identical chambers produces photoacoustic absorption signals which are out-of-phase in the two chambers, whereas noise including flow noise is in-phase in the two chambers. Differential detection therefore doubles the signal and cancels noise to a great extent. In this chapter, we demonstrate the characteristics of photoacoustic trace gas detection of O₂, CO₂ and H₂S in a DHR with distributed feedback (DFB) diode lasers near 1.6 μm, and O₂ detection near 760 nm. Improvements on the DHR technique are reported, including a multipass arrangement and using two independent lasers.

4.1.1. External Cavity Diode Laser (ECDL)

Diode lasers are widely used in a variety of experiments in atomic, molecular and optical physics. Diode lasers are a smaller, cheaper, and more reliable alternative to gas lasers. They are efficient but usually have poor wavelength control compared with other lasers. The wavelength of a diode laser depends on the bandgap energy of the semiconductor material. Some representative values are shown in Table 4.1 The laser action happens in an optical resonator where photons stimulate the return of excited, active medium resulting in the stimulated emission of more photons of identical wavelength.⁹⁰ Wavelength stability can be achieved by operating the laser in a longer external cavity which can provide frequency selectivity by optical feedback. In an external cavity diode laser (ECDL), the rear face of the diode has a high reflectivity and the front face has low reflectivity. The laser cavity on the front side is thus not provided by the diode front face, but it is completed by the diffraction off an external grating, providing optical feedback.^{90,91}

ECDL uses frequency selective feedback to achieve narrow linewidth and the ability to tune the wavelength. This is typically achieved with diffraction gratings in the Littrow or Littman-Metcalf configurations, as shown in Figure 4.1.^{90,92,93,94}

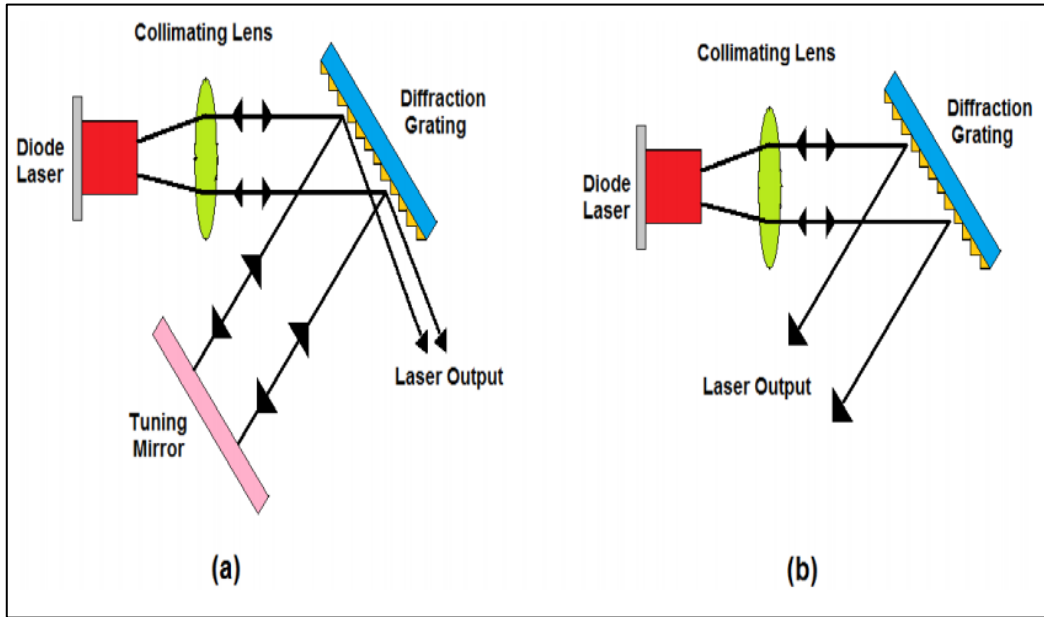


Figure 4.1. External cavity diode laser (a) Littman-Metcalf configuration, (b) Littrow configuration, ref [90].

In this project, the Littman-Metcalf configuration was used in the ECDL. The advantage of the Littman-Metcalf configuration is that the angle and the beam position remain stable because rotation of a tuning mirror is used to achieve the variation in wavelength.⁹⁰ The first order grating diffraction reflects from the mirror, then the first order is diffracted once more before being fed back to the active medium of the diode. The two diffraction steps impart high losses. This results in a lower maximum output power, while having higher side mode suppression, resulting in narrower linewidths.

The second type of external cavity diode laser is a Littrow configuration. This type uses a diffraction grating to select the wavelength. In this design, the diffraction of zeroth order beam of the grating is directed out of the laser, and the first-order diffracted beam is directed back to the laser diode. A main advantage of Littrow configuration over Littman-Metcalf is that it has the possibility to reach a higher output power through fewer losses on the grating. On the other hand, the Littrow configuration has the disadvantage that with changes in the diffraction grating position, the output beam direction changes, which is inconvenient for many applications.⁹⁰

Table 4.1. Wavelengths of some commercially available diode lasers, ref [90].

Compound	Wavelength (nm)
InGaN	390–420
ZnSe	460–530
AlGaInP	630–680
GaInP	670
Ga _{1-x} Al _x As	620–895
GaAs	904
InGaAs	980
InGaAsP	1100–1650
InGaAsSb	1700–4400
PbEuSeTe	3300–5800
PbSSe	4200–4800
PbSnTe	6300–29 000
PbSnSe	8000–29 000

4.1.2. Distributed Feed-Back (DFB) Laser

A DFB laser diode is a popular technique as a selective mechanism to control wavelength or frequency by an etched diffraction grating within the laser waveguide structure. It can achieve single frequency mode operation over broad current ranges and temperatures. DFB diode lasers are of particular interest, because diodes with a tuning range of typically 10 nm which emit single mode are available in almost the entire spectral region between 1 μm and 2 μm . In this region enough strong absorption lines free from interference with other atmospheric gases like CO₂ and H₂O are present, or the combination band of H₂S centered at 1.58 μm , which overlaps with the weaker combination bands is suitable. The basic idea of the (DFB) laser is illustrated in Figure 4.2. There is a relationship between the grating which is affected by the temperature, and therefore changing the temperature tunes the wavelength.⁹⁵ DFB lasers have a smaller tuning range than an ECDL, but in comparison to the ECDL laser, they are easy to use and cheaper.

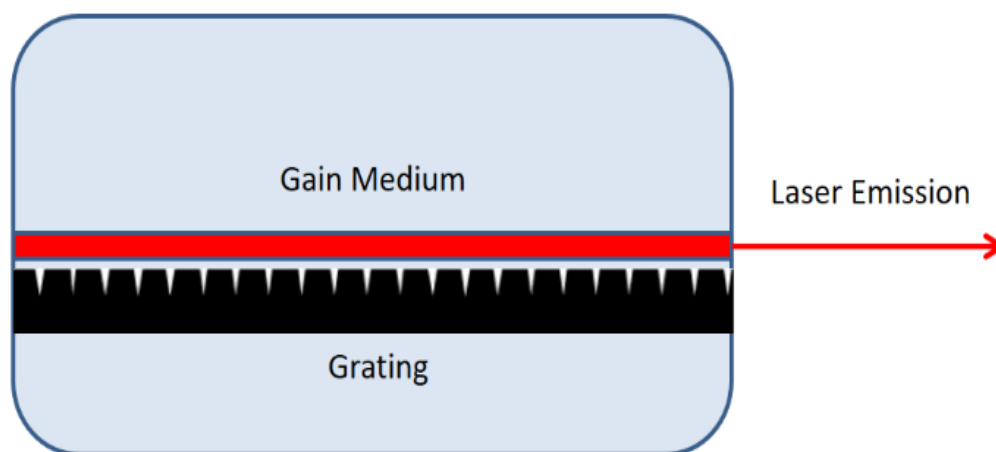


Figure 4.2. Scheme of DFB Laser

4.1.3. Lock-In Amplifier

The Lock-In Amplifier (LIA) is a tool that is used to detect a small periodic signal buried in noise. Essentially, a LIA filters a signal with the same frequency and phase as a reference and minimises noise components which do not have the right frequency and phase by applying smoothing with an adjustable time constant. The LIA requires a reference frequency. It can be obtained from the function generator controlling the current modulation to the laser. The signal is then passed through a low pass filter. In this project, a home-built analogue multiple feedback band-pass filter is used to filter the microphone signals, which is then further processed by a home-built LIA which use an additional 100 x input amplification.

4.2. Aims

This chapter describes a new home-built system, photoacoustic spectroscopy in an acoustic differential Helmholtz resonator (DHR). In this chapter, the characterisations of this system, including; detection limit, sensitivity, laser power, and wavelength tuneability is explained. In the following chapter, applications of the system will be discussed, including time-dependent monitoring of the bacterial growth and aerobic metabolism of microbes and detection of H₂S and CO₂ impurities in natural gas (explained in chapter 5).

4.3. Experimental

In this project, two kinds of laser systems were used, the first is an external cavity diode laser (ECDL) system that provides the largest tuning range, and the second is a distributed feedback (DFB) laser diode which emits in a narrow range of wavelengths. Both systems have a central wavelength at around $1.57\ \mu\text{m}$, which is in the NIR region where a range of gases such as H_2S and CO_2 have absorptions which are interesting for this project.

4.3.1. The Set-Up of the ECDL system

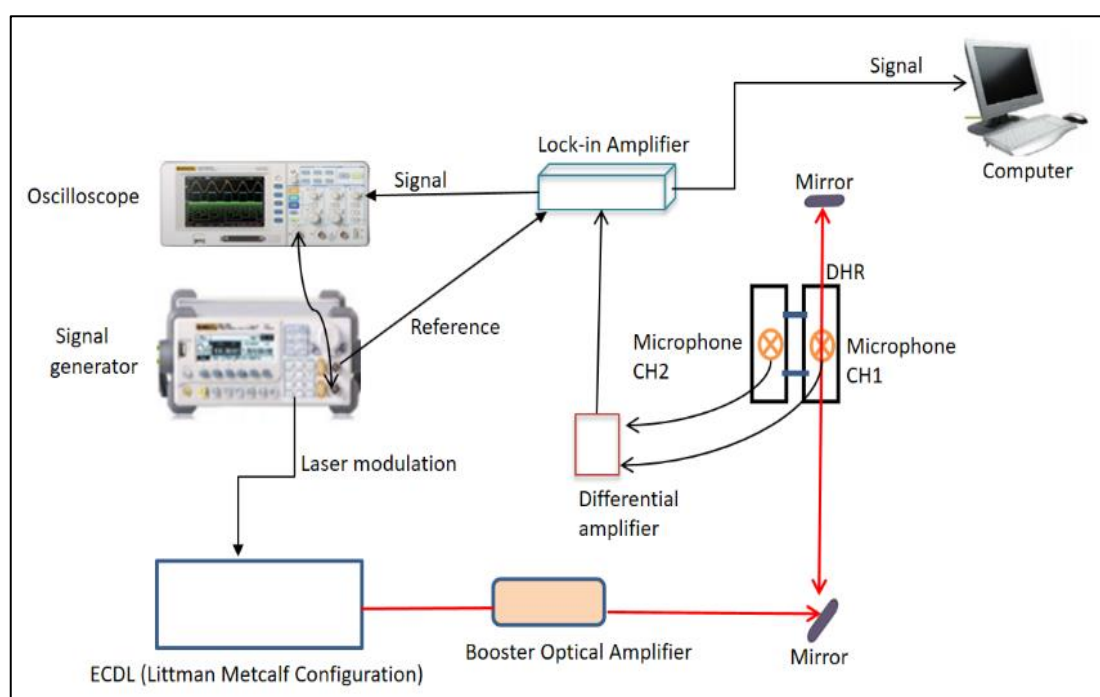


Figure 4.3. Schematic diagram of Photoacoustic experimental set up using an ECDL.

Figure 4.3 shows the schematic diagram of the photoacoustic spectroscopy experiment set up using an ECDL system in the first part in this project. In the first part in this project, wide wavelength tunability is required to explore suitable absorption lines for the detection of CO_2 and H_2S . The continuous wave NIR light source is a tuneable ECDL system in the Littman-Metcalf configuration (Thorlabs-TLK-L1550M), tuneable from $1550\ \text{nm} - 1620\ \text{nm}$ or $6150\ \text{cm}^{-1} - 6450\ \text{cm}^{-1}$. The laser power is then further amplified in a fibre coupled booster optical amplifier. The laser power booster (ThorLabs S9FC1004P) is set at current of $300\ \text{mA}$ for the CO_2 and H_2S measurements, which gives a maximum power of about $30\ \text{mW}$ in the NIR with single mode, cw output. The ECDL emits a beam from the front side of the diode to the grating which allows wavelength tuning. The first order reflection is fed-back into the laser diode via a mirror and a second pass through the grating. The mirror movement is controlled by a motor controller (ThorLabs - TDC001). The mirror movement was set at the lowest speed possible of

0.003 mm s⁻¹ with a micrometre movement from 0-7 mm to get the best quality (mode-hop free) spectrum possible of CO₂ and H₂S. The laser output is via a glass fibre bonded to the rear side of the diode. After amplification in the booster optical amplifier, the diode laser light passes through one of the compartments of DHR which will be explained later in detail.

4.3.2. The Set-Up of the DFB laser system

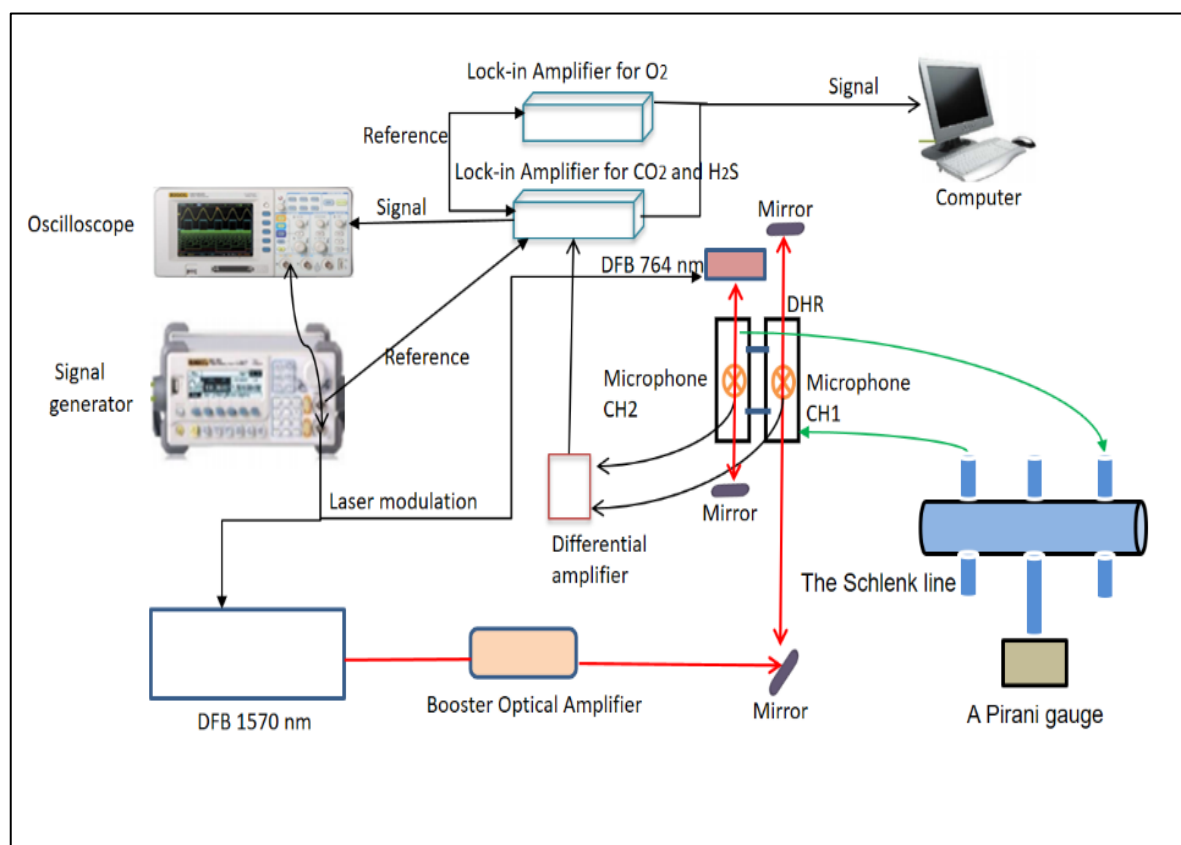


Figure 4.4. Schematic diagram of PA experimental set up use DFB for detect CO₂ and H₂S and red diode laser for detect O₂ at 764 nm.

The ECDL system was used to find out suitable absorption lines of CO₂ and H₂S. After establishing suitable wavelengths, a DFB laser which is temperature tuneable was used for the final measurements.

In the second part of the project, as shown in Figure 4.4, a InGaAs/InP DFB laser diode (Mitsubishi FU-650SDFFL49M56D) was used for detecting CO₂ and H₂S. It emitted in a narrow range at around 1553 nm - 1570 nm or 6357 cm⁻¹ – 6378 cm⁻¹ in the NIR. A thermoelectric cooled mount (ThorLabs TCLDM9) was used to control the diode temperature. Wavelength tuning is accomplished by changing the diode temperature. The tuning range of the temperature was between 20-60°C, using a control voltage to increase temperature by a rate

of $0.02 \text{ }^\circ\text{C s}^{-1}$. The diode current was constant at around 13 mA. The DFB laser was also amplified by a booster optical amplifier to get a power of around 30 mW in cw operation, or 15 mW in the pulsed operation for photoacoustic detection with 50 % duty cycle.

4.3.3. General Set-Up for the system

The DFB or ECDL laser is amplified by a booster optical amplifier (Thorlabs - S9F1004P) which provides a maximum power of about 30 mW in cw operation. The laser power is modulated by a signal generator on the control input of the laser to produce pulses with 50 % duty cycle to produce photoacoustic signal. With 50 % duty cycle, the average laser power is 15 mW. The laser beam is then directed into one compartment (CH1) of the resonant DHR cell. After passing through the cell, an additional mirror located at the back of the compartment reflects the beam back to get a double absorption pass to increase the signal. The resonant DHR cell has two electret microphones (Knowles-EK-23024) connected, labelled channel 1 (CH1) and channel 2 (CH2). The two microphones are connected to a differential amplifier (Dr. Hippler, home-built, with 100 x input amplification) as shown on the photo and the schematic in Figure 4.5. The differential amplifier amplifies the differential signal CH1-CH2 of the microphones, because signals in the two compartments of the DHR are out of phase.

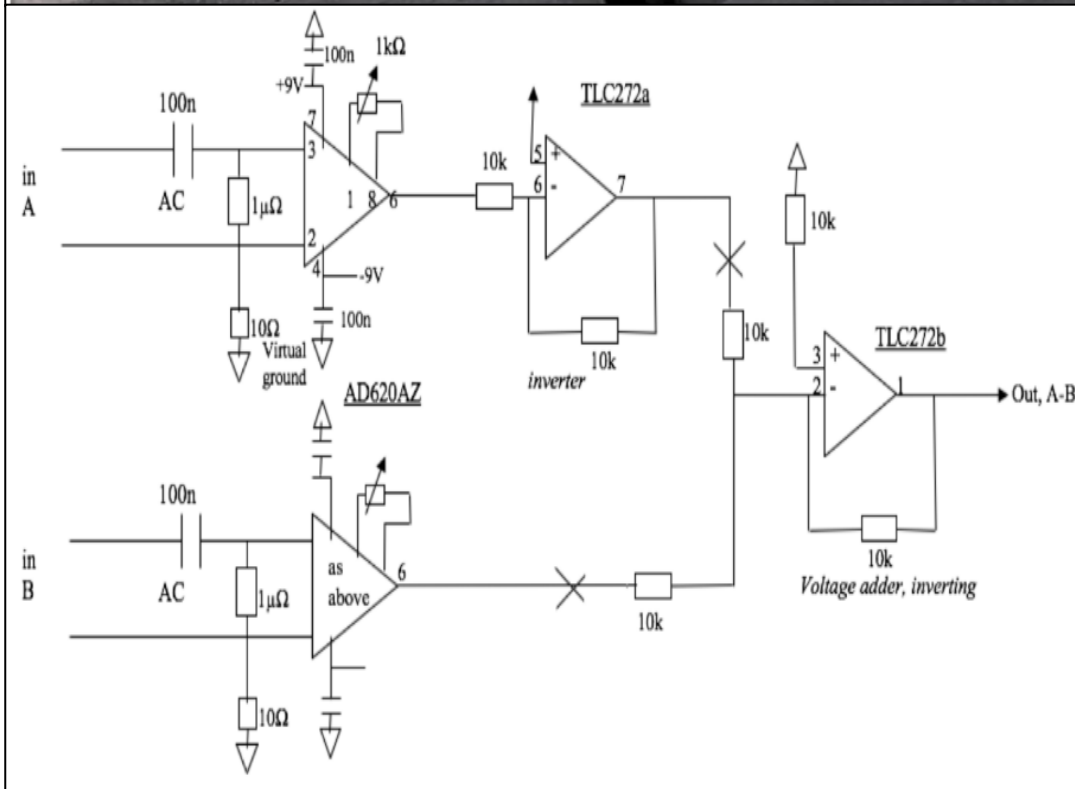
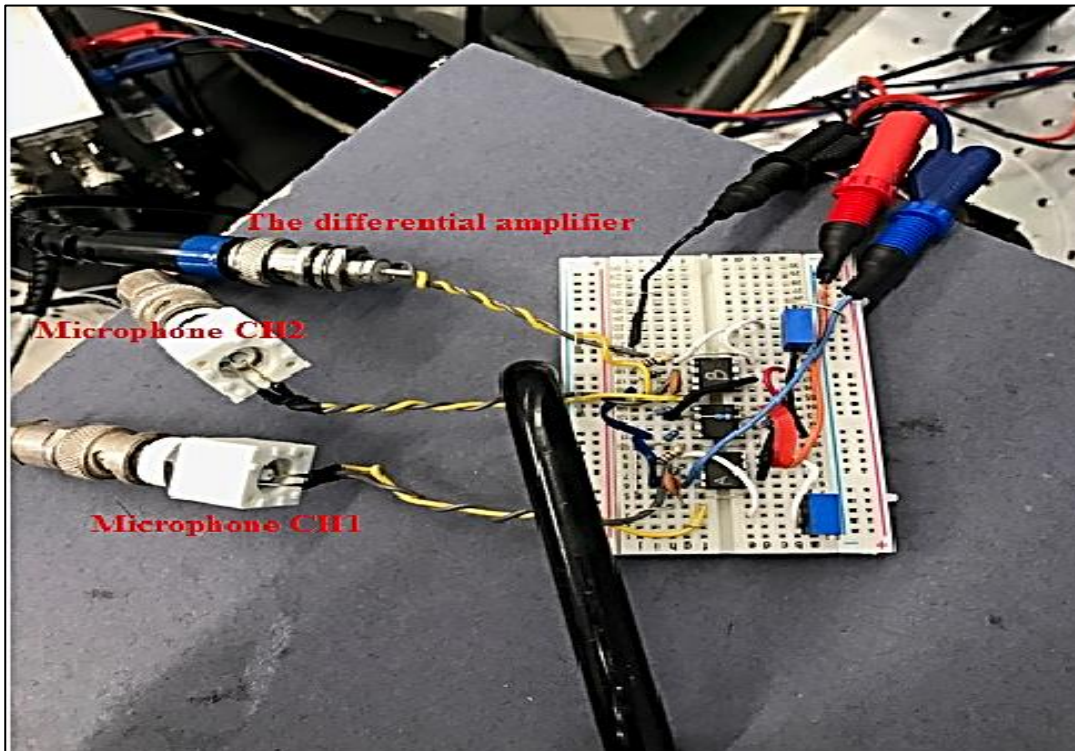


Figure 4.5. Photo and schematic of the home-built differential amplifier.

The electret microphones have a wide range of frequency response which starts at 100 Hz and extends to above 10 kHz as shown in Figure 4.6. The differential amplifier takes the difference between CH1 and CH2, amplifies it by a factor of 100 and then sends it to a home-built lock-in amplifier which further greatly reduces noise.

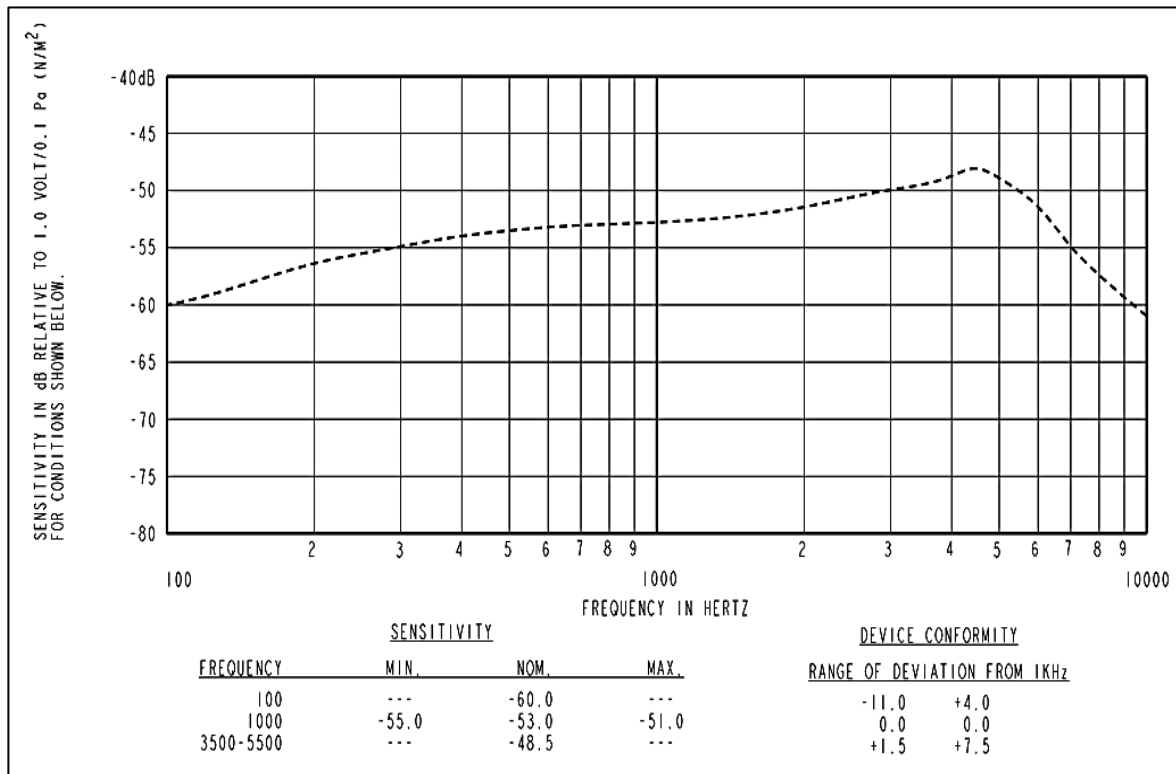


Figure 4.6. Frequency response of the Knowles electret microphone between (100-10000 Hz), ref [96].

The differential Helmholtz resonator (DHR) cell is based on a design published in reference [49]. The DHR cell chambers or compartments are made of glass. They have a length of 10 cm with a diameter of 1 cm and the connecting capillary tubes have a length of 10 cm and a diameter of 0.2 cm, as shown in Figure 4.7. Each compartment has in the middle one electret microphone (Knowles EK-23024) attached to it from the outside, but open to the inside. The compartments have glass windows at their end to allow laser light passing through; the windows are slightly tilted to avoid back reflections into the laser. The entire cell is wrapped in heating wire and thermal insulation to keep it at around 45 °C, to avoid water condensation in biological experiments, as shown in Figure 4.8.

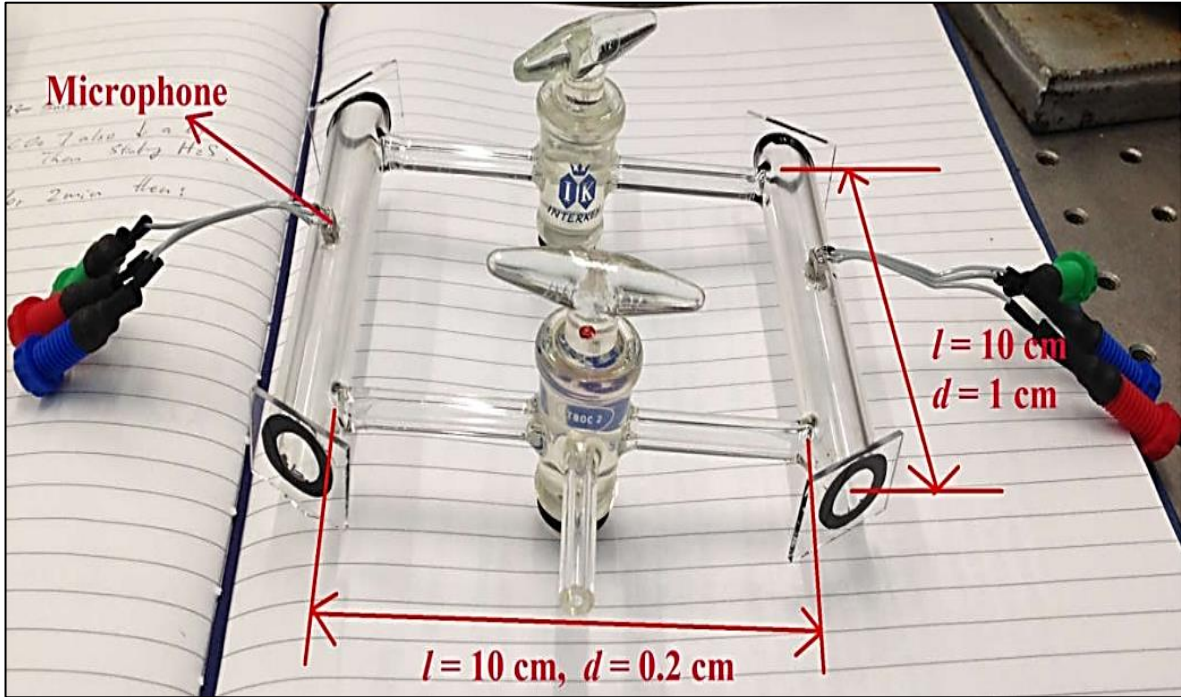


Figure 4.7. Photograph of the (DHR) with two microphones.

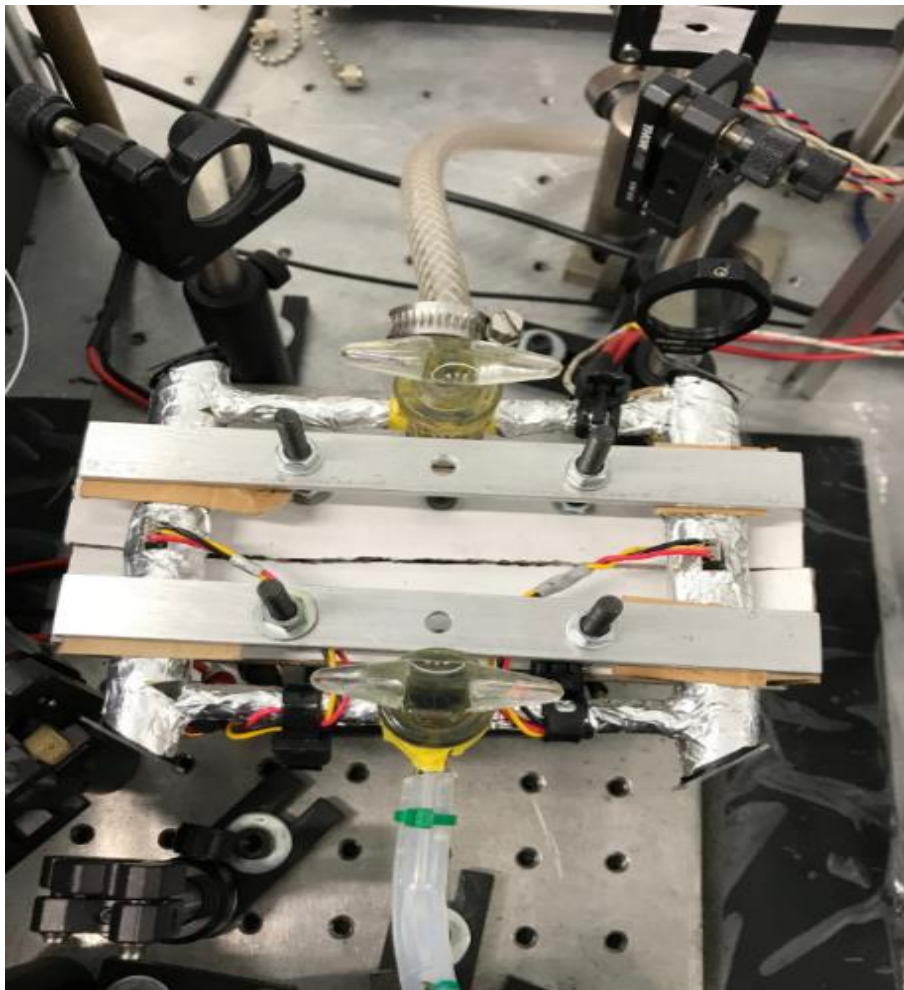


Figure 4.8. DHR is covered with aluminium foil and under it is wrapped with heating wire.

Diode laser light passes through one of the compartments and is reflected back once at a slight angle to double the interaction path length. After laser light is absorbed by molecules inside compartment 1, collisional deactivation leads to a temperature jump and pressure expansion (photoacoustic effect). This pressure build up will then travel to compartment 2 via the connecting capillaries. If the laser light is pulsed, the pressure build up will travel from compartment 1 to 2, leaving a pressure depression behind in 1, and then back again to 1 when the laser is off, leaving a pressure depression behind in 2. If the laser is modulated periodically, periodical pressure waves (sound) are thus created in compartment 1 and compartment 2 which have the same frequency and amplitude, but opposing phases in compartment 1 and compartment 2. If the laser modulation matches a resonance frequency of the cell, a standing wave develops with maximum amplitude (resonant photoacoustics). The acoustic resonance is a pressure oscillation between compartment 1 and 2, not a longitudinal acoustic resonance as in the more commonly used organ pipe photoacoustic resonators. The resonance frequency is given by the cell dimensions. It also depends linearly on the speed of sound and thus on the inverse of the square root of the molar mass of the medium inside the resonator.

Characteristic features of a DHR are its low resonance frequency, and effective noise cancellation and signal enhancement by differential amplification of microphone signals 1 – 2. Genuine absorption signals inside the cell are out-of-phase between microphones 1 and 2; differential amplification 1 – 2 therefore doubles the signal as shown Figure 4.9. External noise and flow noise, however, will affect the two symmetrical compartments in nearly the same way, creating a noise signal which is in phase in 1 and 2. In this case, differential amplification 1 – 2 leads to effective cancellation of noise as shown in Figure 4.10. This noise cancellation and signal enhancement make DHR an attractive choice for trace gas detection applications. The differential signals (1-2) are processed in lock-in amplifiers which further greatly reduce noise.

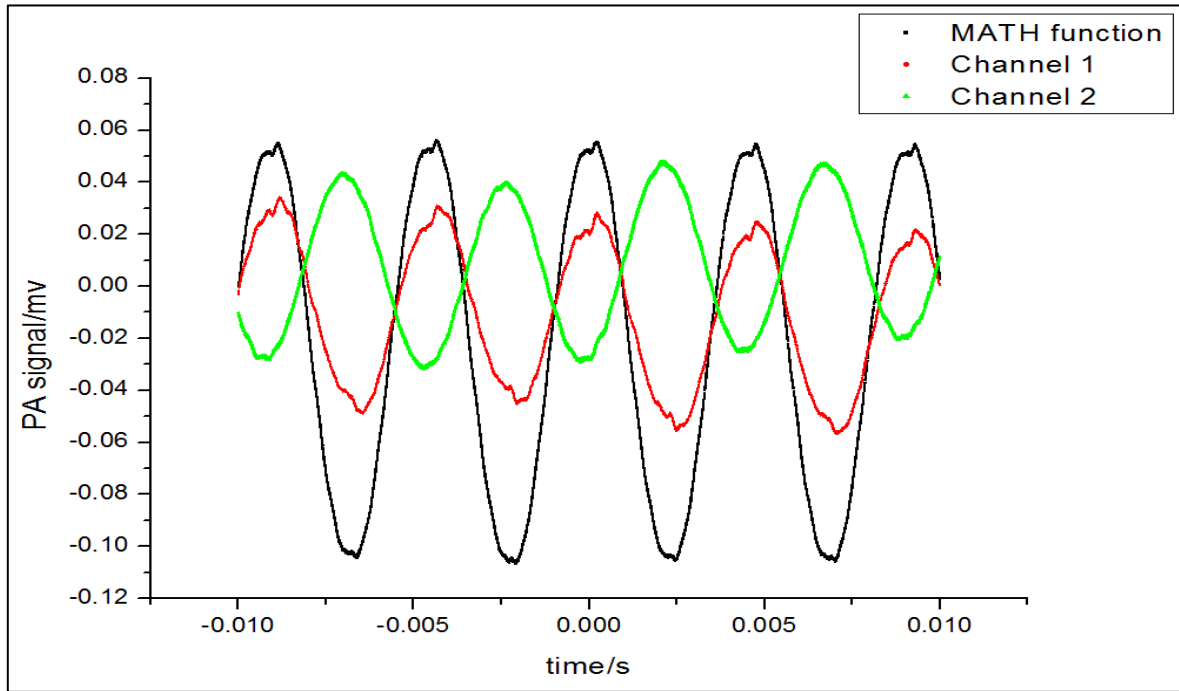


Figure 4.9. Oscilloscope traces of the signal from microphone 1 (red), microphone 2 (green), and the differential signal 1-2 (black), demonstrating signal enhancement (CO₂ absorption near 1.57 μm).

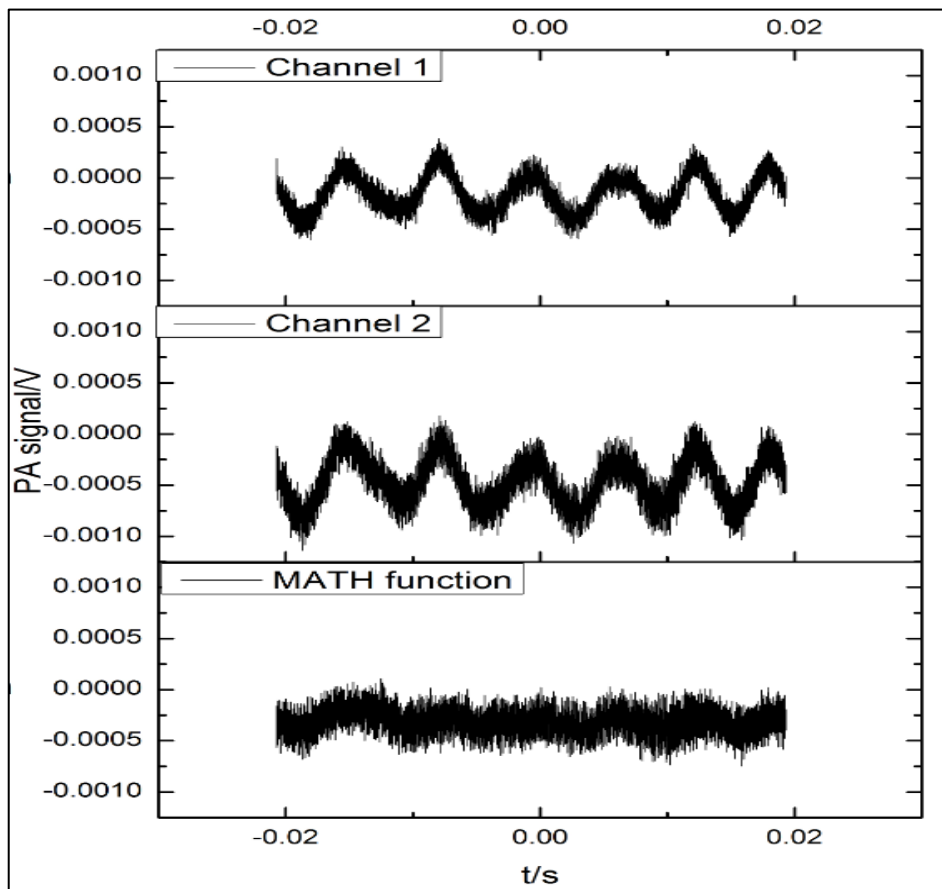


Figure 4.10. Screen shots of the oscilloscope to demonstrate noise cancelation by the math function, channel 1-channel 2.

To demonstrate the noise cancellation due to the differential amplification further, the ambient noise picked up by the microphones is compared in a configuration where both microphones are connected to the differential amplifier, giving CH1-CH2 as signal, and a configuration where only one microphone is connected, giving CH1 without any DHR noise cancellation. Figure 4.11 shows the noise in the DHR cell with one (red line) and with two (black line) microphones. The standard deviation of the noise trace with one microphone is 0.145mV and with the differential signal with two microphones it is 0.006mV, clearly demonstrating the noise cancellation by the DHR principle. After the differential amplification and noise cancellation, the PA signal is further amplified and processed by the lock-in amplifier and is then sent to the computer. The processed signal is also simultaneously displayed on an oscilloscope (Rigol- DS1054). The signal generator (Rigol- DG1022A) is connected to the diode current driver to modulate the laser output in order to generate an acoustic resonance. The signal output is also connected as reference to the lock-in amplifier. A LabVIEW (National Instruments) programme is used to control the scanning of the laser and for data acquisition and data analysis. Origin 8 software was used throughout to plot graphs and spectra.

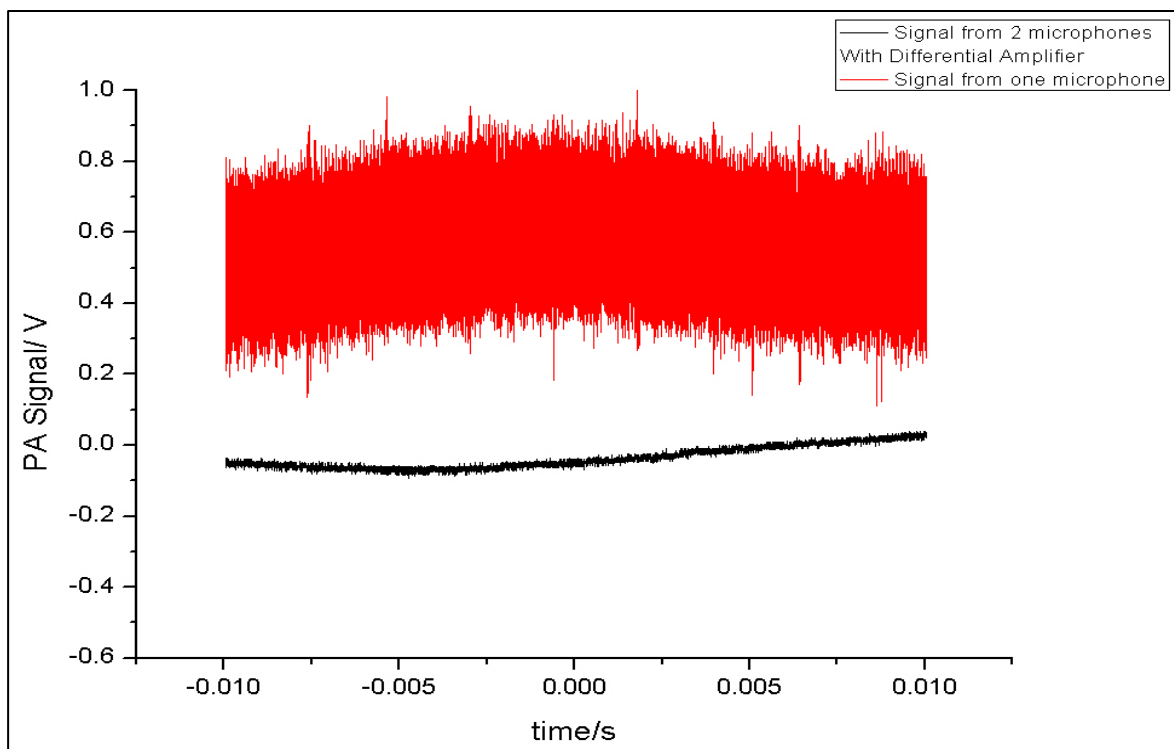


Figure 4.11. Comparison of PA noise signals with one microphone, CH1, and with two microphones in differential amplification, CH1-CH2.

Figure 4.12 shows the effect of using different integration times for the lock-in amplifier during a scan of 1 atm CO₂. It is evident that an integration time of 100 ms results in a spectrum with a better signal-to noise ratio than when an integration time of 10 ms is used, because essentially more averaging and smoothing occurs.

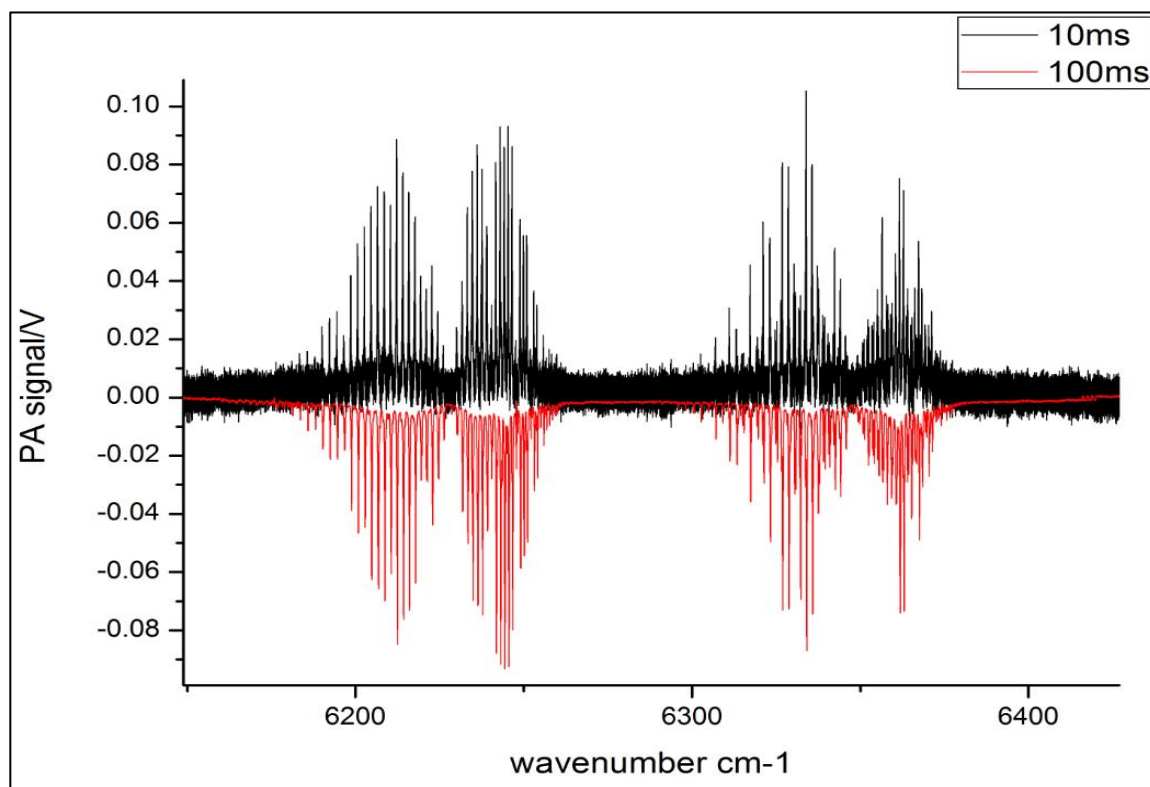


Figure 4.12. CO₂ scan with different integration time settings, 10 ms (black curve), and 100 ms (red curve). The red curve is mirrored for a better visual comparison.

4.3.4. Determination of the Resonance Frequency of the DHR

The differing resonance frequency for CO₂ and H₂S in DHR can be calculated in order to find out the relationship between resonance frequency, molecular weight of the gas mixture inside the resonator and the temperature. The resonance frequency depends on the speed of sound inside the resonator. The speed of sound in air at 20 °C is 343 ms⁻¹, but this is dependent on various parameters. The speed of sound is faster in solid materials and slower in gases because gaseous molecules are farther spaced. The speed of a sound is affected by two properties of matter: the flexible properties and density.

In resonance, the wavelength of the acoustic resonance (λ) is determined by the chamber length of the cell which changes very little with a change of temperature. However,

the speed of sound c changes significantly with temperature and composition, and via the wave equation the resonance frequency change, as in Equations 39 and 40.

$$c = f \lambda \quad \text{Equation 39}$$

where f is the frequency of the resonance sound wave, λ is the wavelength of the sound which is fixed by the dimensions of the chamber. The speed of sound is c and given by

$$c = \sqrt{\frac{\gamma RT}{M}} \quad \text{Equation 40}$$

In the kinetic theory of gases, where γ is the adiabatic constant (heat capacity ratio), R the gas constant, T the absolute temperature and M is the molecular mass of the gas. In a gas mixture, an average M has to be used.

Applying Equation 40 in the plot shown in Figure 4.13 demonstrates a positive correlation between resonance frequency / Hz and $\sqrt{T / K}$. The sound travels faster in the warmer air than cooler air. For example, the speed of sound at 40 °C is 355 ms⁻¹ compared with 343 ms⁻¹ at 20 °C, because an increase in temperature causes the molecules to move faster and this accounts for the increase in the speed of sound.

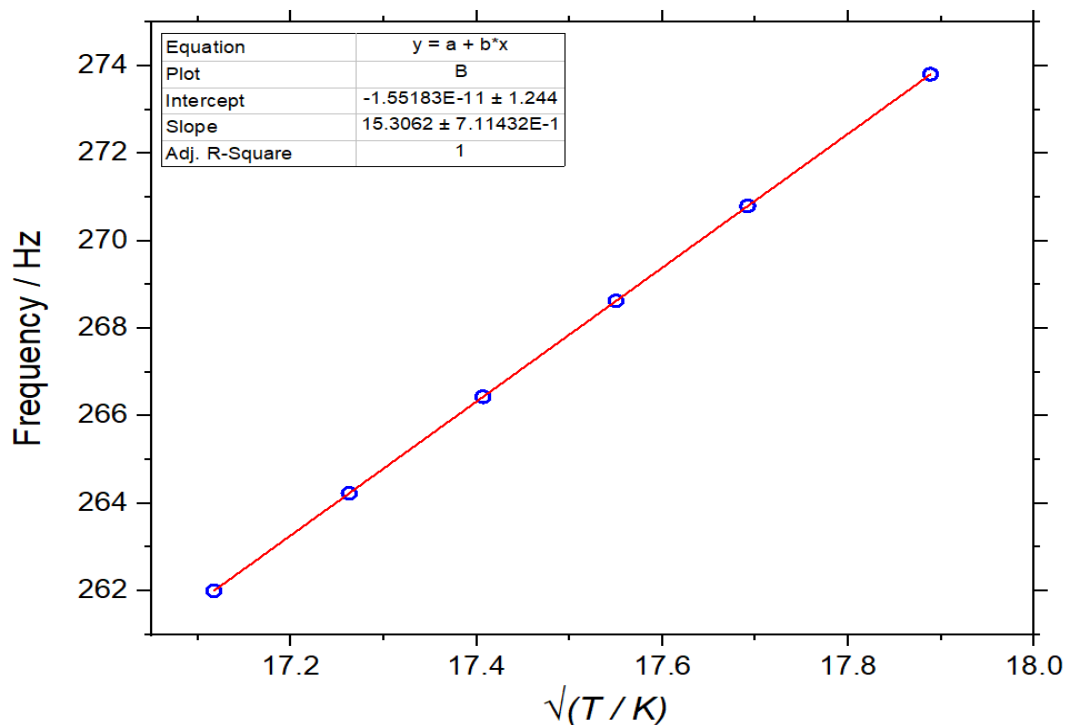


Figure 4.13. A plot of the calculated resonance frequency as a function of the square root of temperature as calculated by Equation 40.

Figure 4.14 shows a negative correlation between calculated resonance frequency and square root of $1/M$ of CO_2 in atm N_2 . In a dilution series of one gas (for example CO_2) in 1 atm of air or N_2 , the total pressure in the chamber is constant but the composition changes and therefore M changes in Equation 40. Increase in the ratio of CO_2/N_2 results in an increase in the overall density of gaseous mass within the chamber, as a molecule of CO_2 weighs more than a molecule of N_2 (M of $\text{CO}_2 = 44 \text{ g mol}^{-1}$, M of $\text{N}_2 = 28 \text{ g mol}^{-1}$). This affects sound. Sound waves have kinetic energy. Therefore, the sound in dense matter will travel at a slower rate.

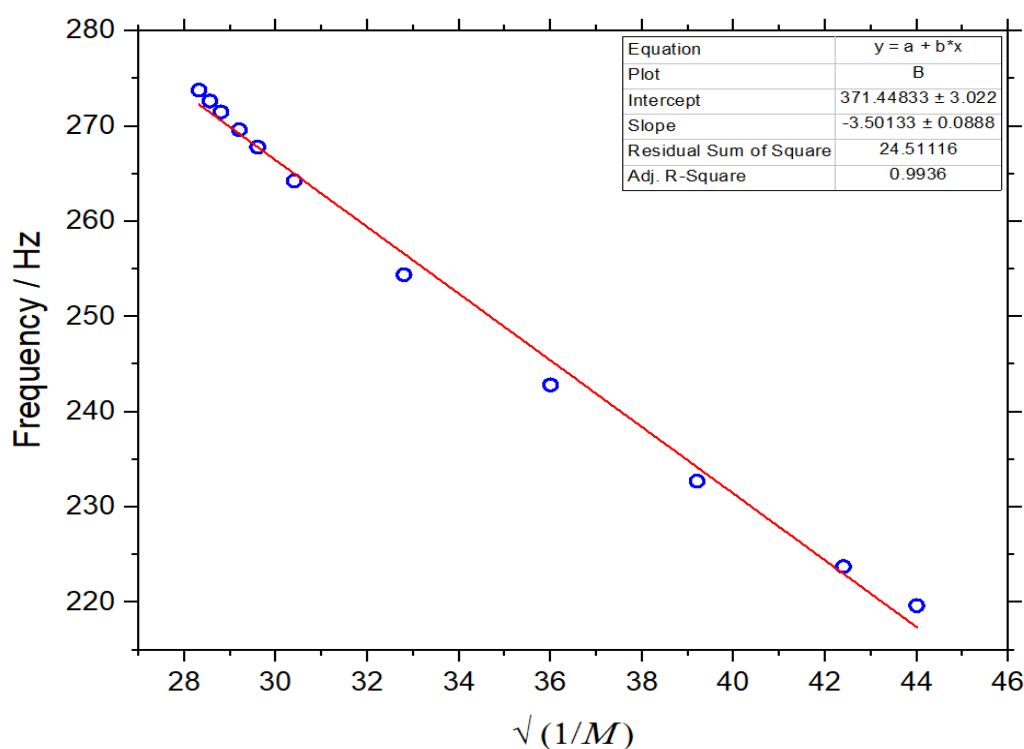


Figure 4.14. A plot showing the negative correlation between the calculated resonance frequency and $\sqrt{\frac{1}{M}}$ of CO_2 in atm N_2 .

In Figure 4.15, the resonance frequency, f is experimentally determined by using 1 atm of CO_2 observing a near-IR transition of CO_2 . The figure shows PA response as a function of modulation frequency. The PA response is represented by a Lorentzian curve. A Lorentzian curve fit gives $f = 220 \pm 0.690 \text{ Hz}$ as resonance frequency. The uncertainty is given by the standard deviation of the Lorentzian curve fit. In Figure 4.15, the distortions at the base to the left and right of the Lorentzian curve may be due to a phase shift going through the resonance. The resonance frequency has a quality factor $Q = 7$ for this DHR cell. The quality factor Q is defined as the ratio between the resonance frequency f and the frequency bandwidth at $1/\sqrt{2}$ of the maximum of the resonant profile.

At low CO₂ concentrations in 1 atm N₂, this frequency shifts down to 261± 0.603 Hz (the resonance frequency of pure N₂ or air, see Figure 4.16) and in natural gas (essentially CH₄) it shifts up to 320± 0.678 Hz, consistent with the changes in molar masses. The uncertainty is given by the standard deviation of the Lorentzian curve fits. Since the aim of the project is the detection of low concentrations in air, the resonance frequency of air (261Hz) is used as modulation frequency for the laser. The final calibration curve has been obtained with 261 Hz modulation frequency for the detection of CO₂, H₂S and O₂ in 1 atm air / N₂, see below.

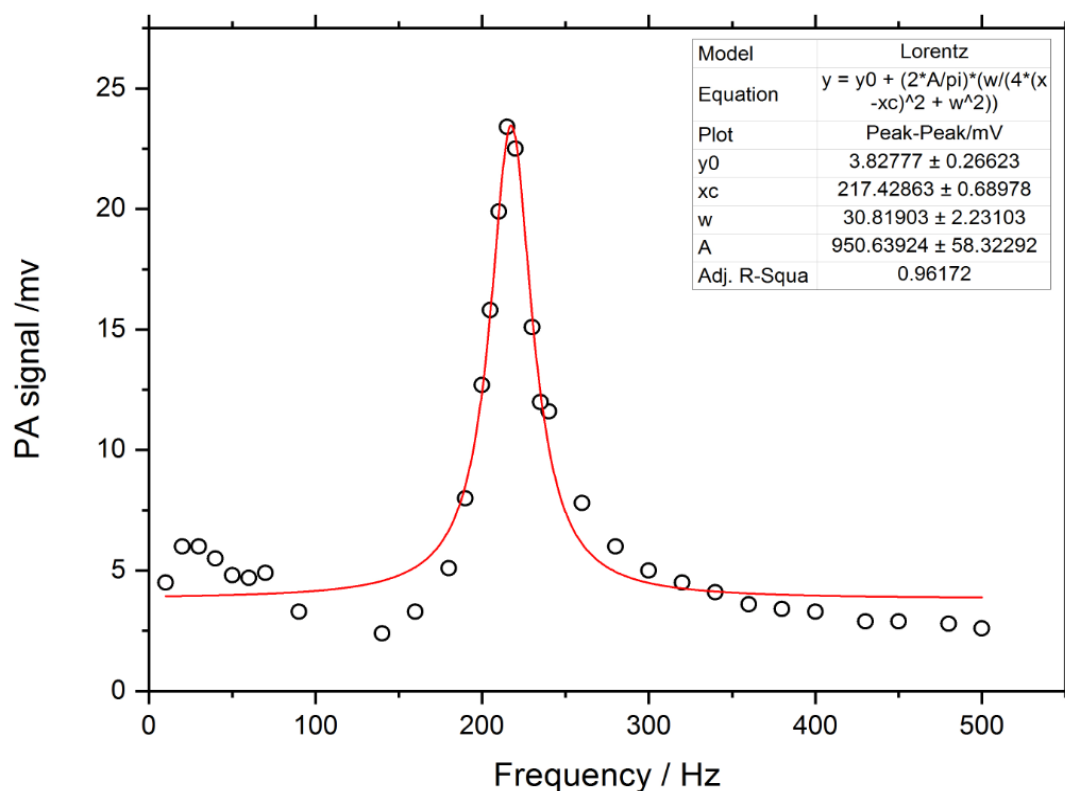


Figure 4.15. Photoacoustic response measured in 1 atm CO₂ to determine the resonance frequency in 100% CO₂.

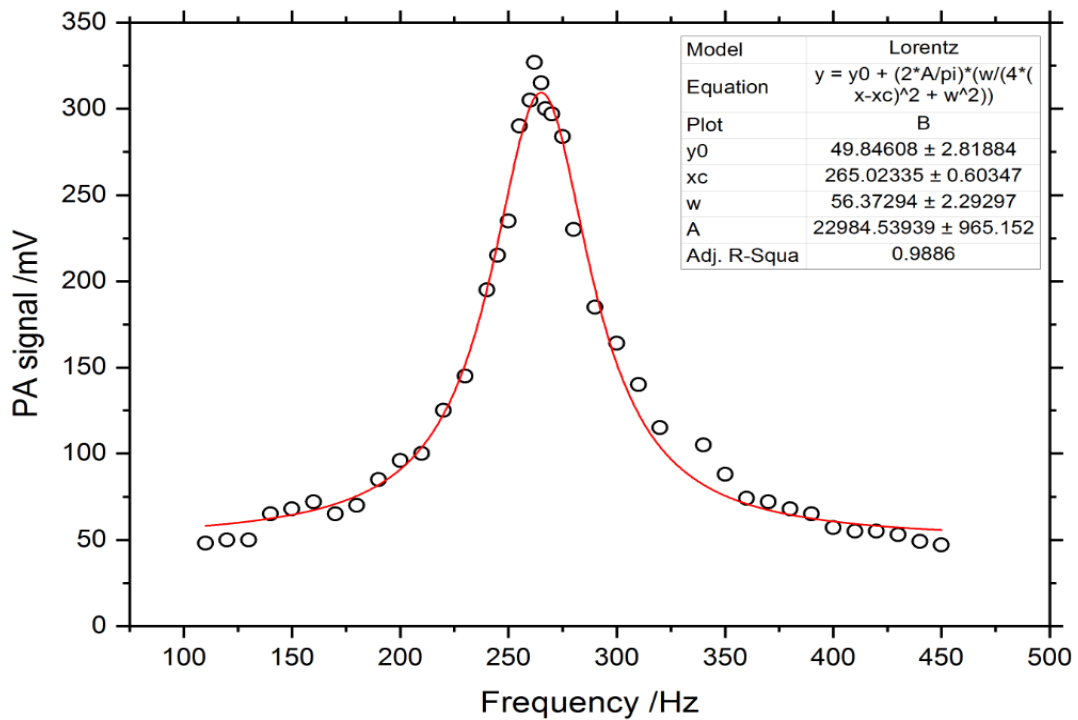


Figure 4.16. Photoacoustic response measured in 100 mbar CO₂ in 1 atm in N₂ to determine the resonance frequency for detection of low concentrations in essentially pure N₂ or air.

The frequency and modulation of the diode current can be controlled by the signal generator as shown in Figure 4.17. The figure shows the modulation applied to the diode current, essentially switching on and off the laser periodically, and the PA signal resulting from this modulation. The PA signal is in phase (red line), it follows the laser power modulation closely (black line).

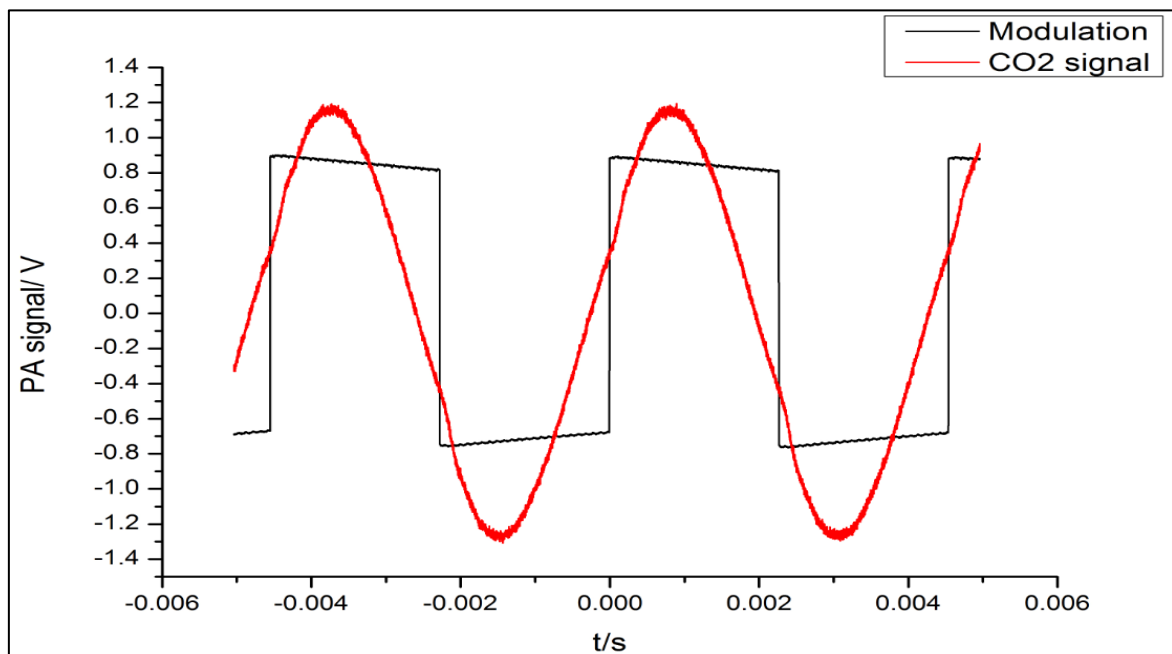


Figure 4.17. The photoacoustic signal of CO₂ and the modulation applied to the diode laser by the signal generator.

4.3.5. Theoretical Absorption Cross Sections of O₂ in the Red and CO₂ in the Near-IR

It is important before starting any experiment to estimate the expected response to plan the experiment thoroughly. Therefore, before starting trace detection by photoacoustic spectroscopy, a data base survey was made to estimate what kind of sensitivity can be expected for O₂ detection in the red in comparison to the near-IR CO₂ detection. According to theory, photoacoustic signal is proportional to absorption cross section and the laser power. Absorption cross sections have been obtained from the HITRAN data base.⁸⁴ In Figures 4.18 and 4.19, the absorption cross sections of O₂ between 13000 – 13200 cm⁻¹ and of CO₂ between 6100 – 6400 cm⁻¹ are shown. The absorption cross sections were calculated for 1 atm air broadening. As can be seen from Figure 4.19, peak absorption cross sections of CO₂ are about 0.007 pm². The O₂ highest peaks have absorption cross sections of 0.006 pm² which is comparable to CO₂. Therefore, the photoacoustic signals are expected to be similar, provided the laser power in the red and in the near-IR are similar. Since similar signal and sensitivity with photoacoustic detection of O₂ compared to CO₂ is expected, and since CO₂ has been detected before, it was decided to do this experiment because the theoretical analysis has shown that it should work.

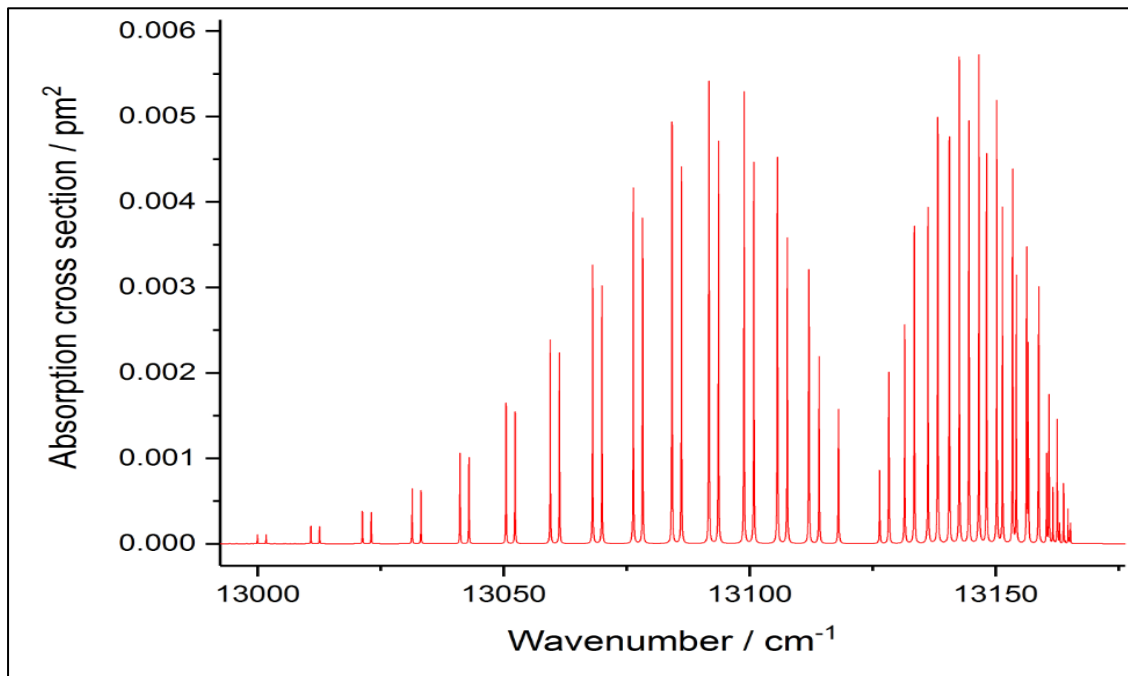


Figure 4.18. Absorption cross section of O₂, according to the HITRAN data base data, with 1 atm air pressure broadening.

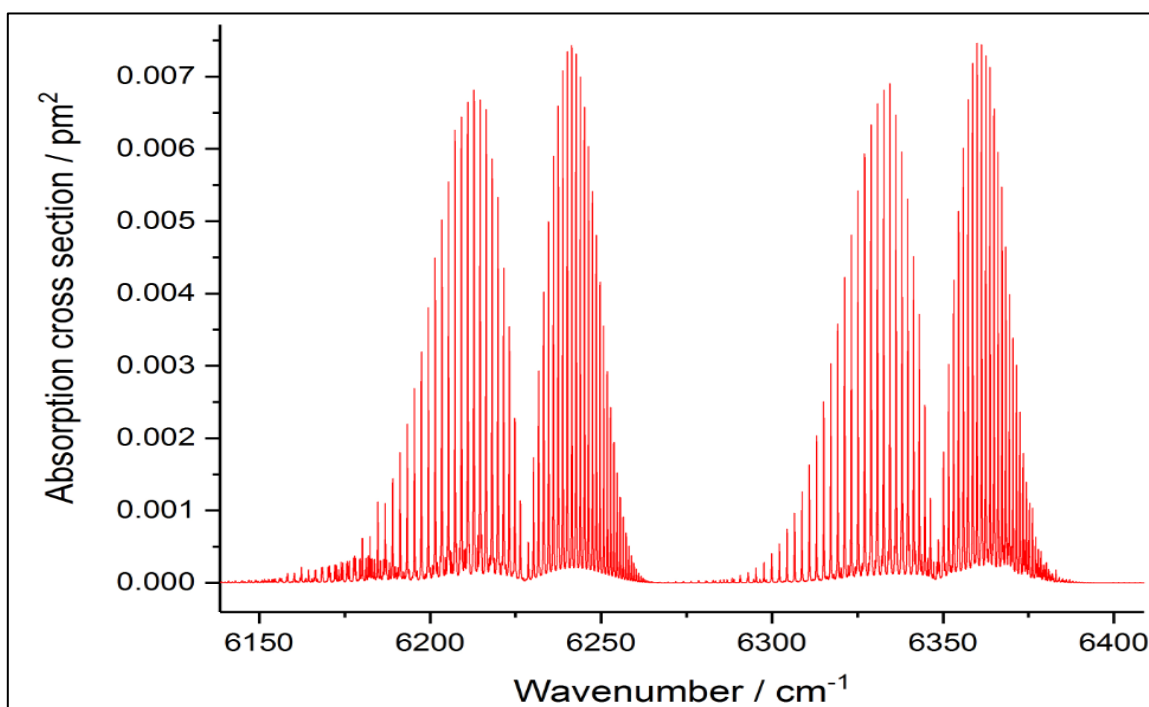


Figure 4.19. Absorption cross section of CO₂, according to the HITRAN data base data, with 1 atm air pressure broadening.

4.3.6. Preparation of Gas Mixtures

Mixtures of gases were prepared in a glass balloon, using freeze-pump-thaw cycles to purify gases, on a gas handling Schlenk line as shown in Figure 4.20. The Schlenk line has several taps to control the gas flow, a Pirani pressure gauge is used for measurement of low pressures in the range of 1×10^{-3} mbar, and a diaphragm gauge (Leybold Vacuum GmbH CTR 90) for accurately measuring higher pressures in the range of 100 Torr. Typically, the system is evacuated until a base pressure of less than 1×10^{-3} mbar is achieved. To prevent condensable gases reaching the pumps, a liquid nitrogen cooled trap is used.

To prepare a sample balloon containing a known pressure of gases (CO₂, H₂S), two glass balloons were prepared first, one contained pure CO₂ (typically 1000 mbar, sublimed from dry ice), the other fully evacuated to the 1×10^{-3} mbar base pressure to facilitate the gas transfer from the other balloon. The desired amount of CO₂ or H₂S was transferred to the evacuated glass balloon, then N₂ from the laboratory gas line was used to complete the total pressure in the balloon until 1000 mbar. The gas balloon containing the known concentration of CO₂ or H₂S was then connected to the PA set up. The DHR cell in the photoacoustic set-up was completely evacuated until around 10^{-2} mbar to facilitate the gas transfer from the sample balloon into the DHR cell for analysis.



Figure 4.20. Photo of the gas handling line. (A) roughing pump bypass tap, (B) vacuum pump for low pressure (1×10^{-3} mbar), (C) trap of liquid nitrogen, (D) the Schlenk line, (E) pressure gauge for higher pressures, (F) the glass balloon to be filled with sample, (G) a Pirani gauge and (H) Pirani gauge read-out unit for low pressures.

4.4. Results and Discussions

4.4.1. External Cavity Diode Laser (ECDL) Characterisation

Characterisation of the ECDL is important in order to know which molecular absorptions can be excited by the diode laser. As a first step, it is important to know the tuneability range of the wavelength, which is controlled by the motor arm which in turn controls the mirror in the Littman-Metcalf configuration to determine the laser wavelength by the grating feedback. The wavelength is directly controlled by the mirror rotation; the motor arm is connected to the PC for easy control of the mirror movement between distances from 0-8 mm. By tuning the mirror motor position very gradually (0.003 mm/s), a high resolution spectrum of the IR-active species is obtained. It is important to obtain the relationship between mirror position and laser wavelength or wavenumber by calibration. The conversion was obtained by comparing peaks on the measured CO₂ spectrum with peaks from the HITRAN data base reference spectrum.⁸⁴ Calibration is accomplished by comparing the experimental spectrum with CO₂ line positions. Figure 4.21 shows the wavenumber of diode laser emission against mirror motor position after calibration. It shows that the ECDL can be tuned between 6150 – 6450 cm⁻¹ by tuning the grating mirror.

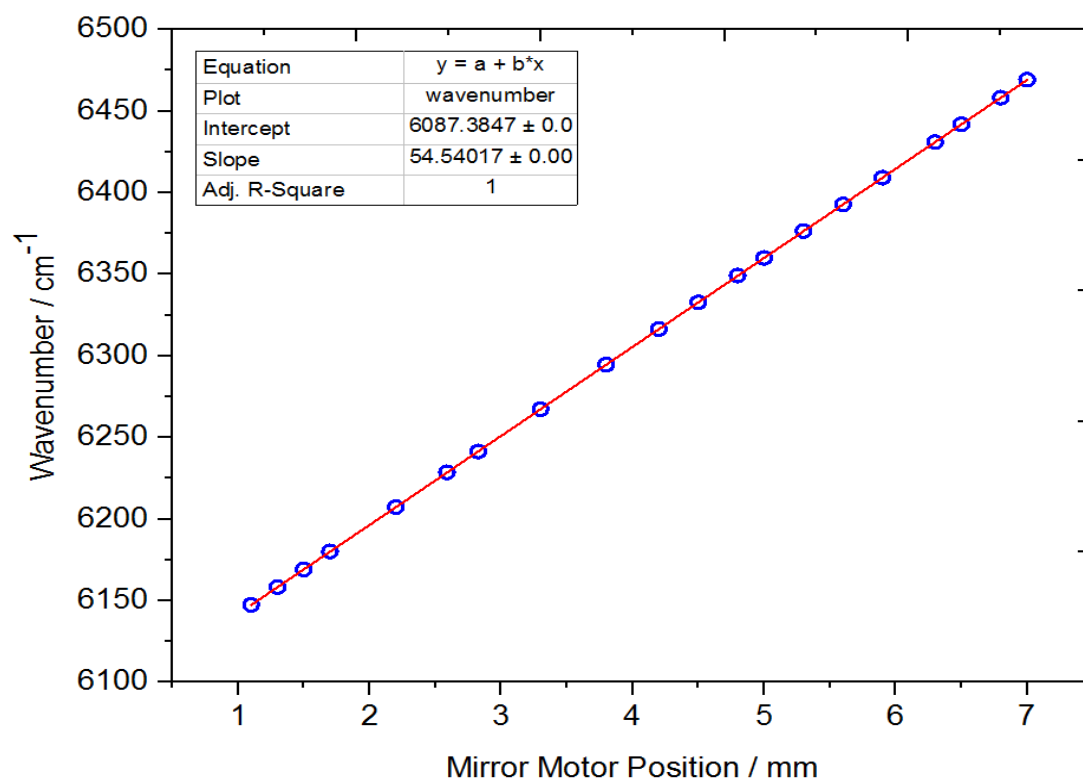


Figure 4.21. Wavenumber of diode laser emission against mirror motor position.

4.4.2. Calibration Spectrum of Carbon Dioxide (CO₂) with HITRAN Data Base

CO₂ is used to optimise the setup of the laser system and the PA detection, because it is much less toxic than H₂S gas, it is easier to handle, and its spectroscopic properties are well known. The measurements conducted have a signal integration time of 330 ms, a lock-in amplification of $\times 10$, and optimised phase shift between the modulation frequency and the photoacoustic signal in the lock-in amplifier. The laser power booster is set at 300 mA for the CO₂ measurements, which gives a maximum power of about 15 mW NIR with the modulated laser at 50 % duty cycle.

Figure 4.22 shows the spectrum of CO₂ buffered in N₂ recorded in the DHR system. The spectrum of CO₂ (red line) is compared against a reference spectrum from a data base, HITRAN (black line). HITRAN is a high resolution molecular spectroscopic database which is the standard compilation of spectroscopic reference data for molecular absorptions, from microwave to ultraviolet wavelengths.⁸⁴ Figure 4.22 shows good general agreement between measured and expected line position and line intensities. There are some irregularities, e.g. lines missing below 6200 cm⁻¹. They are most likely due to limitations of the laser such as tuning range and mode hops.

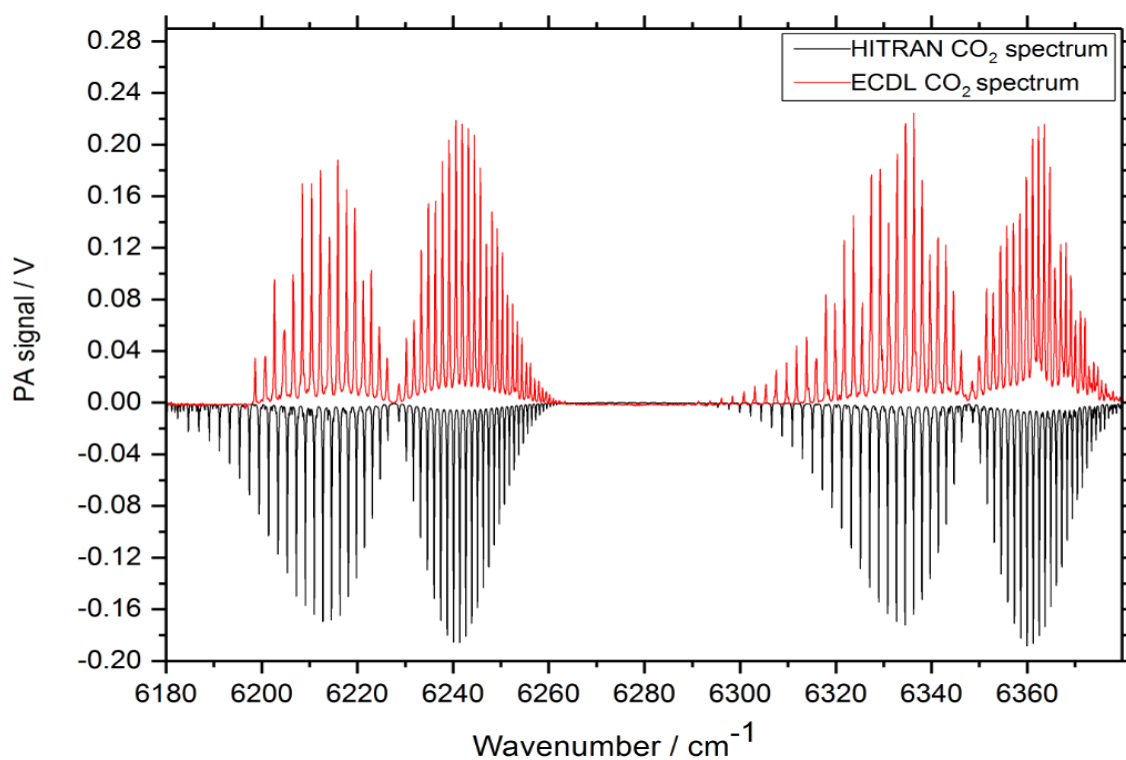


Figure 4.22. The spectrum of CO₂ buffered in N₂ (red line) compared against HITRAN (reference) CO₂ spectrum (black line).

The main aim of using the ECDL was to obtain an overview of strong CO₂ absorptions in the NIR. An ECDL is well suited for this purpose since it is tuneable over a wide range of wavelength. Based on this preliminary work with the ECDL, a DFB diode was selected to cover some strong CO₂ and H₂S absorption. Although a DFB laser has a much smaller tuning range than an ECDL, it has better single-mode performance and is easier to tune by temperature control, and it is also less costly.

4.4.3. Hydrogen Sulfide (H₂S) Measurements Using ECDL

In this part, the ECDL laser is used to measure a full spectrum of H₂S which is compared with the HITRAN data base⁸⁴ as shown in Figure 4.23. This is useful to determine the correct peaks and find the best peak to make calibrations. Tuning is done by the movement of the mirror in the ECDL set up, giving wavelength tuneability between 6150 – 6400 cm⁻¹. All the measurements conducted have an integration time of 330 ms, lock-in amplification of 10, and optimised phase shift between the modulation frequency and the photoacoustic signal in the lock-in amplifier. The laser power booster is set at 300 mA as for the CO₂ measurements, which gives a maximum power of about 30 mW NIR cw, or 15 mW at 50% duty cycle after modulation. Figure 4.23 shows the spectrum of H₂S with 1 atm N₂ recorded in the DHR system. The spectrum of H₂S (red line) is compared against a reference spectrum from a data base, HITRAN (black line).

In addition, the measured spectrum of H₂S is compared with the HITRAN data base including spectra for H₂O and CO₂, in order to ensure that the line which is chosen to make the trace gas measurement and calibration for H₂S is not overlapping with any interfering lines of H₂O or CO₂. The comparison is shown in Figure 4.24.

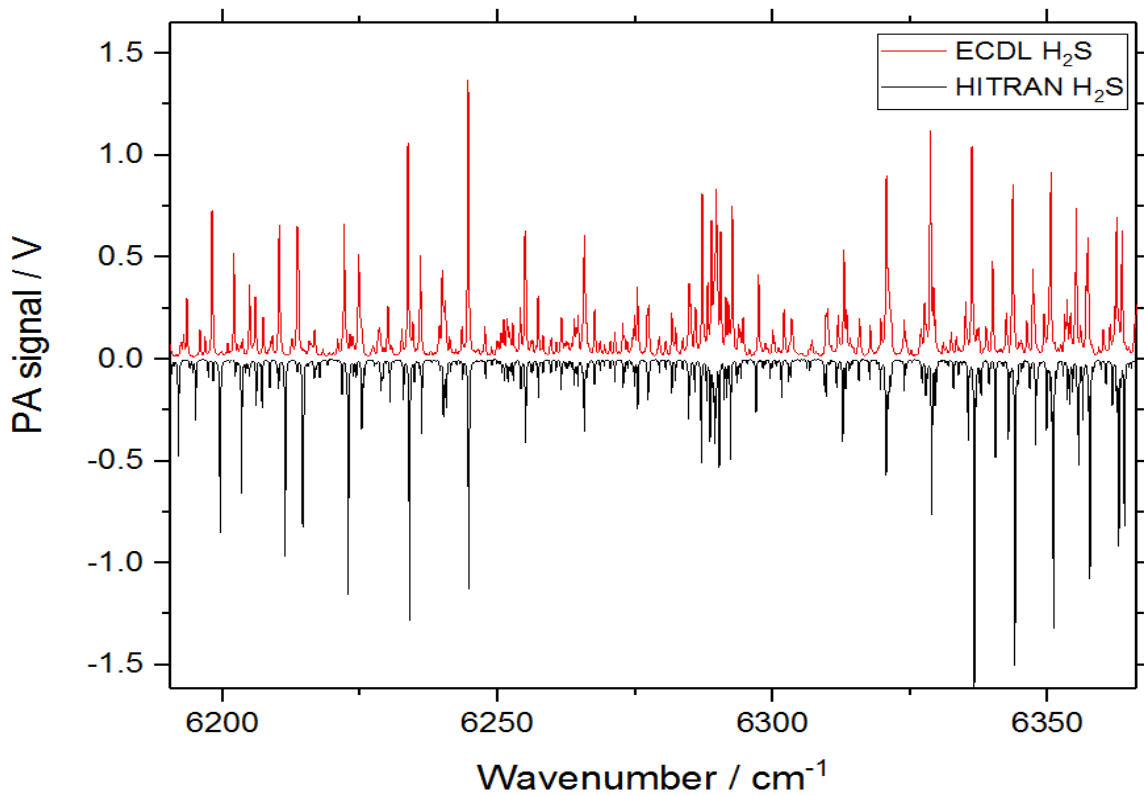


Figure 4.23. A measured spectrum of H₂S (red line) compared with the HITRAN reference spectrum (black line).

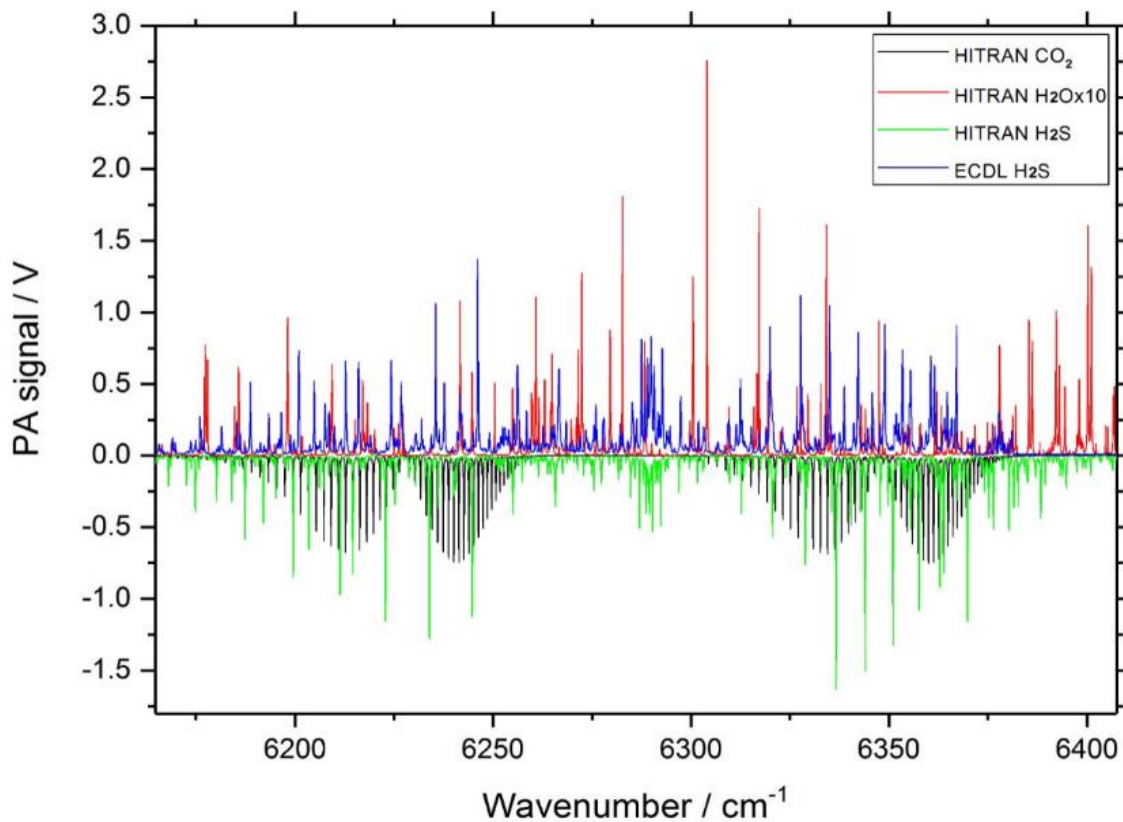


Figure 4.24. A comparison of the HITRAN data for H₂O (red line), CO₂ (black line) and H₂S (green line) with the measured H₂S spectrum (blue line).

4.4.4. Calibration Spectrum of Carbon Dioxide (CO₂) with HITRAN Data Base by using the DFB laser system

A DFB laser is used instead of the ECDL in the final PA set up. As before, calibration samples are prepared directly from CO₂ which has been purified from dry ice using freeze-pump-thaw cycles and mixed with N₂ to 1 atm total pressure. The samples are then transferred in a glass balloon to the DHR cell, as explained before.

In a DFB laser, wavelength tuning is controlled by the temperature setting of the diode. The rate of temperature change was of 0.02 °C s⁻¹ in order to collect the spectrum with good spectral resolution. The integration time was 1 s and amplification setting x10 in the lock in amplification. The laser power was at 15 mW using power booster with the modulated laser at 50 % duty cycle, essentially the same power as with the ECDL system.

Figure 4.25 shows the relationship between temperature of DFB and wavenumber from which Equation 41 is obtained. According to the calibration, a 1 °C increase of temperature corresponded to approximately 0.52 cm⁻¹ change in wavenumbers, as shown in Figure 4.26. A practical temperature range is between 20 – 60 °C. As shown in Figure 4.26 this corresponds to a wavenumber range of between 6354 - 6380 cm⁻¹. The strongest line within this range is the R (18) line of CO₂ at 6361.250 cm⁻¹ with peak absorption cross section $\sigma_{\text{peak}} = 0.00757 \text{ pm}^2$ (1 bar air pressure broadened) according to the HITRAN data base.⁸⁴ This line will be used for CO₂ detection.

$$\tilde{\nu} / \text{cm}^{-1} = 6388.7565 - 0.5220 \times T / ^\circ\text{C} \quad \text{Equation 41}$$

Since the final wavelength calibrations will always be made with HITRAN reference lines, and Equation 41 is only used for initial calibrations, no error analysis was attempted for Equation 41 (the uncertainties in the linear fitting procedure are given in the inset of Figure 4.25).

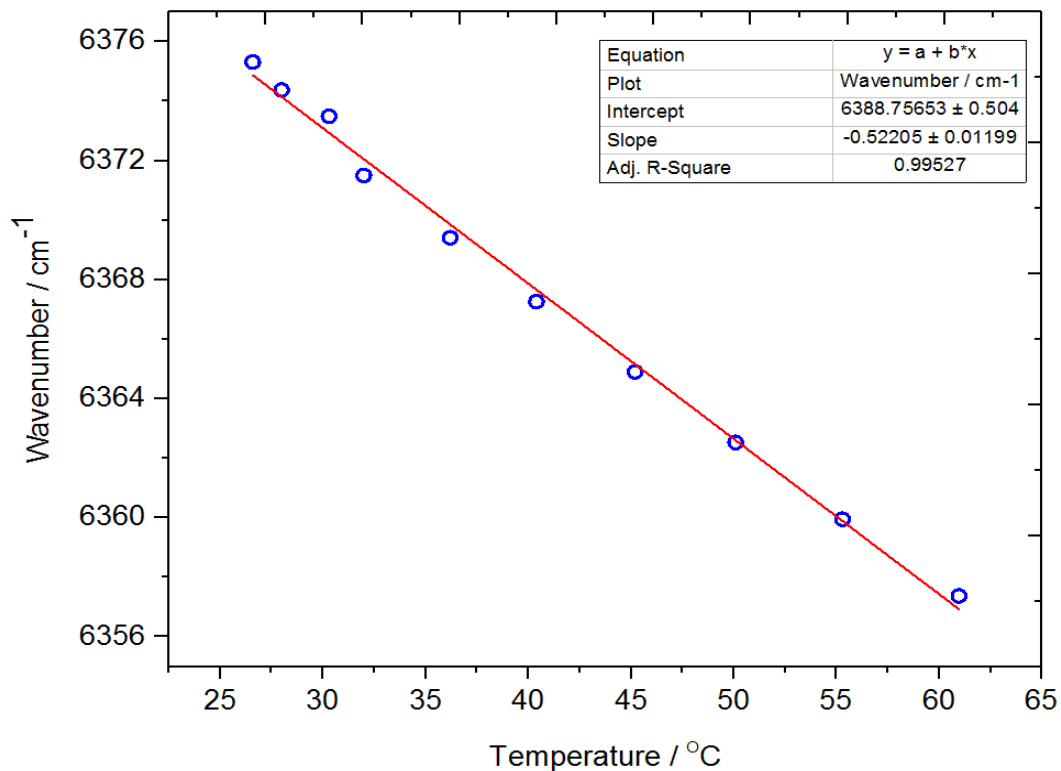


Figure 4.25. A calibration graph of the DFB's temperature compared with the wavenumber emitted.

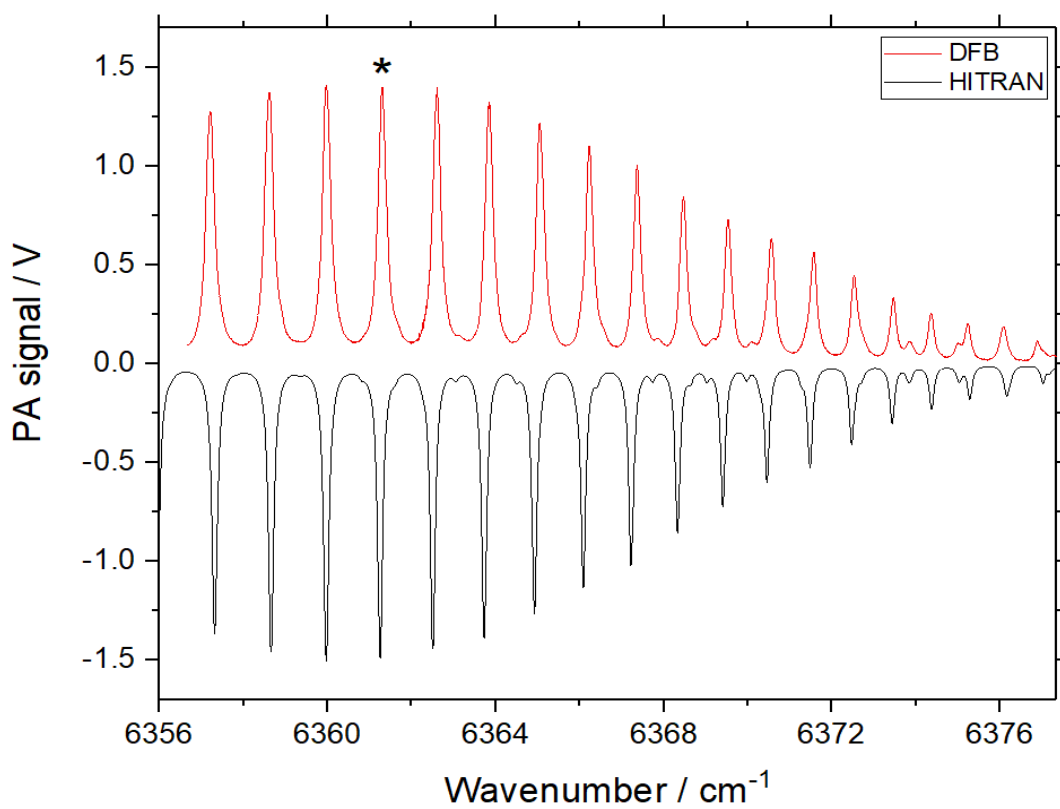


Figure 4.26. A spectrum of CO₂ produced by the DFB upon varying the temperature between 20 – 60 °C. In red the measured photoacoustic spectra, in black a reference spectrum from the HITRAN data base.⁸⁴

Figure 4.27 provides an overview of absorptions within the accessible range from the HITRAN database at 1 atm air broadening, including absorption of CO₂, H₂S and also water absorptions to assess whether water will interfere with CO₂ or H₂S detection. This figure is comparable to Figure 4.24, except with a shorter wavenumber range of the HITRAN database. Water quite often interferes very severely in 'real life' applications, in particular in the region of mid-IR fundamental vibrations. Fortunately, the absorption features of water are very weak in this near-IR region, with absorption cross sections below $4 \times 10^{-5} \text{ pm}^2$.⁸⁴ In this chapter, we aim for the detection CO₂ or H₂S in air. The peaks chosen are all well isolated with negligible interference with each other and with water at normal abundance.

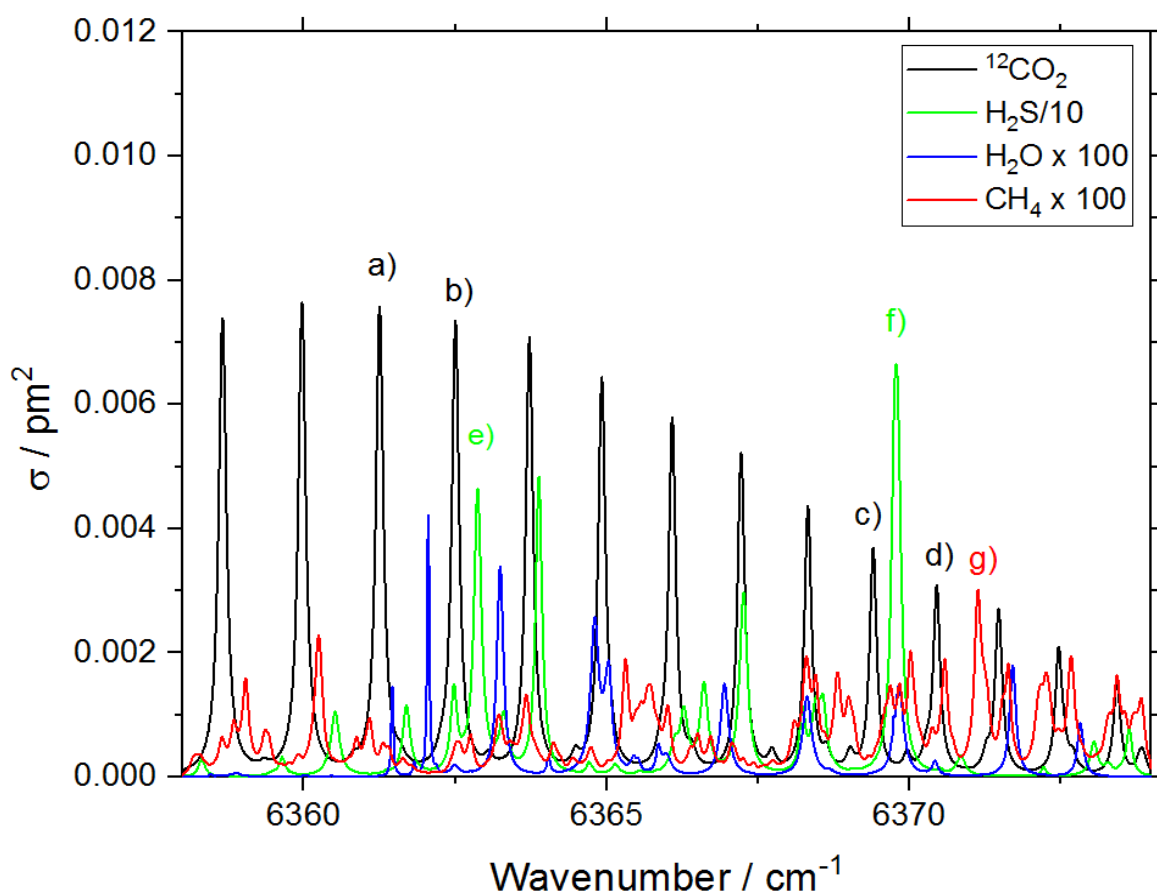


Figure 4.27. HITRAN absorption cross sections (1 atm air pressure broadening) of CO₂ (black), H₂S (green, scaled $\times 0.1$), water vapour (blue, scaled $\times 100$) and methane CH₄ (red, scaled $\times 100$).⁸⁴ Lines **a**) to **d**) are CO₂ peaks, **e**) and **g**) H₂S peaks and **g**) is a CH₄ peak.

The CO₂ absorptions in Figure 4.27 are part of the *R*-branch of the 3ν₁ overtone. The strongest line (labelled **a**) in Fig. 4.27) is the *R*(18) line at 6361.28 cm⁻¹ with peak absorption cross section $\sigma_{\text{peak}} = 0.00757 \text{ pm}^2$ (1 atm air pressure broadened).⁸⁴ This line is indicated as well by an asterisk in Figure 4.26. It has been chosen for detection of CO₂ because it is one of the strongest CO₂ lines accessible to the laser.

In Figure 4.28, the blue data points represent measured peak signals of the *R*(18) line from measurements of known CO₂ concentrations which have been prepared on the gas handling line, expressed as partial pressure (buffered with 1 atm of N₂). The calibration shows a good linear response in the logarithmic plot with an *R*² value of 0.998. The slope is 1.08 in the logarithmic plot which means there is a slight deviation from a linear relationship between partial pressure and photoacoustic signal. This deviation is most likely be caused by the change of gas composition, from a mixture of CO₂ and N₂ at high concentrations to essentially just N₂ at low concentration, which changes the acoustic behaviour. The noise level of the experiment has been determined by the standard deviation (σ) of the baseline to be 0.98 mV with the laser still on. It represents the noise floor at 1 s integration time. The calibration line intersects this level at a concentration of 0.160 mbar CO₂ in 1 atm N₂, giving the noise equivalent detection limit at 1 s integration time with the 30 mW laser as shown in Figure 4.28. The noise equivalent detection limit is therefore 0.160 mbar which is 160 ppmv of CO₂ at 1 atm total pressure and 1s integration time. Note that this is the *noise equivalent* detection limit (1 σ limit); practical detection limits are often quoted as 3 σ in the literature. In Figure 4.28, statistical error bars are included for each measurement. To estimate the uncertainty in the noise equivalent detection limit, the calibration line can be moved within the error bars to give the range of 160 ppmv \pm 40 ppmv for the intersect, which may serve as an estimate for the uncertainty. Since photoacoustic signal scales linearly with laser power and statistical noise decreases with the square root of integration time, improved detection limits are achievable with higher laser power and longer integration times. Normalizing to absorption cross section, laser power and integration time, a noise equivalent normalized absorption coefficient $\alpha = 8.3 \times 10^{-9} \text{ cm}^{-1} \text{ W s}^{1/2}$ is calculated (see Appendix 4). This detection limit should be adequate for the biological measurements which will follow from this experiment. To further demonstrate the sensitivity of the DHR scheme, ambient, fresh air from the outside was measured as shown in Figure 4.29. At 1 s integration time of each data point displayed, the *R*(18) line due to CO₂ at natural abundance (410 ppmv) can clearly be distinguished above the noise level.

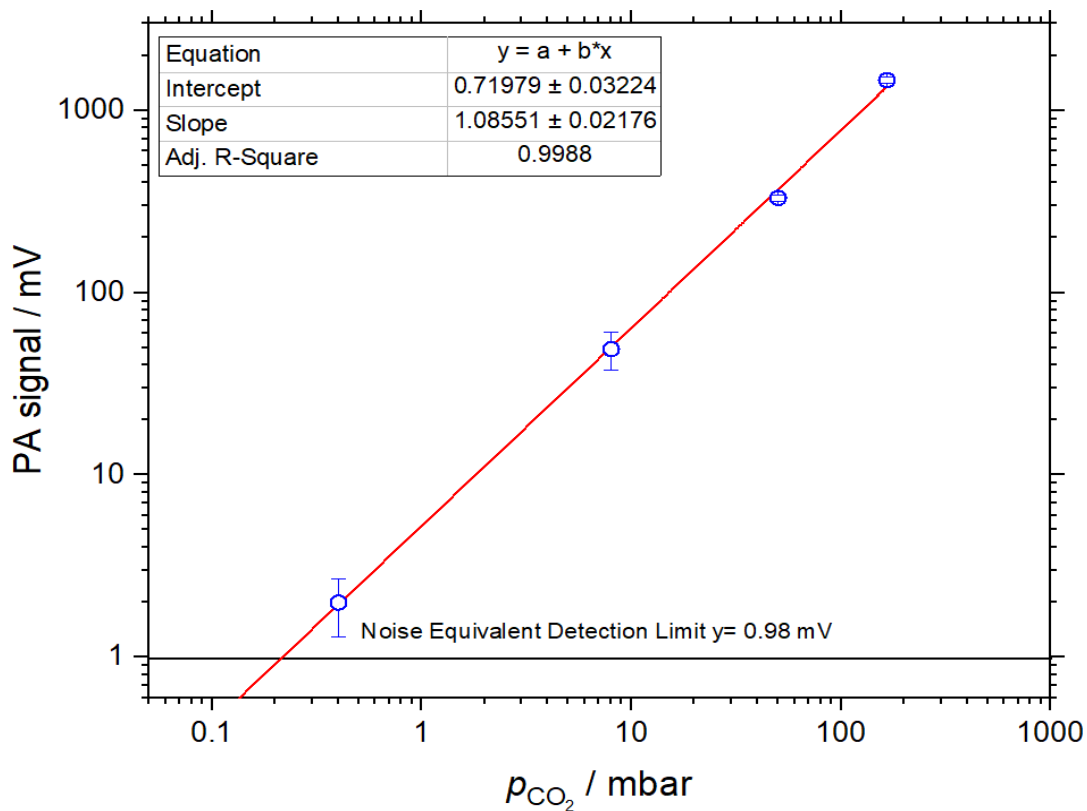


Figure 4.28. Calibration line for partial pressures of CO₂ using the peak at 6361.28cm⁻¹, and determination of the noise equivalent detection limit. Error bars represent standard deviation (1 σ) of experimental replicates.

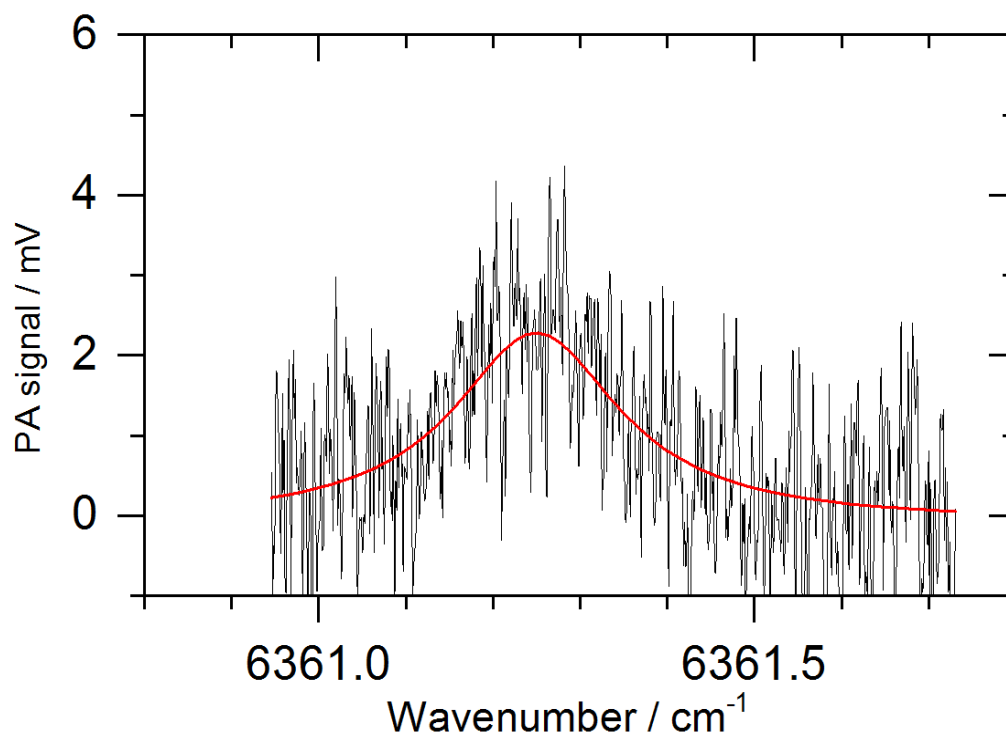


Figure 4.29. Photoacoustic spectrum of CO₂ at natural abundance in 1 atm of ambient air. Red: Lorentzian line fit of the R(18) line of CO₂.

4.4.5. Hydrogen Sulfide (H₂S) Measurements in Air/ N₂ Using a DFB laser at 1.57 μm

Within the tuning range of the near-IR DFB diode laser (6360 – 6378 cm^{-1}), H₂S absorption features can be accessed which can be used for trace gas detection in the differential Helmholtz resonator. Figure 4.30 provides a comparison of the HITRAN data base compared to a PA measurement of 150 mbar of H₂S using the DFB laser system. The strongest feature is at 6369.8 cm^{-1} , a feature of the $\nu_1\nu_2\nu_3$ combination band. It is indicated by the asterisk in Figure 4.30 and labelled **f**) in Figure 4.27. It is used for H₂S detection. Its peak absorption cross section is $\sigma_{\text{peak}} = 0.0665 \text{ pm}^2$ (1 atm air pressure broadened)⁸⁴, about 9 \times stronger than the CO₂ line used for CO₂ detection.

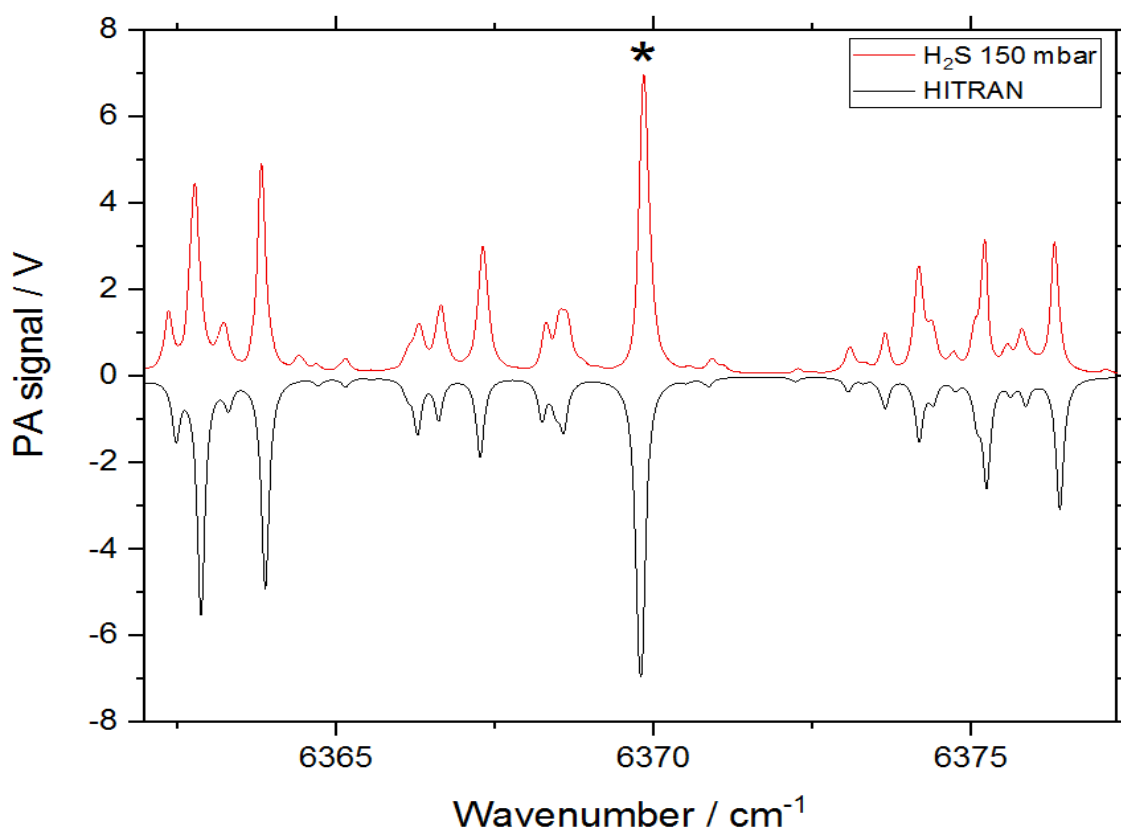


Figure 4.30. A PA spectrum in the DHR of 150 mbar H₂S (red line) using the DFB laser, compared to the HITRAN reference spectrum (black line).

Figure 4.31 is the calibration for H₂S detection observing the peak height of the 6369.8 cm⁻¹ feature in 1 atm N₂. With the same noise limit of 0.98 mV at 1 s integration time, a noise-equivalent detection limit of 0.022 mbar or 22 ppmv in 1 atm N₂ is obtained with the 30 mW laser. In Figure 4.31, statistical error bars are included for each measurement. To estimate the uncertainty in the noise equivalent detection limit as before for CO₂, the calibration line can be moved within the error bars to give the range of 22 ppmv ± 8 ppmv for the intersect, which may serve as an estimate for the uncertainty.

The much lower detection limit compared to CO₂ is due to the stronger absorption of H₂S. The detection limit is below the immediately dangerous to life or health limit (IDLH) of 100 ppmv;²⁹ the DHR sensor may therefore be useful as a safety monitor for toxic levels of H₂S, in particular if additional integration time or spectral line fitting procedures improve the detection limit.

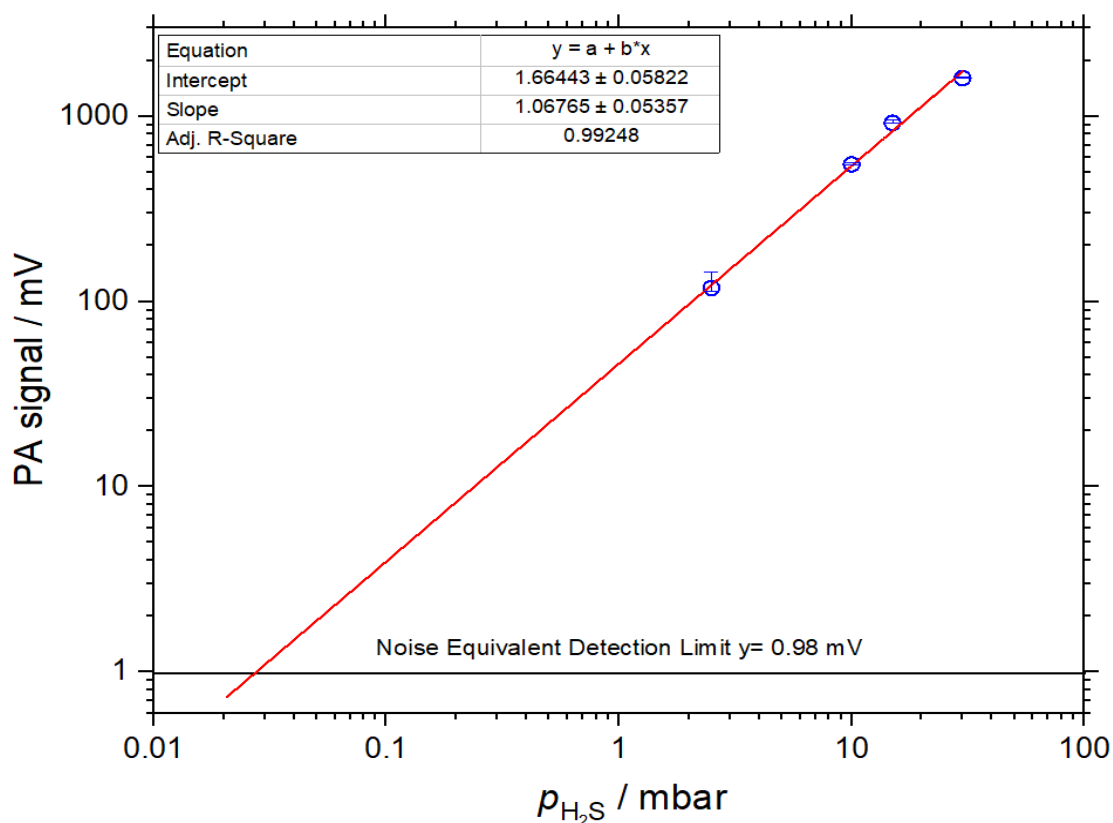


Figure 4.31. Calibration line for partial pressure of H₂S in 1 atm N₂ using the peak at 6369.8cm⁻¹, and determination of the noise equivalent detection limit. Error bars represent standard deviation (1 σ) of experimental replicates.

4.4.6. Photoacoustic Detection of Molecular Oxygen Near 764 nm

Molecular oxygen (O_2) does not have an IR-active vibration, but it can be detected by an electronic absorption band in the red, the $b^1\Sigma_g^+(v=0) \leftarrow X^3\Sigma_g^-(v=0)$ band of molecular oxygen (the “A band”) near 760 nm. It is a very weak, formally forbidden transition with absorption cross-sections of the same order than the near-IR combination bands of CO_2 and H_2S near 1.57 μm . Some of the strongest rotational lines of the A band are within the range of our DFB diode laser (EYP-DFB-0764-00040-1500-TOC03-0002). It emitted in a narrow range at around 763 nm - 765 nm or 13106.15 cm^{-1} - 13071.89 cm^{-1} with power 35 mW. Wavelength tuning is accomplished by changing the diode temperature. The tuning range of the temperature was between 24 – 38 $^{\circ}C$. Figure 4.32 shows the photoacoustic spectrum of 1 bar air obtained in the DHR, by temperature tuning the laser from 24 – 38 $^{\circ}C$. Good agreement with literature data (HITRAN) for O_2 absorption is obtained.⁸⁴ The relationship between temperature of DFB and wavelength was given by a monochromator (Shamrock, SR-163) measuring the wavelength of the red diode. Measured wavelength as a function of the temperature of the diode is shown in Figure 4.33. The uncertainties of the linear fit for the calibration line are shown in the inset of the Figure 4.33.

The strongest line is used for analysis of O_2 ; it is marked by an asterisk in Figure 4.32. The transition is the $P(11)$ line at 764.280 nm (vacuum) which has a peak absorption cross section of $\sigma_{\text{peak}} = 0.00478\text{ pm}^2$ (1 bar pressure broadened).⁸⁴ At an abundance of 210 mbar in 1 bar air, the peak photoacoustic signal of this line is 310 mV. The standard deviation of the baseline, 0.88 mV at 1 s integration time, can serve as an estimate of the noise level. A noise equivalent detection limit of 0.60 mbar (600 ppmv) of O_2 in 1 bar of air at 35 mW peak power and 1 s integration time is thus obtained. Normalizing to the absorption cross section, the laser power and integration time, a noise equivalent normalized absorption coefficient $\alpha = 2.2 \times 10^{-8}\text{ cm}^{-1}\text{ W s}^{1/2}$ is calculated (see Appendix 5). Taking into account the simplicity of the DHR setup, this compares favourably with detection limits of more complex photoacoustic schemes, such as quartz cantilever enhanced photoacoustic spectroscopy where $\alpha = 4.8 \times 10^{-9}\text{ cm}^{-1}\text{ W s}^{1/2}$ was reported for photoacoustic detection of oxygen by a 30 mW DFB diode near 760 nm.⁵¹ In an application where the head space above an aqueous solution is measured (as in the bacterial suspensions at 37 $^{\circ}C$), 600 ppmv of O_2 in the gas phase corresponds to an oxygen concentration of 12 ppb per mole in the solution, using Henry's law and Henry's constant at 37 $^{\circ}C$ (see Appendix 6).

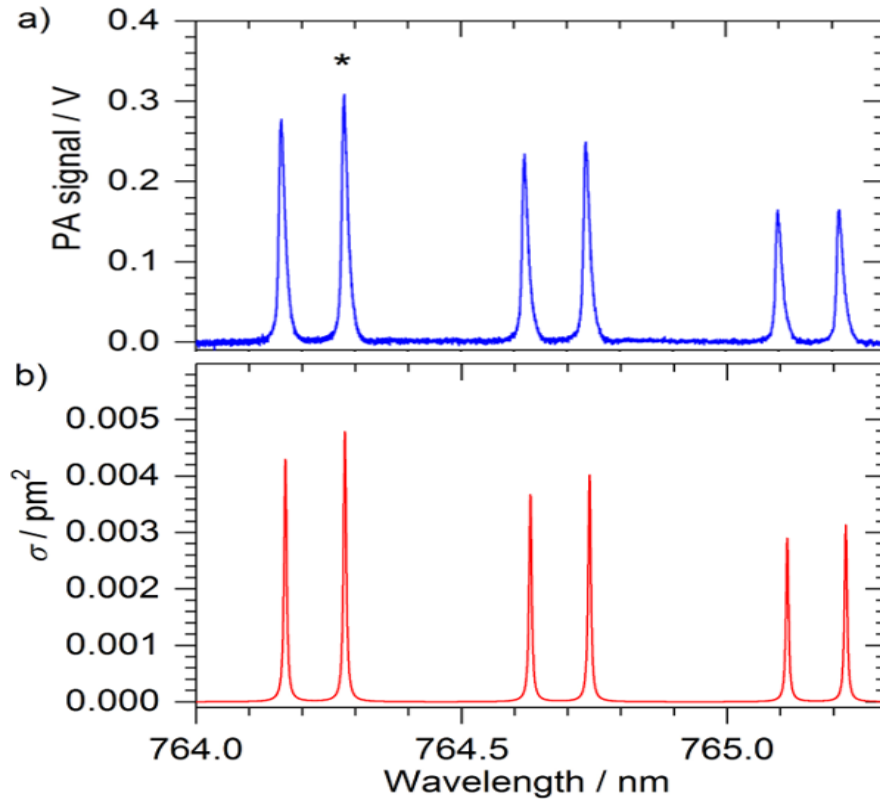


Figure 4.32. a) Photoacoustic spectrum of 1 bar air in the Helmholtz resonator, obtained by temperature tuning the DFB laser from 24 – 38 °C. The peak marked by the asterisk is used for detection of molecular oxygen. b) HITRAN absorption cross sections (1 bar air pressure broadening) of molecular oxygen in the A band.⁸⁴

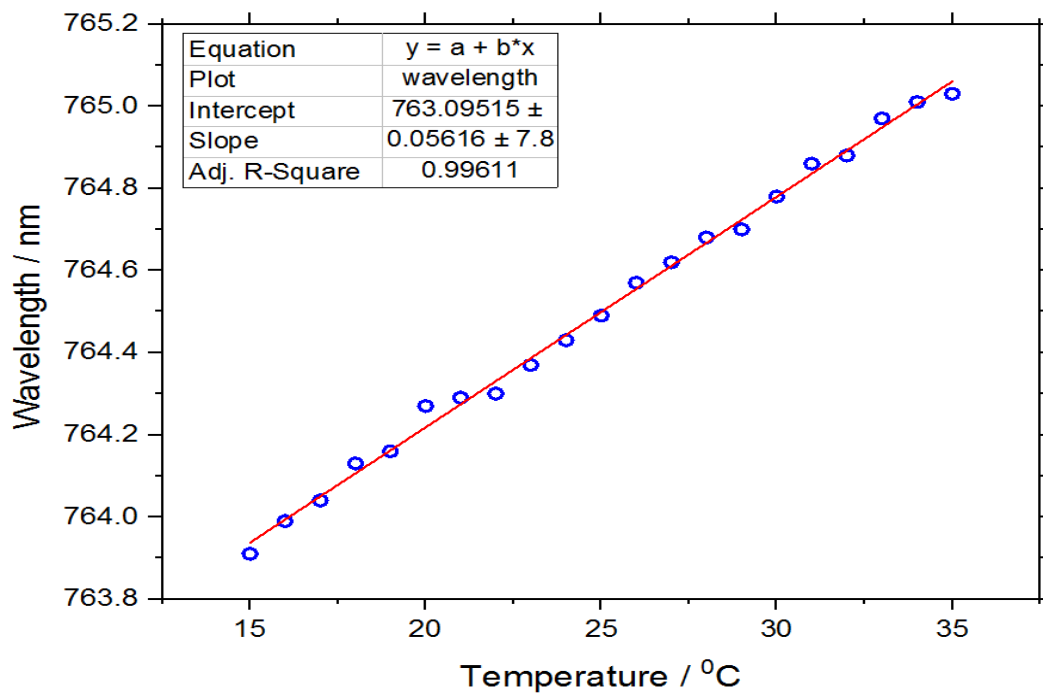


Figure 4.33. A calibration graph of the red DFB diode laser's temperature compared with emitted wavelength (nm) as given by the monochromator (Shamrock, SR-163).

4.4.7. Demonstrating the Distinction of $^{12}\text{CO}_2$ and $^{13}\text{CO}_2$ Isotopomers in Preparation of Biology Experiments

Different isotopomers have different vibrational spectra. PA spectroscopy can therefore be used to distinguish between different isotopomers. Isotopic labelling can be used to probe biological mechanisms, to give a very relevant application example. In the next chapter, the carbon source for aerobic metabolism of *E. coli* will be investigated using a mix of two labelled sugars ^{13}C -glucose and ^{12}C -lactose, to examine if *E. coli* shows a preference for one sugar over the other. Therefore in preparation for these experiments, it is necessary to know the positions of peaks for the different isotopically labelled CO_2 molecules before starting to apply any biology experiments. Figure 4.34 provides an overview from the HITRAN data base⁸⁴ for $^{13}\text{CO}_2$ (red line) and $^{12}\text{CO}_2$ (blue line) in the region accessible to the near IR DFB laser. From this figure it can be seen that in the region $6370 - 6373 \text{ cm}^{-1}$, there are separated $^{13}\text{CO}_2$ and $^{12}\text{CO}_2$ signals.

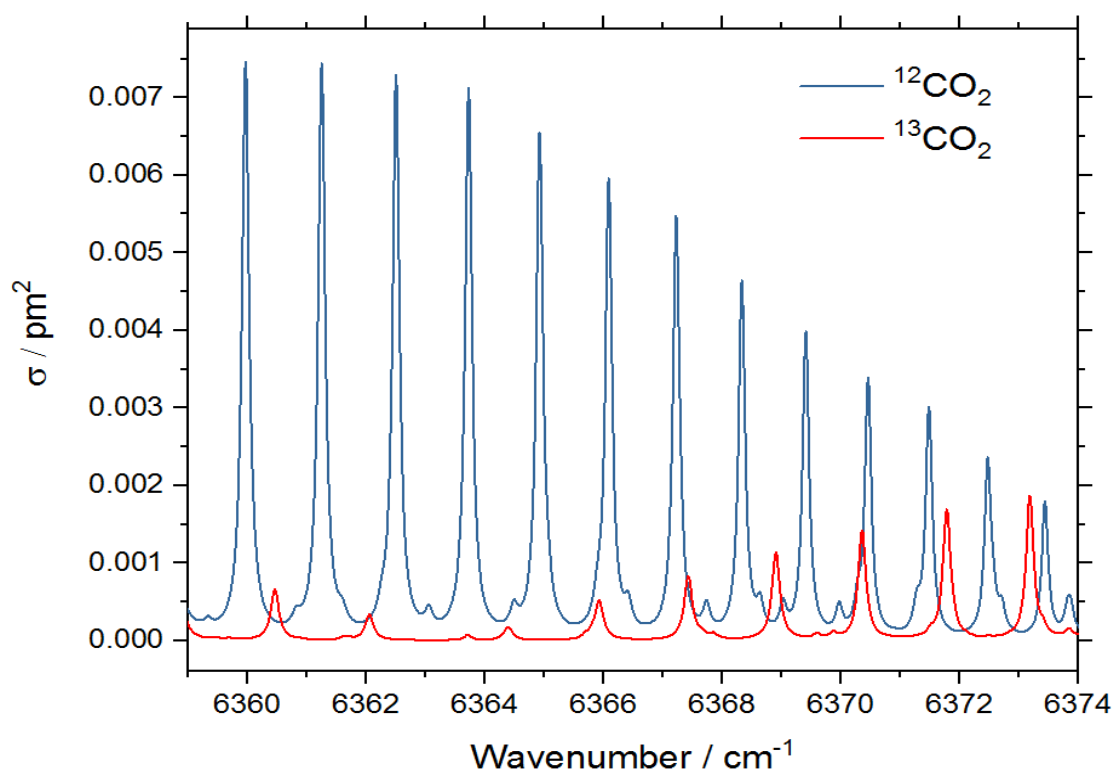


Figure 4.34. Overview from the HITRAN data base⁸⁴ for $^{13}\text{CO}_2$ (red line) and $^{12}\text{CO}_2$ (blue line).

The tuning range of the near-IR DFB diode laser $6370 - 6373 \text{ cm}^{-1}$ corresponds to a temperature range from $29.5 - 33.7 \text{ }^\circ\text{C}$, it can be used for detecting $^{13}\text{CO}_2$ and $^{12}\text{CO}_2$ in a single scan. To demonstrate this further, Figure 4.35 (a) shows a mixture of $^{13}\text{CO}_2$ and $^{12}\text{CO}_2$ from the HITRAN data base⁸⁴ comparing with an experimental measurement of a mixture of $^{13}\text{CO}_2$

and $^{12}\text{CO}_2$, as measured by PA in the DHR cell, shown in Figure 4.35 (b). Good agreement is found between theory and experiment. The peak at 6371.7 cm^{-1} shown in Figure 4.35 (b) is a strong line for $^{13}\text{CO}_2$. The absorption cross section for this peak is $\sigma_{\text{peak}} = 0.0017\text{ pm}^2$ (1 bar air pressure broadened), as shown in Figure 4.35 (a). This line will be used for $^{13}\text{CO}_2$ detection in the biology experiments described in detail in the next chapter. For quantitative $^{12}\text{CO}_2$ and $^{13}\text{CO}_2$ detection in this range, the previous calibration for the $R(18)$ line can be used if adjustment is made for the different absorption cross sections.

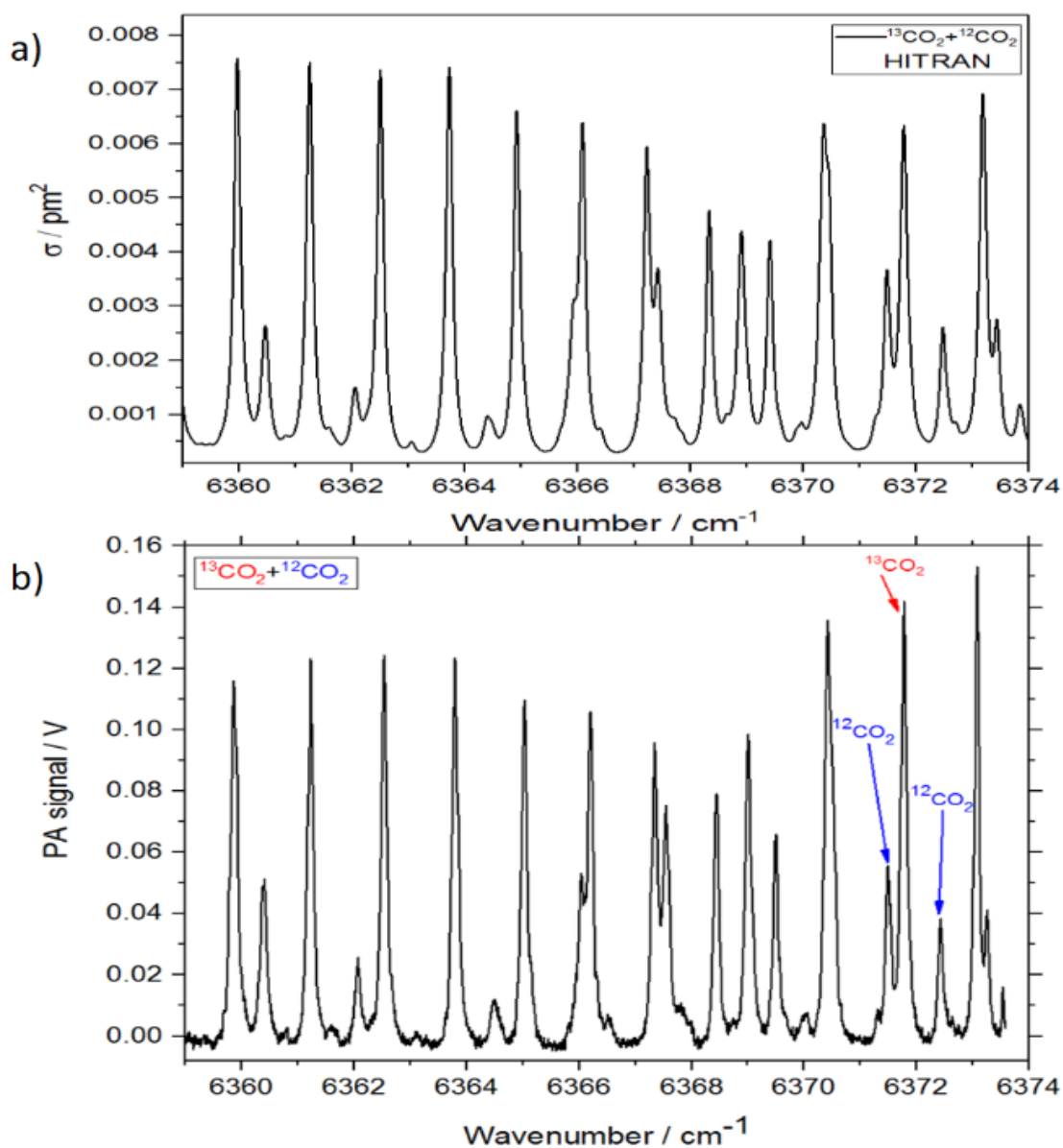


Figure 4.35. Comparison of theoretical and experimental spectra of a mixture of $^{13}\text{CO}_2$ and $^{12}\text{CO}_2$: a). Data from the HITRAN data base⁸⁴, b) experimental data from a PA scan by using the DHR cell.

4.5. Conclusions

Due to the inherent signal amplification and noise cancellation, photoacoustic spectroscopy in a differential Helmholtz resonator has great potential for trace gas analysis, with possible applications including safety monitoring of toxic gases, applications in the biosciences and for natural gas analysis in petrochemistry. In this chapter, a set-up is described employing near-IR and red diode lasers for the detection of CO₂, H₂S, and O₂ in 1 bar of air/N₂, in static and flow cell measurements and improvements are introduced including a multipass arrangement and using two independent lasers simultaneously. With the red diode laser, O₂ can be detected at 764.280 nm (vacuum). A noise equivalent detection limit of 0.60 mbar (600 ppmv) of O₂ in 1 bar of air at 35 mW peak power and 1 s integration time is obtained. Normalizing to the absorption cross section, the laser power and integration time, a noise equivalent normalized absorption coefficient $\alpha = 2.2 \times 10^{-8} \text{ cm}^{-1} \text{ W s}^{1/2}$ is calculated. Within the tuning range of the near-IR DFB diode laser (6357 – 6378 cm⁻¹), CO₂ and H₂S absorption features can be accessed for trace gas detection, with a noise equivalent detection limit of 0.160 mbar (160 ppmv) CO₂ in 1 bar N₂ at 1 s integration time with the 30 mW laser. This corresponds to a noise equivalent normalized absorption coefficient $\alpha = 8.3 \times 10^{-9} \text{ cm}^{-1} \text{ W s}^{1/2}$. Due to stronger absorption cross-sections, the noise equivalent detection limit of H₂S in 1 bar N₂ is 0.022 mbar (22 ppmv). At this level, the scheme may be useful for safety monitoring of toxic H₂S. Similar detection limits apply to trace impurities in 1 bar natural gas which is the topic of chapter 5. Detection limits scale linearly with laser power and with the square root of integration time.

In this chapter, the set-up and the calibrations which have been used for O₂, ¹²CO₂, ¹³CO₂ and H₂S have been characterised in detail to understand the system very well before starting with applications. In the next chapter, we want to explore the possibility of isotopic labelling experiments which take advantage of the different spectroscopic signatures of isotopes and to apply DHR PA spectroscopy to biological application and to petrochemistry.

Chapter 5. Trace Gas Analysis in the Biosciences and Petrochemistry

Photoacoustic spectroscopy (PAS) and Cavity-Enhanced Raman Spectroscopy (CERS) can detect headspace gases above a microbiological culture in a closed system. PAS and CERS have a detection limit for gases in the ppm per volume range. In this chapter, two applications of these techniques are demonstrated. The first demonstration involves investigating the aerobic respiration in the mixed sugar metabolism of *Escherichia coli* (*E. coli*), section 5.1. Both techniques are able to monitor O₂ and CO₂ and its isotopomers with excellent sensitivity and time resolution to characterise bacterial growth and metabolism.

The second application (section 5.2) is about trace gas analysis of CO₂, H₂S and O₂ by near-IR and red diode laser photoacoustic spectroscopy in a DHR to study the L-cysteine metabolism of *E. coli*, and for trace gas detection in natural gas (petrochemistry).

5.1. Cavity Enhanced Raman and Helmholtz Resonator Photoacoustic Spectroscopy to Monitor the Mixed Sugar Metabolism of *E.coli*

This section forms part of a scientific publication which has just been submitted and accepted (16/9/2019). A reprint of the full article can be found in the Appendix.

“Cavity Enhanced Raman and Helmholtz Resonator Photoacoustic Spectroscopy to Monitor the Mixed Sugar Metabolism of E.coli”, by George D. Metcalfe, Saeed Alahmari, Thomas W. Smith, and Michael Hippler, accepted by Analytical Chemistry.

For this paper, I have joint first authorship with my work colleague George D. Metcalfe. George and I performed all DHR and CERS experiments and analysis, as well as supporting calculations. Dr Thomas Smith assisted in interpretation of experiments and also performed the preliminary experiments, under the supervision of Dr Michael Hippler.

5.1.1. Introduction

Spectroscopic methods are best suited for non-intrusive *in situ* measurements in a closed system.^{5,97} Advantages of spectroscopy are real-time data acquisition with high selectivity and sensitivity, including the distinction of isotopomers.^{2,3,4,8,9,10} This enables a further investigation into how *E. coli* metabolises a mixture of two isotopically distinct sugars,

^{13}C -glucose ($^{13}\text{C}_6\text{H}_{12}\text{O}_6$) and ^{12}C -lactose ($^{12}\text{C}_{12}\text{H}_{22}\text{O}_{11}$). The metabolism of ^{13}C -glucose will produce $^{13}\text{CO}_2$ while the metabolism of lactose will produce $^{12}\text{CO}_2$. The ability of an analytical technique to distinguish isotopes will allow isotope labelling experiments to find out sources and sinks of carbon dioxide generated.

Spectroscopic detection of O_2 consumption and CO_2 production enables monitoring of the growth of *E. coli*. CO_2 detection is particularly relevant to study the metabolism and activity of bacteria, because it is a product of aerobic respiration of converting glucose into energy. Monitoring of molecular O_2 complements such metabolism studies. O_2 detection is also very relevant in biotechnology, for example to ensure that there is no oxygen in a bioreactor in anaerobic fermentation processes.

E. coli will be grown in a medium at different concentrations of glucose to investigate the effects on the metabolic activity. These experiments are to demonstrate how spectroscopic headspace gas detection can monitor different growth conditions. This chapter will demonstrate the strengths of Raman and photoacoustic spectroscopy (PAS) to investigate the metabolism of *E. coli*.

E. coli grown in a mixture of ^{13}C -glucose and ^{12}C -lactose will be used in this research, $^{13}\text{CO}_2$ production from ^{13}C -glucose is expected to occur first, then a diauxic shift should occur after *E. coli* consume all of ^{13}C -glucose. Then $^{12}\text{CO}_2$ production from the metabolism of ^{12}C -lactose should occur.^{98,99}

5.1.1.1. Spectroscopic Detection of Headspace Gases

The metabolic activities of life forms consume or produce gases. This statement is true right down to the microscopic scale of microorganisms, such as the bacterium *E. coli*. Bacteria generate or consume gases in solution, dissolved gases are in equilibrium with the gases in the headspace. Depending on solubilities, the dissolved gases that are produced by bacteria may enter the headspace. The equilibrium between headspace gases and dissolved gases is described by Henry's Law as in Equation 42:

$$c = k p, \quad \text{Equation 42}$$

where c is the concentration of a dissolved gas in the solution, k is the Henry's Law constant for the gas at a fixed temperature, and p is the partial pressure of the gas in the headspace above the solution.

Monitoring p in a closed system and using Henry's Law gives insight into the total amount of gas in the headspace and solution. The consumption and production of gases provides information about the metabolic activity of microorganisms. Headspace gas detection is possible with spectroscopic techniques. This section will demonstrate the capability of vibrational spectroscopy for allowing *in situ* analytical measurements of trace gases. In a closed system, laser light passing through the headspace for gas monitoring is non-intrusive. Spectroscopy has this advantage over other direct methods that are intrusive to monitor metabolic activity, for example mass spectrometry or gas chromatography.

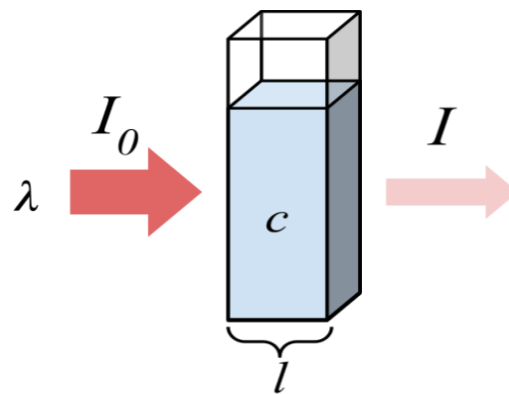


Figure 5.1. The principle of optical density measurements where the initial light with wavelength λ and intensity I_0 , is scattered by a microbiological culture sample to give the scattered light intensity I .

Figure 5.1 shows measurement of an optical density (OD) which is a conventional technique used for approximating cell growth and metabolic activity.¹⁰⁰ Light which has a specific λ is scattered by a microbiological culture proportional to the bacterial concentration. The disadvantage of this method is that it cannot distinguish between living cells, dead cells and debris.¹⁰¹ The advantage of OD measurements is that it helps to distinguish the different phases of bacterial growth.¹⁰¹

$$OD = -\lg\left[\frac{I_0}{I}\right] = \varepsilon * c * l \quad \text{Equation 43}$$

Equation 43 is used to find OD, where “ I_0 ” is the first intensity of light before passing through a sample, “ I ” is the intensity of light after being transmitted through the sample, “ ε ” is the scattering coefficient, “ c ” is the sample concentration and “ l ” is the pathlength.¹⁰²

5.1.1.2. Growth phases of *E. Coli*

The most important feature of any technique used to monitor bacterial growth and metabolism is that it is able to distinguish between the different phases of growth. There are four main phases of bacterial growth as shown in Figure 5.2.¹⁰³ During the lag phase, bacteria adjust to their environment and are not yet ready to divide. Once bacteria have adapted to their medium and growth conditions, the exponential phase (log phase) begins when the bacteria begin to divide and doubling occurs depending on a range of conditions, including the growth medium. The point at which the rate of new bacteria created matches the rate of older bacteria dying is called the stationary phase, this is due to some growth-limiting factors such as bacteria consuming the entirety of one critical species required for growth. Finally, the death phase is the death of the bacteria and end of the metabolic activity. In aerobic respiration and anaerobic fermentation, the size of each cell increases and the overall biomass. Also, the growth of an *E. Coli* culture is sensitive to pH and temperature, 37 °C being the optimum growth temperature.

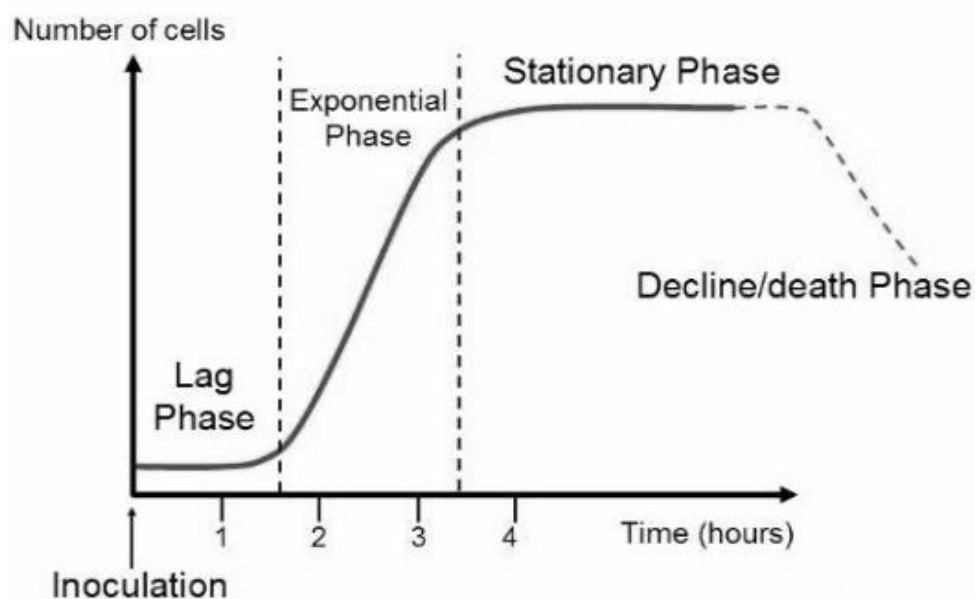


Figure 5.2. The four main phases of bacterial growth: lag phase, log (exponential) phase, stationary phase, and death phase.¹⁰³

Monitoring headspace gases by spectroscopic techniques can distinguish between these different phases. For example, the transition from the lag phase to the exponential phase causes an increase in metabolic activity as the number of bacterial cells begins to increase.

5.1.1.3. Glucose-Lactose Diauxie in *E. coli*

In the growth of *E. coli* in medium containing glucose, at a concentration incomplete to support full growth, and containing lactose, glucose is the preferred carbon source for most bacteria as its metabolism results in faster growth rates compared to other sugars.¹⁰⁴ Through a process called catabolite repression, *E. coli* display a metabolic switch from glucose to lactose metabolism. Under the presence of a preferred carbon source, repression of the genes involved in the metabolism of the less preferred sugar occurs.¹⁰⁵ When *E. coli* finish the preferred carbon source, a diauxic shift occurs where the bacteria stop growth until it is ready for metabolising the less preferred sugar. Figure 5.3 shows a diauxic shift between two growth phases A and B for a microorganism metabolising a mixture of sugars. Bacteria start with a preferred carbon source such as glucose being metabolised, which is phase A. The second sugar such as lactose is then metabolised in phase B. In Figure 5.3, no bacterial growth occurs between phases A and B, therefore the diauxic shift has a lag phase before the bacteria continue with lactose.¹⁰⁶ Such lag phases are often, but not always observed.⁹⁹

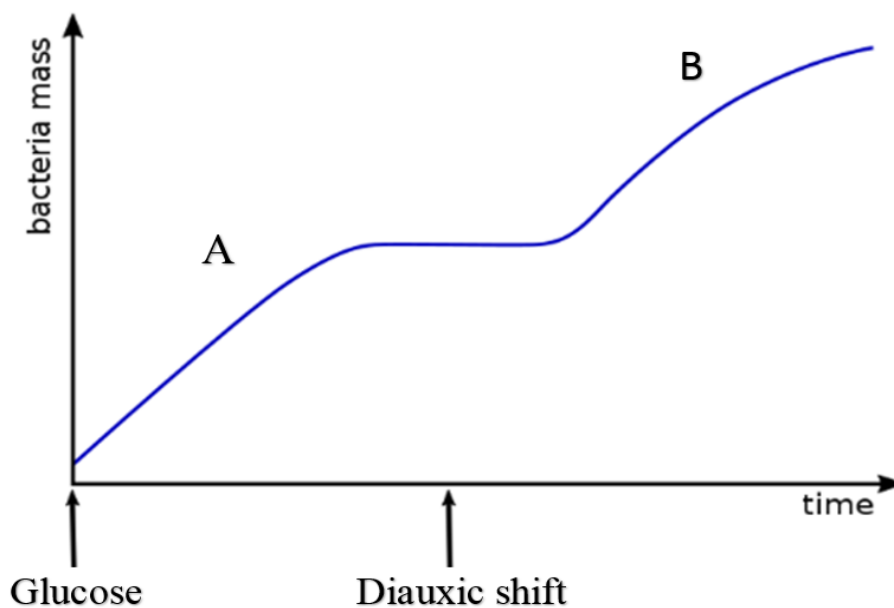


Figure 5.3. A diauxic shift between growth phases A and B as a microorganism metabolises a mixture of sugars.

5.1.2. Aims

The aims of this section 5.1. are to demonstrate two techniques for the monitoring of the headspace gases consumed and produced by microorganisms, by using Cavity Enhanced Raman spectroscopy (CERS) and Photoacoustic spectroscopy where a differential Helmholtz resonator (DHR) is employed. The demonstrations of these techniques involve investigating the aerobic respiration in the mixed sugar metabolism of *E. coli*. The simultaneous measurements of O₂ consumption and CO₂ production by *E. coli* can be achieved using CERS and DHR in photoacoustic spectroscopy. *E. coli* grown in a medium supplemented with sugars will allow detection of changes in the metabolic activity. Spectroscopy can also distinguish between isotopomers. The experiment with mixed sugars to feed *E. coli* will demonstrate that spectroscopic headspace gas detection can be used to investigate metabolic preferences. The carbon source of aerobic metabolism of *E. coli* will be investigated using a mixture of two isotopically labelled sugars, ¹³C-glucose and ¹²C-lactose. M9 minimum growth medium is used since it does not include a carbon source which could conflict with the experiments involving isotopically labelled sugars. Therefore, *E. coli* growth in this medium was suitable to monitor ¹³C labelled sugars. ¹³CO₂ from glucose is expected to be produced preferentially to ¹²CO₂ from lactose due to the diauxic shift to lactose metabolism.

5.1.3. Experimental

5.1.3.1. General setup of Cavity Enhanced Raman Spectroscopy (CERS) with Optical Feedback

The original cw-CERS optical feedback setup has been described before in detail in the group's previous publications.^{5,2,10} In this setup, an inexpensive cw laser diode system emits light (Hitachi HL6322G, 40 mW, 636 nm, **LD**). The light is directed into an optical cavity comprised of two concave super mirrors (**SM & PSM**, Newport SuperMirrors™, $R > 0.9998$, 583 – 633 nm, 1 m radius of curvature, 1 inch diameter, $l = 35$ cm mirror separation). Multiple reflections in the high finesse optical cavity create a laser power build up between the mirrors. The principle advantage of CERS as an application of Raman spectroscopy is the power build up, because this increases Raman signal. CERS is ideal for detecting gases which are not IR-active, for example homonuclear diatomic molecules.

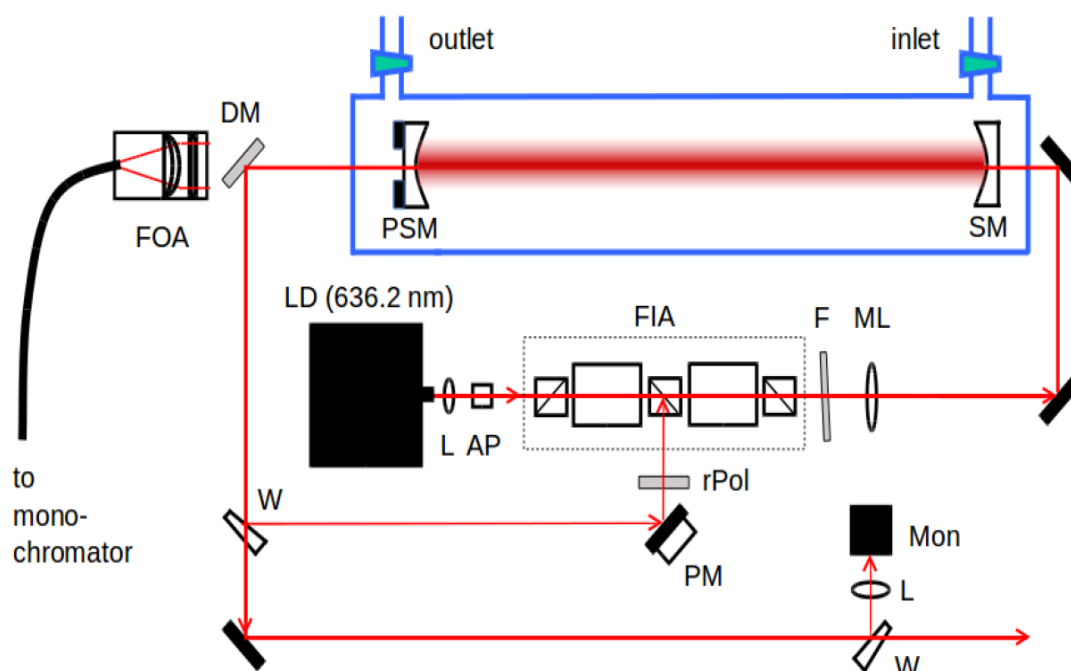


Figure 5.4. Schematic of the CERS experimental setup.²

Figure 5.4 shows a schematic of the CERS experimental setup where laser radiation from a cw-laser diode **LD** passes through a lens **L** which is collimated then passes through an anamorphic prism pair **AP** (Thorlabs PS870) before reaching a Faraday rotator isolator assembly **FIA**. The **FIA** contains two Faraday isolators to avoid potentially damaging back

reflections returning to the laser diode. After the **FIA**, the laser radiation passes through a short-pass filter **F** (Thorlabs FES0650, 650 nm cut-off) which works as a clean-up filter for the laser to take away spurious weak emission bands at longer wavelengths which could contaminate the red shifted (Stokes) Raman bands. Then the beam passes through a mode matching lens (**ML**, $f = 100$ mm) before being coupled inside the optical cavity, to focus the beam to ensure efficient coupling into the cavity. There are also unwanted back reflections of laser radiation from the first cavity mirror **SM** that does not enter the optical cavity. The purpose of the **FIA** is to prevent these back reflections from reaching and damaging the **LD**. When the laser wavelength matches the resonance conditions of the cavity, optical power build up within the cavity occurs, which is enough to generate detectable levels of Raman scattered light from dilute samples of gaseous down to mixing ratios in the ppmv region.

Optical class glass windows (BK7, 20 mm clear aperture, 0.5 mm thickness) are used for the cavity entrance and exit beam paths. A Semrock RazorEdge dichroic mirror **DM** separates the Stokes Raman signals from the 636 nm excitation light exiting the cavity and Rayleigh scattered light. The Raman signals are then coupled into the fiber optical assembly **FOA** (1 inch diameter, $f = 25.4$ mm lens) and transferred to the monochromator (Shamrock SR-750-A, with Andor iVac DR32400 CCD camera cooled to -60 °C). The excitation light exiting the cavity is used for optical feedback to ensure lasing at the correct frequency by locking the **LD** to the optical cavity. Optical feedback is achieved using a glass wedge **W**, piezo mounted mirror **PM**, and a rotating polarizer **rPol** to adjust the intensity. A second glass wedge **W** diverts some of the 636 nm light to a photodiode **Mon** (Thorlabs PDA015A) to monitor light intensity, the strength and stability of cavity resonances, which helps the alignment of the feedback beam.

The monochromator is equipped with different resolution gratings, a low (150 lines mm^{-1} blazed at 750 nm), medium (600 lines mm^{-1} blazed at 500 nm) and high-resolution grating (1200 lines mm^{-1} blazed at 750 nm) mounted on a rotating turret as shown Figure 5.5. All the measurements described in this chapter use the medium resolution grating, which covers Raman shifts of between roughly 1200 cm^{-1} and 2400 cm^{-1} for 636 nm laser excitation. This is enough to observe the fundamental Raman transitions of small gaseous molecules in a single acquisition.

The optical cavity is connected to a vacuum pump to evacuate air and other gases. The optical cavity is inside a vacuum-tight glass enclosure which is ideal for the detection of the

trace gases within. The detection limit for gases of the CERS setup outlined here is around 100 ppm per volume.⁵ Cavity resonances are not constant. The resulting variation in Raman intensity effects all bands equally, therefore signals can be normalised through use of a suitable internal standard by using the peak of N₂ Q-branch (2329 cm⁻¹) because N₂ is inert to the metabolic activity so the amount present in the system remains constant (810 mbar). Other relevant gaseous analytes which have been observed include CO₂ (1285 cm⁻¹ and 1388 cm⁻¹), O₂ (1556 cm⁻¹), and H₂O (3653 cm⁻¹), as shown later in the Raman spectrum of Figure 5.7. The headspace volume of a flask containing the bacterial suspension at 37 °C is circulated via a peristaltic pump (3 l/h) to the CERS cell in a closed system.

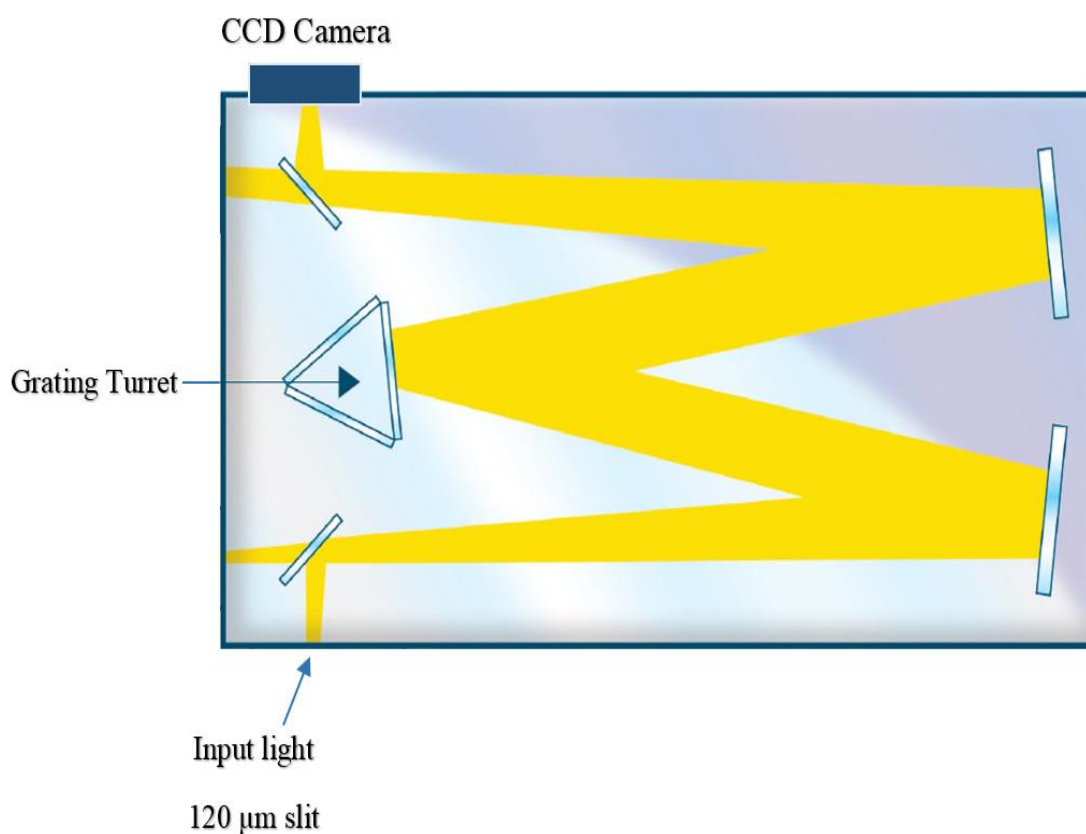


Figure 5.5. Shamrock 750 Czerny-Turner spectrograph used this monochromator for CERS measurements.

5.1.3.2. Starter Culture Preparation

5.1.3.2.1. Description of Growth Media

First of all, sterilisation of all glassware and growth media which was used in the experiment was done by either heating inside of an autoclave (15 minutes at 121 °C) or filter sterilisation (0.22 µm filter). Sterilisation of growth media is essential before coming into contact with bacterial samples to avoid contamination. In this project two different media were used, Lysogeny Broth (LB) and M9 minimal medium.

LB is a rich medium where bacteria grow well because it contains many sources of carbon. A minimal medium M9 has to be chosen for mixture sugar experiments. M9 does not contain a carbon source without a supplemented sugar making it useful to determine which sugar has been consumed during mixed sugar metabolism. LB medium was prepared by dissolving tryptone (10 g L⁻¹), sodium chloride (10 g L⁻¹) and yeast extract (5 g L⁻¹) in deionised water. To prepare LB-agar plates, bacteriological agar was added (15 g L⁻¹) to LB solution to make plates for growing *E.coli* colonies.

For preparation of M9 medium, M9 Minimal Salts, a 5× solution that contains monopotassium phosphate (15 g L⁻¹), disodium phosphate (64 g L⁻¹), sodium chloride (2.5 g L⁻¹) and ammonium chloride (5 g L⁻¹) were bought from Sigma Aldrich.

The M9 trace elements solution contains ethylenediaminetetraacetic acid (EDTA) (5 g L⁻¹) in 800 ml water. The pH was adjusted to 7.5 with NaOH, and then the following components were added in the quantities mentioned below, and water was added to a final volume of 1 L. The components are anhydrous ferric chloride (498 mg L⁻¹), zinc chloride (84 mg L⁻¹) and solutions of 0.1 M copper (II) chloride dehydrate (0.765 mL), 0.2 M cobalt (II) chloride hexahydrate (0.21 mL), 0.1 M boric acid (1.6 mL) and 1 M manganese (II) chloride tetrahydrate (8.1 µL).

M9 minimal medium was prepared by mixing solutions of M9 Minimal Salts, 5× (200 mL) and 1 M glucose (20 mL), which corresponds to M9 with a final concentration of 20 mM supplemented glucose, to give an example for preparing M9 supplemented with 20 mM glucose. 1 M magnesium sulfate (1 mL), 1 M calcium chloride (0.3 mL), 4 mM biotin (1 mL), 3.8 mM thiamin (1 mL) and a trace elements solution (10 mL) was finally added. The solution was then made up to 1 L with deionised water.

5.1.3.2.2. *E. coli* Starter Cultures

All preparation of biological work was done under sterile conditions in the presence of a Bunsen burner. A frozen 50:50 LB: glycerol stock (stored at $-78\text{ }^{\circ}\text{C}$) of *Escherichia Coli* (strain K-12 MG1655) was streaked onto antibiotic-free LB-agar plate. Plates were incubated (16 hours $37\text{ }^{\circ}\text{C}$) to allow for growth of single colonies, then the plates were covered in parafilm and stored in the fridge at $5\text{ }^{\circ}\text{C}$. The plates were replaced every 4 weeks. From the plate, a single colony of *E. coli* was isolated and used to inoculate sterile LB (50 ml) before placing inside a shaker incubator (5 hours at $37\text{ }^{\circ}\text{C}$ and 200 rpm) allowing for growth until the OD_{600} of the starter culture was around 0.7.

5.1.3.3. Sample Preparation

5.1.3.3.1. Sample Preparation Using M9 Minimal Medium

When using M9 medium to grow *E. coli*, a 500 mL round-bottom flask with a side arm sealed with a glass stopper held all sample cultures. 1 mL of the starter culture was added directly to the flask containing 250 mL of M9 media supplemented with sugar depending on the kind of experiment. M9 medium was used for isotopic labelling experiments with the mixed sugars of ^{13}C -glucose (U-13C6, 99% CLM-1396, CK isotopes) and ^{12}C -lactose (Sigma-Aldrich), because M9 does not contain a carbon source without a supplemented sugar which is useful to determine what kind of sugar has been consumed to produce carbon dioxide.

5.1.3.3.2. Sample Preparation Using LB Rich Medium

When using LB medium to grow *E. coli*, this was also incubated in a LB starter culture (5 hours, $37\text{ }^{\circ}\text{C}$). After 5 hours, 1 mL of the starter culture ($\text{OD}_{600} \approx 0.8$) was transferred into a 500 mL autoclaved round bottom flask, then added to fresh LB and D-glucose (10 mM or 20 mM) was added as before. As before, the final volume is 250 mL.

5.1.3.4. Monitoring Aerobic Respiration of *E. coli* by Using CERS and DHR Separately

5.1.3.4.1. CERS Measurements

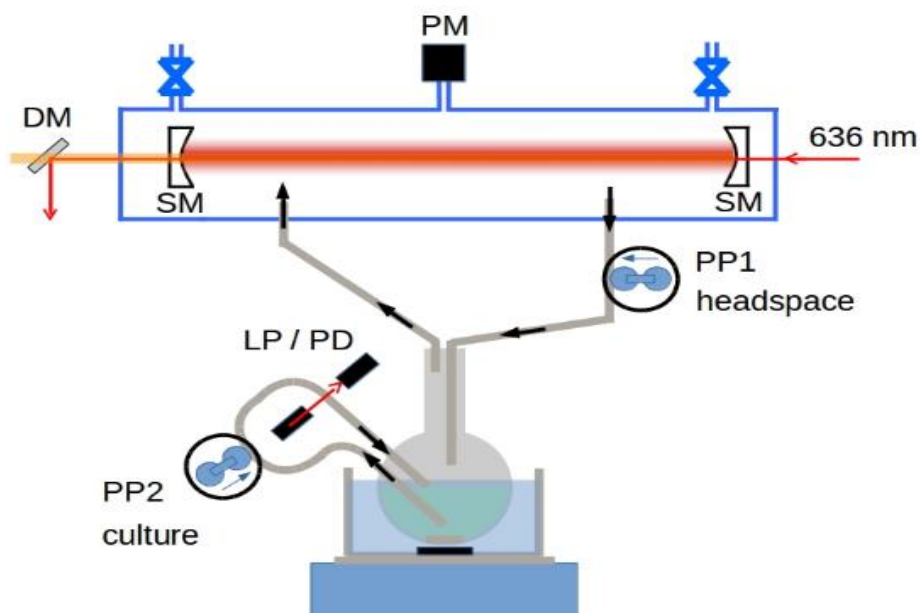


Figure 5.6. Schematic of the experimental setup for CERS and OD₆₀₀ measurements.

Figure 5.6 shows a schematic of the experimental setup for CERS measurements of the aerobic respiration of *E. coli*. The 500 mL round-bottom flask was connected to a custom stopper with two glass capillary feedthroughs to allow headspace gas circulation to and from the optical cavity in a closed system. Tubing connected one glass capillary to a peristaltic pump (PP1, 3 l/h) and then to the optical cavity, with the second set of tubing connecting the optical cavity back to the second glass capillary in a closed system. The water bath was set to 37 °C to heat the flask. A stirrer hotplate with fast stirring controlled the water bath temperature. Rapid stirring within the flask helped to ensure efficient transfer of gas between the solution and headspace. The second peristaltic pump (PP2, 3 l/h) pumps the solution culture through the side arms, to allow for *in situ* measurements of turbidity (OD). A laser pointer LP of 650 nm was shone through a 1 cm a cuvette to measure the OD₆₀₀. The photodiode PD and laser were connected to a voltmeter and the computer for data recording.

For recording Raman spectra, Andor Solis imaging and spectrograph software was used. The software controlled the 750 mm focal length monochromator (Andor SR-750) and cooled the CCD camera to -60 °C (Andor iDus). The integration time was 30 s for recording spectra.

The medium resolution grating with 600-lines mm^{-1} was used for all the measurements because it is very suitable for distinguishing of $^{12}\text{CO}_2$ and $^{13}\text{CO}_2$ isotopomers. The first step to recording Raman spectra is to take the background spectrum, so a vacuum pump was connected to evacuate the CERS setup, and then the background spectrum was taken. Then the cavity was filled with laboratory air by opening a gas inlet tube, and the flask containing the culture was connected. In this experiment the setup is filled with lab air (~79 % nitrogen, ~21 % oxygen by volume) in a closed system. The headspace volume is 720 mL. Raman measurements were taken at regular time intervals.

The kinetics acquisition mode in the Andor Solis software recorded Raman spectra every 180 s. An Arduino microprocessor board controlled the turning on and off of the diode laser in time with the measurements, as well as recording the total pressure (p total) inside of the closed CERS setup via a capacitance pressure gauge.

The variations of power inside of the optical cavity resulted in variations of the Raman signal intensities. A Raman band ($880 - 1035 \text{ cm}^{-1}$) is produced from silica in the glass windows of the optical cavity and remains visible in the background spectrum under vacuum. This band was used to normalise against power variations, as this silica band scaled with laser power. By comparing the silica band intensities in the background spectrum with the silica band of the sample, this allowed intensity calibration of the sample spectra. Then subtracting the background spectrum from each calibrated sample spectrum obtained background corrected and intensity normalised Raman spectra. Alternatively, to normalize Raman signals, the N_2 peak of air can be used since in the closed system, N_2 is not consumed or produced by the bacterial metabolism.

Figure 5.7 shows the CO_2 and O_2 Raman lines used for the measurement. It shows the $\nu_1/2\nu_2^0$ Q -branches of the Fermi resonance pair of $^{12}\text{CO}_2$ (1285 cm^{-1} and 1387 cm^{-1}). The energy of the first excited state of the symmetric stretching vibration of CO_2 is close to the energy of the second excited state of the bending vibration. Both states have the same symmetry, therefore they mix to give two new symmetric states known as a Fermi resonance pair.¹⁰⁷ Also, Figure 5.7 shows the Q -branch of the O_2 stretching vibration (1555 cm^{-1}), the Q -branch of the N_2 stretching vibration (2329 cm^{-1}). The $^{13}\text{CO}_2$ stretching vibrations (about 1265 and 1370 cm^{-1}) represent the ^{13}C isotopomer of CO_2 .

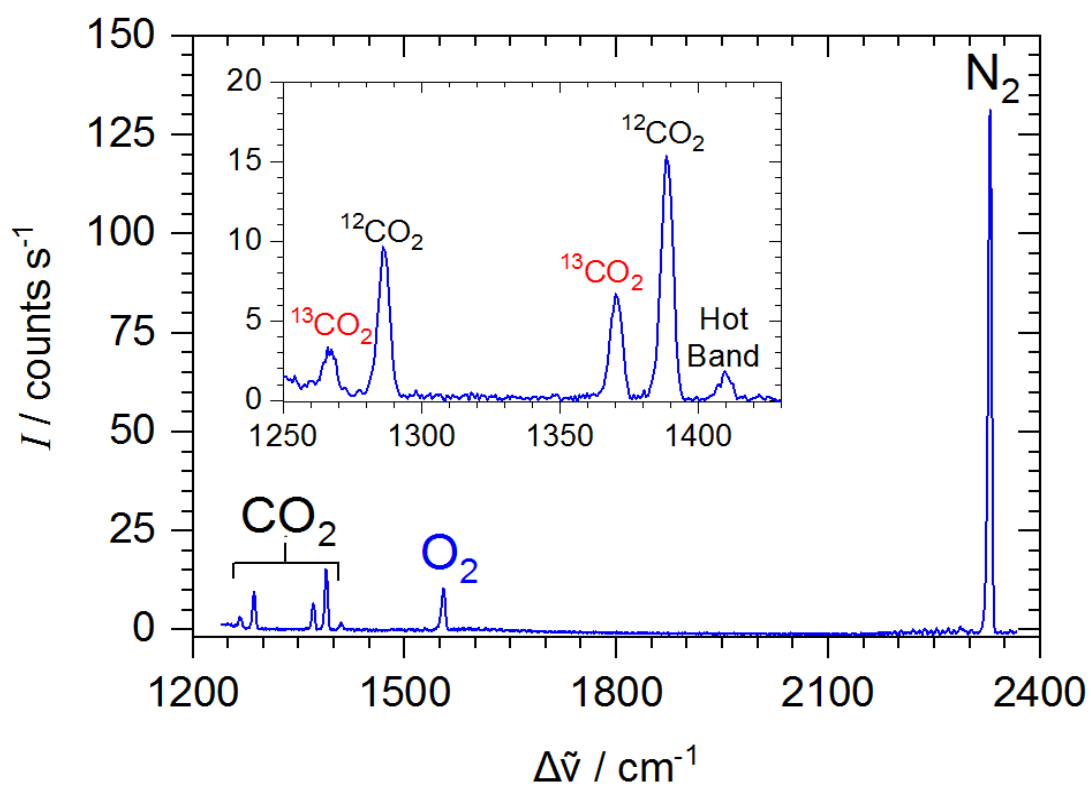


Figure 5.7. A background corrected and intensity normalised Raman spectrum after 2 days growth for *E. coli* in M9 minimal medium supplemented with 3 mM ^{13}C - glucose and 20 mM ^{12}C -lactose.

5.1.3.4.2. DHR Measurements

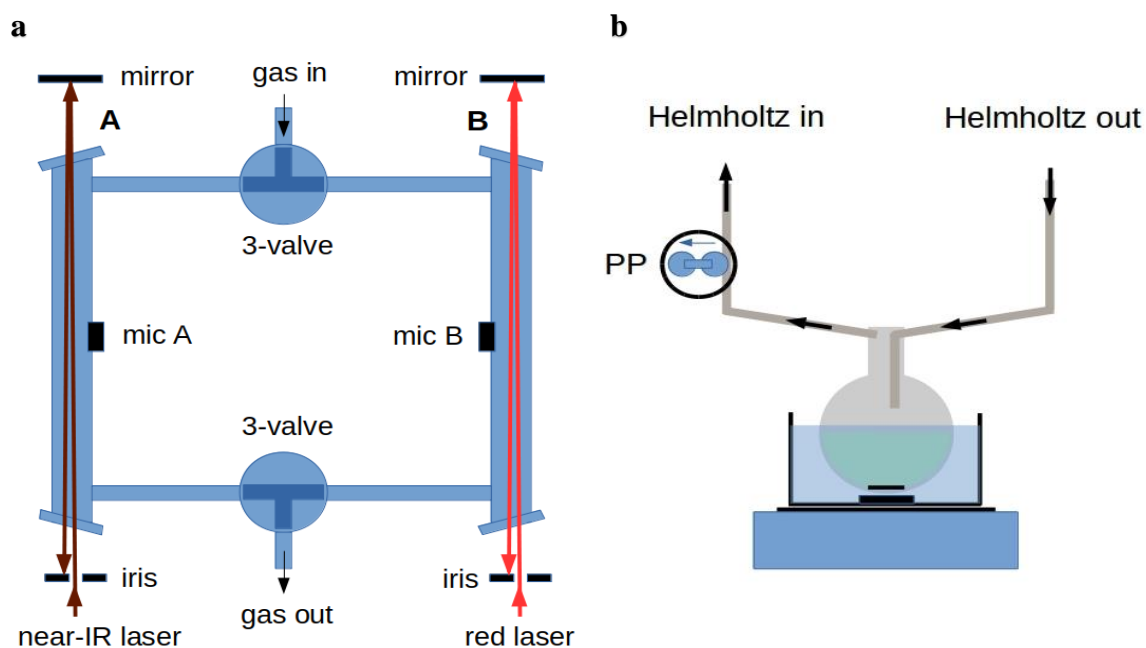


Figure 5.8. Scheme of the experimental setup. (a) Differential Helmholtz resonator with the two laser beams (see main text for more details). (b) In biological experiments, the head space of a round-bottom flask in a thermostated water bath is circulated to the Helmholtz resonator via a peristaltic pump (PP).

Figure 5.8 (a) shows a schematic of the experimental setup of DHR for biology measurements of the aerobic respiration of *E. coli*. Figure 5.8 (b) shows the flask that is connected to the DHR resonator with short gas transfer tubes in a closed system, giving a total headspace gas volume of 510 ml. To enhance gas flow, a peristaltic pump (3 l/h) was used to cycle the flask headspace through the DHR resonator as shown in Figures 5.8 (b). In a test to characterize the experimental time resolution, CO₂ or H₂S gas was injected into the flask and the appearance time of the gas was measured in the Helmholtz resonator; equilibrium is reached within about 3 min. A stirrer hotplate with fast stirring controlled the water bath temperature set at 37 °C. Stirring within the flask also helped with the transfer of gas between the solution and headspace. Figure 5.9 shows a photograph of the front view of the PAS setup with the flask.

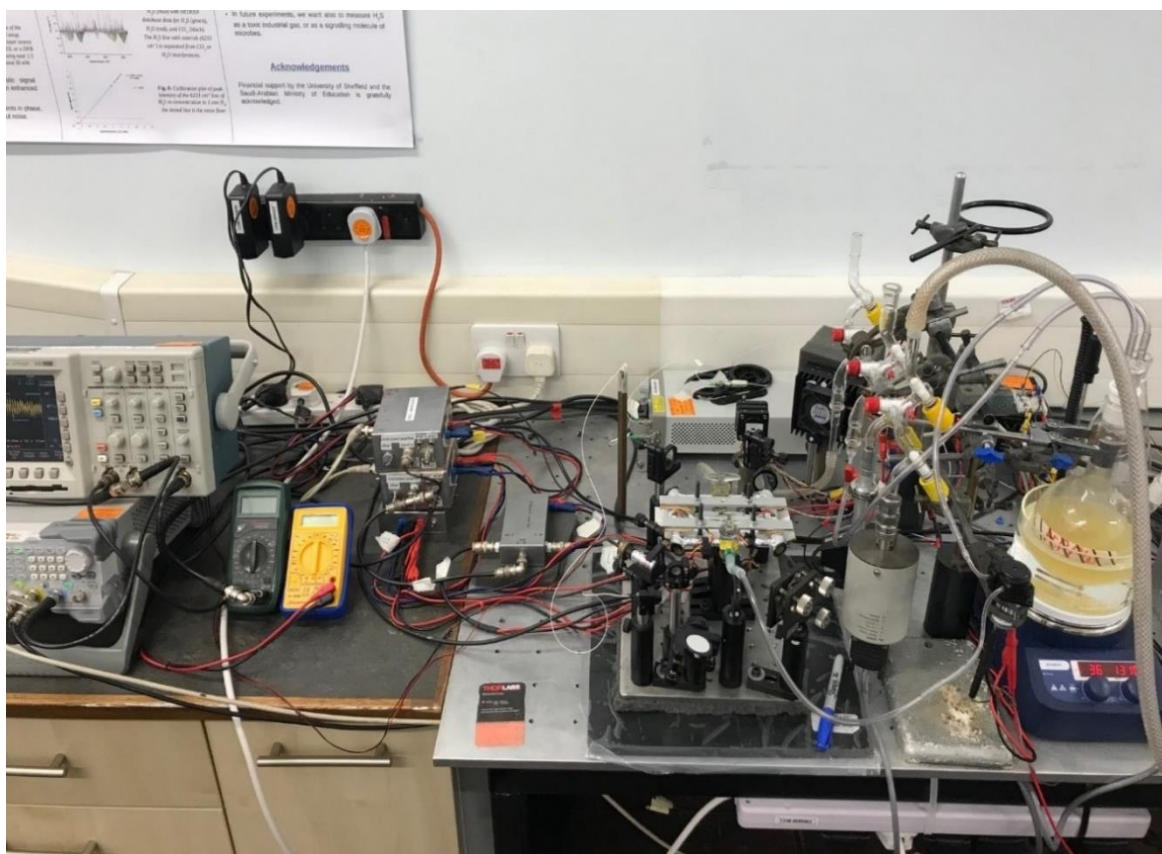


Figure 5.9. Biology experimental setup for photoacoustic spectroscopy headspace monitoring of CO₂ and O₂ in a differential Helmholtz resonator of respiring *E. coli* cultures. The gas in the headspace is circulated in a closed system by using a peristaltic pump.

As described in the previous chapter 4, a near-IR single-mode DFB diode (Mitsubishi FU-650SDF, 4 mW) is amplified in a booster optical amplifier (Thorlabs S9FC1004P) to 30 mW peak power. This laser is passed through CH1 (as explained in the previous chapter 4), scanning between 6362 – 6360 cm⁻¹ by temperature tuning between 51-54 °C, to detect ¹²CO₂. The peak position of ¹²CO₂ is 6361.25 cm⁻¹. For ¹³CO₂, the temperature tuning range was 29.5-34 °C, with the peak position of ¹³CO₂ of 6371.7 cm⁻¹. The red laser (35 mW DFB diode laser Eagleyard EYP-DFB-0764) is directed through the other compartment CH2 scanning between 13084.9 – 13082.9 cm⁻¹. The O₂ position of the peak is 13084.0 cm⁻¹. The peristaltic pump is off for the duration of the scans because this affects the acoustic noise. Once both scans (CH1 and CH2) are complete, the peristaltic pump is turned on and cycles the gas through the DHR for 15 minutes. Both lasers are modulated by their injection current at the acoustic resonance frequency with a square-wave giving a 50% duty cycle.

For recording absorption spectra for CO₂ and O₂, an Arduino board controlled the turning on and off of the diode laser in time with the measurements, as well as recording the

total pressure p inside the system via a capacitance pressure gauge. The integration time was 1 s per data point for recording spectra. The first step was to use a vacuum pump to evacuate the DHR setup. Then the setup was filled with laboratory air by opening a gas inlet tube and then closing it, and the flask containing the culture was connected to the system. Like CERS, this setup is a closed system. The data are analysed to fit a peak which was calibrated to obtain partial pressure. Data were analysed and displayed using Origin 8 software.

Figure 5.10 shows a mixture of $^{13}\text{CO}_2$ and $^{12}\text{CO}_2$ of the head space above a bacterial solution as measured by PAS in the DHR cell. The peak at 6371.7 cm^{-1} is a strong line for $^{13}\text{CO}_2$ as explained in chapter 4. This line will be used for $^{13}\text{CO}_2$ detection in the biology experiments.

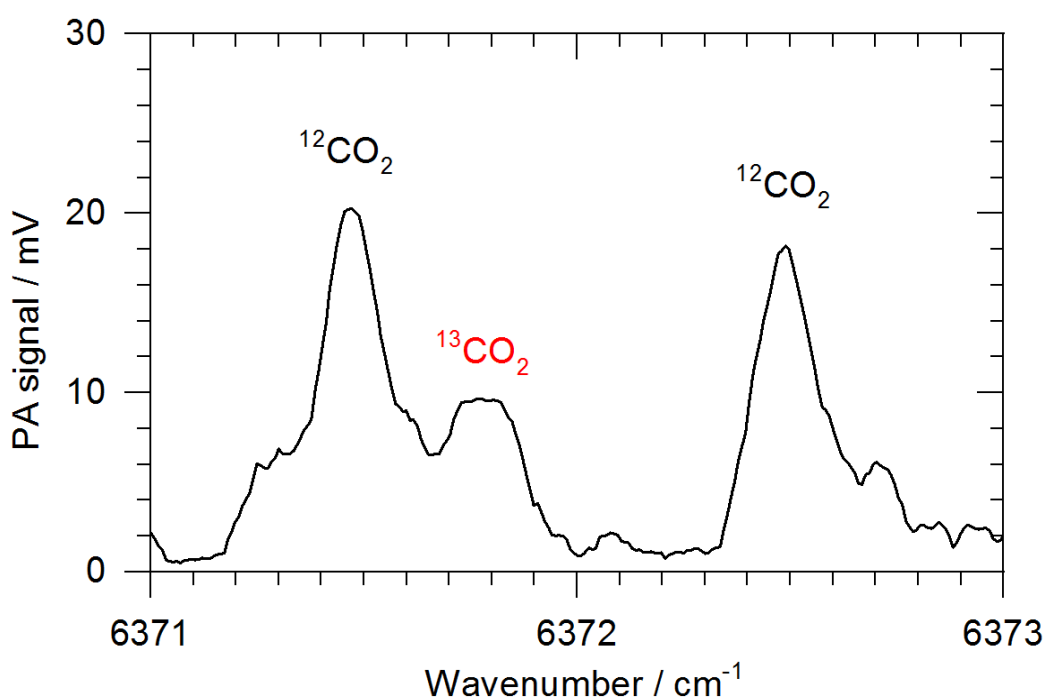


Figure 5.10. Experimental spectrum of a mixture of $^{13}\text{CO}_2$ and $^{12}\text{CO}_2$ of the head space above a bacterial culture, obtained by a PAS scan by using the DHR cell.

5.1.3.5. pH, OD₆₀₀ and Biomass Measurements

For all biology experiments, pH and biomass of *E. coli* were measured at the end of the experiment. A 50 mL sample of the final culture was taken and centrifuged (10 minutes at 4000 rpm) to separate the medium away from the biomass. By using a Jenway pH meter 3305, the pH of the medium was determined. The centrifuge tube containing the biomass was placed in the lab to dry the sample for several days, then it could be weighed to estimate a dry biomass value. At the end of an experiment and after exhausting the oxygen supply, the increase in cell density is characterized by OD₆₀₀ \approx 1.5-2.0. The final pH of the solution was typically 4.5 to 5.0 due to organic acids generated during the metabolism. For comparison, fresh LB has pH \approx 6.8, and fresh M9 has pH \approx 6.9. At the beginning, the cellular material within the 250 ml suspension has a typical dry weight of 0.2 mg, which by the end of a typical experiment increases to 60 mg, reflecting bacterial growth.

5.1.4. Results and Discussion

5.1.4.1. Measuring the different phases of *E. coli* growth in Rich LB Medium Using OD₆₀₀ Measurements and Monitoring of the Headspace Gases

In a demonstration of the application of photoacoustic spectroscopy detection in a DHR and CERS in the biosciences, these techniques monitored O₂, and CO₂ during the metabolism of sugars by *E. coli*. During aerobic metabolism, microbes convert O₂ and sugars or other suitable organic substrates to CO₂, with typically one unit of CO₂ produced per unit O₂ consumed as shown in Equation 1.



OD measurements are widely used in the biosciences to characterise growth but they suffer from a decrease in accuracy at high cell concentrations. The main disadvantage of this method is that it cannot distinguish between living cells, dead cells, death phase, and wreckages/debris.¹⁰¹ The advantage of OD measurements is that they are good at distinguishing some phases of bacterial growth like lag phase, log phase and stationary phase.^{101,108} Any technique used to investigate metabolic activity must be able to distinguish between the different phases of growth. During the monitoring of the headspace gases by spectroscopy, spectroscopic techniques can be used to distinguish between these different phases. For example, through the transition from the lag phase to the log phase, there is an increase in the metabolic activity as the number of bacterial cells begins to increase. Monitoring of headspace gases can distinguish between these different phases.⁵ For example, when transitioning from the lag phase to the log phase there will be an increase in gas uptake and production as the number of bacterial cells begins to increase. The monitoring of headspace gases has an advantage over OD measurements as the headspace is better defined than a microbiological culture where dead cells and debris cause inaccuracies in OD measurements.

For rapid growth, *E. coli* is grown in LB medium which is a nutritionally rich medium containing all the amino acids and vitamins essential for rapid bacterial growth. By using the CERS technique, the changes in CO₂ and O₂ can be recorded, while simultaneously measuring the OD₆₀₀ to track the growth cycle of *E. coli*, as shown in Figure 5.11. The figure shows different phases of *E. coli* growth which are the lag phase (labelled A), exponential phase (B), stationary phase (C), and death phase (D). With OD₆₀₀ measurement and the spectroscopic measurements, it is apparent that the lag phase started from the beginning until about 3 h. The

OD measurements show that after 3 h the log phase (exponential phase) started until about 5 h when the stationary phase started. When monitoring the headspace gases using CERS, it is clear that the death phase started at about 20 h. This indicates that *E. coli* continue growth from about 5 h until 20 h under these O₂ limited conditions. The OD measurements are not able to determine the transition from stationary to death phase, essentially because the scattering cannot distinguish living and dead cells.

Figure 5.11 shows the monitoring of the aerobic respiration of *E. coli* in LB medium supplemented with 20 mM glucose. LB medium contains multiple carbon sources in the tryptone and yeast extract as well as the supplemented glucose. During aerobic metabolism, *E. coli* convert O₂ and sugars or other suitable organic substrates to CO₂, with typically one unit of CO₂ produced per unit O₂ consumed in a 1:1 ratio, as shown in Equation 1. In our closed system, dissolved O₂ is negligible and of the total CO₂, about 18% is in solution (Henry's law). The decreasing oxygen partial pressure p (O₂) curve resembles an exponential decay curve while the increasing p (CO₂) values resemble an increasing exponential curve. When O₂ is completely consumed inside the system, the CO₂ production stops. This indicates *E. coli* growth has entered the death phase (labelled D) at about 20 h. The death phase (D) is distinct by the values of p (O₂) and p (CO₂) being a plateau at 0 mbar and about 170 mbar respectively. In addition, with the 18 % of dissolved CO₂ in the solution the corrected total p (CO₂) will be around 210 mbar which is perfectly 1:1 with the amount of oxygen consumed.

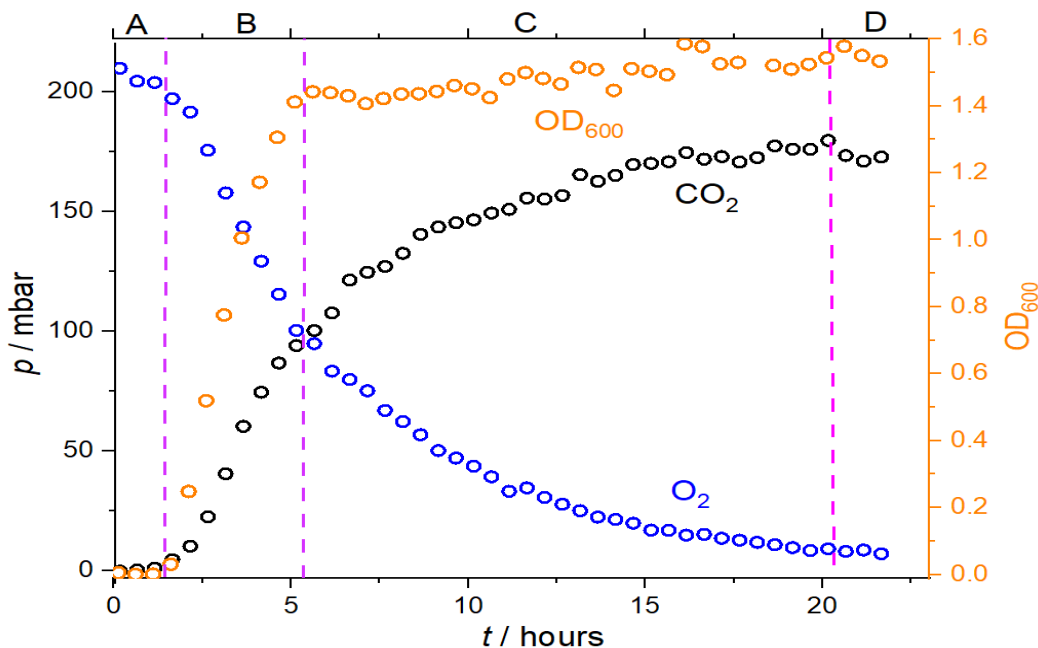


Figure 5.11. The graph shows O₂ consumption (blue), CO₂ production (black) and OD₆₀₀ measurement (brown) of *E. coli* growth in LB medium supplemented with 20 mM glucose using CERS. The dashed line (purple) shows the separation between the different growth phases of *E. coli*.

In addition to identifying the differences between *E. coli* growth in different media, the kinetics of O₂ consumption and CO₂ production can be used to investigate the different phases of *E. coli* growth. The natural logarithm of the exponential decay of pressure of O₂ would be expected to give a linear relationship with respect to time for a single first-order kinetic regime. A plot of the natural logarithm of O₂ pressure is shown in Figure 5.12 to determine different phases of *E. coli* growth, to distinguish three different phases (A, B+C and D) of O₂ consumption during the growth of *E. coli* in LB medium supplemented with 20 mM glucose. Phase A is the lag phase with no change in O₂, followed by phase B+C of O₂ consumption (exponential growth and stationary), while phase D is the death phase at the end of *E. coli* metabolism, because the growth-limit depends on the *p* O₂ inside the system.

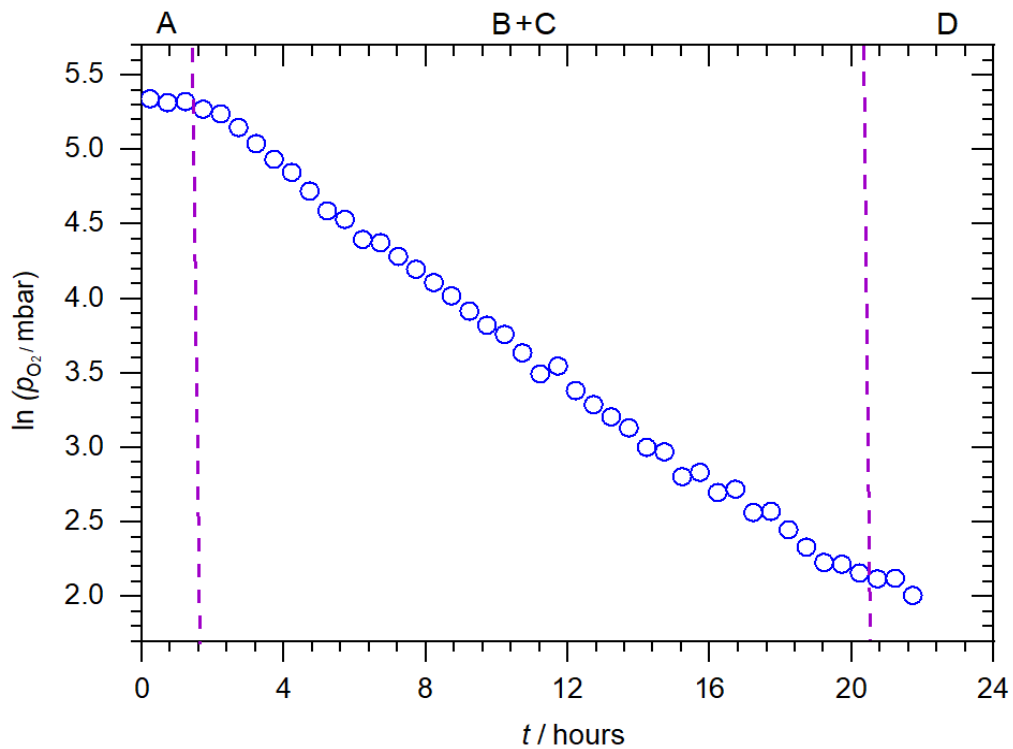
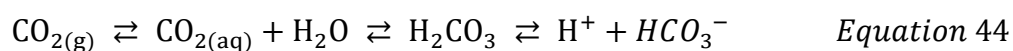


Figure 5.12. The change in O₂ consumption, shown in a natural logarithm scale, of *E. coli* growth in LB medium supplemented with 20 mM glucose by using CERS, showing distinct kinetic regimes.

O₂ was the growth-limiting factor for growth of *E. coli* in LB medium supplemented with 20 mM glucose. LB medium is a rich medium where the nutrients are bountiful and are not growth-limiting. Under these conditions, in the CERS system, the growth limit is not the glucose concentration: it would have to be below 4 mM to be growth-limiting (see Appendix

1) in CERS. If the glucose concentration is higher than 4 mM, the growth-limiting depends on the p_{O_2} inside the system which always starts from 210 mbar in 1 atm until all the O_2 is consumed, then *E. coli* will die. Due to the lower headspace volume and hence the lower concentration of oxygen, the supplemented glucose concentration would have to be below 2.8 mM to be growth-limiting in the PAS system. If the concentration of sugar is higher than 2.8 mM, the growth-limiting depends on the $p(O_2)$ inside the PAS system (see Appendix 7).

Figure 5.13 shows the experiment of 10 mM of glucose in LB medium but using the DHR as a different detection method. The results of CERS or DHR are similar and show the same behaviour. In Figure 5.13, the total amount of a substance in the gas phase can be calculated using the ideal gas law. At equilibrium, the molarity of a dissolved gas can be calculated from its partial pressure using Henry's law. 1 mbar of an ideal gas corresponds to 2.05×10^{-5} mol in the head space (510 ml) in the PAS system (see Appendix 7). Using Henry's constants at 37 °C,¹⁰⁹ 1 mbar corresponds to 2.5×10^{-5} mol CO_2 , or 9.9×10^{-7} mol O_2 in the solution (250 ml). About 22 % of the total CO_2 is dissolved in solution in the PAS system (see Appendix 8), whereas for O_2 , the amount of dissolved O_2 is negligible. Some small amount of dissolved CO_2 (less than 2 %) will react to form carbonic acid H_2CO_3 as in Equation 44. This carbonic acid can dissociate to the bicarbonate ion HCO_3^- depending on the pH. The bacterial suspension has pH 4.2 in LB medium at the end. At this pH, the amount of H_2CO_3 and HCO_3^- in solution was calculated to be negligible. Since only about 22 % of the total CO_2 is in solution in DHR, while 18% of total CO_2 is in solution in CERS, of which only a small amount will be converted into carbonic acid, this loss of CO_2 can be neglected to a first approximation.



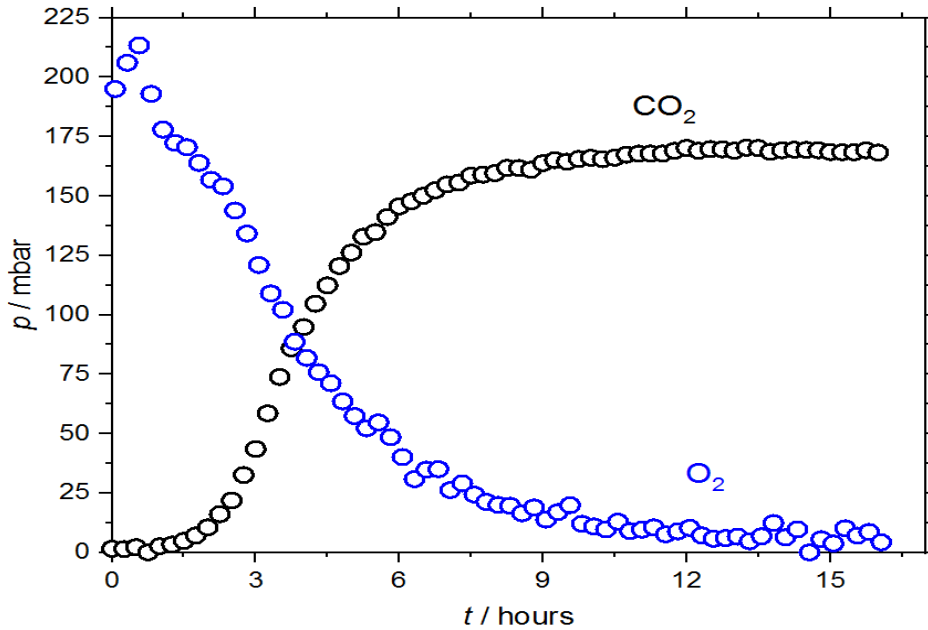


Figure 5.13. O₂ consumption (blue plot) and CO₂ production (black plot) of *E. coli* growth in LB medium supplemented with 10 mM glucose measured by using DHR.

5.1.4.2. Measuring the Different Phases of *E. coli* Growth in M9 Medium (Minimal Medium) Supplemented with Glucose by Monitoring of the Headspace Gases and OD₆₀₀

M9 medium is a minimal medium where the only carbon source is the supplemented sugar, there is no other significant source. Studying *E. coli* growth in M9 medium with supplemented sugars is very important to understand before monitoring growth in M9 medium supplemented with mixtures of glucose and lactose. There are distinct differences in growing *E. coli* in M9 medium compared to growing in LB medium. Figure 5.14 shows O₂ consumption and CO₂ production by a suspension of *E. coli* in M9 medium supplemented with 20 mM glucose using CERS. The death phase was reached after 20 h of *E. coli* growth in LB medium compared to 36 h growth in M9 medium. *E. coli* grows faster in LB medium than M9 medium because LB is a rich medium containing many essential nutrients, such as amino acids and peptides, which allow for rapid growth. Figure 5.14 shows that the growth of *E. coli* in M9 medium does not display the 1:1 ratio of O₂ consumption to CO₂ production. p (O₂) decreased until 0 mbar while p (CO₂) increased to around 105 mbar with 16 % of total CO₂ in solution. Taking the dissolved CO₂ into account, there is about 80 mbar of CO₂ missing. At equilibrium, the molarity of a dissolved gas can be calculated from its partial pressure using Henry's law. 1

mbar of an ideal gas corresponds to 3.1×10^{-5} mol in the head space (770 ml) in the CERS system (see Appendix 1). Using Henry's law to calculate the percentage of CO₂ in solution, this is equivalent to 16 % of total CO₂ produced in solution while the concentration of dissolved O₂ is negligible (see appendix 2). To explain the missing CO₂, there are two hypotheses. First hypothesis is that CO₂ is possibly converted into carbonic acid H₂CO₃, then H₂CO₃ can dissociate to the bicarbonate anion HCO₃⁻, and carbonate anion, CO₃²⁻ as in Equation 44. To test this hypothesis, we have added HCl at the end point to acidify the solution. This should drive out CO₂ from the solution. But there was not a significant increase in CO₂ in the head space, so this hypothesis does not apply. This hypothesis is further rejected because the amount of conversion of CO₂ to H₂CO₃ in solution is calculated to be negligible (see Appendix 3). The pH of the M9 medium supplemented with 20 mM glucose at the end of *E. coli* activity was 5.6.

The second hypothesis is that not all glucose is fully oxidised to CO₂ because some of the carbon from of glucose is needed for the building of biomass for the growth. Since the minimal medium cannot provide it, it is taken from the glucose. About 80 mbar of CO₂ is missing at the end of the experiment which corresponds to approximately 2.5 mmol. The dry weight of bacteria at the end is about 60 mg. Assuming that about 50% of this is carbon,⁹⁸ the bacteria contain about 2.5 mmol carbon in total, in good agreement with the missing CO₂.

In LB medium, tryptone provides a source of essential amino acids, and the yeast extract offers a source of various organic compounds required for growth. *E. coli* grown in LB medium does not have to synthesise these species from glucose which is likely why O₂ consumption and CO₂ production show the expected 1:1 ratio. *p* total as shown in Figure 5.15 (a) shows that carbon goes into the biomass during the exponential growth phase (B) in M9, and to a slower/lesser extent during the stationary phase (C). In LB, no carbon goes into biomass, as can be seen from *p* total in Figure 5.15 (b). In LB, it has a perfectly 1:1 ratio, and there is no distinction between stationary/death phase.

Figure 5.14 shows also the natural logarithm of the pressure of O₂ to distinguish two different phases (A and B) of O₂ consumption during the growth of *E. coli* in M9 medium supplemented with 20 mM glucose. Phase A is the lag phase then followed by phase B, the log phase which shows O₂ consumption. Plotting $\ln p$ (O₂) against time reveals two phases: one corresponding to no *E. coli* activity and the other corresponding to the log phase and stationary phase of *E. coli* in which O₂ consumption begins alongside glucose conversion into CO₂ and biomass. During the log phase, more glucose is needed converting to biomass components than

during the stationary phase, thus cell growth in the log phase may require a faster production of biomass components than during the stationary phase when the cell density reaches an equal amount of living and dead cells.¹¹⁰ The oxygen decay extends from the exponential phase to the stationary phase with a rate constant $k = 0.134 \text{ h}^{-1}$ or half-life $t_{1/2} = 5.18 \text{ h}$ which is much slower than in LB which is a rate constant $k = 0.189 \text{ h}^{-1}$.

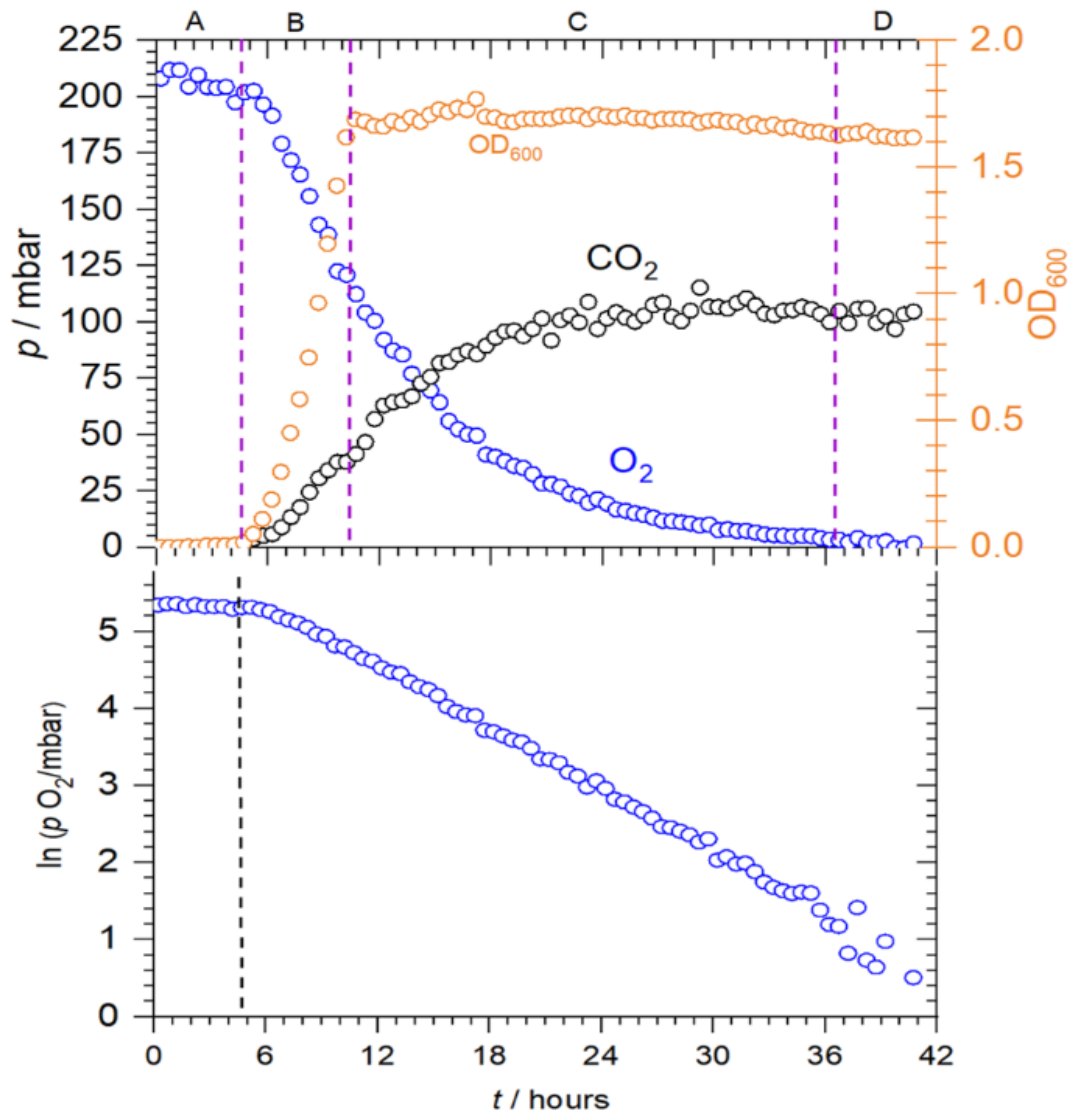


Figure 5.14. The upper plot shows *E. coli* growth in M9 medium supplemented with 20 mM glucose by monitoring using CERS, O_2 consumption (blue), CO_2 production (black) and measuring OD_{600} (brown). The dashed line (purple) separates the growth phases of *E. coli*. The lower plot displays the decay of O_2 on a logarithmic scale, the change in natural logarithm scale of O_2 consumption by *E. coli* growth.

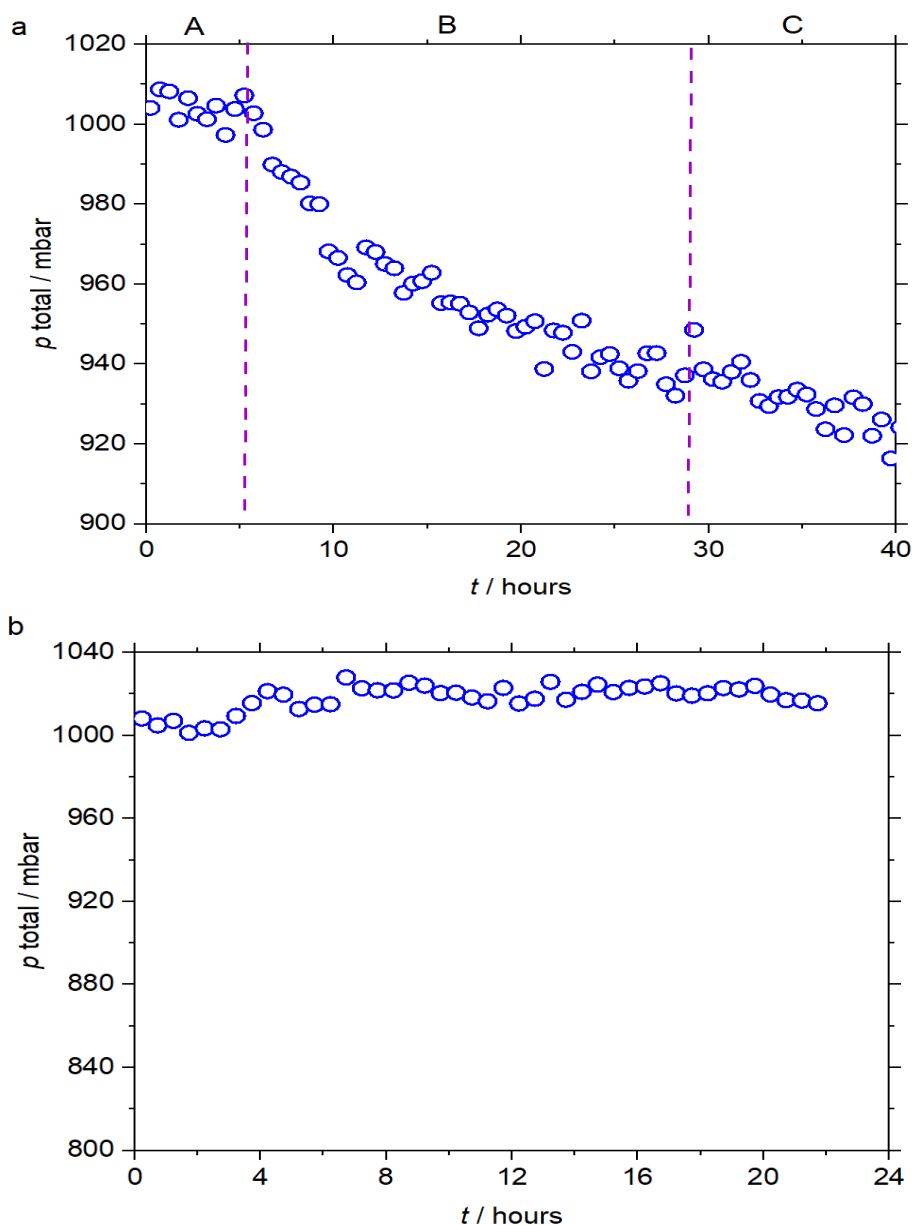


Figure 5.15. (a) p_{total} (the sum of p_{O_2} , p_{N_2} and p_{CO_2} , corrected for dissolved CO_2) for the experiment of *E. coli* growth in M9 medium supplemented with 20 mM glucose. (b) p_{total} for the experiment of *E. coli* growth in LB medium supplemented with 20 mM glucose.

Figure 5.16 shows the experiment of 10 mM of glucose in M9 medium as in Figure 5.14 but using the DHR as a different detection method. This figure is a repeat of Figure 5.14 but using a different detection method and with a different concentration of 10 mM glucose. In this figure, the O_2 and CO_2 concentrations during the metabolism of glucose by *E. coli* is shown to be very similar to Figure 5.14. During aerobic metabolism, microbes convert O_2 and sugars to CO_2 , but there is not one unit of CO_2 produced per unit O_2 consumed as in LB medium.

M9 medium is considered a minimal medium which does not contain carbon sources, therefore not all glucose is fully oxidised to CO_2 . The death phase started after about 18 h, faster than with the experiment on CERS. This is explained by the different experimental conditions, including different glucose and oxygen concentrations. $p(\text{CO}_2)$ is about 110 mbar in the death phase which is close to $p(\text{CO}_2)$ in the CERS experiment as shown in Figure 5.14.

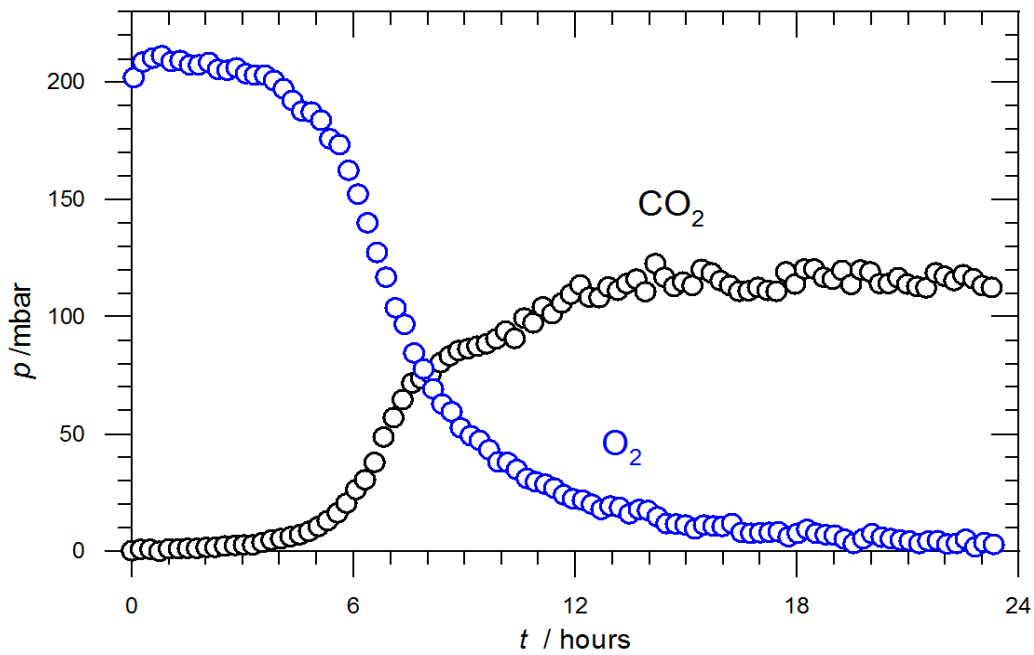


Figure 5.16. O_2 consumption (blue) and CO_2 production (black) of *E. coli* growth in M9 medium supplemented with 10 mM glucose, measured by DHR.

5.1.4.3. Measuring the Different Phases of *E. coli* Growth in M9 Medium Supplemented with Mixed Sugars without Isotopic labelling by Monitoring of the Headspace Gases and OD₆₀₀

The growth of *E. coli* with a mixture of sugars (glucose and lactose) in M9 medium indicates complicated growth behaviour because *E. coli* metabolise glucose preferentially to lactose. The growth rate is higher metabolising glucose than metabolising lactose. For optimal growth in a medium containing both glucose and lactose, *E. coli* will repress the expression of genes which help metabolise lactose.¹⁰⁵ Lactose metabolism will continue to be inhibited until the glucose is depleted and then the *E. coli* will return to using lactose when the glucose is completely finished. Figure 5.17 shows the first step to measure the sugar mixture, *E. coli* growth in M9 medium supplemented with just 3 mM glucose by using CERS. The figure also shows the natural logarithm of O₂ consumption of *E. coli* in the lower plot. In this experiment, a low concentration of glucose is used in order to know how much O₂ consumption and how much CO₂ production occurred using glucose before switching to the alternative sugar. The 3mM of glucose produced around 27 mbar of CO₂. At the same time, *E. coli* growth phases were measured by using OD₆₀₀ to distinguish the different growth phases of *E. coli*. The lag phase (A) started from 0 until around 5 h, where no increase in the bacteria cells is indicated by the OD₆₀₀. The log phase (B) and stationary phase(C) started from 5 h until around 10 h, here p (O₂) decreases and there is an increase in p (CO₂) as well. The death phase is started from 10 h until the completion of the experiment due to the exhaustion of glucose. In this experiment, the glucose was the growth-limiting factor for growth of *E. coli* in M9 medium supplemented with 3 mM glucose because the growth-limiting for CERS would be 4 mM of sugar.

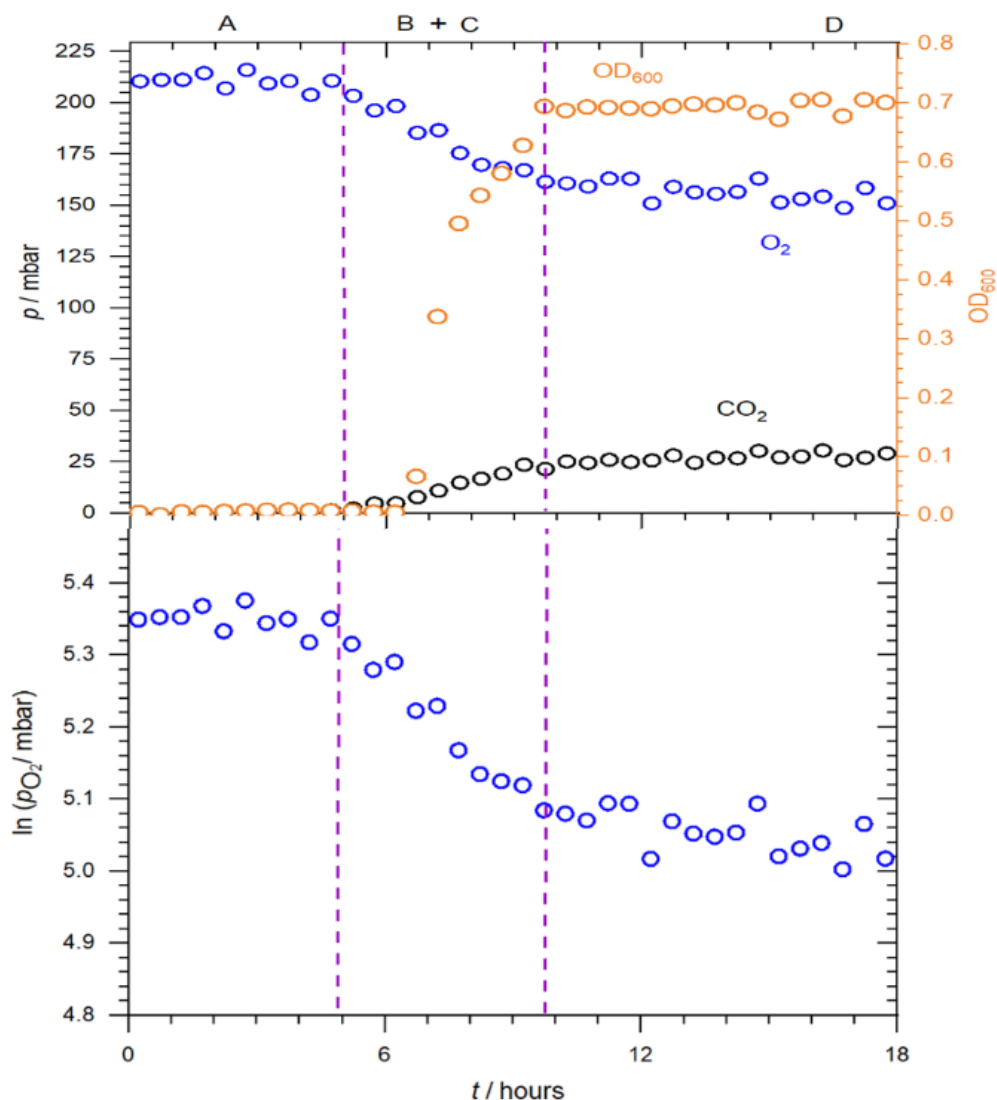


Figure 5.17. The upper plot shows *E. coli* growth in M9 medium supplemented with 3 mM glucose measured by using CERS, O₂ consumption (blue), CO₂ production (black) and measuring OD₆₀₀ (brown). The dashed line (purple) separates the growth phases of *E. coli*. The lower plot displays the decay of O₂ on a logarithmic scale, the change in natural logarithm scale of O₂ consumption by *E. coli* growth.

Figure 5.18 shows the experiment of 2.5 mM of glucose in M9 medium like Figure 5.17 but using the DHR as a different detection method in order to validate the results. There is a lower concentration of glucose because the supplemented glucose concentration would have to be below 2.8 mM to be growth-limiting in the PAS system, due to the lower headspace volume. In this figure, the concentrations of O₂, and CO₂ during the metabolism of glucose by *E. coli* are shown. During aerobic metabolism, microbes convert O₂ and sugars to CO₂; as calculated, 2.5 mM of glucose produced around 25 mbar of CO₂. All the phases of *E. coli* growth are very

clear in this figure as explained previously. The death phase started after around 12 h which is very similar to the experiment as shown in Figure 5.17.

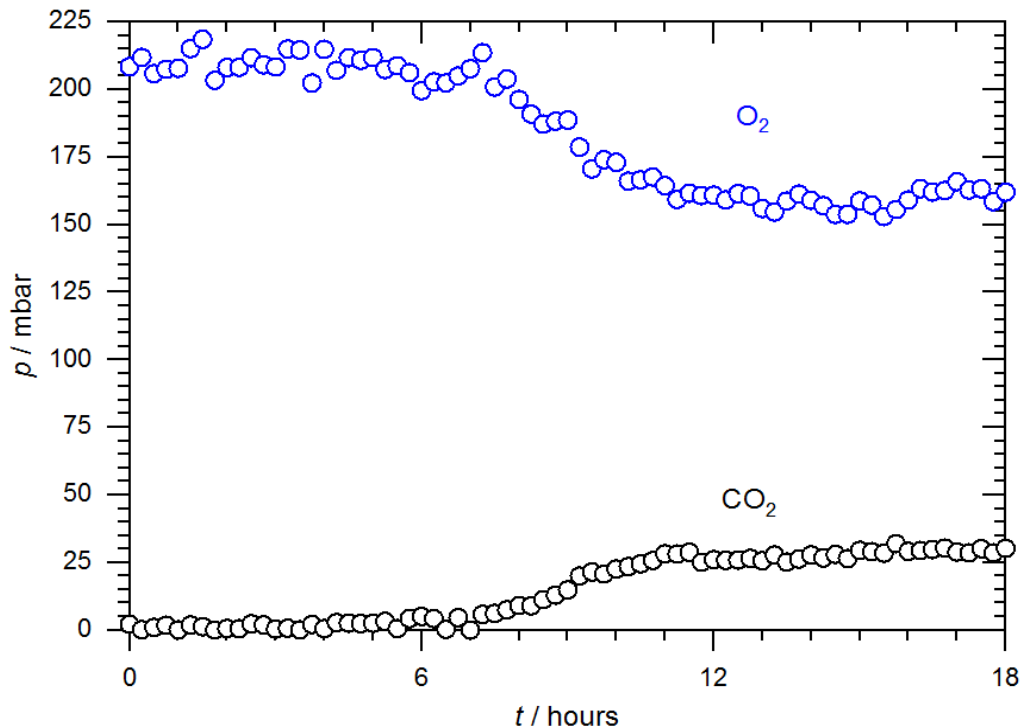


Figure 5.18. This graph shows O₂ consumption (blue) and CO₂ production (black) of *E. coli* growth in M9 medium supplemented with 2.5 mM glucose measured by using DHR.

Figure 5.19 shows the growth of *E. coli* in M9 medium supplemented with 20 mM lactose by using CERS and measuring OD₆₀₀ at the same time to distinguish the phases of *E. coli* growth. Figure 5.20 shows the same experiment but using DHR, where the concentration of lactose was 10 mM because the headspace volume and therefore the oxygen supply of the systems are not equal. Figure 5.19 shows also the change in natural logarithm scale of O₂ consumption by *E. coli* growth in the lower plot. The lag phase finished at 6 h then the log phase started until around 12 h. O₂ consumption is at a constant rate and the death phase is reached after 30 h in CERS and after 24 h when using DHR. The exponential decay of oxygen is characterised by an uptake rate of $k = 0.155 \text{ h}^{-1}$ in the CERS experiment. This is somewhat faster compared to glucose, but probably not different enough to allow the distinction between lactose and glucose metabolism just from a measurement of the uptake rate. The final pressure of CO₂ is 125 mbar in CERS, considering the 16% of CO₂ which is dissolved in solution and some amount of carbon being in the biomass. There is a slight difference in p (CO₂) with the death phase in DHR where the final pressure is around 147 mbar, this is due to the different

conditions in the experiment like concentration, and volume. The aim of these experiments with lactose alone is to study the behaviour of the growth phases of *E. coli* in the presence of a different sugar than glucose.

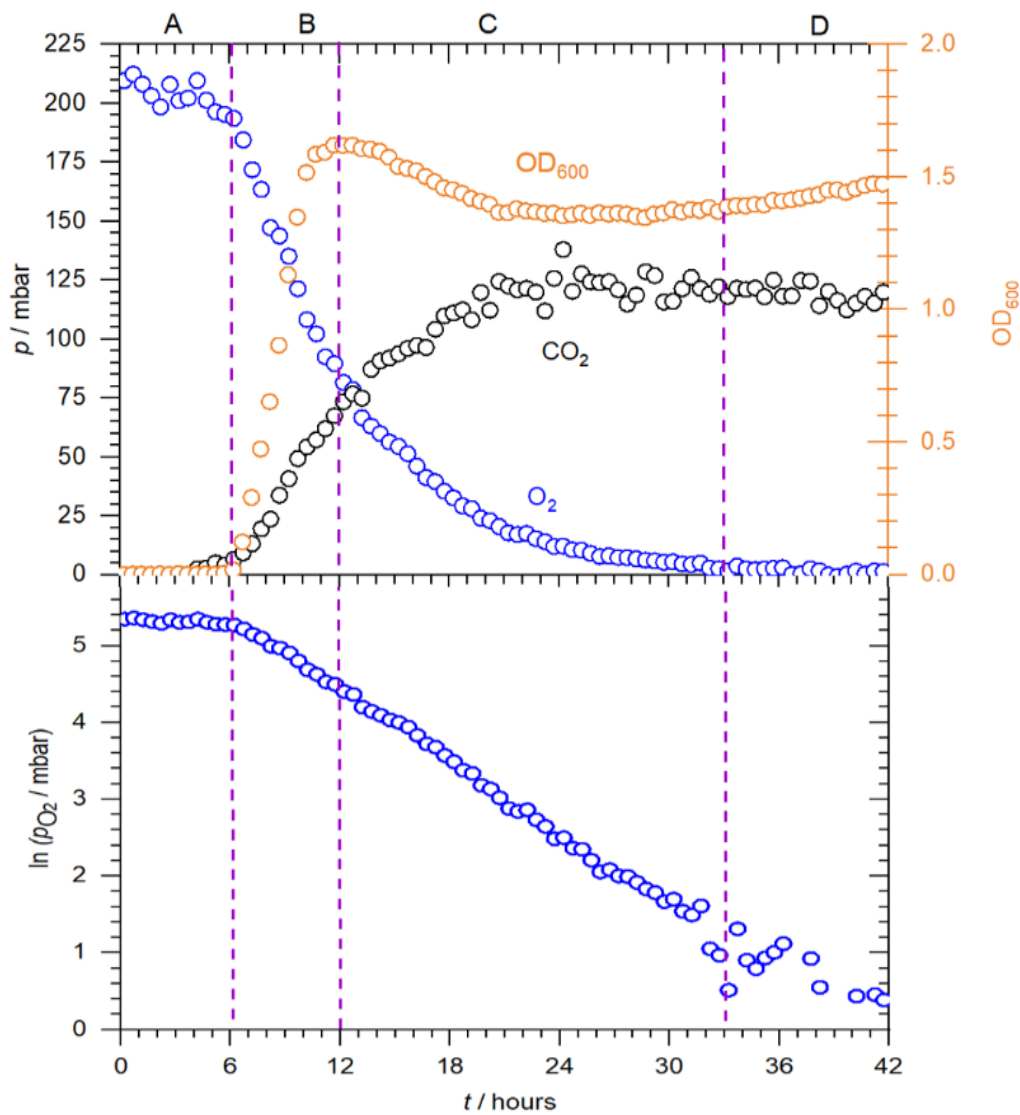


Figure 5.19. The upper plot shows O₂ consumption (blue plot), CO₂ production (black) and measurement of OD₆₀₀ (brown) of *E. coli* growth in M9 medium supplemented with 20 mM lactose by using CERS. The dash line (purple) separates the different growth phases of *E. coli*. The lower plot displays the decay of O₂ on a logarithmic scale, the change in natural logarithm scale of O₂ consumption by *E. coli* growth.

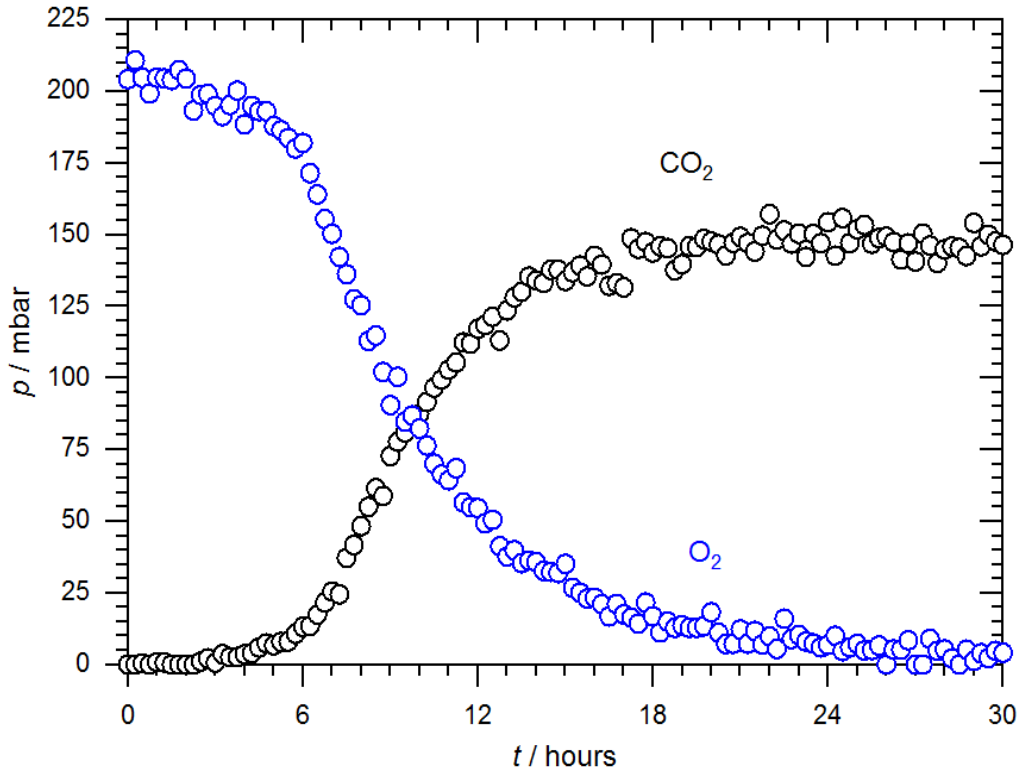


Figure 5.20. The graph shows O₂ consumption (blue) and CO₂ production (black) of *E. coli* growth in M9 medium supplemented with 10 mM lactose by using DHR.

For optimal growth in a medium containing both glucose and lactose, *E. coli* will repress the expression of genes which help metabolise lactose. Catabolite repression of lactose will continue until the total depletion of glucose. Figure 5.21 shows *E. coli* grown in M9 medium supplemented with a mixture of 3 mM ¹²C-glucose and 20 mM ¹²C-lactose by using CERS. Glucose is expected to be metabolised preferentially to lactose, and a diauxic shift corresponding to a change to the metabolism of lactose should occur. However, the OD₆₀₀ measurements cannot distinguish between the two kinds of sugar metabolism. Under our conditions, no diauxic shift or lag phase is noticeable in the OD measurement, nor in the unlabelled spectroscopic measurements.

The lag phase finished at about 6 h. The lower plot in 5.21 displays the decay of O₂ on a logarithmic scale, the change in natural logarithm scale of O₂ consumption by *E. coli* growth. *E. coli* metabolises glucose preferentially to lactose but there is no way to distinguish the different behaviour in the CO₂ produced by the metabolism of glucose or lactose because both are ¹²C-sugars, both yielding ¹²CO₂. Figure 5.22 shows also a mixture of 2.5 mM ¹²C-glucose and 10 mM ¹²C-lactose measured by using DHR to compare this result with CERS's

experiment. As shown in Figure 5.21 and 5.22, behaviour is very similar. The log phases started at about 6 h in the two figures. The final readings in the two figures are p (CO_2) of about 125 mbar which represents the death phase. The aim of these experiments is to compare them with the next part in which isotope labelling experiments are used in order to distinguish isotopes, $^{13}\text{CO}_2$ and $^{12}\text{CO}_2$.

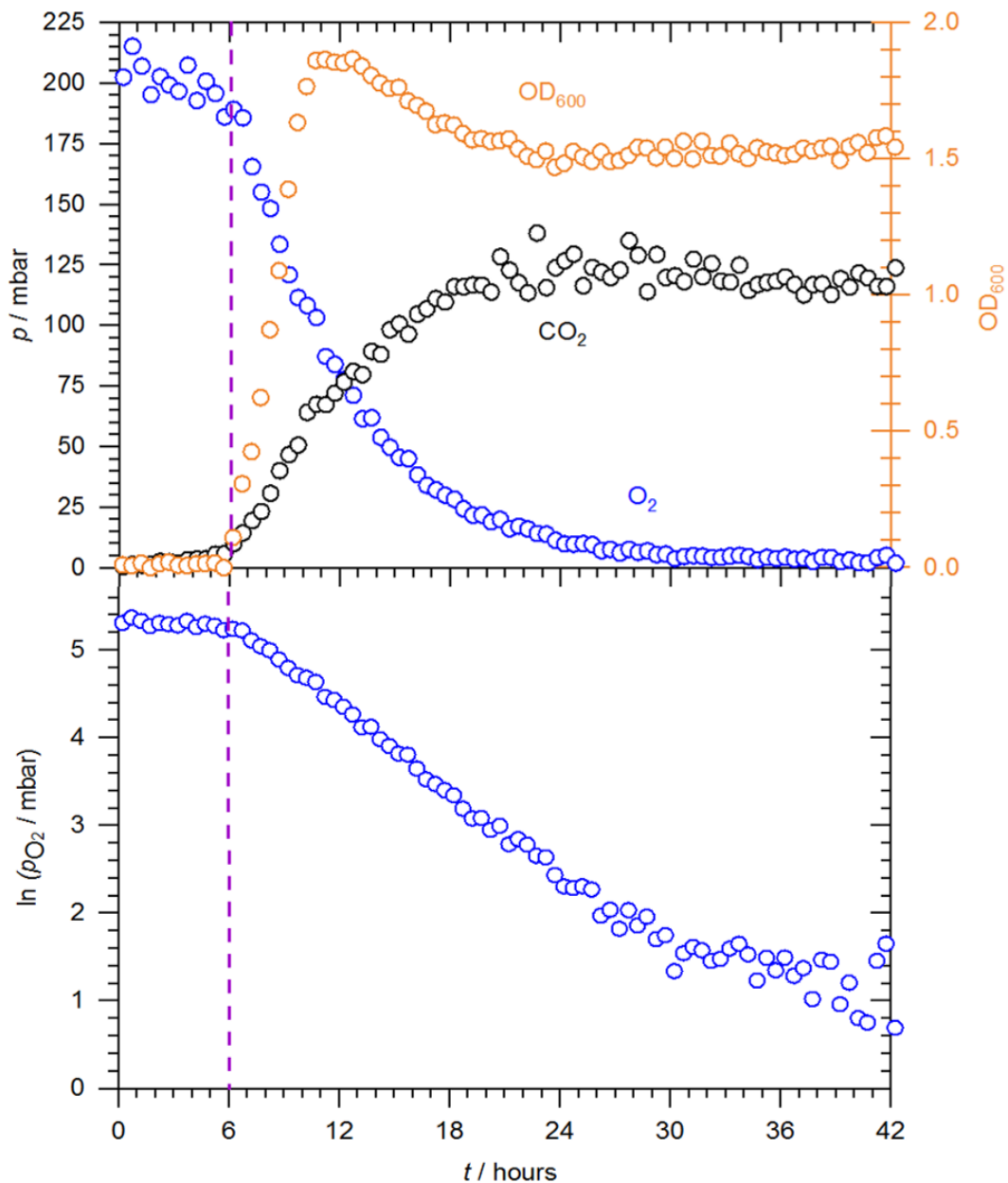


Figure 5.21. The upper plot shows *E. coli* growth in M9 medium supplemented with 3 mM glucose and 20 mM lactose, measured by using CERS. The lower plot displays the decay of O₂ on a logarithmic scale, the change in natural logarithm scale of O₂ consumption by *E. coli* growth.

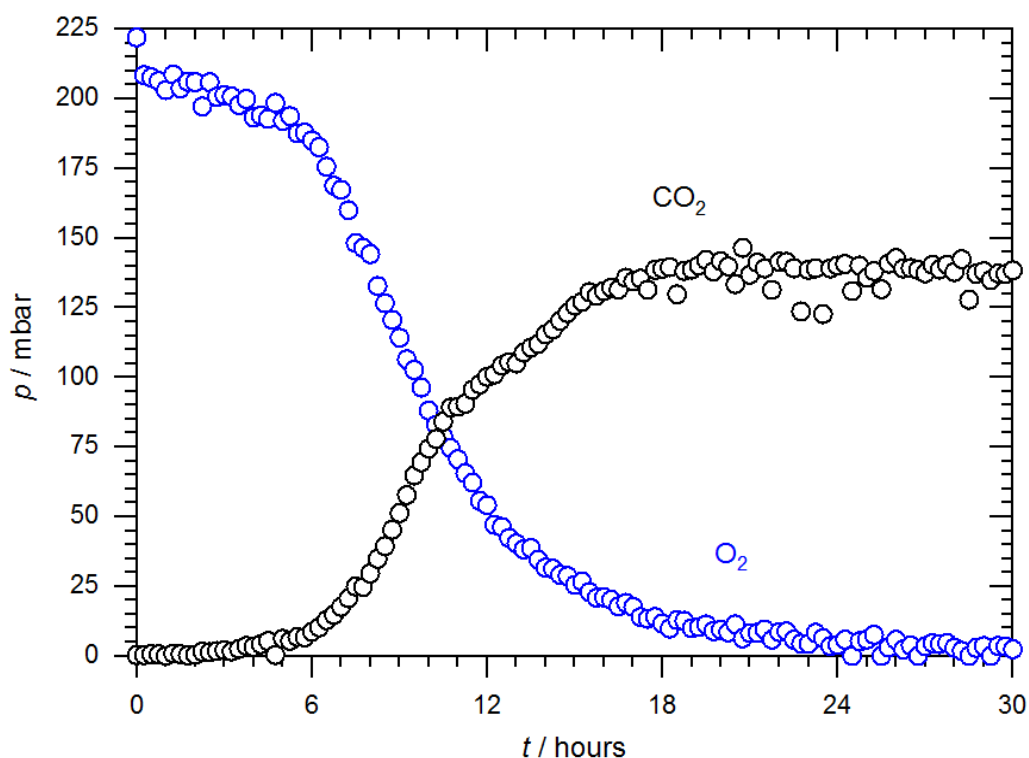


Figure 5.22. The graph shows O₂ consumption (blue) and CO₂ production (black) of *E. coli* growth in M9 medium supplemented with 2.5 mM glucose with 10 mM lactose, measured by using DHR.

5.1.4.4. Measuring the Different Phases of *E. coli* growth in M9 Medium Supplemented with a Mixture of Sugars with Isotopic Labelling by Monitoring of the Headspace Gases

Investigating the production of ¹³CO₂ and ¹²CO₂ from the metabolism of a mixture of ¹³C-glucose and ¹²C-lactose can show the preference for glucose metabolism. The Fermi resonance pairs of the isotopomers ¹³CO₂ and ¹²CO₂ can be distinguished by CERS as indicated by the Raman spectrum shown in Figure 5.7. The absorption peaks for ¹³CO₂ and ¹²CO₂ as shown in Figure 5.10 can be distinguished by PAS.

Figure 5.23 (a) shows $p(\text{O}_2)$, $p(^{13}\text{CO}_2)$ and $p(^{12}\text{CO}_2)$ during the growth of *E. coli* in M9 medium supplemented with 3 mM ¹³C-glucose and 20 mM ¹²C-lactose by using CERS. Figure 5.23 (b) is a zoom in from 4-12 h of Figure 5.23 (a) to distinguish more clearly between

$^{13}\text{CO}_2$ which is coming from ^{13}C -glucose and $^{12}\text{CO}_2$ which is coming from ^{12}C -lactose. Supplementing M9 medium with a high concentration of lactose and a low amount of ^{13}C -glucose indicated the strong preference of the metabolism of glucose over lactose. The figure shows this preference as $p(^{13}\text{CO}_2)$ increased by 27 mbar until ^{13}C -glucose was exhausted. Then $^{12}\text{CO}_2$ is produced which is from lactose, then it increased to 125 mbar similar to the amount of CO_2 produced from 3mM glucose on its own. As the isotopomers of CO_2 can be distinguished for the first 5 h, it is clear that *E. coli* metabolised ^{13}C -glucose and then ^{12}C -lactose. There is some slight overlap when ^{13}C -glucose concentration becomes very low. Lactose cannot be consumed until ^{13}C -glucose is very low or zero. In the first stage of metabolism the concentration of ^{13}C -glucose is the growth-limiting factor, after the first 10 hours of growth the ^{13}C -glucose is depleted, then lactose is metabolised where ^{12}C -lactose concentrations are sufficiently large so that O_2 is the growth-limiting factor. The depletion of ^{13}C -glucose is shown in Figure 5.23 (b) where $^{13}\text{CO}_2$ no longer increases past 27 mbar. The production of $^{13}\text{CO}_2$ occurs in the first 10 hours and then there is the production of $^{12}\text{CO}_2$ after about 8 hours, continuing until the *E. coli* have died. The values of $p(^{13}\text{CO}_2)$ and $p(^{12}\text{CO}_2)$ show the preference of the metabolism of glucose over lactose. Despite the concentration of lactose being six times greater than the concentration of glucose, the metabolism of glucose is still preferred over lactose.

Figure 5.24 (a) shows $p(\text{O}_2)$, $p(^{13}\text{CO}_2)$ and $p(^{12}\text{CO}_2)$ during the growth of *E. coli* in M9 medium supplemented with 2.5 mM ^{13}C -glucose and 10 mM ^{12}C -lactose measured by using DHR. Figure 5.24 (b) is a zoom in from 7-14 h of Figure 5.24 (a) to distinguish between $^{13}\text{CO}_2$ which is coming from ^{13}C -glucose and $^{12}\text{CO}_2$ which is coming from ^{12}C -lactose. After the initial 9 hours of *E. coli* metabolism, there are no further signs of activity, then after 9 hours $p(\text{O}_2)$ was decreasing, and $p(^{13}\text{CO}_2)$ increasing until about 20 mbar, similar as in Figure 5.23, taking into account the slightly different concentrations. After 12 hours, $p(^{13}\text{CO}_2)$ does not increase due to ^{13}C -glucose depletion. The increase in $p(^{12}\text{CO}_2)$ indicates *E. coli* is only metabolising lactose after about 11 hours. $^{12}\text{CO}_2$ production continues until depletion of O_2 . The 11 hours mark in bacterial growth represent the diauxic shift between the metabolism of predominantly glucose and the metabolism of lactose. Figures 5.23 and 5.24 have similar conditions and for this reason the results are very close. It is interesting to note that there is no apparent lag between glucose and lactose metabolism (diauxic lag), although short lag phases (1/2 h – 1 h) have been observed before in the literature.⁹⁹

In conclusion, CERS and DHR enabled successful monitoring of a variety of different growth phases and behaviour for aerobic suspensions of *E. coli* in LB or M9 medium supplemented with sugars. These techniques are ideal for studying aerobic metabolism because of the ability to monitor O₂ consumption and CO₂ production simultaneously. To summarise, two methods were used to monitor the respiration and metabolism of *E. coli*. With isotopically labelled sugars, CERS and DHR are both capable of distinguishing metabolic preferences and reaction mechanisms, such as glucose being first metabolised, and then lactose.

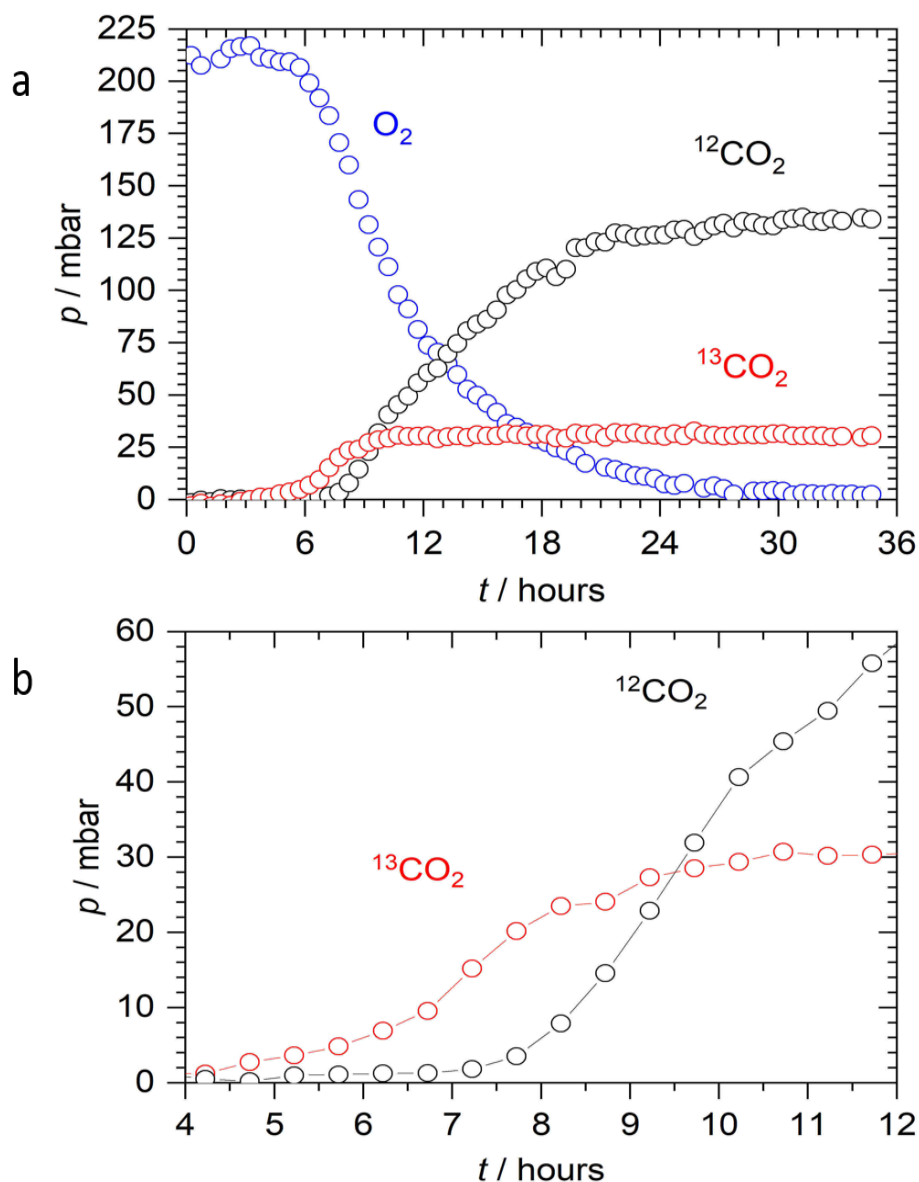


Figure 5.23. (a) O₂ consumption and (¹²CO₂ and ¹³CO₂) production by a suspension of *E. coli* in M9 medium supplemented with 3 mM ¹³C-glucose and 20 mM ¹²C-lactose by using CERS, (b) zoom in for figure (a) between 4-12 h to illustrate the differences between (¹³CO₂ and ¹²CO₂).

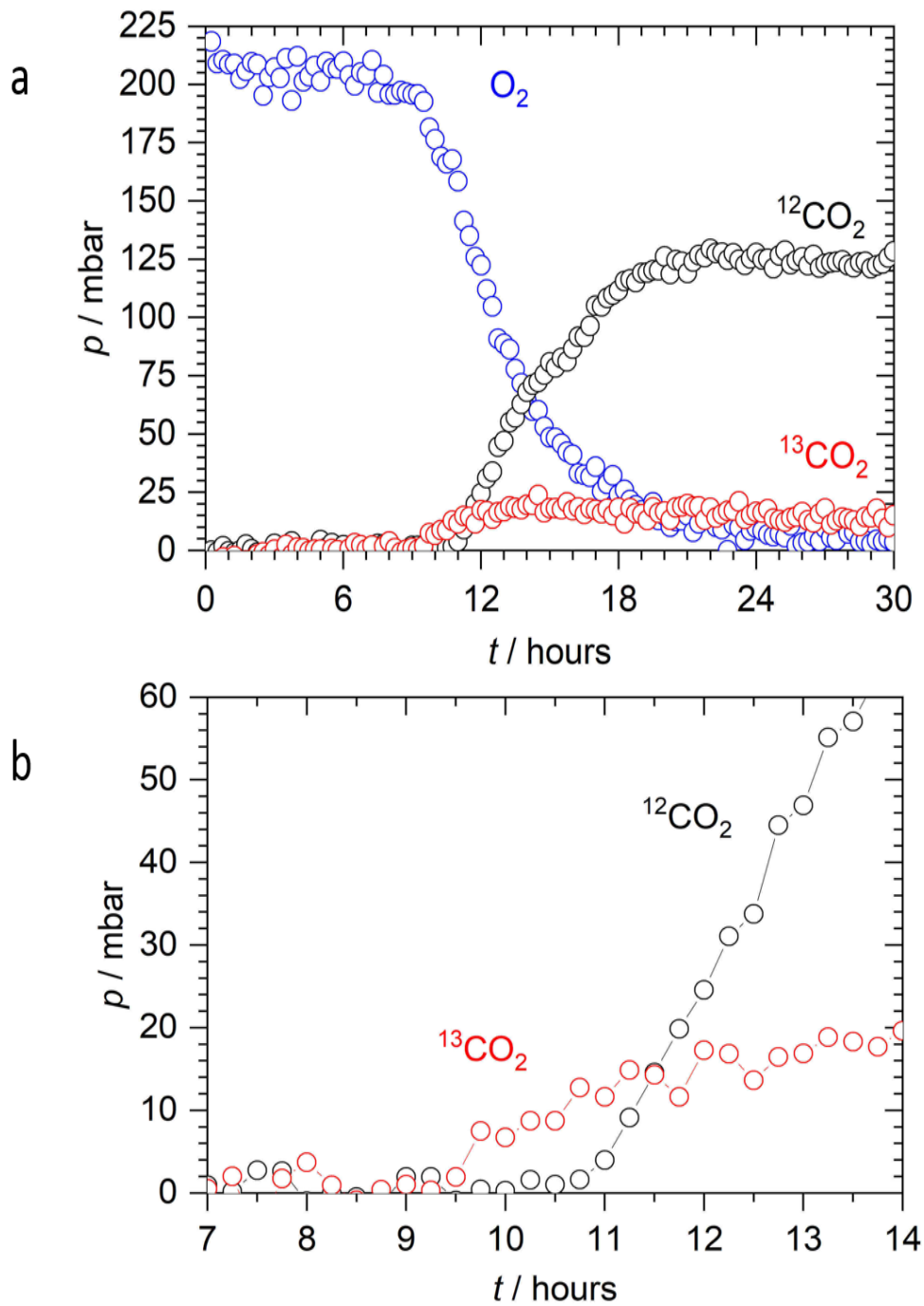


Figure 5.24. (a) O_2 consumption and ($^{12}CO_2$ and $^{13}CO_2$) production by a suspension of *E. coli* in M9 medium supplemented with 2.5 mM ^{13}C -glucose and 10 mM ^{12}C -lactose by using DHR, (b) zoom in for figure (a) between 7-14 h to illustrate the differences between ($^{13}CO_2$ and $^{12}CO_2$).

5.2. Trace Gas Analysis of CO₂, H₂S and O₂ by Near-IR and Red Diode Laser Photoacoustic Spectroscopy in a Differential Helmholtz Resonator: Applications in the Biosciences (L-Cysteine metabolism) and Natural Gas analysis (Petrochemistry)

This section together with the previous chapter 4 forms part of a scientific publication [ref. 89]. The initial work was done in collaboration with an MChem student (Xiu-Wen Kang). A reprint of the full article can be found in the Appendix.

“Diode Laser Photoacoustic Spectroscopy of CO₂, H₂S and O₂ in Differential Helmholtz Resonator for Trace Gas Analysis in the Biosciences and Petrochemistry”, by Saeed Alahmari, Xiu-Wen Kang, and Michael Hippler, *Analytical & Bioanalytical Chemistry*, 411, 2019, 3777-3787. Selected as ‘paper in forefront’ by the journal.

5.2.1. Aims

In this section, we demonstrate photoacoustic trace gas detection of CO₂, O₂ and H₂S in natural gas (NG) and to study the aerobic L-cysteine metabolism of microbes. A DFB diode laser near 1.57 μm is used for CO₂ and H₂S detection, and a DFB laser for O₂ detection near 760 nm. The set-up has been used for simultaneous *in situ* monitoring of O₂, CO₂ and H₂S in the L-cysteine metabolism of microbes (*E. coli*), and for the analysis of CO₂ and H₂S impurities in natural gas. We will introduce first applications, including time-dependent monitoring of the bacterial growth and aerobic metabolism of microbes, and detection of H₂S impurities in natural gas.

5.2.2. Experimental

5.2.2.1. Preparation of a Glass Balloon of Defined Gas Mixtures of H₂S in NG, and CO₂ in NG to be Used for Calibrations

The mixtures of gases were prepared in a glass balloon using freeze-pump-thaw purification on a gas handling Schlenk line as shown in Figure 3.18 in chapter 3. Calibrated gas mixtures containing CO₂ sublimed from dry ice or H₂S (Sigma-Aldrich, 99.5+%) were prepared on a glass vacuum line equipped with capacitance pressure gauges (Baratron). The gases were purified by repeated freeze-pump-thaw cycles and buffered to 1 bar total pressure by natural gas. NG was sampled from a gas tap within the PC teaching laboratory of the University (gas supplied *via* National Grid, UK); NG is essentially CH₄ with some additional minor components.

5.2.2.2. Monitoring H₂S Production from L-Cysteine in 2YT Medium of LB

5.2.2.2.1. YT Growth Medium Preparation

First of all, sterilisation of all glassware which is used in the experiment is required by either heating inside of an autoclave (2 hours at 121 °C) or filter sterilisation (0.22 µm filter) of solutions. Growth medium solutions are to be sterilised before coming into contact with bacterial samples. Lysogeny Broth LB or 2YT (two times yeast tryptone) growth medium was prepared as a solution of tryptone (8 g), yeast extract (5 g) and sodium chloride (2.5 g) in deionised water (500 ml).

5.2.2.2.2. Sample Preparation Using L-Cysteine Hydrochloride Monohydrate

For bacterial measurements, 50 ml of sterile 2YT medium (a rich medium containing yeast extract and tryptone) was inoculated with a single colony of *E. coli* (wild type, strain K-12 MG1655) and incubated for 5 h at 37 °C. It was added to 50 ml of sterile 2YT to give a 100 ml suspension in a 500 ml round bottom flask, The flask was kept with constant stirring at 37 °C in a thermostated water bath. The flask was connected to the DHR resonator with short gas transfer tubes in a closed system, giving a total gas volume of 660 ml, as shown in Figure 5.25. To enhance gas flow, a peristaltic pump (3 l/h) was used to cycle the flask headspace through the DHR resonator in a closed system as shown in Figure 5.8.

To observe O_2 , CO_2 and H_2S in the aerobic respiration of *E. coli*, a cysteine solution (L-cysteine hydrochloride anhydrous, Sigma) dissolved in 7 ml of water was injected via a septum (Suba-Seal) as a source of sulfur to induce production of H_2S . An aqueous solution of L-cysteine hydrochloride monohydrate was prepared for all experiments using different concentrations of L-cysteine hydrochloride monohydrate (1 mM, 1.7 mM, and 4 mM).



Figure 5.25. Experimental setup for a typical bacterial H_2S measurement.

5.2.2.3. Biological Measurements Using DHR

The near-IR single-mode DFB diode (Mitsubishi FU-650SDF, 4 mW) was amplified in a booster optical amplifier (Thorlabs S9FC1004P) to 30 mW peak power. This laser passed through CH1 of the Helmholtz resonator. A spectral scan taking 255 s between the range of wavenumber $6371 - 6368.8 \text{ cm}^{-1}$ was achieved by tuning the diode temperature from $33.9 - 38 \text{ }^\circ\text{C}$. The peak position used for observation of H_2S is 6369.78 cm^{-1} and of CO_2 is 6370.46 cm^{-1} , these positions were calibrated before the start of the biological measurements.

For measuring O_2 , the red laser (35 mW DFB diode laser Eagleyard EYP-DFB-0764) was directed through the other compartment CH2 of the Helmholtz resonator and was scanned in a spectral scan between the range of wavenumber $13084.9 - 13082.9 \text{ cm}^{-1}$ taking 120 s. The position of the O_2 peak used for observation is 13084.0 cm^{-1} . The peristaltic pump was switched off for the duration of the scans because it would introduce noise. Once both scans (CH1 and CH2) were complete, the peristaltic pump was turned on again, cycling the gas through the DHR for 15 minutes before starting a new scan. Both lasers were modulated by their injection current at the acoustic resonance frequency with a square-wave giving a 50% duty cycle.

For recording absorption spectra for CO_2 , H_2S and O_2 , a microprocessor on an Arduino board controlled the turning on and off of the diode laser in time with the measurements, as well as recording the total pressure p inside the system via a capacitance pressure gauge and recording the data from the lock-in amplifier. The integration time of the lock-in amplifier was set at 1 s. Before an experiment a vacuum pump was used to evacuate the DHR setup. Then the DHR was filled with laboratory air, and then the flask which contained the culture was connected to the system. In this experiment the setup is a closed system. The spectral data was analysed by fitting Lorentzian peaks to the spectra to obtain the partial pressures from the fitted peak height using the previous calibration.

5.2.2.4. pH and Final OD_{600} Measurements

At the end of all biology experiments, pH and biomass of *E.coli* produced were measured. 50 mL sample of the final culture was taken and centrifuged (10 minutes at 4000 rpm) to separate the medium from the biomass. By using a Jenway pH meter 3305, the pH of the solution was determined. The pH was between $7.2 - 7.3$ in all experiments at the end of the metabolism. The pH of fresh 2YT was 6.9 without *E. coli*. At the beginning of an experiment, the suspension has typically $\text{OD}_{600} \approx 0.6$ (optical density at 600 nm in a 1 cm cuvette). The final OD_{600} of *E. coli* in medium was between $2 - 2.1$ for all experiments.

5.2.3. Results and Discussions

5.2.3.1. Detection of H₂S and CO₂ Impurities in Natural Gas Samples

Trace gas analysis of natural gas is a very relevant task in petrochemistry. Natural gas is mainly methane, but depending on the source or provenance, it may also contain minor components like higher alkanes, components of no caloric value such as N₂ and CO₂, and H₂S. To demonstrate the capability of our scheme for trace gas detection of H₂S and CO₂ impurities in natural gas samples, we have sampled natural gas from a gas tap within the department and scanned the near-IR photoacoustic spectrum between 6369 – 6372 cm⁻¹ and compared it with the HITRAN data base as shown in Figure 4.27 in chapter 4. In this region, there are CO₂ transitions (peaks labelled **b**) and **c**) in Figure 4.27) and a separated H₂S transition (labelled **f**), that means there is no overlapping between CO₂ and H₂S peaks.

In 1 bar of natural gas, the acoustic resonance frequency shifts to about 320 Hz, and the photoacoustic signal has also slightly different phase shifts compared to 1 bar air or N₂. We have verified that after optimization, essentially the same calibration, noise levels and detection limits as shown for N₂ apply, in particular a 25 ppmv noise equivalent detection limit for H₂S in 1 bar natural gas at 1 s integration time.

Figure 5.26 **a**) shows a scan of 1 bar natural gas; in the spectral region, there are weak CO₂ transitions due to natural CO₂ impurities, **b**) and **c**) in Figure 5.26 **a**). In addition to a very weak H₂O absorption peak at the position of the H₂S peak **d**) discussed before, there are also weak CH₄ absorptions with $\sigma_{\text{peak}} = 1.5 \times 10^{-5} \text{ pm}^2$,⁸⁴ about 5000 times weaker than H₂S. Assuming a similar sensitivity of photoacoustic signals, the noise limit will be exceeded at methane pressures above 100 mbar. Unlike water discussed before in chapter 4, this has to be considered in natural gas samples, where at 1 bar total pressure, methane will typically be between 900 – 1000 mbar. In the spectrum of Figure 5.26 **a**), these CH₄ transitions at the position of the H₂S have a peak value of about 10 mV, above 10× the noise level at 1 s integration time. To correct for these weak absorptions, we suggest to extend the spectral region to include the separate peak **e**) of methane to establish the content of CH₄, and then subtract methane proportionally at the position of the H₂S, as demonstrated in Figure 5.26. A comparison with the HITRAN data base and our previous calibration shows the presence of 14 mbar CO₂ in the 1 bar sampled natural gas, or 1.4% CO₂ content, very similar to a previously reported measurement using Raman detection.² Reassuringly, no H₂S is apparent within our detection limit. To demonstrate the sensitivity to H₂S detection, we have prepared a sample of

3 mbar H₂S in 1 bar natural gas. The measurement is shown in Figure 5.26 **b**). The methane background is essentially as in pure natural gas. According to the calibration, there is 16 mbar or 1.6% CO₂, very close to the previous measurement of pure natural gas; the slight deviation might be explained by purity fluctuations in the natural gas line. The measured H₂S content is 2.8 mbar, very close to the nominally 3 mbar as prepared.

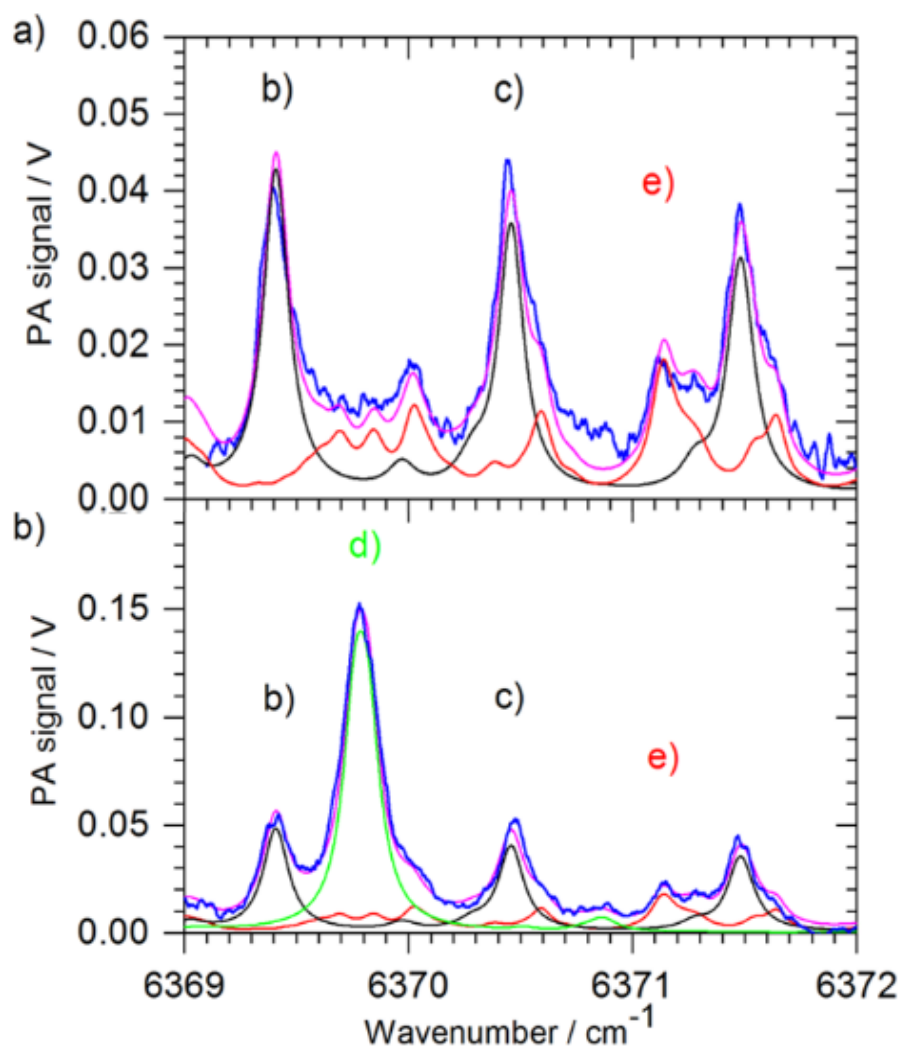


Figure 5.26. CH₄, CO₂ and H₂S transitions of natural gas samples. **a)** 1 bar natural gas (sampled 29/10/2018). **b)** 3 mbar H₂S in 1 bar natural gas (sampled 7/11/2018). The blue trace is the photoacoustic signal. In red, black, green and magenta are HITRAN data for CH₄, CO₂, H₂S and the sum, respectively. The peak labels are as in Figure 4.27 in chapter 4.

5.2.3.2. Monitoring O₂, CO₂ and H₂S During the Metabolism of L-cysteine by *E. coli*

In a further demonstration of the application of photoacoustic detection in a Helmholtz resonator in the biosciences, we monitor O₂, CO₂ and H₂S during the metabolism of *L*-cysteine by *E. coli*. During aerobic metabolism, microbes convert O₂ and sugars or other suitable organic substrates to CO₂, with approximately one unit of CO₂ produced per unit O₂ consumed. In addition, if *L*-cysteine is present, they may produce H₂S, with approximately one unit of H₂S produced per unit of cysteine consumed. In our closed system, O₂, CO₂ and H₂S are mostly in the gas phase, with some minor amount dissolved in the suspension. The total amount in the gas phase can be calculated by the ideal gas law. At equilibrium, the molarity of a dissolved gas can be calculated from its partial pressure using Henry's law. 1 mbar of an ideal gas corresponds to 2.6×10^{-5} mol in the head space (660 ml). Using Henry's constants at 37 °C,¹⁰⁹ 1 mbar correspond to 2.6×10^{-6} mol CO₂, 6.6×10^{-6} mol H₂S or 1.1×10^{-7} mol O₂ in the solution (100 ml). Some small amount of dissolved CO₂ (less than 1%) will react to form carbonic acid H₂CO₃. With a pK_{a1} = 6.37 (see Appendix 9), about 90% of this carbonic acid will dissociate to the bicarbonate ion HCO₃³⁻ at the pH range of the bacterial suspension (6.9–7.2). Since only about 10% of the total CO₂ is in solution, of which only a small amount will be converted into carbonic acid, this loss of CO₂ can be neglected to a first approximation. Being an acid, dissolved H₂S can dissociate into HS⁻; with a pK_{a1} = 7.02 (see Appendix 10), about half of dissolved H₂S will dissociate at the pH range of the suspension. With about 25% of total H₂S being in solution, of which about 50% is lost in the form of HS⁻, this effect needs to be taken into account when considering the total sulfur balance arising from the conversion of cysteine. In a control experiment, we injected 11 mbar of H₂S in an empty flask after the first scan and we observed no dissociation of H₂S, it is constant with time, as shown in Figure 5.27.

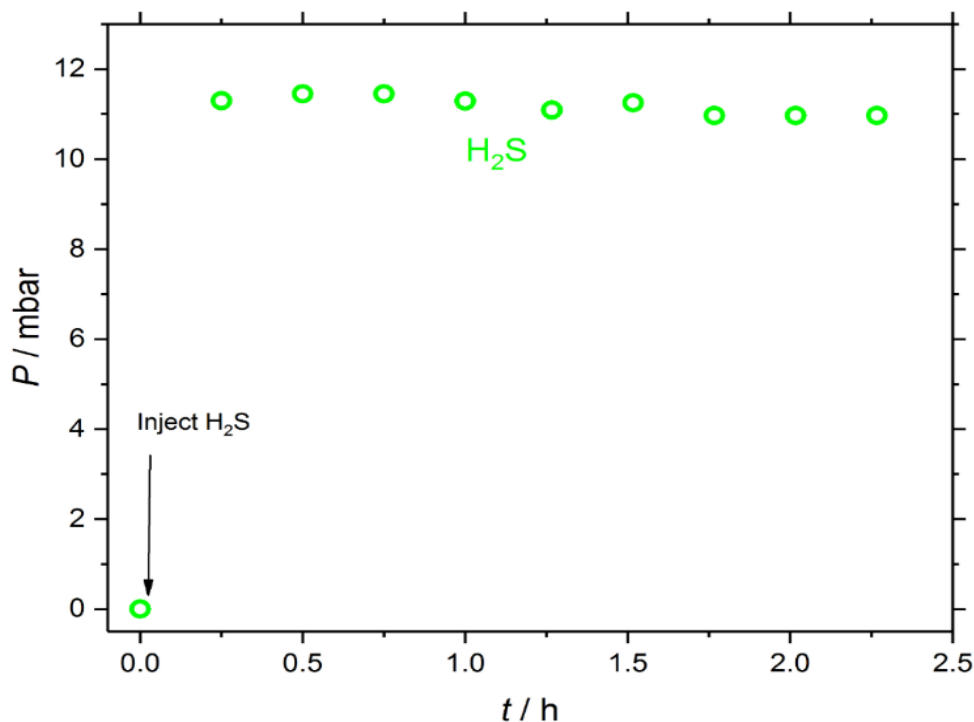


Figure 5.27. Time dependent concentration of H₂S when injected after the first scan ($t = 0$) into an empty flask.

In the biological experiments, we monitor O₂ with the red diode and convert photoacoustic signal into mbar using the previous calibration (see chapter 4, section O₂). For simultaneous monitoring of CO₂ and H₂S, we use the near IR diode scanning between 6369 – 6371 cm⁻¹. In this range, the CO₂ peaks labelled **b**) and **c**) can be found, and in-between, the strong H₂S peak labelled **d**). Figure 5.28 shows a typical scan of the head space above the bacterial suspension. Fitting three Lorentzian curves to the observed peaks **b**), **c**) and **d**) and using the previous calibration, photoacoustic signal is converted into mbar of H₂S and CO₂. Measurements were repeated every 15 min to obtain time-dependent concentrations of the head space.

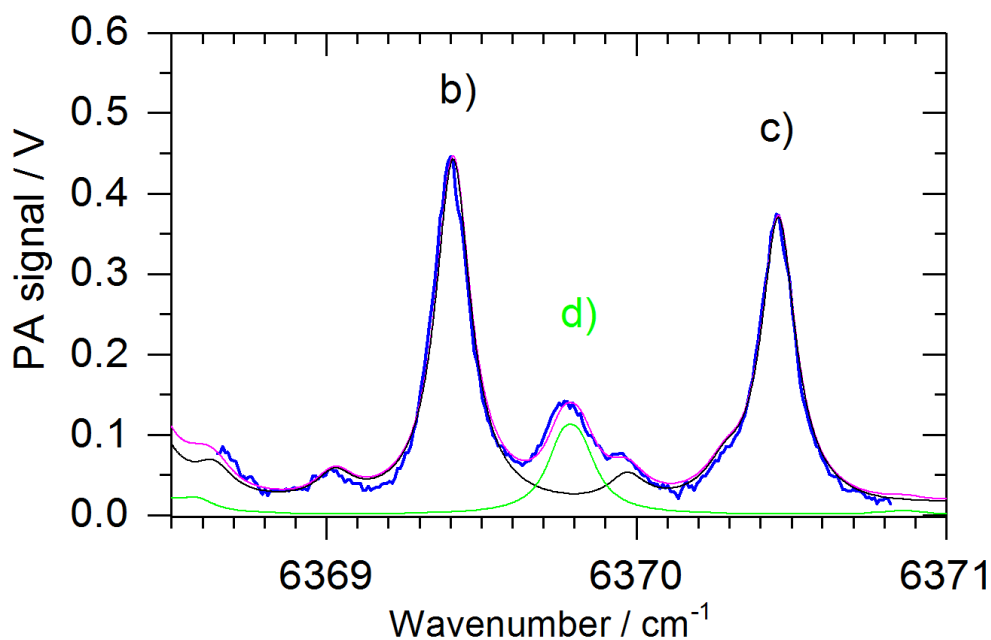


Figure 5.28. Typical scan of the head space above a bacterial suspension (2 h after injecting 1 mM cysteine, see Figure 5.29). The blue trace is the photoacoustic signal. In black, green and magenta are HITRAN data for 98 mbar CO₂, 2.2 mbar H₂S and the sum, respectively. The peak labels are as in Figure 4.27 in chapter 4.

Figure 5.29 shows a typical example of time-dependent concentrations, where 1 mM cysteine was injected into the *E. coli* suspension in 2YT medium after a delay of about 1 h. Before injection, no traces of H₂S are apparent. Due to aerobic respiration of *E. coli*, O₂ is slowly decaying and CO₂ formed in an about 1:1 ratio, as expected (see also Figure 5.30). After injection of cysteine, metabolism accelerates noticeably, and H₂S is formed after a short lag phase of about 20 min. Within 1 h, H₂S peaks to about 2.2 mbar. Apparently all cysteine is converted by then, and H₂S concentrations fall very slowly afterwards. The 2.2 mbar H₂S corresponds to about 0.09 mmol in the head space and suspension. This is almost exactly the amount of cysteine injected, demonstrating complete conversion of cysteine within 1 h. The slow decay of H₂S is genuine and not due to leaks, since we do not observe decays for CO₂. H₂S is known to stick to surfaces and gets easily absorbed which may explain the decaying pressure later on. Experiments were repeated several times, including different concentrations of cysteine (1–4 mM) as shown in Figures 5.29 and 5.30 respectively, always showing the same qualitative behaviour and complete conversion of cysteine into H₂S within about 1-3 h. In a control experiment, we injected cysteine into sterile 2YT medium without observing any H₂S evolving, proving that the H₂S production is by the microbes, as shown in Figure 5.31. The current application demonstrates *in situ* monitoring of trace gases in the head space above bacterial suspensions in a closed system by Helmholtz photoacoustic detection.

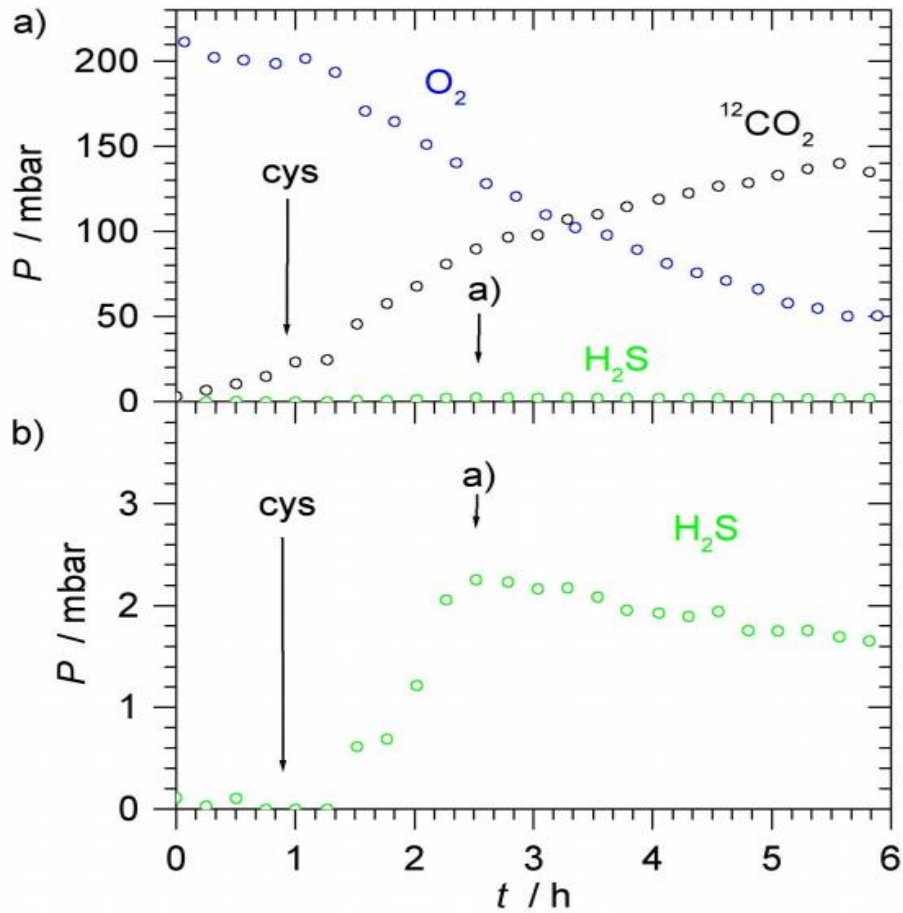


Figure 5.29. Time dependent concentrations of O₂, CO₂ and H₂S in the head space during the metabolism of 1 mM L-cysteine by *E. coli* in 100 ml 2YT.

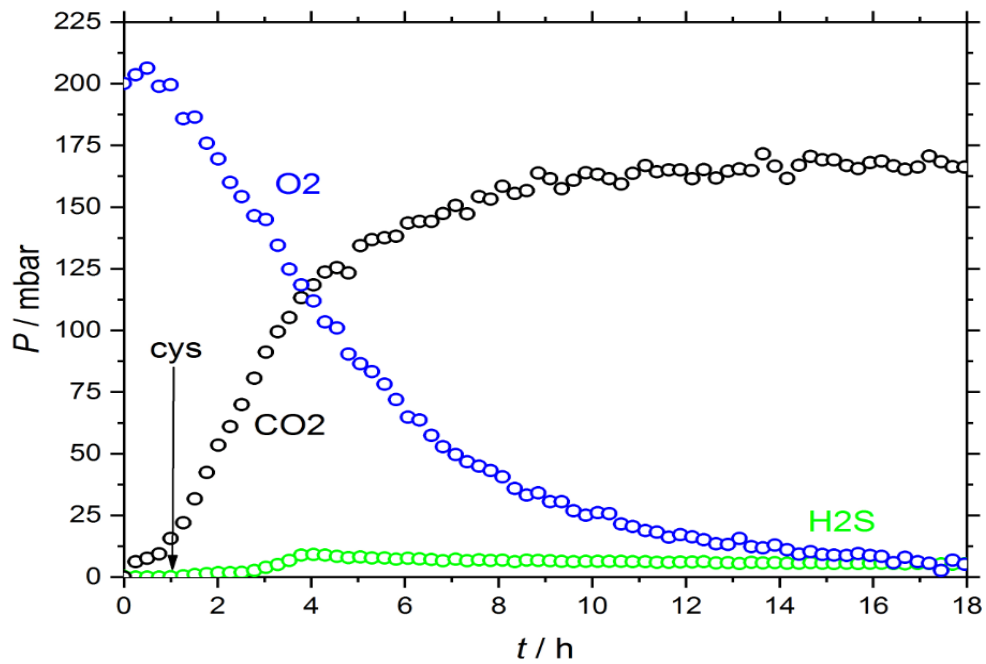


Figure 5.30. Time dependent concentrations of O₂, CO₂ and H₂S in the head space during the metabolism of 4 mM L-cysteine by *E. coli* in 100 ml 2YT.

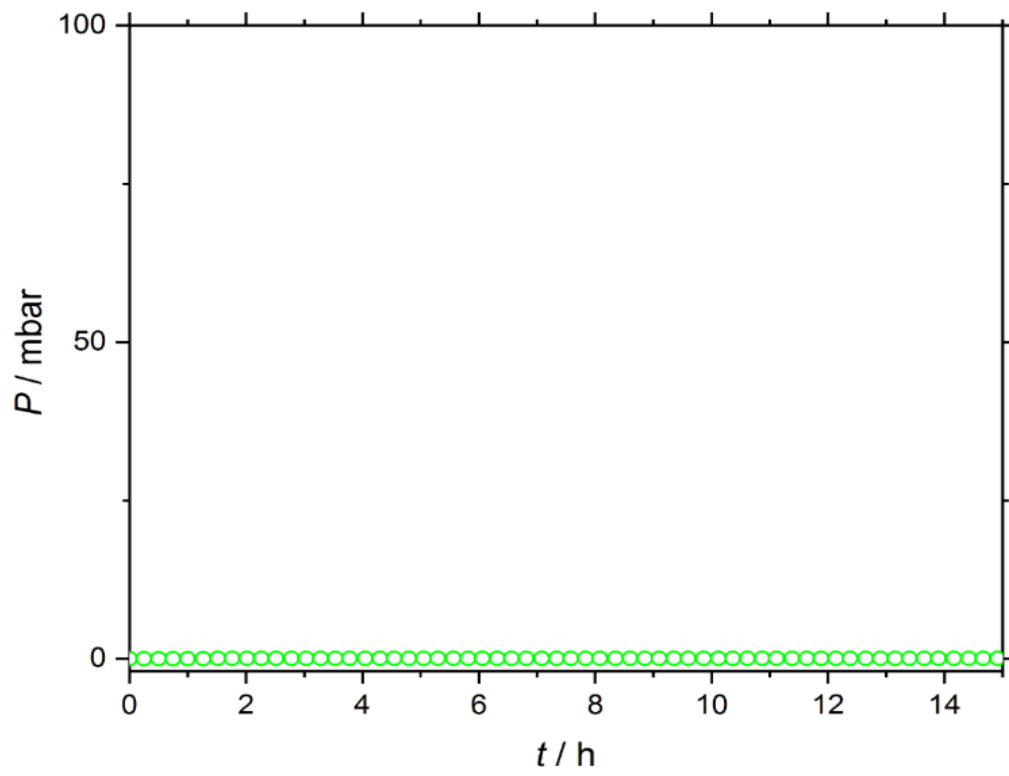


Figure 5.31. Shows the injection of cysteine into sterile 2YT medium without observing any H_2S .

5.2.4. Conclusions

IR spectroscopy (PAS in DHR) and CERS have the potential to act as two complementary techniques in biosciences, in addition to well-established techniques such as OD measurements. This chapter has demonstrated this with the investigations into the aerobic respiration of *E. coli* by using the two different methods. PAS has the superior sensitivity making it ideal for trace gas detection at low ppm concentrations. Due to the selection rules governing IR and Raman spectroscopy, CERS can identify homonuclear diatomic molecules. The investigation into the aerobic respiration of *E. coli* is an example of a scenario where both CERS and DHR are suited for trace gas detection. IR spectroscopy cannot detect O₂ consumption therefore a specific red diode laser for detecting O₂ was used in the red range, which makes the comparison between O₂ consumption and CO₂ production possible.

Monitoring O₂ consumption and CO₂ production together is vital as the two may not always correspond in magnitude. *E. coli* grown in M9 medium supplemented with glucose did not show the expected 1:1 ratio of O₂ consumption to CO₂ production compared to previous work monitoring with LB medium. Monitoring aerobic respiration with IR and Raman spectroscopy helps to understand the metabolic activity. The research with CERS and DHR determined the higher amount of O₂ consumption than CO₂ production is not due to CO₂ dissolved in solution but depends on the medium used. The hypothesis is that the conversion of glucose into biomass in minimal media results in more O₂ consumption than CO₂ production. O₂ consumption and CO₂ production, and OD measurements showed the four main phases of *E. coli* growth.

As spectroscopy can distinguish between isotopomers, isotopic labelling can be used to probe reaction mechanisms. Demonstrations were carried out with the spectroscopic techniques to highlight this capability. With CERS and DHR, the monitoring of the metabolism of a mixture of ¹³C-glucose and ¹²C-lactose found that the metabolic preference is towards glucose first. Due to the strong inclination towards glucose metabolism, *E. coli* does not metabolise ¹²C-lactose until to the completion of ¹³C-glucose. After exhaustion of the ¹³C-glucose supply, ¹²C-lactose metabolism occurs with no diauxic shift lag phase under our conditions. The success of the results obtained by the two investigations shows that both CERS and DHR are useful tools in the biosciences.

Furthermore, in this chapter, a set-up is described employing near-IR and red diode lasers for the detection of CO₂ and H₂S in NG by photoacoustic detection in a DHR. The noise

equivalent detection limit of H₂S in 1 bar N₂ is 0.022 mbar (22 ppmv) as explained in chapter 4. At this level, the scheme may be useful for safety monitoring of toxic H₂S. Similar detection limits apply to trace impurities in 1 bar NG. Taking into account the simplicity of the DHR set-up, the detection limits compare favourably with more involved photoacoustic schemes. Possible interferences due to weak water and methane absorptions have been discussed and shown to be either negligible or easy to correct. We have demonstrated two selected application examples for H₂S detection by DHR photoacoustic spectroscopy. The set-up has been used successfully for simultaneous *in situ* monitoring of O₂, CO₂ and H₂S in the biosciences, for example in the cysteine metabolism of microbes (*E. coli*), and for the analysis of CO₂ and H₂S impurities in natural gas.

Chapter 6. General Conclusions and Future Work

A novel set of techniques in vibrational spectroscopy (PAS and CERS) have been applied to measurements of headspace gases generated and consumed by *E. coli*. In addition, PAS has been applied to detect H₂S and CO₂ in NG and generated from *E. coli*. Both techniques have great potential in the biosciences and in petrochemistry, as demonstrated by the applications introduced.

Due to the inherent signal amplification and noise cancellation, photoacoustic spectroscopy in a differential Helmholtz resonator (DHR) has great potential for trace gas analysis, with possible applications including safety monitoring of toxic gases, applications in the biosciences and for natural gas analysis in petrochemistry. Photoacoustic detection is one of the most sensitive optical absorption techniques, but it suffers from ambient acoustic noise and flow noise introduced by sampling gases; this ultimately limits detection limits. A DHR has the advantage that the symmetrical resonator composed of two identical chambers produces photoacoustic absorption signals which are out-of-phase in the two chambers, whereas noise including flow noise is in-phase in the two chambers. Differential detection therefore doubles the signal and cancels noise to a great extent. In this project, trace gas detection of CO₂ and H₂S by PAS in a DHR was demonstrated with a DFB diode laser near 1.6 μm , and O₂ detection with a DFB diode laser near 764 nm. Also, first applications were introduced, time-dependent monitoring of the bacterial growth and aerobic metabolism of microbes and detection of H₂S and CO₂ impurities in NG, as explained in chapter 5.

Chapter 4 described a set-up employing near-IR and red diode lasers for the detection of CO₂ and O₂ in 1 bar of air/N₂ and NG, in static and flow cell measurements and introduced improvements including a multipass arrangement and using two independent lasers simultaneously. With the red diode laser, O₂ can be detected at 764.280 nm. A noise equivalent detection limit of 0.60 mbar (600 ppmv) of O₂ in 1 bar of air at 35 mW peak power and 1 s integration time is obtained. Normalizing to the absorption cross section, the laser power and integration time, a noise equivalent normalized absorption coefficient $\alpha = 2.2 \times 10^{-8} \text{ cm}^{-1} \text{ W s}^{1/2}$ is calculated. Within the tuning range of the near-IR DFB diode laser (6357 – 6378 cm^{-1}), CO₂ and H₂S absorption features can be accessed for trace gas detection. CO₂ has a noise equivalent detection limit of 0.160 mbar (160 ppmv) for CO₂ in 1 bar N₂ at 1 s integration time with the 30 mW laser. This corresponds to a noise equivalent normalized absorption coefficient $\alpha = 8.3 \times 10^{-9} \text{ cm}^{-1} \text{ W s}^{1/2}$. Due to stronger absorption cross-sections, the noise equivalent detection limit of H₂S in 1 bar N₂ is 0.022 mbar (22 ppmv). At this level, the scheme

may be useful for safety monitoring of toxic H₂S. Similar detection limits apply to trace impurities in 1 bar NG. Possible interferences due to weak water and methane absorptions have been discussed and shown to be either negligible or easy to correct. Using Henry's law, the 1 s noise equivalent detection limits for the head space gases O₂, CO₂ and H₂S translate into detection limits of the dissolved gases in the solution of 16 ppb per mole for dissolved O₂, 76 ppb for CO₂ and 27 ppb for H₂S.

As an advantage of spectroscopic detection, PAS and CERS can be used to distinguish between different isotopomers. Isotopic labelling can be used to probe biological mechanisms. The carbon source for metabolism of aerobic *E. coli* have been investigated using a mix of two labelled sugars, ¹³C-glucose and ¹²C-lactose, to examine if *E. coli* shows a preference for one sugar over the other. In preparation for such studies, it is necessary to know the positions of peaks for the different isotopically labelled CO₂ molecules before starting to apply any biology experiments. This was characterised in chapter 4 for ¹²CO₂ and ¹³CO₂ to understand the system very well before starting with any isotopical labelling applications.

Monitoring O₂ consumption and CO₂ production together is vital as the two may not always correspond in magnitude. *E. coli* grown in M9 minimal medium supplemented with glucose did not show the expected 1:1 ratio of O₂ consumption to CO₂ production as expected from previous work monitoring with rich LB medium. The research with CERS and PAS in the DHR determined a higher amount of O₂ consumption than CO₂ production. This is not due to CO₂ dissolved in solution but depends on the medium used. Our hypothesis is the conversion of glucose into biomass in minimal media results in more O₂ consumption than CO₂ production. The minimal medium cannot provide a carbon source, therefore carbon is taken from the sugar. The dry weight of bacteria at the end of a typical experiment was about 60 mg. Assuming that about 50% of this is carbon, the bacteria contain about 2.5 mmol carbon in total, in good agreement with the missing CO₂. On the other hand, in rich LB medium, tryptone provides a source of essential amino acids, and the yeast extract offers a source of various organic compounds required for growth. *E. coli* grown in LB medium does not have to synthesise these species from glucose which is likely why O₂ consumption and CO₂ production show the expected 1:1 ratio.

In the biosciences, OD measurements are a standard, widely used technique to characterise bacterial growth. In chapter 5, we have discussed and shown some of its shortcomings if used on its own without supporting complementary measurements. OD

measurements are an indirect indicator of bacterial growth. They suffer from interferences and they cannot distinguish living cells from dead cells and debris. OD measurements can therefore not provide sufficient information once the OD becomes constant during the stationary phase of bacterial growth. They also cannot distinguish diauxic growth without a diauxic lag phase present. The spectroscopic measurements, however, can clearly and unambiguously distinguish the different stages of bacterial growth characterising the growth phases in the different media studied, LB and M9.

Spectroscopy can distinguish between isotopomers. This capability can be used to probe reaction mechanisms. This is demonstrated in this thesis using both spectroscopic techniques to highlight this capability. With CERS and PAS in the DHR, the monitoring of the metabolism of the mixture of ^{13}C -glucose and ^{12}C -lactose found that the metabolic preference is towards glucose first. $^{13}\text{CO}_2$ and $^{12}\text{CO}_2$ production shows that because of the strong inclination towards glucose metabolism, *E. coli* does not metabolise ^{12}C -lactose until to the completion of ^{13}C -glucose. After exhaustion of the ^{13}C -glucose supply, ^{12}C -lactose metabolism occurs with no diauxic shift lag phase under our conditions. The success of the results obtained by the two investigations shows that both CERS and PAS in the DHR are useful tools in the biosciences.

CERS and DHR enabled successful monitoring of a variety of different growth phases and behaviour for aerobic suspensions of *E. coli* in LB (rich medium) or M9 medium (minimal medium) supplemented with sugar. These techniques are ideal for studying aerobic metabolism because of the ability to monitor O_2 consumption and CO_2 production simultaneously. CERS may find use in the biosciences for investigating microorganisms that use or generate homonuclear diatomic gases, such as O_2 , H_2 or N_2 , during their metabolic activities. IR detection with DHR can be used in the biosciences to investigate heteronuclear molecules like H_2S and CO_2 . To summarise, in this chapter 5 two methods were used to monitor the respiration of *E. coli*. With the use of isotopically labelled sugars, CERS and PAS are capable of distinguishing metabolic preferences as well as probing reaction mechanisms such as glucose being metabolised first, then lactose second.

In addition, this thesis demonstrated two further selected application examples. The DHR set-up has been used successfully for simultaneous *in situ* monitoring of O_2 , CO_2 and H_2S in the biosciences, for example in the cysteine metabolism of microbes (*E. coli*), and for the analysis of CO_2 and H_2S impurities in NG as described in chapter 5

In the future, the Hippler group is planning further work to miniaturize the DHR set-up and to apply the technique to the measurement of NG samples from different sources and to investigate the metabolism of microbes with applications in studying the role of H₂S as a signalling molecule in microbial systems. Due to the low cost of diode lasers and microphone detection, the relatively simple and robust set-up, the inherent signal amplification and noise cancellation, the suitability for static and flow cell measurements, the good detection limits and the spectroscopic selectivity which minimizes interferences, trace gas analysis in a differential Helmholtz resonator with near-IR and red diode lasers has great potential for many applications ranging from the biosciences to safety monitoring to petrochemistry. In future work, the CERS technique will be explored to study aerobic and anaerobic metabolism of microbes, for example in the production of biohydrogen by anaerobic fermentation of sugars or other suitable compounds by microbes.

References

- 1 C. L. Spencer, V. Watson and M. Hippler, *Analyst*, 2012, **137**, 1384–1388.
- 2 M. Hippler, *Anal. Chem.*, 2015, **87**, 7803–7809.
- 3 R. Salter, J. Chu and M. Hippler, *Analyst*, 2012, **137**, 4669–4676.
- 4 R. Keiner, T. Frosch, T. Massad, S. Trumbore and J. Popp, *Analyst*, 2014, **139**, 3879–3884.
- 5 T. W. Smith and M. Hippler, *Anal. Chem.*, 2017, **89**, 2147–2154.
- 6 M.W. Sigrist, *Air Monitoring by Laser Photoacoustic Spectroscopy*, Chemical Analysis, Wiley, New York, chapter 4., 1994.
- 7 A. Miklós, P. Hess and Z. Bozóki, *Rev. Sci. Instrum.*, 2001, **72**, 1937–1955.
- 8 B. Lavorel, G. Millot, G. Rouille, H. Berger and H. W. Schrötter, *J. Mol. Struct.*, 1992, **273**, 49–59.
- 9 S. Hanf, R. Keiner, D. Yan, J. Popp and T. Frosch, *Anal. Chem.*, 2014, **86**, 5278–5285.
- 10 M. Hippler, C. Mohr, K. A. Keen and E. D. McNaghten, *J. Chem. Phys.*, 2010, **133**, 1–8.
- 11 G. A. West, J. J. Barrett, D. R. Siebert and K. V. Reddy, *Rev. Sci. Instrum.*, 1983, **54**, 797–817.
- 12 J. Zhu, A. Sanchez, G. N. Bennett and K.-Y. San, *Metab Eng*, 2011, **40**, 704–712.
- 13 S. Alahmari and M. Hippler, in *Advanced Photonics*, (BGPP, IPR, NP, NOMA, Sensors, Networks, SPPCom, SOF), OSA Technical Digest (online) (Optical Society of America, 2018), 2018, p. SeM2J.4.
- 14 W. J. Ingledew and R. K. Poole, *Microbiol. Rev.*, 1984, **48**, 222–271.
- 15 A. H. Romano and T. Conway, *Res Microbiol*, 1996, **147**, 448–455.
- 16 A. Buhr, K. Flükiger and B. Erni, *Biochem. Mol. Biol.*, 1994, **324**, 23437–23443.
- 17 D. Schneider, T. Pohl, J. Walter, K. Dörner, M. Kohlstädt, A. Berger, V. Spehr and T.

- Friedrich, *Biochim. Biophys. Acta - Bioenerg.*, 2008, **1777**, 735–739.
- 18 A. R. Eberly, K. A. Floyd, C. J. Beebout, S. J. Colling, M. J. Fitzgerald, C. W. Stratton, J. E. Schmitz and M. Hadjifrangiskou, *Mol. Sci.*, 2017, **18**, 1–12.
- 19 G. Muyzer and A. J. M. Stams, *Nat. Rev. Microbiol.*, 2008, **6**, 441–454.
- 20 H. Kimura, *Antioxid. Redox Signal.*, 2015, **22**, 362–376.
- 21 K. Shatalin, E. Shatalina, A. Mironov and E. Nudler, *Science*, 2011, **334**, 986–990.
- 22 T. Oguri, B. Schneider and L. Reitzer, *J. Bacteriol.*, 2012, **194**, 4366–4376.
- 23 N. Awano, M. Wada, H. Mori, S. Nakamori and H. Takagi, *Appl. Environ. Microbiol.*, 2005, **71**, 4149–4152.
- 24 N. Awano, M. Wada, A. Kohdoh, T. Oikawa, H. Takagi and S. Nakamori, *Appl. Microbiol. Biotechnol.*, 2003, **62**, 239–243.
- 25 K. Tanizawa, *J. Biochem.*, 2011, **149**, 357–359.
- 26 A. Varga, Z. Bozóki, M. Szakáll and G. Szabó, *Appl. Phys. B Lasers Opt.*, 2006, **85**, 315–321.
- 27 V. Spagnolo, P. Patimisco, R. Pennetta, A. Sampaolo, G. Scamarcio, M. S. Vitiello and F. K. Tittel, *Opt. Express*, 2015, **23**, 7574.
- 28 T. L. Guidotti, *Occup Med*, 1996, **46**, 367–371.
- 29 IDLH Documentation for Hydrogen Sulfide, National Institute for Occupational Safety and Health (NIOSH); <https://www.cdc.gov/niosh/idlh/7783064.html>. Accessed 21 Nov 2018.
- 30 A. Szabó, Á. Mohácsi, G. Gulyás, Z. Bozóki and G. Szabó, *Meas. Sci. Technol.*, 2013, **24**, 7.
- 31 A. Varga, Z. Bozoki, M. Szakall and G. Szabo, *Eur. Geosci. Union*, 2007, **9**, 315–321.
- 32 H. Moser and B. Lendl, *Appl. Phys. B Lasers Opt.*, 2016, **122**, 1–11.
- 33 E. Dupuit, A. Dandrieux, P. Kvapil, J. Ollivier, G. Dusserre and O. Thomas, *Analisis*, 2000, **28**, 966–972.

- 34 H. P. Sanderson, R. Thomas and M. Katz, *Air Pollut. Control Assoc. ISSN*, 2012, **2470**, 2–5.
- 35 L. Huber and H. Obbens, *J. Chromatogr. A*, 1985, **349**, 465–468.
- 36 F. Vandecruys, E. Brauns, W. Engelen, F. De Schutter and J. Vangrunderbeek, *Solid State Ionics*, 1998, **112**, 95–102.
- 37 T. Hübert, L. Boon-brett, G. Black and U. Banach, *Sensors and Actuators*, 2011, **157**, 329–352.
- 38 S. Schilt, L. Thévenaz, M. Niklés, L. Emmenegger and C. Hüglin, *Spectrochim. Acta - Part A Mol. Biomol. Spectrosc.*, 2004, **60**, 3259–3268.
- 39 H. Wu, L. Dong, X. Liu, H. Zheng, X. Yin, W. Ma, L. Zhang, W. Yin and S. Jia, *Sensors*, 2015, **15**, 26743–26755.
- 40 H. Wu, L. Dong, H. Zheng, X. Liu, X. Yin, W. Ma, L. Zhang, W. Yin, S. Jia and F. K. Tittel, *Sensors Actuators, B Chem.*, 2015, **221**, 666–672.
- 41 Z. Yunusa, M. N. Hamidon, A. Kaiser and Z. Awang, *Sensors & Transducers*, 2014, **168**, 61–75.
- 42 T. Holzberg, R. Watson, V. Brown, S. Andar, K. Kostov, Y. Tolosa and G. Rao, *Curr. Opp. Biotechnol*, 2018, **22**, 115–127.
- 43 D. Romanini, A. A. Kachanov and F. Stoeckel, *Chem. Phys. Lett.*, 1997, **270**, 538–545.
- 44 Y. He, M. Hippler and M. Quack, *Chem. Phys. Lett.*, 1998, **289**, 527–534.
- 45 M. Hippler and M. Quack, *Chem. Phys. Lett.*, 1999, **314**, 273–281.
- 46 M. Hippler and M. Quack, *J. Chem. Phys.*, 2002, **116**, 6045–6055.
- 47 M. Hippler, L. Oeltjen and M. Quack, *J. Phys. Chem. A*, 2007, **111**, 12659–12668.
- 48 G. Busse and D. Herboeck, *Appl. Opt.*, 1979, **18**, 3959–3961.
- 49 V. Zéninari, B. Parvitte, D. Courtois, V. A. Kapitanov and Y. N. Ponomarev, *Infrared Phys. Technol.*, 2003, **44**, 253–261.
- 50 J. Rouxel, J. G. Coutard, S. Gidon, O. Lartigue, S. Nicoletti, B. Parvitte, R. Vallon, V.

- Zéninari and A. Glière, *Sensors Actuators, B Chem.*, 2016, **236**, 1104–1110.
- 51 H. Cattaneo, T. Laurila and R. Hernberg, *Appl. Phys. B Lasers Opt.*, 2006, **85**, 337–341.
- 52 A. Kachanov, S. Koulikov and F. K. Tittel, *Appl. Phys. B Lasers Opt.*, 2013, **110**, 47–56.
- 53 T. Laurila, H. Cattaneo, T. Pöyhönen, V. Koskinen, J. Kauppinen and R. Hernberg, *Appl. Phys. B Lasers Opt.*, 2006, **83**, 285–288.
- 54 J. Rouxel, J. G. Coutard, S. Gidon, O. Lartigue, S. Nicoletti, B. Parvitte, R. Vallon, V. Zéninari and A. Glière, *Sensors Actuators, B Chem.*, 2016, **236**, 1104–1110.
- 55 N. C. Fernelius, *Opt. Soc. Am.*, 1979, **18**, 1784.
- 56 W. Chen, A. A. Kosterev, F. K. Tittel, X. Gao and W. Zhao, *Appl. Phys.*, 2018, **90**, 311–315.
- 57 S. Hansen, B. B. and W. Stenby, *Appl. Spectrosc.*, 2001, **55**, 745–749.
- 58 J. Kiefer, T. Seeger, S. Steuer, S. Schorsch, M. Lehrstuhl and A. Leipertz, *Meas. Sci. Technol.*, 2008, **19**, 9pp.
- 59 M. A. Buldakov, B. V Korolev, I. I. Matrosov, D. V Petrov, A. A. Tikhomirov and E. Systems, *Appl. Spectrosc.*, 2013, **80**, 124–128.
- 60 S. C. Eichmann, J. Kiefer, J. Benz, T. Kempf, A. Leipertz and T. Seeger, *Meas. Sci. Technol.*, 2014, **25**, 075503.
- 61 S. Manohar and D. Razansky, *Adv. Opt. Photonics*, 2016, **8**, 586–617.
- 62 F. J. M. Harren, G. Cotti, J. Oomens and L. Hekkert, *Encycl. Anal. Chem.*, 2000, 2203–2226.
- 63 V. Holm, (Victoria University Master Thesis), 2013.
- 64 R. D. Kamm and C. E. Hackett, *Am. Inst. Phys.*, 1973, **23**, 23.
- 65 [Http://hearinghealthmatters.org/waynesworld/2016/light-em-mr-bell/](http://hearinghealthmatters.org/waynesworld/2016/light-em-mr-bell/) accessed 9/2/2017, Figure from Christopher Schweised.

- 66 B. Widom, *Am. Inst. Phys.*, 1960, **32**, 913–923.
- 67 J. Besson, (Ecole Polytechnique Federale De Lausanne PhD Thesis), 2006.
- 68 H. Yi, R. Maamary, X. Gao, M. W. Sigrist, E. Fertein and W. Chen, *Appl. Phys. Lett.*, 2015, **106**, 101–109.
- 69 T. Kuusela and J. Kauppinen, *Appl. Spectrosc. Rev.*, 2007, **42**, 443–474.
- 70 A. Miklós, S. Schäfer and P. Hess, in *Encyclopedia of Spectroscopy and Spectrometry*, New York, 2nd Editio., 2010, pp. 1815–1822.
- 71 J. Chung, (The University of Sheffield, PhD Thesis), 2015.
- 72 W. M. Sigrist, in *Encyclopedia of Spectroscopy and Spectrometry*, New York, 2nd Editio., 2010, pp. 1800–1809.
- 73 A. Elia, P. M. Lugarà, C. di Franco and V. Spagnolo, *Sensors*, 2009, **9**, 9616–9628.
- 74 D. C. Dumitras, D. C. Dutu, C. Matei, A. M. Magureanu, M. Petrus and C. Popa, *J. Optoelectron. Adv. Mater.*, 2007, **9**, 3655–3701.
- 75 K. Song, H. K. Cha, V. A. Kapitanov, Y. N. Ponomarev, A. P. Rostov, D. Courtois, B. Parvitte and V. Zeninari, *Appl. Phys. B Lasers Opt.*, 2002, **75**, 215–227.
- 76 V. Zeninari, V. A. Kapitanov, D. Courtois and Y. N. Ponomarev, *Infrared Phys. Technol.*, 1999, **40**, 1–23.
- 77 W.-U, L. Brilliet and A. Gallagher, *Phys. Rev. A At., Mol., Opt. Phys*, 1980, **22**, 1012–1017.
- 78 E. Riedle and J. Neusser, *Chem. Phys*, 1984, **80**, 4686–4693.
- 79 R. W. Fox and L. Hollberg, *Opt. Soc. Am.*, 1999, **16**, 2247–2254.
- 80 D. A. King and R. J. Pittaro, *Opt. Lett*, 1998, **23**, 774–776.
- 81 J. M. Hollas, *Modern Spectroscopy*, John Wiley & Sons Ltd, Chichester, 4th edn., 2004.
- 82 P. Atkins and J. DePaula, *Atkins' Physical Chemistry*, Oxford, New York, 8th edn., 2006.

- 83 B. Stuart, *Infrared Spectroscopy: Fundamentals and Applications*, John Wiley, First., 2004.
- 84 I. E. Gordon, L. S. Rothman, C. Hill, R. V. Kochanov, Y. Tan, P. F. Bernath, M. Birk, V. Boudon, A. Campargue, K. V. Chance, B. J. Drouin, J. M. Flaud, R. R. Gamache, J. T. Hodges, D. Jacquemart, V. I. Perevalov, A. Perrin, K. P. Shine, M. A. H. Smith, J. Tennyson, G. C. Toon, H. Tran, V. G. Tyuterev, A. Barbe, A. G. Császár, V. M. Devi, T. Furtenbacher, J. J. Harrison, J. M. Hartmann, A. Jolly, T. J. Johnson, T. Karman, I. Kleiner, A. A. Kyuberis, J. Loos, O. M. Lyulin, S. T. Massie, S. N. Mikhailenko, N. Moazzen-Ahmadi, H. S. P. Müller, O. V. Naumenko, A. V. Nikitin, O. L. Polyansky, M. Rey, M. Rotger, S. W. Sharpe, K. Sung, E. Starikova, S. A. Tashkun, J. Vander Auwera, G. Wagner, J. Wilzewski, P. Wcisło, S. Yu and E. J. Zak, *J. Quant. Spectrosc. Radiat. Transf.*, 2017, **203**, 3–69.
- 85 A. Smekal, *Naturwissenschaften*, 1923, 873–875.
- 86 G. Landsberg and L. Mandelstam, *Naturwissenschaften*, 1928, 557–558.
- 87 N. Ahlawat, *J. Comput. Sci. Inf. Technol.*, 2014, **3**, 680–685.
- 88 J. R. Gosz, D. I. Moore, C. N. Dahm and S. Hofstadler, *Environment*, 1990, **32**, 103–110.
- 89 S. Alahmari, X. Kang and M. Hippler, *Anal. Bioanal. Chem.*, 2019, **411**, 3777–3787. <https://doi.org/10.1007/s00216-019-01877-0>.
- 90 H. Nasim and Y. Jamil, *Laser Phys. Lett.*, 2013, **10**, 043001.
- 91 C. E. Wieman and L. Hollberg, *Rev. Sci. Instrum.*, 1991, **62**, 1–20.
- 92 S. D. Saliba, M. Junker, L. D. Turner and R. E. Scholten, *Appl. Opt.*, 2009, **48**, 6692–700.
- 93 L. Ricci, M. Weidemüller, T. Esslinger, V. Vuletic, W. König and T. W. Hansch, *Opt. Commun.*, 1995, **117**, 541–549.
- 94 A. S. Arnold, J. S. Wilson and M. G. Boshier, *Am. Inst. Phys.*, 1998, **69**, 1236.
- 95 H. G. Shiraz, *Distributed Feedback Laser Diodes and Optical Tunable Filters*, Chichester, First., 2003.

- 96 Knowles EK-23024 microphone manual, microphone PA information.pdf.
- 97 O. W. V Richards and F. W. Haynesi, *Plant Physiol*, 1932, 139–144.
- 98 R. Grosz and G. Stephanopoulos, *Biotechnol. Bioeng.*, 1983, **25**, 2149–2163.
- 99 M. L. Siegal, *PLOS Biol.*, 2015, 1–7.
- 100 K. Stevenson, A. F. McVey, I. B. N. Clark, P. S. Swain and T. Pilizota, *Sci. Rep.*, 2016, **6**, 4–10.
- 101 J. A. Myers, B. S. Curtis and W. R. Curtis, *BMC Biophys.*, 2013, **6**, 4.
- 102 J. A. Myers, B. S. Curtis and W. R. Curtis, *BMC Biophys.*, 2013, **6**, 4.
- 103 M. Zwietering, I. Jongenburger, F. M. Rombouts and K. van Riet, *Environ. Microbiol.*, 1990, 56.
- 104 W. F. Loomis and B. Magasanik, *J. Bacteriol.*, 1967, **93**, 1397–1401.
- 105 B. Görke and J. Stülke, *Nat. Rev. Microbiol.*, 2008, **6**, 613–624.
- 106 E. Mostovenko, A. M. Deelder and M. Palmblad, *BMC Microbiol.*, 2011, **11**, 126–131.
- 107 G. Amat and M. Pimbert, *J. Mol. Spectrosc.*, 1965, **16**, 278–290.
- 108 B. G. Hall, H. Acar, A. Nandipati and M. Barlow, *Mol. Biol. Evol.*, 2014, **31**, 232–238.
- 109 www.webbook.nist.gov/chemistry, accessed 16/10/2018.
- 110 P. Pletnev, I. Osterman, P. Sergiev, A. Bogdanov and O. Dontsova, *Acta Naturae*, 2015, **7**, 22–33.
- 111 A. H. England, A. M. Duffin, C. P. Schwartz, J. S. Uejio, D. Prendergast and R. J. Saykally, *Chem. Phys. Lett.*, 2011, **514**, 187–195.
- 112 G. Lal and M. Thomas, *Biochim. Biophys.*, 1972, **21**, 70–76.

Appendix

1. Growth-Limiting Conditions of *E. coli* using CERS

In this section the calculation is shown of O₂ concentration in the growth of *E. coli* in M9 medium supplemented with 20 mM glucose by using CERS. By using the ideal gas law Equation 45 can be calculated, the number of moles of a gas per its partial pressure in 1 mbar in the CERS setup.

$$pV = nRT, \quad \text{Equation 45}$$

where V is the volume of the headspace in the CERS setup, equal to 0.77 L or $7.7 \times 10^{-3} \text{ m}^3$, R is the gas constant, equal to $8.314 \text{ J K}^{-1} \text{ mol}^{-1}$, p is equal to 100 pa (1 mbar) and T is 310 K (37 °C).

$$n = \frac{pV}{RT} = \frac{7.7 \times 10^{-3} \text{ m}^3 \times 100}{8.314 \text{ J K}^{-1} \text{ mol}^{-1} \times 310}$$

$$n(\text{gas in CERS}) = 3.1 \times 10^{-5} \text{ mol mbar}^{-1}$$

$p(\text{O}_2)$ is always at first 210 mbar due to filling the CERS setup with 1 atm of laboratory air. The moles of oxygen in the CERS setup at the start, $n(\text{O}_2)$, can be calculated.

$$n(\text{O}_2) = n(\text{gas in CERS}) \times p(\text{O}_2)$$

$$n(\text{O}_2) = 3.1 \times 10^{-5} \text{ mol mbar}^{-1} \times 210 \text{ mbar}$$

$$n(\text{O}_2) = 6.5 \times 10^{-3} \text{ mol} = 6.5 \text{ mmol}$$

According the Equation 1 for aerobic respiration, there is a 1:6 ratio of glucose to O₂.



Dividing $n(\text{O}_2)$ by 6 gives 1.1 mmol, thus if the number of moles of glucose, $n(\text{glucose})$, is greater than 1.1 mmol, then the growth-limiting factor is O₂. If $n(\text{glucose})$ is less than 1.1 mmol, then the growth-limiting factor is glucose. Equation 46 gives the relationship between $n(\text{glucose})$ and the concentration of glucose $c(\text{glucose})$. To show that 20 mM of supplemented glucose gives O₂ growth-limiting conditions, $n(\text{glucose})$ must be calculated.

$$n(\text{glucose}) = c(\text{glucose})V \quad \text{Equation 46}$$

where V is the volume of the solution, equal to 250 mL or 0.25 L. 20 mM of glucose corresponds therefore to $20 \times 10^{-3} \text{ mol L}^{-1}$.

$$n(\text{glucose}) = 20 \times 10^{-3} \text{ mol L}^{-1} \times 0.25 \text{ L}$$

$$n(\text{glucose}) = 5 \times 10^{-3} \text{ mol} = 5 \text{ mmol}$$

So, since 5 mmol of glucose is larger than 1.1 mmol, O_2 is growth-limiting for 20 mM of supplemented glucose. The $c(\text{glucose})$ below which glucose becomes growth limiting is:

$$c(\text{glucose}) = \frac{n(\text{glucose})}{V}$$

$$c(\text{glucose}) = \frac{1.1 \text{ mmol}}{0.25 \text{ L}} = 4.4 \text{ mM}$$

2. Dissolved O_2 and CO_2 in the Solution

In this section, the amount O_2 and CO_2 which is dissolved in a solution is calculated using Henry's law, given in Equation 47.

$$c = kp, \quad \text{Equation 47}$$

where k is the Henry's law constant. At 37 °C (source NIST webbook)¹⁰⁹

$$k(\text{O}_2) = 1.0 \times 10^{-3} \text{ mol L}^{-1} \text{ bar}^{-1} = 9.9 \times 10^{-7} \text{ mol L}^{-1} \text{ mbar}^{-1}$$

$$k(\text{CO}_2) = 2.5 \times 10^{-2} \text{ mol L}^{-1} \text{ bar}^{-1} = 2.5 \times 10^{-5} \text{ mol L}^{-1} \text{ mbar}^{-1}$$

Using 210 mbar of O_2 at the start of the measurements, $c(\text{O}_2)$ in solution can be calculated as

$$c(\text{O}_2) = k(\text{O}_2) p(\text{O}_2)$$

$$c(\text{O}_2) = 9.9 \times 10^{-7} \text{ mol L}^{-1} \text{ mbar}^{-1} \times 210 \text{ mbar}$$

$$c(\text{O}_2) = 2.1 \times 10^{-4} \text{ mol L}^{-1}$$

As the volume of solution is 0.25 L^{-1} , the moles of dissolved oxygen $n(\text{O}_2)_{\text{aq}}$ are:

$$(\text{O}_2)_{\text{aq}} = 2.1 \times 10^{-4} \text{ mol L}^{-1} \times 0.25 \text{ L}$$

$$n(\text{O}_2)_{\text{aq}} = 5.2 \times 10^{-5} \text{ mol} = 0.05 \text{ mmol}$$

0.05 mmol of dissolved O₂ is negligible compared to the 6.5 mmol of total O₂. Using 105 mbar of CO₂ typically produced by *E. coli* in M9 medium supplemented with 20 mM glucose, $c(\text{CO}_2)$ and $n(\text{CO}_2)_{\text{aq}}$ can be calculated as

$$c(\text{CO}_2) = k (\text{CO}_2) p(\text{CO}_2)$$

$$c(\text{CO}_2) = 2.5 \times 10^{-5} \text{ mol L}^{-1} \text{ mbar}^{-1} \times 105 \text{ mbar}$$

$$c(\text{CO}_2) = 2.6 \times 10^{-3} \text{ mol L}^{-1}$$

$$n(\text{CO}_2)_{\text{aq}} = 2.6 \times 10^{-3} \text{ mol L}^{-1} \times 0.25 \text{ L}$$

$$n(\text{CO}_2)_{\text{aq}} = 6.6 \times 10^{-4} \text{ mol} = 0.65 \text{ mmol}$$

Using n (gas CERS) to calculate the moles of CO₂ gas in the head space:

$$n(\text{CO}_2) = n (\text{gas CERS}) \times p(\text{CO}_2)$$

$$n(\text{CO}_2) = 3.1 \times 10^{-5} \text{ mol mbar}^{-1} \times 105 \text{ mbar}$$

$$n(\text{CO}_2) = 3.3 \times 10^{-3} \text{ mol} = 3.3 \text{ mmol}$$

The total moles of CO₂ in the headspace and solution is 4.0 mmol with 16 % of total CO₂ being dissolved in solution in the CERS experiments.

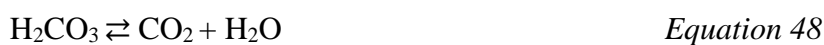
$$n(\text{CO}_2)_{\text{total}} = n(\text{CO}_2)_{\text{g}} + n(\text{CO}_2)_{\text{aq}}$$

$$n(\text{CO}_2)_{\text{total}} = 3.3 \text{ mmol} + 0.65 \text{ mmol}$$

$$n(\text{CO}_2)_{\text{total}} = 4.0 \text{ mmol}$$

3. Carbonate Equilibria

This section shows that the concentration of H₂CO₃ and HCO₃⁻ is negligible in solution compared to the concentration of CO₂ that is dissolved and in the headspace. Equation 48 shows the hydration of CO₂ to H₂CO₃ with the equilibrium constant for the hydration of CO₂, $K_{\text{hyd}}(\text{CO}_2)$, defined in Equation 49.¹¹¹



$$K_{\text{hyd}}(\text{CO}_2) = \frac{c(\text{CO}_2)}{c(\text{H}_2\text{CO}_3)} \quad \text{Equation 49}$$

$K_{hyd}(\text{CO}_2)$ at 37 °C is 340.¹¹² $c(\text{CO}_2)$ was determined to be 2.6 mM when there is 105 mbar of CO_2 in the headspace. 16 % of the total CO_2 which is produced by *E. coli* is dissolved as $c(\text{CO}_2)_{\text{aq}}$. $c(\text{H}_2\text{CO}_3)$ can then be calculated as:

$$c(\text{H}_2\text{CO}_3) = \frac{c(\text{CO}_2)}{K_{hyd}(\text{CO}_2)}$$

$$c(\text{H}_2\text{CO}_3) = \frac{2.6 \text{ mmol L}^{-1}}{340} = 7.6 \times 10^{-3} \text{ mmol L}^{-1} = 7.6 \text{ } \mu\text{M}$$

$c(\text{H}_2\text{CO}_3)$ is therefore negligible compared to $c(\text{CO}_2)$.

The dissociation of H_2CO_3 to HCO_3^- with the equilibrium constant for the dissociation of H_2CO_3 is shown in Equation 50, with $K_{dis}(\text{H}_2\text{CO}_3)$, defined in Equation 51.¹¹²



$$K_{dis}(\text{H}_2\text{CO}_3) = \frac{c(\text{H}^+)c(\text{HCO}_3^-)}{c(\text{H}_2\text{CO}_3)} \quad \text{Equation 51}$$

$K_{dis}(\text{H}_2\text{CO}_3)$ at 37 °C is $8.4 \times 10^{-7} \text{ mol L}^{-1}$.¹¹² The pH of 5.7 can be converted to $c(\text{H}^+)$ using Equation 52.

$$c(\text{H}^+) = 10^{-\text{pH}} \quad \text{Equation 52}$$

$$c(\text{H}^+) = 10^{-5.7}$$

$$c(\text{H}^+) = 2.0 \times 10^{-6} \text{ mol L}^{-1}$$

$c(\text{HCO}_3^-)$ can then be calculated as

$$c(\text{HCO}_3^-) = \frac{K_{dis}(\text{H}_2\text{CO}_3) c(\text{H}_2\text{CO}_3)}{c(\text{H}^+)}$$

$$c(\text{HCO}_3^-) = \frac{8.4 \times 10^{-7} \text{ mol L}^{-1} \times 7.6 \times 10^{-6} \text{ mol L}^{-1}}{2.0 \times 10^{-6} \text{ mol L}^{-1}}$$

$$c(\text{HCO}_3^-) = 3.2 \times 10^{-6} \text{ mol L}^{-1} = 3.2 \text{ } \mu\text{M}$$

$c[\text{HCO}_3^-]$ is therefore negligible compared to $[\text{CO}_2]$ ($3.2 \text{ } \mu\text{M} \ll 2.6 \text{ mM}$).

4. A Noise Equivalent Normalized Absorption Coefficient for CO₂ in PAS

First, we need to get the concentration c from the ideal gas law.

$$c = \frac{N}{V}, \text{ unit cm}^{-3}$$

$$pV = nRT = \frac{N}{N_A} RT \quad \therefore C = \frac{N}{V} = \frac{P}{RT} N_A$$

where p is the pressure in Pa, $R=8.314 \text{ J mol}^{-1}\text{K}^{-1}$, N_A Avogadro's constant

$$C = \frac{P}{R \times T} = \frac{16 \text{ Pa}}{(8.31) \times (298 \text{ K})} \times 6.022 \times 10^{23} = 3.89 \times 10^{22} \text{ m}^{-3}$$

m^{-3} is convert into cm^{-3} by dividing by 10^6

$$C = \frac{3.89 \times 10^{22}}{10^6} = 3.89 \times 10^{15} \text{ cm}^{-3}$$

$$\alpha = \sigma \times C = 7.57 \times 10^{-23} \text{ cm}^2 \times 3.89 \times 10^{15} \text{ cm}^{-3} = 2.94 \times 10^{-7} \text{ cm}^{-1}$$

Normalizing to the absorption cross section, the laser power and integration time, the noise equivalent normalized absorption coefficient is

$$\alpha = 2.94 \times 10^{-7} \text{ cm}^{-1} \times 0.03 \text{ W} \times \sqrt{1} \text{ s} = 8.3 \times 10^{-9} \text{ cm}^{-1} \text{ W s}^{1/2}$$

where σ is the absorption cross section in cm^2 , α the absorption coefficient in cm^{-1} .

5. A Noise Equivalent Normalized Absorption Coefficient for O₂ in PAS

The same method of calculation is used, with different detection pressure, absorption cross section, and laser power corresponding to the O₂ experiment,

$$p = 60 \text{ Pa}$$

$$\sigma = 4.78 \times 10^{-23} \text{ cm}^2$$

$$\text{Power} = 0.035 \text{ W}$$

Normalizing to the absorption cross section, the laser power and integration time, the noise equivalent normalized absorption coefficient for detection of O₂ is found as

$$\alpha = 2.2 \times 10^{-8} \text{ cm}^{-1} \text{ W s}^{1/2}$$

6. Calculating the Detection Limit of O₂ in an Aqueous Solution

600 ppmv of O₂ in the gas phase corresponds to an oxygen concentration of 12 ppb per mole in the solution. By using Henry's law and Henry's constant 1.07×10^{-6} mol/L. mbar at 37 °C we can calculate this value:

$$c(\text{O}_2) = kp$$

$$c(\text{O}_2) = 1.07 \times 10^{-6} \text{ mol/L mbar} \times 0.6 \text{ mbar} = 6.42 \times 10^{-7} \text{ mol/L}$$

Then divide this value by the concentration of pure water

$$= \frac{6.42 \times 10^{-7} \text{ mol/L}}{55 \text{ mol/L}} = 1.17 \times 10^{-8} \cong 12 \text{ ppb}$$

7. Growth-Limiting Conditions of *E coli* Using PAS

By using the ideal gas law in Equation 53, n can be calculated, the number of moles of a gas per its partial pressure in 1 mbar in the PA setup.

$$pV = nRT, \quad \text{Equation 53}$$

where: V is the volume of the headspace in the PA setup equal to 0.510 L or $5.1 \times 10^{-3} \text{ m}^3$, R is the gas constant equal to $8.314 \text{ J K}^{-1} \text{ mol}^{-1}$, p equal to 100 pa (1 mbar) and T is 298 K (25 °C).

$$n = \frac{pV}{RT} = \frac{5.1 \times 10^{-3} \text{ m}^3 \times 100}{8.314 \text{ J K}^{-1} \text{ mol}^{-1} \times 298}$$

$$n(\text{gas in PA}) = 2.05 \times 10^{-5} \text{ mol mbar}^{-1}$$

$p(\text{O}_2)$ is always at first 210 mbar due to filling of the PAS setup with 1 atm of laboratory air. The moles of oxygen in the PAS setup at the start, $n(\text{O}_2)$, can be calculated.

$$n(\text{O}_2) = n(\text{gas in PAS}) \times p(\text{O}_2)$$

$$n(\text{O}_2) = 2.05 \times 10^{-5} \text{ mol mbar}^{-1} \times 210 \text{ mbar}$$

$$n(\text{O}_2) = 4.3 \times 10^{-3} \text{ mol} = 4.3 \text{ mmol}$$

Dividing $n(\text{O}_2)$ by 6 gives 0.7 mmol, thus if the number of moles of glucose, $n(\text{glucose})$, is greater than 0.7 mmol, then the growth-limiting factor is O₂. If $n(\text{glucose})$ is less than 0.7 mmol,

then the growth-limiting factor is glucose. Equation 26 gives the relationship between $n(\text{glucose})$ and concentration of glucose $c(\text{glucose})$.

The $c(\text{glucose})$ below which glucose becomes growth limiting is:

$$c(\text{glucose}) = \frac{n(\text{glucose})}{V}$$

$$c(\text{glucose}) = \frac{0.7 \text{ mmol}}{0.25 \text{ L}} = 2.87 \text{ mM}$$

8. Calculating the amount of Dissolved CO₂ in the Solution When Using PAS System

$$c(\text{CO}_2) = k(\text{CO}_2) p(\text{CO}_2)$$

$$c(\text{CO}_2) = 2.5 \times 10^{-5} \text{ mol L}^{-1} \text{ mbar}^{-1} \times 170 \text{ mbar}$$

$$c(\text{CO}_2) = 4.2 \times 10^{-3} \text{ mol L}^{-1}$$

$$n(\text{CO}_2)_{\text{aq}} = 4.2 \times 10^{-3} \text{ mol L}^{-1} \times 0.25 \text{ L}$$

$$n(\text{CO}_2)_{\text{aq}} = 1.05 \times 10^{-3} \text{ mol} = 1.05 \text{ mmol}$$

Using n (gas PAS) to calculate the moles of CO₂ gas in the head space:

$$n(\text{CO}_2) = n(\text{gas PAS}) \times p(\text{CO}_2)$$

$$n(\text{CO}_2) = 2.05 \times 10^{-5} \text{ mol mbar}^{-1} \times 170 \text{ mbar}$$

$$n(\text{CO}_2) = 3.5 \times 10^{-3} \text{ mol} = 3.5 \text{ mmol}$$

The total moles of CO₂ in the headspace and solution is 4.5 mmol with about 22 % of total CO₂ being dissolved in solution in the PAS experiment.

$$n(\text{CO}_2)_{\text{total}} = n(\text{CO}_2)_{\text{g}} + n(\text{CO}_2)_{\text{aq}}$$

$$n(\text{CO}_2)_{\text{total}} = 3.5 \text{ mmol} + 1.05 \text{ mmol}$$

$$n(\text{CO}_2)_{\text{total}} = 4.5 \text{ mmol}$$

9. The Constant used for the Dissociation of Carbonic Acid H_2CO_3 to the Bicarbonate Ion HCO_3^-

$$\text{H}_2\text{CO}_3: \quad \text{pK}_{\text{a}1} = -\log (4.3 \times 10^{-7}) = 6.37$$

10. The Constant used for the Dissociation of H_2S to HS^-

$$\text{H}_2\text{S} : \quad \text{pK}_{\text{a}1} = -\log (9.5 \times 10^{-8}) = 7.02$$



Diode laser photoacoustic spectroscopy of CO₂, H₂S and O₂ in a differential Helmholtz resonator for trace gas analysis in the biosciences and petrochemistry

Saeed Alahmari¹ · Xiu-Wen Kang¹ · Michael Hippler¹

Received: 1 March 2019 / Revised: 16 April 2019 / Accepted: 26 April 2019 / Published online: 20 May 2019

© The Author(s) 2019

Abstract

Photoacoustic spectroscopy in a differential Helmholtz resonator has been employed with near-IR and red diode lasers for the detection of CO₂, H₂S and O₂ in 1 bar of air/N₂ and natural gas, in static and flow cell measurements. With the red distributed feedback (DFB) diode laser, O₂ can be detected at 764.3 nm with a noise equivalent detection limit of 0.60 mbar (600 ppmv) in 1 bar of air (35-mW laser, 1-s integration), corresponding to a normalised absorption coefficient $\alpha = 2.2 \times 10^{-8} \text{ cm}^{-1} \text{ W s}^{1/2}$. Within the tuning range of the near-IR DFB diode laser (6357–6378 cm⁻¹), CO₂ and H₂S absorption features can be accessed, with a noise equivalent detection limit of 0.160 mbar (160 ppmv) CO₂ in 1 bar N₂ (30-mW laser, 1-s integration), corresponding to a normalised absorption coefficient $\alpha = 8.3 \times 10^{-9} \text{ cm}^{-1} \text{ W s}^{1/2}$. Due to stronger absorptions, the noise equivalent detection limit of H₂S in 1 bar N₂ is 0.022 mbar (22 ppmv) at 1-s integration time. Similar detection limits apply to trace impurities in 1 bar natural gas. Detection limits scale linearly with laser power and with the square root of integration time. At 16-s total measurement time to obtain a spectrum, a noise equivalent detection limit of 40 ppmv CO₂ is obtained after a spectral line fitting procedure, for example. Possible interferences due to weak water and methane absorptions have been discussed and shown to be either negligible or easy to correct. The setup has been used for simultaneous in situ monitoring of O₂, CO₂ and H₂S in the cysteine metabolism of microbes (*E. coli*), and for the analysis of CO₂ and H₂S impurities in natural gas. Due to the inherent signal amplification and noise cancellation, photoacoustic spectroscopy in a differential Helmholtz resonator has a great potential for trace gas analysis, with possible applications including safety monitoring of toxic gases and applications in the biosciences and for natural gas analysis in petrochemistry.

Keywords Gas sensors · IR/Raman spectroscopy · Optical sensors · Bioanalytical · Petrochemistry

Introduction

Trace gas detection is essential in many areas of fundamental and applied research, including environmental monitoring, industrial process control and biological applications. In this context, the detection of CO₂, O₂ and H₂S is particularly relevant. Carbon dioxide (CO₂) is the main anthropogenic greenhouse gas with a current ambient level of 410 ppmv in air. It is also a main product of the metabolism of organisms. The ability of an analytical technique to distinguish isotopes will allow isotope labelling experiments to determine sources and

sinks of CO₂. In the urea breath test for *Helicobacter pylori* (*H. pylori*), for example, patients swallow ¹³C-labelled urea. ¹³CO₂ detected in the exhaled breath indicates *H. pylori* infection in the stomach, since only this bacterium can digest urea efficiently to release ammonia and carbon dioxide. CO₂ detection is particularly relevant to study the metabolism and activity of bacteria. Monitoring of molecular oxygen (O₂) complements such metabolism studies. O₂ detection is also very relevant in biotechnology, for example to ensure that there is no oxygen in a bioreactor in anaerobic fermentation processes. Hydrogen sulfide (H₂S) is a very toxic gas which is comparable in toxicity with carbon monoxide [1–3]. It has an immediately dangerous to life or health (IDLH) limit of 100 ppmv in air. It is therefore important to be able to monitor H₂S with great sensitivity and selectivity as a toxic industrial and environmental compound. This is particularly relevant in petrochemistry since H₂S is a common minor component in

✉ Michael Hippler
M.Hippler@sheffield.ac.uk

¹ Department of Chemistry, University of Sheffield, Sheffield S3 7HF, UK

natural gas, but due to its high toxicity, it has been removed at source before the gas can be fed to gas supply lines [2–4]. H₂S is also relevant in biochemistry and microbiology, with an important role as a signalling molecule as well as a cytoprotectant [5–7]. It has been recently reported that H₂S helps defend a number of bacteria against antibiotics, including *Escherichia coli* (*E. coli*) [7]. Understanding the mechanisms of its production by microbes may therefore be very relevant to develop new strategies to protect and enhance the potency of existing antibiotics. Although bacteria are known to produce the gas during the metabolism of sulfur compounds, the biochemistry associated with these processes is not fully understood. In many organisms, H₂S is generated during degradation of the sulfur-containing amino acid L-cysteine. Cysteine desulphhydrases are enzymes which convert cysteine to pyruvate, a source of energy and a key intermediate in the production of ATP. This process releases one equivalent of ammonia and hydrogen sulfide [7, 8]. In microbiology, a common test for H₂S is the lead acetate or the methylene blue assay; although very sensitive, these assays can be difficult to apply for quantitative measurements and may suffer from interferences. Common analytical techniques include gas chromatography (GC) or mass spectrometry (MS); whilst sensitive and selective, they require expensive equipment and have limitations, including difficulties detecting certain components, long analysis times for GC, and the need for sample preparation which prevents real-time, in situ monitoring. Solid-state electrochemical and chemisorbing sensors, where a change in physical properties on adsorption of analyte gas molecules is detected, or acoustic sensors which measure changes in acoustic properties of gas mixtures are also widely used [9, 10]; although detection limits in the ppm range can be achieved, these sensors often suffer from several disadvantages. Chemisorbing sensors, for example, are often affected by ageing and poisoning of the sensor surfaces, from long response and settlement times, and from interferences due to limited selectivity. Acoustic sensors have a response that depends on temperature, and the method lacks selectivity.

In trace gas analysis, spectroscopic detection has distinct advantages due to its quantitative nature and its sensitivity and selectivity due to the very characteristic spectroscopic signature of different molecules. Detection by optical absorption is possible for CO₂ and H₂S using strong fundamental vibrational bands in the mid-IR, or much weaker overtones and combination bands in the near-IR. Although weaker, near-IR absorption offers the advantages of much more convenient optics and light sources in the near-IR. Molecular oxygen (O₂) does not have an IR-active vibration; although Raman detection of its fundamental is possible, Raman scattering is a rather weak process and special Raman enhancement techniques are required to detect gases at the ppmv level, for example by stimulated Raman photoacoustic spectroscopy (PARS) [11] or the recently introduced technique of cavity-enhanced

Raman spectroscopy (CERS) [4, 12–14]. O₂ can be detected by a formally forbidden electronic absorption band in the red, the $b^1\Sigma_g^+ (\nu=0) \leftarrow X^3\Sigma_g^- (\nu=0)$ band (the “A band”) near 760 nm; although weak, the absorption cross sections are comparable to near-IR overtone and combination band absorptions of CO₂ and H₂S. For efficient detection beyond the limitations of conventional, Beer-Lambert-type absorption, absorption pathlengths should be as long as possible, as in the extreme case of cavity ringdown spectroscopy which achieves kilometre effective pathlengths [15–19], or detection should be coupled with a background-free scheme as in photoacoustic spectroscopy [20–27], or a combination of both as in the recently introduced technique of cavity-enhanced resonant photoacoustic spectroscopy (CERPAS) [28, 29]. In photoacoustic spectroscopy, internal excitation of molecules by optical absorption is converted to heat release and pressure increase by collisions; if the excitations are modulated periodically, acoustic waves are induced which can be picked up by microphones. This allows indirect, but very sensitive detection of optical absorption. By detecting in an acoustic resonator and modulating optical excitation at an acoustic resonance frequency, building up of acoustic standing waves further increases sensitivity in resonant photoacoustic spectroscopy [20, 21]. Highest sensitivities are achieved with CERPAS [28, 29] or utilising the excitation of the acoustic modes of a quartz tuning fork (quartz-enhanced or cantilever-enhanced photoacoustic spectroscopy) [26, 27]. A much simpler approach is employing a special acoustic resonator which effectively amplifies signal and reduces noise in a differential Helmholtz resonator (DHR) [22–25].

In this contribution, we report photoacoustic trace gas monitoring in a differential Helmholtz resonator. Photoacoustic detection is one of the most sensitive optical absorption techniques, but it suffers from ambient acoustic noise and flow noise introduced by sampling gases; this ultimately limits detection limits. A DHR has the advantage that the symmetrical resonator composed of two identical chambers produces photoacoustic absorption signals which are out-of-phase in the two chambers, whereas noise including flow noise is in phase in the two chambers. Differential detection therefore doubles the signal and cancels noise to a great extent. DHR photoacoustic spectroscopy has been reported before for methane detection [23]; however, the power of the specific configuration and the underlying principles are not fully appreciated in our opinion. Herein, we demonstrate the capabilities of the technique with three different new and relevant target analytes, trace gas detection of CO₂ and H₂S in a DHR with distributed feedback (DFB) diode lasers near 1.6 μm , and O₂ detection near 760 nm. Improvements on the DHR technique are reported, including a multipass arrangement and using two independent lasers. We also introduce novel applications of DHR detection in the biosciences and in petrochemistry, including time-dependent monitoring of the bacterial growth

and aerobic metabolism of microbes, and detection of H₂S and CO₂ impurities in natural gas.

Experimental

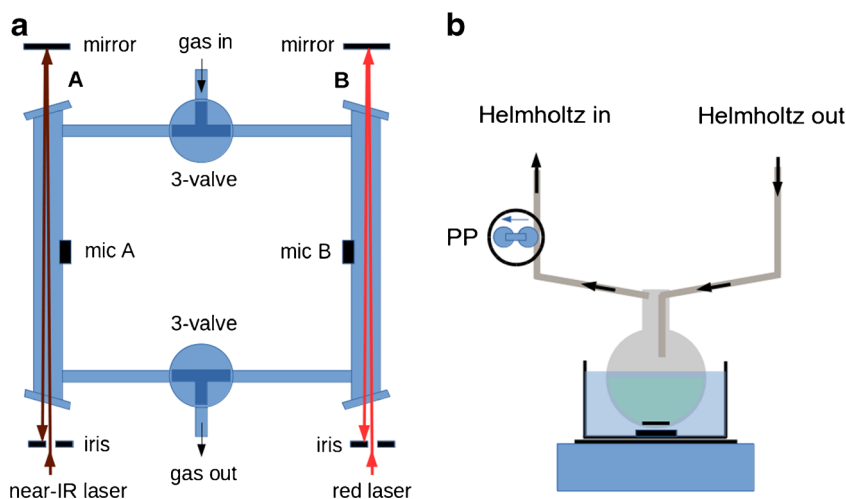
The differential Helmholtz resonator in the present experiment consists of two parts which are made as symmetrical as possible (see Fig. 1a). It follows a design recently published in ref. [23]. It has two identical cylindrical compartments (A and B in Fig. 1a) made of glass, 10 cm long and 1 cm inner diameter (i.d.). The compartments are connected by two capillary glass tubes, 10 cm long and 0.2 cm i.d. Each compartment has in the middle one electret microphone (Knowles EK-23024) attached to it from the outside, but open to the inside. The compartments have glass windows at their end to allow laser light passing through; the windows are slightly tilted to avoid back reflections into the laser. The thin connecting tubes have each a three-way valve in the middle which allows either to separate the Helmholtz resonator for static measurements, or to have a symmetrical gas flow through both compartments in a flow cell configuration. The entire cell is wrapped in heating wire and thermal insulation to keep it at around 45 °C, to avoid water condensation in biological experiments. Diode laser light passes through one of the compartments, e.g. A in Fig. 1a, and is reflected back once at a slight angle to double the interaction path length. An iris acts as a backstop for the reflected beam. Whereas for an organ pipe resonator the laser beam would have to be focussed into the middle of the resonator to enhance the longitudinal acoustic mode, focussing is not required for this DHR resonator since the acoustic mode extends over the entire compartment (see below). This has the advantage that no refocussing is required, and a simple mirror is enough to double the interaction beam path; we have confirmed that this simple arrangement indeed increases photoacoustic signal by about a factor of 2.

After the laser light is absorbed by molecules inside compartment A, collisional deactivation leads to a temperature jump and pressure expansion (photoacoustic effect). This pressure buildup will then travel to compartment B via the connecting capillaries. If the laser light is pulsed, the pressure buildup will travel from A to B, leaving a pressure depression behind in A, and then back again to A when the laser is off, leaving a pressure depression behind in B. If the laser is modulated periodically, periodic pressure waves (sound) are thus created in A and B, which have the same frequency and amplitude, but opposing phases. If the laser modulation matches a resonance frequency of the cell, a standing wave develops with maximum amplitude (resonant photoacoustics). Note that the acoustic resonance is a pressure oscillation between A and B, not a longitudinal acoustic resonance as in the more commonly used organ pipe photoacoustic resonators. The resonance frequency is given by the cell dimensions, and it depends also linearly on the speed of sound c , which for an ideal gas is given by Eq. 1,

$$c = \sqrt{\frac{\gamma RT}{M}}, \quad (1)$$

where T is the temperature, R the gas constant, and γ and M the heat capacity ratio and the molar mass of the medium inside the resonator, respectively. Using a CO₂ absorption line in the near-IR, we obtained a resonance curve (amplitude vs. acoustic frequency). The data are well described by a Lorentzian distribution with resonance frequency $f = 220$ Hz for 1 bar CO₂. In an atmosphere of air or N₂, f increases to 261 Hz, and in natural gas (essentially CH₄) up to 320 Hz, consistent with the changes in molar masses. The quality factor Q is defined as the ratio between the resonance frequency f and the frequency bandwidth at $1/\sqrt{2}$ of the maximum of the resonant profile. For our DHR, $Q \approx 7$ is determined. Q is roughly equivalent to the signal enhancement by the acoustic

Fig. 1 Scheme of the experimental setup. **a** Differential Helmholtz resonator with the two laser beams (see main text for more details). **b** In biological experiments, the head space of a round-bottom flask in a thermostated water bath is circulated to the Helmholtz resonator via a peristaltic pump (PP)



resonance. Due to the changes in resonance frequency with temperature and medium, a calibration is strictly valid only for a given temperature and gas composition. However, due to the relatively low Q factor, slight misalignment of the resonance frequency does not have a large effect on signals. The change in composition from trace gas levels to higher levels will cause a slight curvature of the calibration instead of linearity; this is considered by using a calibration curve instead of a calibration line (see also discussion below). Note that the selectivity of photoacoustic detection is from the spectroscopic signature of gases within a composition, and not from the change in acoustic properties.

Characteristic features of a DHR are its low resonance frequency and effective noise cancellation and signal enhancement by differential amplification of microphone signals A–B. Genuine absorption signals inside the cell are out-of-phase between microphones A and B; differential amplification A–B therefore doubles the signal (see Fig. 2a). External noise and flow noise, however, will affect the two symmetrical compartments in nearly the same way, creating a noise signal which is in phase in A and B. In this case, differential amplification A–B leads to effective cancellation of noise (see Fig. 2b). This noise cancellation and signal enhancement make DHR an attractive choice for trace gas detection applications. The differential signals (A–B) are processed in lock-in amplifiers which further greatly reduce noise.

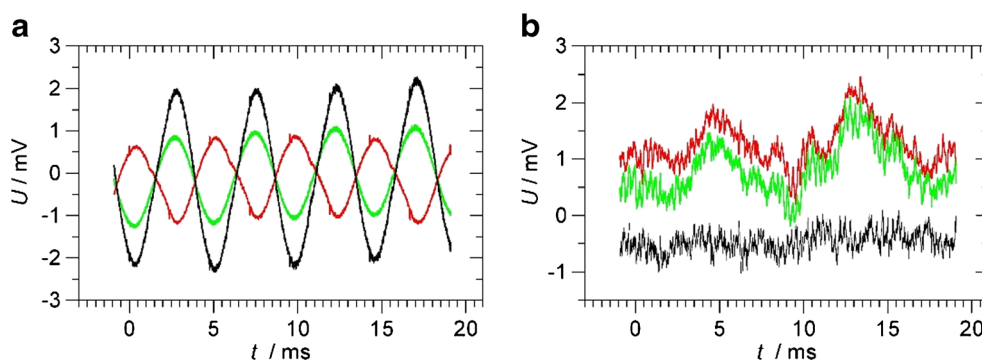
In our setup, two DFB diode lasers are used, i.e. a near-IR laser to detect CO_2 and H_2S near $1.57 \mu\text{m}$ and a red laser near 764 nm to detect O_2 . To simplify the setup, the near-IR laser is directed through one compartment (A), whilst the red laser is directed through the other (B) (see Fig. 1a). In a typical experiment, CO_2 and H_2S are first measured by scanning the near-IR laser; next, O_2 is measured by scanning the red laser. Note that during a scan with one laser, only this laser is on whilst the other is switched off. Both lasers are modulated by their injection current at the acoustic resonance frequency with a square wave giving a 50% duty cycle. The near-IR single-mode DFB diode (Mitsubishi FU-650SDF, 4 mW) is amplified in a booster optical amplifier (Thorlabs S9FC1004P) to 30 mW peak power. The laser is temperature tuneable

between 20 and $60 \text{ }^\circ\text{C}$ to provide a mode-hop-free tuning range from 6378 to 6357 cm^{-1} or from 1.568 to $1.573 \mu\text{m}$. The red laser is a temperature tuneable 35-mW DFB diode laser (Eagleyard EYP-DFB-0764); adjusting the temperature from 18 to $40 \text{ }^\circ\text{C}$ gives a 764.0 – 765.3 -nm mode-hop-free tuning range.

For bacterial measurements, 50 ml of sterile 2YT medium (a rich medium containing yeast extract and tryptone) was inoculated with a single colony of *E. coli* (wild type, strain K-12 MG1655) and incubated for 5 h at $37 \text{ }^\circ\text{C}$. It was added to 50 ml of sterile 2YT to give a 100-ml suspension in a 500-ml round-bottom flask with constant stirring at $37 \text{ }^\circ\text{C}$ in a thermostated water bath. The flask was connected to the DHR resonator with short gas transfer tubes in a closed system, giving a total gas volume of 660 ml. To enhance gas flow, a peristaltic pump (3 l/h) was used to cycle the flask head space through the DHR resonator (see Fig. 1b). In a test to characterise the experimental time resolution, CO_2 or H_2S gas was injected into the flask and the appearance time of the gas was measured in the Helmholtz resonator; equilibrium is reached within about 5 min. To observe O_2 , CO_2 and H_2S in the aerobic respiration of *E. coli*, a cysteine solution (L-cysteine hydrochloride anhydrous, Sigma) dissolved in 7 ml of water is injected via a septum (Suba-Seal) as a source of sulfur to induce the production of H_2S . At the beginning of an experiment, the suspension has typically $\text{OD}_{600} \approx 0.6$ (optical density at 600 nm in a 1-cm cuvette) and a pH of 6.9; at the end, after exhaustion of the oxygen available, the suspension has typically $\text{OD}_{600} \approx 2.2$ and a pH of 7.2.

Calibrated gas mixtures containing CO_2 (sublimed from dry ice) or H_2S (Sigma-Aldrich, 99.5+%) were prepared on a glass vacuum line equipped with capacitance pressure gauges (Baratron). The gases were purified by repeated freeze-pump-thaw cycles and buffered to 1 bar total pressure by N_2 , natural gas or air. Natural gas was sampled from a gas tap within the PC teaching laboratory of the University (gas supplied via National Grid, UK); natural gas is essentially CH_4 with some additional minor components (see ref. [4] for typical compositions).

Fig. 2 Oscilloscope traces of the signal from microphone A (green) and microphone B (red) and the differential signal A–B (black). **a** Signal enhancement (CO_2 absorption near $1.57 \mu\text{m}$). **b** Noise cancellation (flow noise in a flow cell configuration) (see main text for more detail)



Results and discussion

Photoacoustic detection of molecular oxygen near 764 nm

Molecular oxygen (O₂) does not have an IR-active vibration, but it can be detected by an electronic absorption band in the red, the $b^1\Sigma_g^+ (\nu=0) \leftarrow X^3\Sigma_g^- (\nu=0)$ band of molecular oxygen (the “A band”) near 760 nm. It is a very weak, formally forbidden transition with absorption cross sections of the same order as the near-IR combination bands of CO₂ and H₂S near 1.57 μm discussed later. Some of the strongest rotational lines of the A band are within the range of our DFB diode laser. Figure 3 shows the photoacoustic spectrum of 1 bar air obtained in the Helmholtz resonator, by temperature tuning the laser from 24 to 38 °C. A good agreement with literature data (HITRAN) is obtained [30]. The strongest line is used for the analysis of O₂; it is marked by an asterisk in Fig. 3. The transition is the $P(11)$ line at 764.280 nm (vacuum) which has a peak absorption cross section of $\sigma_{\text{peak}} = 0.00478 \text{ pm}^2$ (1 bar pressure broadened) [30].

At an abundance of 210 mbar in 1 bar air, the peak photoacoustic signal of this line is 310 mV. The standard deviation (σ) of the baseline, 0.88 mV at 1-s integration time, can serve as an estimate of the noise level. A noise equivalent detection

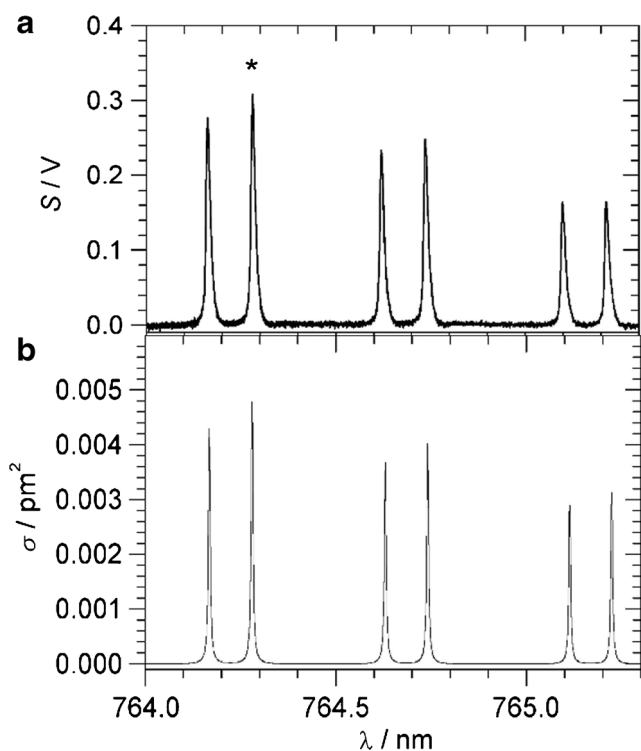


Fig. 3 **a** Photoacoustic spectrum of 1 bar air in the Helmholtz resonator, obtained by temperature tuning the laser from 24 to 38 °C. The peak marked by the asterisk is used for the detection of molecular oxygen. **b** HITRAN absorption cross sections (1 bar air pressure broadening) of O₂ in the A band [30]

limit of 0.60 mbar (600 ppmv) or 0.06% of O₂ in 1 bar of air at 35-mW peak power and 1-s integration time is thus obtained. Note that this is the *noise equivalent* detection limit (1 σ limit); practical detection limits are often quoted as 3 σ in the literature. Since photoacoustic signal scales linearly with laser power and statistical noise decreases with the square root of integration time (see also below), improved detection limits are achieved with higher laser power and longer integration times. Normalising to the absorption cross section, the laser power and integration time, a noise equivalent *normalised* absorption coefficient $\alpha = 2.2 \times 10^{-8} \text{ cm}^{-1} \text{ W s}^{1/2}$ is calculated. Considering the simplicity of the DHR setup, this compares favourably with the detection limits of more complex photoacoustic schemes, such as quartz–cantilever-enhanced photoacoustic spectroscopy where $\alpha = 4.8 \times 10^{-9} \text{ cm}^{-1} \text{ W s}^{1/2}$ was reported for photoacoustic detection of oxygen by a 30-mW DFB diode near 760 nm [26]. In an application where the head space above an aqueous solution is measured (as in the bacterial suspensions at 37 °C, see “Monitoring O₂, CO₂ and H₂S during the metabolism of L-cysteine by E. coli”), 600 ppmv of O₂ in the gas phase corresponds to an oxygen concentration of 12 ppb per mole in the solution, using Henry’s law and Henry’s constant at 37 °C [31].

Photoacoustic detection of H₂S and CO₂ in air/N₂ near 1.57 μm

In this section, we aim for the detection of CO₂ and H₂S in air or N₂. Within the tuning range of the near-IR DFB diode laser (6357–6378 cm^{-1}), CO₂ and H₂S absorption features can be accessed which can be used for trace gas detection. Figure 4 provides an overview from the HITRAN database including the effect of 1 bar air broadening [30]. CO₂ shows part of the R -branch of the $3\nu_1$ overtone, with a characteristic nuclear spin statistic which only allows transitions from even J . The strongest line (labelled A in Fig. 4) is the $R(18)$ line at

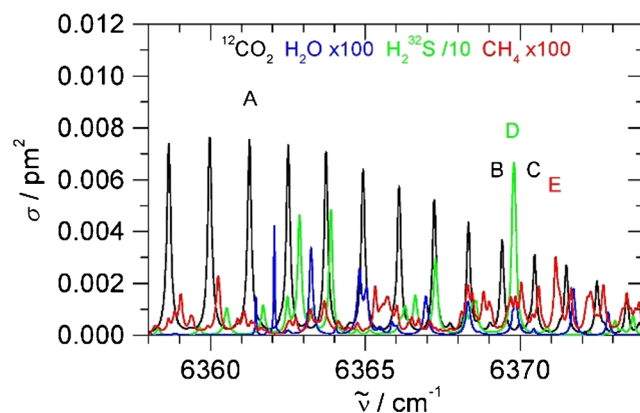


Fig. 4 HITRAN absorption cross sections (1 bar air pressure broadening) of CO₂ (black), H₂S (green, scaled $\times 0.1$), water vapour (blue, scaled $\times 100$) and methane CH₄ (red, scaled $\times 100$) [30]. Lines A to C are CO₂ peaks, D is a H₂S peak and E is a CH₄ peak discussed in the main text

6361.250 cm^{-1} with peak absorption cross section $\sigma_{\text{peak}} = 0.00757 \text{ pm}^2$ (1 bar air pressure broadened) and Lorentzian line shape [30]. This line was used for CO_2 detection. H_2S has unresolved or partially resolved features in the region. The strongest is a feature at 6369.8 cm^{-1} of the $\nu_1\nu_2\nu_3$ combination band (labelled **D** in Fig. 4). This feature was employed for H_2S detection. Its peak absorption cross section is $\sigma_{\text{peak}} = 0.0665 \text{ pm}^2$ (1 bar air pressure broadened), about nine times stronger than the CO_2 line [30]. Figure 4 also displays water absorptions to assess whether water will interfere with CO_2 or H_2S detection. Water quite often interferes very severely in “real-life” applications, in particular in the region of mid-IR fundamental vibrations. Fortunately, the absorption features of water are very weak in this near-IR region, with absorption cross sections below $4 \times 10^{-5} \text{ pm}^2$ [30]. The peaks chosen are well isolated with negligible interference in air (natural gas is discussed separately below). To demonstrate the sensitivity of the DHR scheme, ambient air from the outside was measured (see Fig. 5). At 1-s integration time of each data point, the $R(18)$ line due to CO_2 at natural abundance (410 ppmv) can clearly be distinguished.

In order to characterise the system, calibrated gas mixtures of CO_2 in 1 bar N_2 were prepared and the $R(18)$ line was measured by DHR photoacoustics. The amplitude of the peak vs. CO_2 partial pressure is shown in the calibration plot of Fig. 6a. Good linearity is obtained (black fit line; $y = ax$), although a slightly better fit is obtained by a non-linear fit to $y = ax^b$ (red fit line) with $b = 1.04$. However, the deviation from linearity is not very pronounced. The deviation from linearity is probably caused by the change in the physical properties (e.g. speed of sound) in the mixture, from 200 mbar CO_2 in 1 bar N_2 , to essentially just traces of CO_2 in 1 bar N_2 . At 1-s integration time, the standard deviation of the baseline is about 0.98 mV with the laser still on; this level is indicated by the horizontal, dotted line. It represents the noise

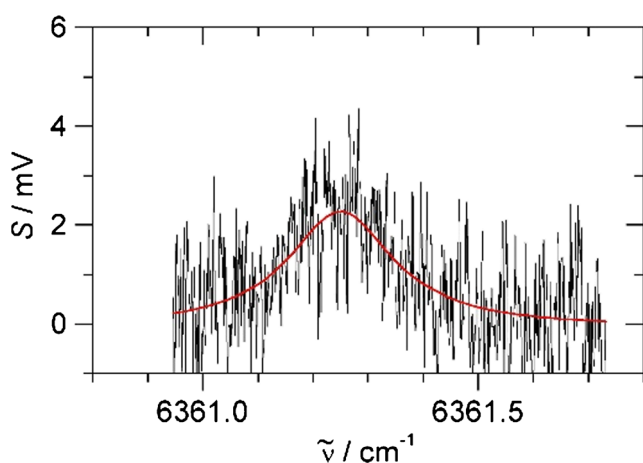


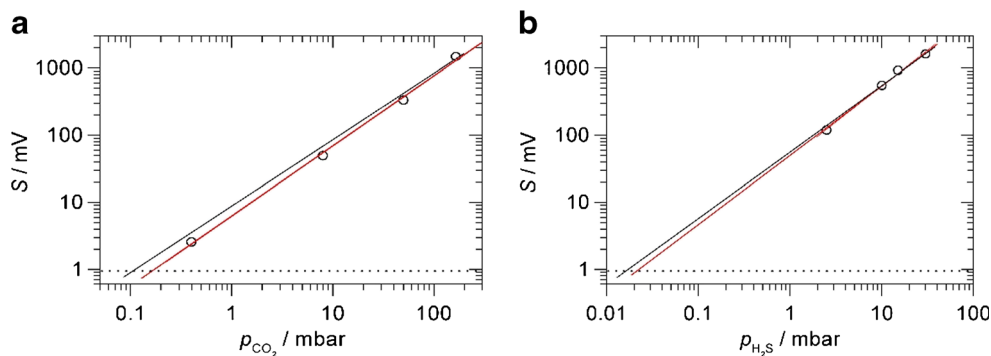
Fig. 5 Photoacoustic spectrum of CO_2 at natural abundance in 1 bar of ambient air. Red: Lorentzian line fit

floor at 1-s integration time. The non-linear red fit line hits the noise level at 0.160 mbar or 160 ppmv CO_2 in 1 bar N_2 , giving the noise equivalent detection limit at 1-s integration time with the 30-mW laser. Normalising to absorption cross section, laser power and integration time, a noise equivalent normalised absorption coefficient $\alpha = 8.3 \times 10^{-9} \text{ cm}^{-1} \text{ W s}^{1/2}$ is calculated. Again, considering the simplicity of the DHR setup, this compares favourably with more involved photoacoustic schemes, such as the quartz–cantilever-enhanced photoacoustic detection reported with $\alpha = 2.2 \times 10^{-9} \text{ cm}^{-1} \text{ W s}^{1/2}$ at 1572 nm [27].

Better detection limits are obtained by longer integration times or by fitting spectral line shapes to several data points in a spectrum. This is demonstrated in Fig. 5, for example, where 410 ppmv of CO_2 in ambient air is clearly detectable despite a noise equivalent limit of 160 ppmv. A spectral line fit of a spectral scan is preferable to having a longer integration time on a single point, because the fit also gives the baseline/background value above which the signal is measured. Following a procedure described in ref. [11], if measurements are made in a reproducible way, there is an a priori knowledge about the expected peak position and the expected line width of the peak. In a Lorentzian line fit of spectral data, the line position and full width at half maximum (FWHM) can be kept fixed based on values obtained in measurements at higher concentration. The only free parameters of the fit are the offset and the peak height. The fitting is insensitive to slow variation of the baseline, removing the need for data manipulation. This restricted spectral fitting procedure greatly increases sensitivity and selectivity and removes the arbitrariness of baseline manipulations [11]. Using 16 data points spread around the central $R(18)$ line within a range of 3 Lorentzian FWHM gives a good representation of the spectral peak to be analysed. Sixteen data points at 1-s integration time require a total measurement time of 16 s. The restricted fit of the gas mixtures used for the calibration line gives peak heights as in Fig. 6a). Repeated restricted fits of a gas mixture without CO_2 (essentially a flat baseline with noise) give small positive and negative peak heights with a standard deviation (noise level) of 0.24 mV. The approximately fourfold improvement on the 0.98-mV noise level at 1-s integration agrees with the expectation that statistical noise decreases with the square root of integration time. The red, non-linear calibration of Fig. 6a) hits the 0.24-mV noise floor at 0.040 mbar CO_2 in 1 bar N_2 , giving a 40 ppmv noise equivalent detection limit at 16-s measurement time.

In a similar calibration for H_2S detection observing the 6369.8- cm^{-1} feature in 1 bar N_2 , the calibration in Fig. 6b) is obtained. The red fit curve shows again a slight non-linearity with $b = 1.06$. With the same noise limit of 0.98 mV at 1-s integration time, a noise equivalent

Fig. 6 Calibration plots. Black: linear fit through origin, $y = a x$. Red: non-linear fit, $y = a x^b$. Horizontal, dotted line: noise floor at 1-s integration time. **a** Observing the 6361.250-cm⁻¹ R(18) line of CO₂ in 1 bar N₂. **b** Observing the 6369.8-cm⁻¹ feature of H₂S in 1 bar N₂ (see main text for more detail)



detection limit of 0.022 mbar or 22 ppmv in 1 bar N₂ is obtained with the 30-mW laser. The much lower detection limit compared to CO₂ is due to the stronger absorption cross section of H₂S. The detection limit is below the immediately dangerous to life or health (IDLH) limit of 100 ppmv; the DHR sensor may therefore be useful as a safety monitor for toxic levels of H₂S, in particular if additional integration time or spectral line fitting procedures improve the detection limit (see above). At the same position of H₂S peak **D**, there is also a very weak water peak with $\sigma_{\text{peak}} = 1.5 \times 10^{-5} \text{ pm}^2$ [30], about 5000 times weaker than H₂S. Assuming a similar sensitivity of photoacoustic signals, the noise limit will be exceeded only at water vapour pressures above 100 mbar, so this will not be a serious interference at ambient temperatures and water vapour pressures. In an application where the head space above an aqueous solution is measured (see next section), 160 ppmv of CO₂ in the gas phase corresponds to a CO₂ concentration of 76 ppb per mole in the solution, and 22 ppmv of H₂S gas corresponds to 27 ppb in solution, using Henry's law and Henry's constants at 37 °C [31].

In previous work using mid-IR quantum cascade lasers (QCL), sub-ppm detection limits have been reported for IR-active molecules including H₂S, in particular when combined with special techniques like frequency modulation (FM) absorption spectroscopy [32, 33]. In a possible extension, mid-IR QCLs could also be used in the DHR scheme to detect IR-active molecules via the stronger fundamental vibrational bands; based on our normalised absorption coefficients, sub-ppm detection limits are then comfortably predicted. The distinct advantages of our approach using near-IR laser and a photoacoustic scheme, however, are (i) convenience and lower costs; near-IR laser sources and detectors are in general much less than one tenth of the costs of a comparable QCL system; (ii) water interferences are much more of a concern in the mid-IR; and (iii) unlike photoacoustic spectroscopy, FM spectroscopy requires reduced pressure to work efficiently to minimise pressure broadening; this is a big disadvantage in the analysis of natural gas, for example, where gas lines are usually at atmospheric or higher pressures.

Monitoring O₂, CO₂ and H₂S during the metabolism of L-cysteine by *E. coli*

In a demonstration of an application in the biosciences, we monitored O₂, CO₂ and H₂S during the metabolism of L-cysteine by *E. coli*. During aerobic metabolism, microbes convert O₂ and sugars or other suitable organic substrates to CO₂, with typically one unit of CO₂ produced per unit O₂ consumed. In addition, if L-cysteine is present, they may produce H₂S, with approximately one unit of H₂S produced per unit of cysteine consumed. In our closed system, O₂, CO₂ and H₂S are mostly in the gas phase, with some minor amount dissolved in the suspension. The total amount in the gas phase can be calculated by the ideal gas law. At equilibrium, the molarity of a dissolved gas can be calculated from its partial pressure using Henry's law. One millibar of an ideal gas corresponds to $2.6 \times 10^{-5} \text{ mol}$ in the head space (660 ml). Using Henry's constants at 37 °C [31], 1 mbar corresponds to $2.6 \times 10^{-6} \text{ mol CO}_2$, $6.6 \times 10^{-6} \text{ mol H}_2\text{S}$ or $1.1 \times 10^{-7} \text{ mol O}_2$ in the solution (100 ml). Some small amount of dissolved CO₂ (less than 1%) will react to form carbonic acid H₂CO₃. With a $\text{pK}_{\text{a}1} = 6.37$, about 90% of this carbonic acid will dissociate to the bicarbonate ion HCO₃⁻ at the pH range of the bacterial suspension (6.9–7.2). Since only about 10% of the total CO₂ is in solution, of which only a small amount will be converted into carbonic acid, this loss of CO₂ can be neglected to a first approximation. Being an acid, dissolved H₂S can dissociate into HS⁻; with a $\text{pK}_{\text{a}1} = 7.02$, about half of dissolved H₂S will dissociate at the pH range of the suspension. With about 25% of total H₂S being in solution, of which about 50% is lost in the form of HS⁻, this effect needs to be considered for the total sulfur balance arising from the conversion of cysteine.

In the experiment, we monitored O₂ with the red diode and converted the photoacoustic signal into millibar using the previous calibration. For simultaneous monitoring of CO₂ and H₂S, we used the near-IR diode scanning between 6369 and 6371 cm⁻¹. In this range, the CO₂ peaks labelled **B** and **C** can be found, and in-between, the strong H₂S peak labelled **D**. Figure 7 shows a typical scan of the head space above the bacterial suspension. Fitting three Lorentzian curves to the observed peaks **B**, **C** and **D** and using the previous calibration,

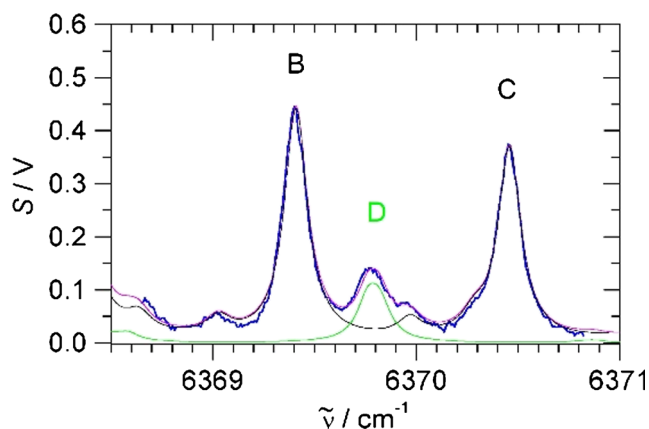


Fig. 7 Typical scan of the head space above a bacterial suspension (2 h after injecting 1 mM cysteine, see Fig. 8). The blue trace is the photoacoustic signal. In black, green and magenta are HITRAN data for 98 mbar CO₂, 2.2 mbar H₂S and the sum, respectively. The peak labels are as in Fig. 4

photoacoustic signal is converted into millibar of H₂S and CO₂. Measurements were repeated every 15 min to obtain time-dependent concentrations of the head space.

Figure 8 shows a typical example of time-dependent concentrations, where 1 mM cysteine was injected into the *E. coli* suspension in 2YT medium after a delay of about 1 h. Before injection, no traces of H₂S are apparent. Due to aerobic respiration of *E. coli*, O₂ is slowly decaying and CO₂ formed in an

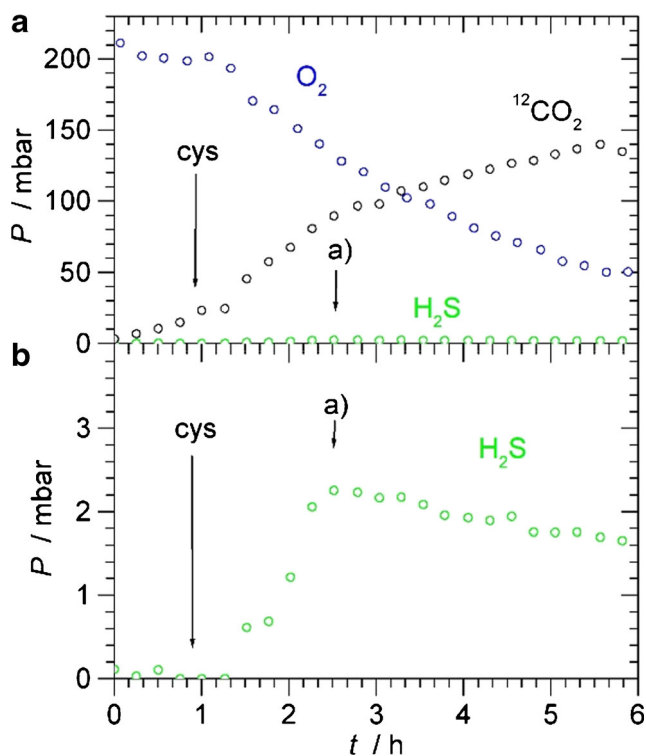


Fig. 8 **a, b** Time-dependent concentrations of O₂, CO₂ and H₂S in the head space during the metabolism of 1 mM L-cysteine by *E. coli* in 100 ml 2YT. **b** has an expanded pressure scale to show the H₂S partial pressure more clearly. “cys” denotes the time of injection of the cysteine

about 1:1 ratio, as expected. After injection of cysteine (labelled “cys” in Fig. 8), metabolism accelerates, and H₂S is formed after a short lag phase of about 20 min. Within 1 h, H₂S peaks to about 2.2 mbar. Apparently, all cysteine is converted by then, and H₂S concentrations fall very slowly afterwards. The 2.2 mbar H₂S corresponds to about 0.09 mmol in the head space and suspension. This is almost exactly the amount of cysteine injected, demonstrating complete conversion of cysteine within 1 h. The slow decay of H₂S is genuine and not due to leaks, since we do not observe decays for CO₂. H₂S is known to stick to surfaces and is easily adsorbed which may explain the decaying pressure. Experiments were repeated several times, including utilising different concentrations of cysteine (1–4 mM). In all cases, the same qualitative behaviour was observed, with complete conversion of cysteine into H₂S occurring within about 1 h. In a control experiment, we injected cysteine into sterile 2YT medium without observing any H₂S evolving, proving that the H₂S production is due to microbial activity. The current application demonstrates in situ monitoring of trace gases in the head space above bacterial suspensions in a closed system by Helmholtz photoacoustic detection. In future work, this method can be employed to study H₂S production by microbes and how it is affected and modulated by different media, feed stock and gene expressions, and its role as signalling molecule and in the defence against antibiotics.

Detection of H₂S and CO₂ impurities in natural gas samples

Trace gas analysis of natural gas is a very relevant task in petrochemistry. Natural gas is mainly methane, but depending on the source or provenance, it may also contain minor components like higher alkanes, components of no caloric value such as N₂ and CO₂ and even toxic compounds like H₂S. “Sour” gas streams contain particularly high levels of CO₂ and H₂S which present a danger to equipment and pipelines and to human health. Due to its high toxicity, H₂S detection is of special concern and it must be removed from the gas stream before the gas can be utilised. To demonstrate the capability of our scheme for trace gas detection of H₂S and CO₂ impurities in natural gas samples, we have sampled natural gas from a gas tap within the Department and scanned the near-IR photoacoustic spectrum between 6369 and 6372 cm⁻¹. In this region, there are CO₂ transitions (peaks labelled **B** and **C** in Figs. 4 and 7) and a separated H₂S transition (labelled **D**). In 1 bar of natural gas, the acoustic resonance frequency shifts to about 320 Hz, and the molecules have also slightly different phase shifts compared to 1 bar air or N₂. We have verified that after optimization, essentially the same calibration, noise levels and detection limits as shown above for N₂ apply, in particular a 25 ppmv noise equivalent detection limit for H₂S in 1 bar natural gas at 1-s integration time.

Figure 9a) shows a scan of 1 bar natural gas; in the spectral region, there are weak CO₂ transitions due to natural CO₂ impurities (B and C in Fig. 9a). In addition to a very weak H₂O absorption peak at the position of the H₂S peak D discussed above, there are also weak CH₄ absorptions with $\sigma_{\text{peak}} = 1.5 \times 10^{-5} \text{ pm}^2$ [30], about 5000 times weaker than H₂S. Assuming a similar sensitivity of photoacoustic signals to methane, the noise limit will be exceeded at methane pressures above 100 mbar. Unlike water discussed above, this must be considered in natural gas samples, where at 1 bar total pressure, methane will typically be between 900 and 1000 mbar. In the spectrum of Fig. 9a), these CH₄ transitions at the position of the H₂S have a peak value of about 10 mV, above ten times the noise level at 1-s integration time. To correct for these weak absorptions, we suggest extending the spectral region to include the separate peak E of methane to establish the content of CH₄, and then subtract methane proportionally at the position of the H₂S, as demonstrated in Fig. 9. A comparison with the HITRAN database and our previous calibration shows the presence of 14 mbar CO₂ in the 1 bar sampled natural gas, or 1.4% CO₂ content, very similar to a previously reported measurement using Raman detection [4]. Reassuringly, no H₂S is apparent within our detection limit. To demonstrate the sensitivity to H₂S detection, we have prepared a sample of 3 mbar H₂S in 1 bar natural gas. The

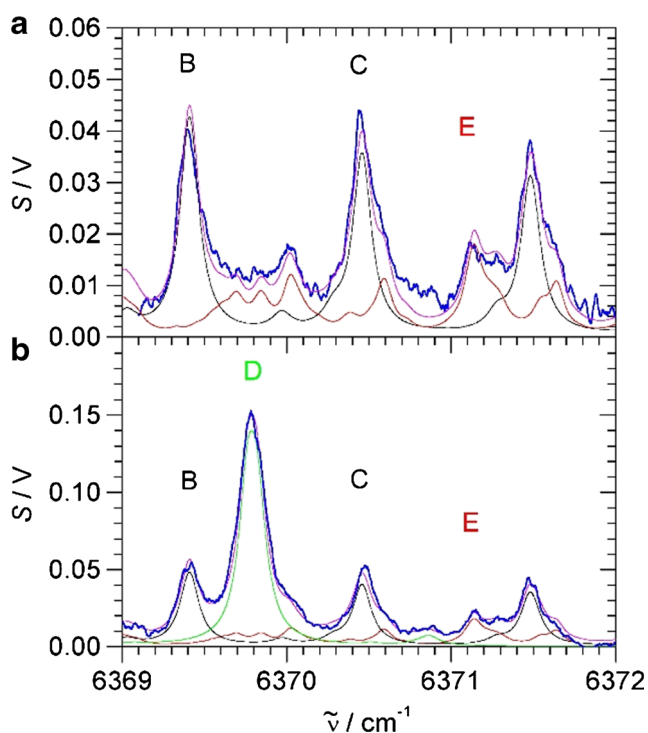


Fig. 9 CH₄, CO₂ and H₂S transitions of natural gas samples. **a** 1 bar natural gas (sampled 29 October 2018). **b** 3 mbar H₂S in 1 bar natural gas (sampled 7 November 2018). The blue trace is the photoacoustic signal. In red, black, green and magenta are HITRAN data for CH₄, CO₂, H₂S and the sum, respectively. The peak labels are as in Fig. 4 (see main text for more details)

measurement is shown in Fig. 9b). The methane background is essentially as in pure natural gas. According to the calibration, there is 16 mbar or 1.6% CO₂, very close to the previous measurement of pure natural gas; the slight deviation might be explained by purity fluctuations in the natural gas line. The measured H₂S content is 2.8 mbar, very close to the nominally 3 mbar as prepared. In future work, we would like to sample natural gas at different sources including natural H₂S impurities, to demonstrate the full potential of our detection scheme for monitoring toxic gases in the petrochemistry.

Conclusions

Due to the inherent signal amplification and noise cancellation, photoacoustic spectroscopy in a differential Helmholtz resonator has a great potential for trace gas analysis, with possible applications including safety monitoring of toxic gases and applications in the biosciences and for natural gas analysis in petrochemistry. In this study, we describe a setup employing near-IR and red diode lasers for the detection of CO₂, H₂S and O₂ in 1 bar of air/N₂ and natural gas, in static and flow cell measurements and introduce improvements including a multipass arrangement and using two independent lasers. With the red diode laser, O₂ can be detected at 764.280 nm (vacuum). A noise equivalent detection limit of 0.60 mbar (600 ppmv) of O₂ in 1 bar of air at 35-mW peak power and 1-s integration time is obtained. Normalising to the absorption cross section, the laser power and integration time, a noise equivalent normalised absorption coefficient $\alpha = 2.2 \times 10^{-8} \text{ cm}^{-1} \text{ W s}^{1/2}$ is calculated. Within the tuning range of the near-IR DFB diode laser (6357–6378 cm⁻¹), CO₂ and H₂S absorption features can be accessed for trace gas detection, with a noise equivalent detection limit of 0.160 mbar (160 ppmv) CO₂ in 1 bar N₂ at 1-s integration time with the 30-mW laser. This corresponds to a noise equivalent normalised absorption coefficient $\alpha = 8.3 \times 10^{-9} \text{ cm}^{-1} \text{ W s}^{1/2}$. Due to stronger absorption cross sections, the noise equivalent detection limit of H₂S in 1 bar N₂ is 0.022 mbar (22 ppmv). At this level, the scheme may be useful for safety monitoring of toxic H₂S. Similar detection limits apply to trace impurities in 1 bar natural gas. Detection limits scale linearly with laser power and with the square root of integration time. At 16-s total measurement time to obtain a spectrum, a noise equivalent detection limit of 40 ppmv CO₂ is obtained after a spectral line fitting procedure, for example. Considering the simplicity of the DHR setup, the detection limits compare favourably with more involved photoacoustic schemes. Possible interferences due to weak water and methane absorptions have been discussed and shown to be either negligible or easy to correct. We have demonstrated two selected application examples. The setup has been used successfully for simultaneous in situ monitoring of O₂, CO₂ and H₂S in the biosciences, for

example in the cysteine metabolism of microbes (*E. coli*), and for the analysis of CO₂ and H₂S impurities in natural gas. Using Henry's law, the 1-s noise equivalent detection limits for the head space gases O₂, CO₂ and H₂S translate into detection limits of the dissolved gases in the solution of 16 ppb per mole for dissolved O₂, 76 ppb for CO₂ and 27 ppb for H₂S.

In the future, we want to explore the possibility of isotope labelling experiments taking advantage of the different spectroscopic signatures of isotopes. We are planning further work to miniaturise the setup and to apply the technique to the measurement of natural gas samples from different sources and to investigate the metabolism of microbes with applications in studying the role of H₂S as a signalling molecule in microbial systems. Due to the low cost of diode lasers and microphone detection, the relatively simple and robust setup, the inherent signal amplification and noise cancellation, the suitability for static and flow cell measurements, the good detection limits and the spectroscopic selectivity which minimises interferences, trace gas analysis in a differential Helmholtz resonator with near-IR and red diode lasers has a great potential for many applications ranging from the biosciences to safety monitoring to petrochemistry.

Acknowledgements We are grateful to Prof. J. Green, Dr. J. Reid and Dr. T.W. Smith for their help and discussions.

Funding information This research received a financial support from the University of Sheffield and the Ministry of Education of Saudi Arabia.

Compliance with ethical standards

Conflict of interest The authors declare that they have no conflict of interest.

Open Access This article is distributed under the terms of the Creative Commons Attribution 4.0 International License (<http://creativecommons.org/licenses/by/4.0/>), which permits unrestricted use, distribution, and reproduction in any medium, provided you give appropriate credit to the original author(s) and the source, provide a link to the Creative Commons license, and indicate if changes were made.

References

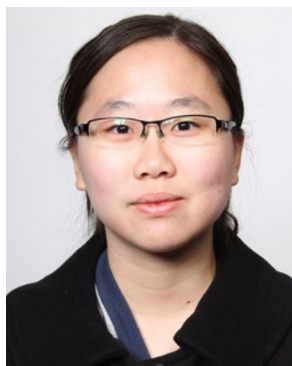
1. IDLH Documentation for Hydrogen Sulfide, National Institute for Occupational Safety and Health (NIOSH); <https://www.cdc.gov/niosh/idlh/7783064.html>. Accessed 21 Nov 2018.
2. Guidotti TL. Hydrogen sulphide. *Occup Med (Lond)*. 1996;46:367–71.
3. Shivanthan MC, Perera H, Jayasinghe S, Karunanayake P, Chang T, Ruwanpathirana S, et al. Hydrogen sulphide inhalational toxicity at a petroleum refinery in Sri Lanka: a case series of seven survivors following an industrial accident and a brief review of medical literature. *J Occup Med Toxicol*. 2013;8:9.
4. Hippler M. Cavity-enhanced Raman spectroscopy of natural gas with optical feedback cw-diode lasers. *Anal Chem*. 2015;87:7803–9. <https://doi.org/10.1021/acs.analchem.5b01462>.
5. Muyzer G, Stams AJ. The ecology and biotechnology of sulphate-reducing bacteria. *Nat Rev Microbiol*. 2008;6:441–54. <https://doi.org/10.1038/nrmicro1892>.
6. Kimura H. Signaling molecules: hydrogen sulfide and polysulfides. *Antioxid Redox Signal*. 2015;22:362–76. <https://doi.org/10.2183/pjab.91.131>.
7. Shatalin K, Shatalina E, Mironov A, Nudler E. H₂S: a universal defense against antibiotics in bacteria. *Science*. 2011;334:986–90. <https://doi.org/10.1126/science.1112699>.
8. Oguri T, Schneider B, Reitzer L. Cysteine catabolism and cysteine desulfhydrase (CdsH/STM0458) in *Salmonella enterica* serovar typhimurium. *J Bacteriol*. 2012;194:4:366–4376. <https://doi.org/10.1128/JB.00729-12>.
9. Hübert T, Boon-Brett L, Black G, Banach U. Hydrogen sensors – a review. *Sensors Actuators B*. 2011;157:329–52. <https://doi.org/10.1016/j.snb.2011.04.070>.
10. Malik R, Tomer VK, Kienle L. Cubic mesoporous Pd–WO₃ loaded graphitic carbon nitride (g-CN) nanohybrids: highly sensitive and temperature dependent VOC sensors. *J Mater Chem A*. 2018;6:10718–30. <https://doi.org/10.1039/c8ta02702a>.
11. Spencer CL, Watson V, Hippler M. Trace gas detection of molecular hydrogen H₂ by photoacoustic stimulated Raman spectroscopy (PARS). *Analyst*. 2012;137:1384–8. <https://doi.org/10.1039/c2an15990b>.
12. Salter R, Chu J, Hippler M. Cavity-enhanced Raman spectroscopy with optical feedback cw diode lasers for gas phase analysis and spectroscopy. *Analyst*. 2012;137:4669–76. <https://doi.org/10.1039/c2an35722d>.
13. Keiner R, Frosch T, Massad T, Trumbore S, Popp J. Enhanced Raman multigas sensing - a novel tool for control and analysis of ¹³CO₂ labeling experiments in environmental research. *Analyst*. 2014;139:3879–84. <https://doi.org/10.1039/c3an01971c>.
14. Smith TW, Hippler M. Cavity-enhanced Raman spectroscopy in the biosciences: in situ, multicomponent and isotope selective gas measurements to study hydrogen production and consumption by *Escherichia coli*. *Anal Chem*. 2017;89:2147–54. <https://doi.org/10.1021/acs.analchem.6b04924>.
15. Romanini D, Kachanov AA, Stoeckel F. Diode laser cavity ring down spectroscopy. *Chem Phys Lett*. 1997;270:538. [https://doi.org/10.1016/S0009-2614\(97\)00406-5](https://doi.org/10.1016/S0009-2614(97)00406-5).
16. He Y, Hippler M, Quack M. High-resolution cavity ring-down absorption spectroscopy of nitrous oxide and chloroform using a near-infrared cw diode laser. *Chem Phys Lett*. 1998;289:527. [https://doi.org/10.1016/S0009-2614\(98\)00424-2](https://doi.org/10.1016/S0009-2614(98)00424-2).
17. Hippler M, Quack M. Cw cavity ring-down infrared absorption spectroscopy in pulsed supersonic jets: nitrous oxide and methane. *Chem Phys Lett*. 1999;314:273–81. [https://doi.org/10.1016/S0009-2614\(99\)01071-4](https://doi.org/10.1016/S0009-2614(99)01071-4).
18. Hippler M, Quack M. High-resolution Fourier transform infrared and cw-diode laser cavity ringdown spectroscopy of the ν₂+2ν₃ band of methane near 7510 cm⁻¹ in slit jet expansions and at room temperature. *J Chem Phys*. 2002;116:6045–55. <https://doi.org/10.1063/1.1433505>.
19. Hippler M, Oeltjen L, Quack M. High-resolution continuous-wave diode laser cavity ring-down spectroscopy of the hydrogen fluoride dimer in a pulsed slit jet expansion: two components of the N = 2 triad near 1.3 μm. *J Phys Chem A*. 2007;111:12659–68. <https://doi.org/10.1021/jp076894s>.
20. Sigrist MW. Air monitoring by laser photoacoustic spectroscopy, chapter 4. In: Sigrist MW, editor. *Air monitoring by spectroscopic techniques, chemical analysis series 127*. New York: Wiley; 1994.

21. Miklós A, Hess P. Application of acoustic resonators in photoacoustic trace gas analysis and metrology. *Rev Sci Instrum.* 2001;72:1937. <https://doi.org/10.1063/1.1353198>.
22. Busse G, Herboeck D. Differential Helmholtz resonator as an optoacoustic detector. *Appl Opt.* 1979;18:3959–61.
23. Zeninari V, Courtois D, Parvite B, Kapitanov VA, Ponomarev YN. Methane detection on the sub-ppm level with a near-infrared diode laser photoacoustic sensor. *Infrared Phys Technol.* 2003;44:253. [https://doi.org/10.1016/S1350-4495\(03\)00135-X](https://doi.org/10.1016/S1350-4495(03)00135-X).
24. Rouxel J, Coutard JG, Gidon S, Lartigue O, Nicoletti S, Parvite B, et al. Miniaturized differential Helmholtz resonators for photoacoustic trace gas detection. *Sensors Actuators B.* 2016;236:1104–10. <https://doi.org/10.1016/j.snb.2016.06.074>.
25. Alahmari S, Hippler M. Helmholtz resonator diode laser photoacoustic spectroscopy for trace gas analysis in the environment and the biosciences. *Advanced Photonics 2018, OSA Technical Digest paper SeM2J.4.* <https://doi.org/10.1364/SENSORS.2018.SeM2J.4>.
26. Cattaneo H, Laurila T, Hemberg R. Photoacoustic detection of oxygen using cantilever enhanced technique. *Appl Phys B Lasers Opt.* 2006;85:337–41. <https://doi.org/10.1007/s00340-006-2336-5>.
27. Laurila T, Cattaneo H, Pöyhönen T, Koskinen V, Kauppinen J, Hemberg R. Cantilever-based photoacoustic detection of carbon dioxide using a fiber-amplified diode laser. *Appl Phys B Lasers Opt.* 2006;83:285; *Ibid.*, 669. <https://doi.org/10.1007/s00340-005-2106-9>.
28. Hippler M, Mohr C, Keen K, McNaghten E. Cavity-enhanced resonant photoacoustic spectroscopy with optical feedback cw diode lasers: a novel technique for ultratrace gas analysis and high-resolution spectroscopy. *J Chem Phys.* 2010;133:044308 (1–8). <https://doi.org/10.1063/1.3461061>.
29. Kachanov A, Koulikov S, Tittel FK. Cavity-enhanced optical feedback-assisted photo-acoustic spectroscopy with a 10.4 μm external cavity quantum cascade laser. *Appl Phys B Lasers Opt.* 2013;110:47–56. <https://doi.org/10.1007/s00340-012-5250-z>.
30. Gordon IE, Rothman LS, Hill C, Kochanov RV, Tan Y, Bernath PF, et al. The HITRAN2016 molecular spectroscopic database. *J Quant Spectrosc Radiat Transf.* 2017;203:3–69. <https://doi.org/10.1016/j.jqsrt.2017.06.038>.
31. www.webbook.nist.gov/chemistry. Accessed 16 Oct 2018.
32. Moser H, Pölz W, Waclawek JP, Ofner J, Lendl B. Implementation of a quantum cascade laser-based gas sensor prototype for sub-ppmv H₂S measurements in a petrochemical process gas stream. *Anal Bioanal Chem.* 2017;409:729–39. <https://doi.org/10.1007/s00216-016-9923-z>.
33. Tütüncü E, Mizaikoff B. Cascade laser sensing concepts for advanced breath diagnostics. *Anal Bioanal Chem.* 2019;411:1679–86. <https://doi.org/10.1007/s00216-018-1509-5>.

Publisher's note Springer Nature remains neutral with regard to jurisdictional claims in published maps and institutional affiliations.



Saeed Alahmari is a final year PhD student from Saudi Arabia in the Department of Chemistry, University of Sheffield. He joined the Hippler group in 2016, doing research in analytical chemistry using Helmholtz resonator photoacoustics and cavity-enhanced Raman spectroscopy in the biosciences and petrochemistry.



Xiu-Wen Kang was an MChem student from Malaysia in the Department of Chemistry, University of Sheffield, from 2012 to 2016. She joined the Hippler group 2015–2016 to do an undergraduate MChem research project focussed on analytical applications of photoacoustic spectroscopy, including Herriott cells and differential Helmholtz resonators. She is now a PhD student in Shanghai Jiao Tong University, China, doing ultrafast laser spectroscopy studies of pro-

tein kinetics.



Michael Hippler is currently a senior lecturer (equivalent to an associate professor) in Physical Chemistry, University of Sheffield, with research interests to develop new laser spectroscopic techniques and to apply new laser sources for fundamental and analytical applications. He pursues analytical applications of laser spectroscopy, sensing and imaging in many collaborations with colleagues and industrial partners. The aim of his research is the development of new

methods and applications of ultra-sensitive laser spectroscopic techniques for analytical applications, including sensor applications of new light sources (DFB-QCL and diode lasers). During his research activities in Zürich and Sheffield, he was able to develop new innovative experimental techniques for laser spectroscopy with great potential for analytical and fundamental applications (ISOS, CERPAS, CERS). Awards and honours received include the 2002 Ruzicka Prize in Chemistry (ETH Zürich), “in honour of his contributions to high-resolution spectroscopy, in particular his experimental development of mass- and isotope-selective spectroscopy and his theoretical description of high-resolution two-photon spectroscopy”, and the 2004 Nernst-Haber-Bodenstein Prize (Deutsche Bunsengesellschaft für Physikalische Chemie), “in honour of outstanding scientific achievements in Physical Chemistry by a younger scientist”. For more information, please see <http://hippler.group.shef.ac.uk>.

Cavity-Enhanced Raman and Helmholtz Resonator Photoacoustic Spectroscopy to Monitor the Mixed Sugar Metabolism of *E. coli*

George D. Metcalfe¹, Saeed Alahmari¹, Thomas W. Smith^{1,2}, and Michael Hippler^{1*}

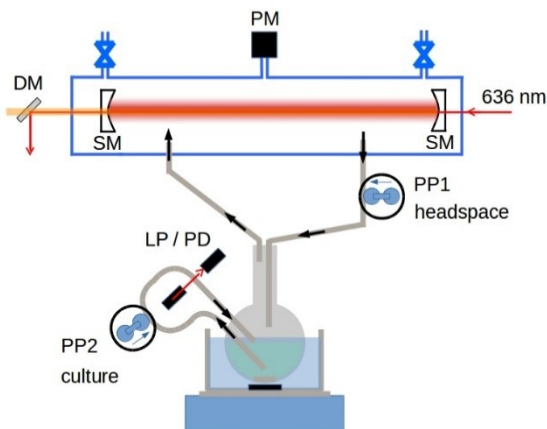
¹ Department of Chemistry, University of Sheffield, Sheffield S3 7HF, UK

² Water and Environmental Engineering Group, Faculty of Engineering and Physical Sciences, University of Southampton, Southampton SO17 1BJ, UK

* Corresponding author. E-Mail: M.Hippler@sheffield.ac.uk

Accepted by Analytical Chemistry, 16/9/2019. DOI: 10.1021/acs.analchem.9b03284

ABSTRACT



We introduce and compare two powerful new techniques for headspace gas analysis above bacterial batch cultures by spectroscopy, Raman spectroscopy enhanced in an optical cavity (CERS) and photoacoustic detection in a differential Helmholtz resonator (DHR). Both techniques are able to monitor O₂ and CO₂ and its isotopomers with excellent sensitivity and time resolution to characterise bacterial growth and metabolism. We discuss and show some of the

shortcomings of more conventional optical density (OD) measurements if used on their own without more sophisticated complementary measurements. The spectroscopic measurements can clearly and unambiguously distinguish the main phases of bacterial growth in the two media studied, LB and M9. We demonstrate how ¹³C isotopic labelling of sugars combined with spectroscopic detection allows the study of bacterial mixed sugar metabolism, to establish whether sugars are sequentially or simultaneously metabolised. For *E. coli*, we have characterised the shift from glucose to lactose metabolism without a classic diauxic lag phase. DHR and CERS are shown to be cost-effective and highly selective analytical tools in the biosciences and in biotechnology, complementing and superseding existing, conventional techniques. They also provide new capabilities for mechanistic investigations and show a great deal of promise for use in stable isotope bioassays.

INTRODUCTION

Microbial metabolism is a complex system of processes which requires interdisciplinary efforts to elucidate the function of each component and its broader connections to the whole system. Microbes consume and produce various chemical compounds. Analysis of these metabolites is an important task in microbiology; for example, it allows the study of metabolic pathways, microbial activity, enzyme reaction mechanisms, interaction with other organisms, and is essential to optimization of industrial processes in biotechnology. In this context, the study of the mixed sugar metabolism of microbes and the resulting diauxie, where two exponential growth phases are observed, is a very relevant topic. The classic example of diauxic growth was first described by Monod after presenting *Escherichia coli* (*E. coli*) with a mixture of glucose and lactose.^{1,2} Monod observed biphasic exponential growth of *E. coli*, intermitted by a lag phase of minimal growth, due to the sequential consumption of glucose followed by lactose. Glucose is the preferred carbon source for *E. coli*, as well as many other organisms.³ These microbes typically only feed on other sugars when glucose is not present. The regulatory mechanism by which expression of genes required for the utilization of secondary carbon sources is prevented in the presence of a preferred substrate is known as carbon catabolite repression (CCR).⁴ CCR enables microbes to increase their fitness by optimizing growth rates in natural environments that provide complex mixtures of nutrients. On the other hand, in industrial processes, such as biofuel production, CCR is one of the barriers for increased yield of fermentation products.⁵ During *E. coli* glucose-lactose diauxie, the presence of glucose represses the *lac* operon, a set of genes coding for the *lac* permease and β -galactosidase which are required for lactose uptake and lactose hydrolysis to catabolizable glucose and galactose sub-units, respectively.⁶

Optical density (OD) measurements are commonly used to monitor diauxic growth.^{1,2,7} They rely on the principle that transmitted light is lost due to scattering by the microbial culture. The OD is thus an indirect measure of the concentration of microbial cells. OD measurements are simple, but they suffer from interferences since they cannot distinguish living cell from debris, dead cells or precipitates. The diauxic lag phase between the consumption of the first nutrient and the second often gives a distinct plateau in OD values due to the temporary halt in growth. However, this classic picture of diauxic growth intermitted with a lag phase is not always the case. Some strains of budding yeast when presented with a mixture of glucose and galactose exhibit a very brief diauxic lag phase and little change in growth rates between glucose and galactose consumption.⁸ Furthermore, although glucose sits at the top of the sugar hierarchy for *E. coli* and is frequently consumed first, mixed non-glucose sugars may exhibit simultaneous metabolism rather than sequential.⁹ OD measurements alone cannot

provide sufficient information into mixed sugar metabolism. Another common method for monitoring diauxic growth is sampling the microbial culture for high performance liquid chromatography analysis to determine changes in mixed sugar concentrations during metabolic activity.¹⁰⁻¹² Analytical methods that require sampling are not ideal as they consume the analyte and require extra considerations for preventing contamination of the system.

Gas composition is another process parameter frequently monitored online in bioreactors. O₂ and CO₂ are two key gases to consider.¹³ O₂ availability is a key parameter for aerobic bioprocesses as well as anaerobic systems that are sensitive to disruption by O₂, such as production of biohydrogen. CO₂ is a key by-product of both aerobic respiration and fermentation and can be monitored to closely follow these processes. Dissolved gases can be monitored by gas sensitive electrode-based sensors, some of which have the advantage of not consuming the analyte. However, most sensors are invasive as they must be submerged in the microbial culture and often have a limited lifespan under operating conditions of the bioreactor due to poisoning. Online, solution-based sensors create challenges such as the requirement for including an additional port on the bioreactor, increased risk of contamination and challenges associated with sterilisation and needing to frequently calibrate the sensor, which is often impossible without process contamination. Disadvantages also include interferences with other components, ageing, temperature dependence, and long response and settlement times. The measurement of partial pressures in the effluent headspace gases can give a good approximation of dissolved gases *via* Henry's law and eliminates the need to use invasive devices. Gas chromatography (GC) and mass spectrometry (MS) are two common methods of gas phase analysis. However, both techniques require sampling, are expensive, require frequent calibration and have limitations, including difficulties detecting certain components. Also, chromatographic techniques rely upon the spatial separation of the compounds that are being quantified, and so are only of use on a non-continual basis.¹⁴ Spectroscopic methods for gas phase analysis offer numerous benefits including high precision and accuracy, no sampling necessary and the ability to perform non-invasive real-time measurements. Detection in the near-IR has the advantage of low-cost light sources and detectors; the sensitivity, however, suffers due to low absorption cross-sections. In addition, relevant homonuclear molecules including O₂ cannot be observed by IR-absorption due to unfavourable selection rules. Molecular O₂ has two main absorption bands in its UV-vis spectrum, one deep in the UV at 145 nm and the other at 760 nm.^{15,16} O₂ detection at 145 nm faces interferences by water vapour and CO₂ and the weak absorption lines at 760 nm typically provide detection limits that are of little practical use. Raman spectroscopy, in contrast, can detect homonuclear molecules, but it has very low sensitivity.

Both near-IR absorption and Raman spectroscopy need special enhancement techniques to be useful in gas phase analysis.

Recently, two new techniques were introduced for sensitive and selective trace gas detection, near-IR absorption enhanced by photoacoustic detection in a differential Helmholtz resonator (DHR),¹⁷⁻²⁰ and cavity-enhanced Raman spectroscopy (CERS).²¹⁻²⁵ In this contribution, we apply these techniques to the study of metabolic growth of microbes and we compare their performance and suitability for applications in the biosciences and biotechnology. We demonstrate that both spectroscopic techniques can clearly and unambiguously distinguish all the main phases of bacterial growth, monitor the consumption of a mixed organic feedstock using ¹³C isotopic labelling of sugars and can be employed to establish whether the various components are sequentially or simultaneously metabolised.

EXPERIMENTAL

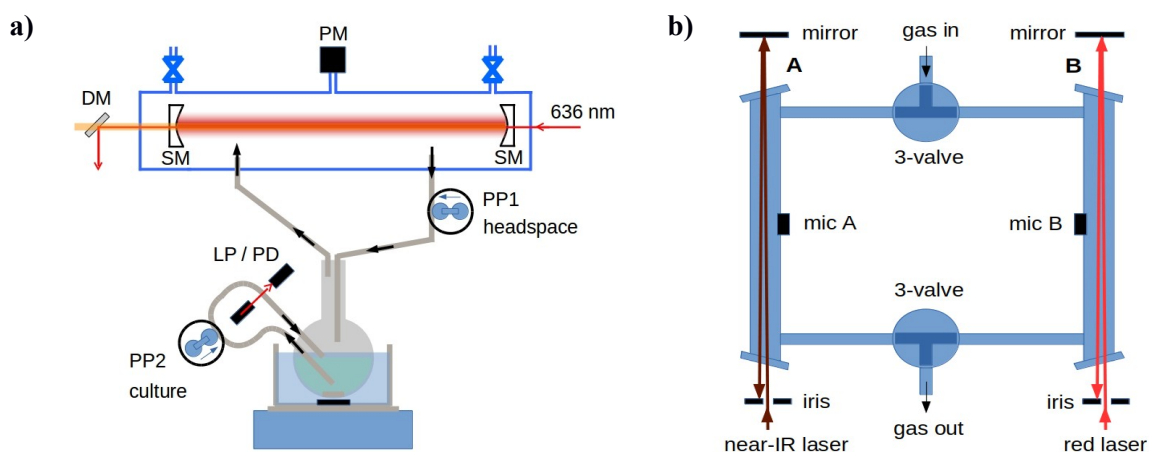


Fig 1. Schemes of the experimental set-ups. See main text for details. **a)** CERS with bacterial suspension attached and peristaltic pumps cycling the headspace for CERS and the culture solution for OD measurements. **b)** Differential Helmholtz Resonator.

The headspace above bacterial cultures is analysed by Raman (CERS) or diode laser photoacoustic (DHR) spectroscopy. The CERS set-up has been described in detail before.^{21,23,24} Here, we provide a brief outline and describe some modifications and improvements. A higher power diode is employed (Opnext HL63133DG), lasing at 636.7 nm. At full driving current, the laser can provide up to 170 mW continuous wave (cw) power, but in CERS it is operated at a reduced power of 40 mW to facilitate single mode operation. The laser output is coupled *via* a short-pass filter and two Faraday isolators into an optical cavity composed of two highly-reflective mirrors (Newport SuperMirrors, $R >$

99.99%), SM in Fig. 1a). To simplify the set-up, no anamorphic prism pair or mode matching lens are used; mode matching/focussing into the cavity is achieved by optimizing the distance of the collimating lens of the diode. If the laser wavelength matches the cavity length, an optical resonance builds up laser power inside the cavity by up to three orders of magnitude enhancing Raman signals (CERS). After the cavity, a dichroic mirror DM separates excitation light from Raman signals which are coupled into a fibre and transferred to the spectrometer (Shamrock SR-750-A, with Andor iVac DR32400 camera at -60 °C). The 600 lines/mm grating provides a 1200 cm^{-1} spectral range at 5 cm^{-1} resolution which covers CO_2 , O_2 and N_2 Raman peaks and can easily resolve $^{12}\text{CO}_2$ and $^{13}\text{CO}_2$ (see Fig. 2a). Part of the laser light is diverted back to the diode for optical feedback, locking the laser to the cavity. The diode injection current is modulated around one cavity mode; in each cycle, the wavelength changes until it is self-locking by optical feedback to a longitudinal cavity mode. In a simplification of the set-up, no attempts are made for an active stabilization of the laser since the optical self-locking is strong enough to keep accidental resonances at duty cycles between 50-80%. To normalize Raman signals, the N_2 peak of air can be used since, in the closed system, N_2 is not consumed or produced by the bacterial metabolism. Alternatively, Si peaks presumably originating from the SM mirror glass substrates can also be used for convenient *in situ* calibration. Raman intensity is converted to partial pressure using tabulated integrated peak areas.²³

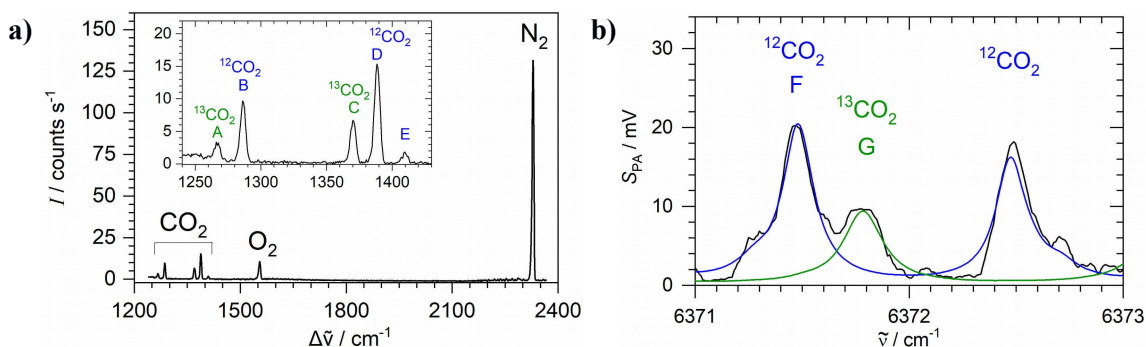


Fig 2. Spectral signatures used to identify $^{12}\text{CO}_2$ and $^{13}\text{CO}_2$ in the headspace of the mixed sugar aerobic metabolism (^{13}C -glucose, ^{12}C -lactose) of *E. coli*. **a)** CERS Raman spectrum of 800 mbar N_2 , 65 mbar O_2 , 73 mbar $^{12}\text{CO}_2$ and 31 mbar $^{13}\text{CO}_2$. **b)** DHR absorption spectrum (black) of 6.5 mbar $^{12}\text{CO}_2$ and 5.0 mbar $^{13}\text{CO}_2$. In blue and green are HITRAN data for $^{12}\text{CO}_2$ and $^{13}\text{CO}_2$, respectively.

The DHR set-up has been described in detail in a previous publication.²⁰ In short, optical absorption in a differential Helmholtz resonator (see Fig. 1b) creates sound waves (photoacoustic effect) in the two chambers A and B which are 180-degrees out-of-phase. Acoustic noise, including flow noise, will be mostly in-phase. Differential detection of sound in A minus B therefore doubles signals and

effectively cancels noise. Two temperature-tuned distributed feedback (DFB) diode lasers are used, a near-IR laser (Mitsubishi FU-650SDF, amplified to 30 mW in a booster optical amplifier Thorlabs S9FC1004P) to detect CO₂ near 1.57 μ m, and a red laser (35 mW, Eagleyard EYP-DFB-0764) to detect O₂ near 764 nm. To simplify the set-up, the near-IR laser is directed through one compartment (A), while the red laser is directed through the other (B) (see Fig. 1b). In a typical experiment, CO₂ is first measured by scanning the near-IR laser; next, O₂ is measured by scanning the red laser.²⁰ Both lasers are modulated by their injection current at the acoustic resonance frequency with a square-wave at 50% duty cycle. The near-IR spectrum allows the distinction of ¹²CO₂ and ¹³CO₂ (see Fig. 2b). Photoacoustic signal is converted to partial pressure using our previous calibration and HITRAN absorption cross-sections.^{20,26}

The molarity of a dissolved gas can be calculated from its partial pressure using Henry's law.²⁷ A small proportion of dissolved CO₂ will react with water to form carbonic acid, which will be at equilibrium with bicarbonate and carbonate ions, depending on the pH. With a typical acidic pH below 5 at the end of an experiment, less than 1% of dissolved CO₂ will be lost to carbonic acid and carbonates.

For each measurement, 50 ml of sterile LB (lysogeny broth, a nutrient rich growth medium) was inoculated with a single colony of *E. coli* (wild type, strain K-12 MG1655) and incubated for 5 h at 37 °C to grow to typically 1.0 OD₆₀₀ (OD at 600 nm in a 1 cm cuvette). 1 ml of the suspension was then centrifuged to remove LB medium and resuspended in 250 ml fresh, sterile M9 (a minimal, defined medium containing only essential salts and vitamins) or LB solution. The medium was supplemented with D-glucose and/or D-lactose (*puriss. p.a.*, Sigma-Aldrich). For isotope labelling experiments, fully ¹³C substituted glucose (U-13C6, 99% CLM-1396, CK isotopes) was used. In mixed sugar experiments, we used larger concentrations of lactose compared to glucose to show the preference for glucose more clearly. This is in line with most previous studies of glucose-lactose diauxie which have used a lactose concentration that was up to one order of magnitude greater than the glucose concentration.²⁸⁻³⁰ The glucose concentration was selected to ensure that oxygen was not depleted so that the shift to lactose metabolism could occur, while still producing appreciable CO₂ from glucose metabolism.

The bacterial batch culture in a 500 ml flask was kept at 37 °C in a thermostated water bath under constant stirring. The headspace was circulated *via* a peristaltic pump (3 l/h) through the spectroscopic cell in a closed, vacuum tight system (see Fig. 1a). The total headspace gas volume in the CERS system is 720 ml, and 510 ml in the DHR system. The transfer tubes and cells were kept at *ca.* 45 °C using heating wire to avoid water condensation. This was particularly important and effective to avoid

condensation on the high-performance cavity mirrors which would spoil their reflectivity. In control experiments, we measured the appearance time from the suspension flask to the spectroscopic measurement cell to be less than 5 min.^{20,24} To characterize bacterial growth by measuring the OD *in situ* and simultaneously, another peristaltic pump circulated part of the suspension through a 1 cm glass cuvette, through which a red laser pointer (1 mW, 650 nm) was shining (see Fig. 1a); after calibration with a UV-vis spectrometer, the transmitted intensity as observed by a photodiode is converted to OD₆₀₀. At the end of an experiment and after exhausting the oxygen supply, the increase in cell density is characterized by OD₆₀₀ ≈ 1.5-2.0. The final pH of the solution was typically 4.5 to 5.0 due to organic acids generated during the metabolism. For comparison, fresh LB has pH ≈ 6.8, and fresh M9 has pH ≈ 6.9. At the beginning, the cellular material within the 250 ml suspension has a typical dry weight of 0.2 mg, which by the end of a typical experiment increases to 60 mg, reflecting bacterial growth. All experiments were repeated at least three times showing essentially the same behaviour.

RESULTS AND DISCUSSION

1. *E. coli* metabolism in LB or M9 supplemented with glucose or lactose

In a first set of experiments, we studied the oxygen-limited growth of *E. coli* batch cultures in LB or M9 medium supplemented with a single sugar, glucose or lactose. Fig. 3 shows typical time-dependent partial pressures of O₂ and CO₂ as measured by CERS with simultaneous OD measurements for *E. coli* in LB supplemented with 20 mM glucose. Also included in Fig. 3 (middle panel) is the total pressure $p'_{\text{total}} = p_{\text{O}_2} + p_{\text{CO}_2} + p_{\text{N}_2}$ and the respiratory quotient (RQ), the ratio of CO₂ produced to O₂ consumed, where CO₂ is corrected to account for the approximately 18% of dissolved CO₂ according to Henry's law.²⁷ After a lag phase of approximately 2 h ('A' in Fig. 3), oxygen consumption and CO₂ production begin indicating the onset of exponential bacterial growth ('B' in Fig. 3). This is also indicated by the increase of OD up to a peak value of about 1.5 in Fig. 3, lower panel. After around 5.5 h, the OD plateaus, indicating the onset of the stationary phase ('C' in Fig. 3). The living bacteria in the stationary population still consume O₂ and produce CO₂. During the exponential phase B and stationary phase C, the oxygen uptake rate is constant, as indicated by the almost perfect exponential decay fit of oxygen partial pressure in Fig. 3, with a rate constant $k = 0.189 \text{ h}^{-1}$ or half-life $t_{1/2} = 3.67 \text{ h}$. These results are confirmed in three repeat experiments which show a lag phase between 1.5 – 2 h, onset of stationary phase between 5 – 6 h, and an oxygen uptake rate within 0.15 – 0.19 h⁻¹.

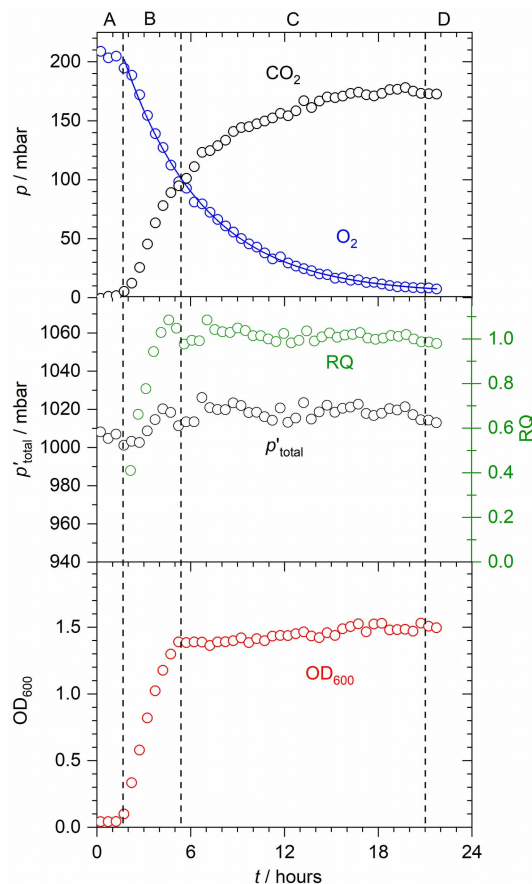
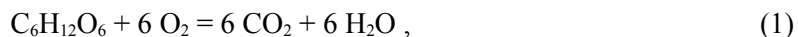


Fig. 3. CERS measurement of the headspace in the aerobic *E. coli* metabolism of unlabelled glucose (20 mM) in rich LB medium. A to D denote different phases of bacterial growth: lag phase, exponential growth, stationary phase and end of aerobic respiration, respectively. **Upper panel:** partial pressures of O_2 and CO_2 , including an exponential decay fit of p_{O_2} ; **middle panel:** p'_{total} (total of N_2 , O_2 and corrected CO_2 pressures) and respiratory quotient RQ (ratio of CO_2 produced to O_2 consumed); **lower panel:** simultaneous OD measurements of the bacterial culture.

During cellular energy production by aerobic respiration with glucose as a carbon source, the sugar is oxidised to CO_2 and H_2O . Full conversion is described by the stoichiometry of Eq. 1,



so that for each unit of O_2 consumed, one unit of CO_2 is formed. For carbohydrates, the respiratory quotient RQ is therefore typically about 1.0. Like OD measurements, the RQ can be used to distinguish between the exponential phase B and stationary phase C as shown in Fig. 3, middle panel, where a constant RQ of about 1.0 (within 2% in the three repeat experiments) is reached during stationary growth. The 1:1 ratio between O_2 consumed and CO_2 produced can also be observed in the constant total pressure during stationary growth in Fig. 3, middle panel. A typical *E. coli* cell contains

approximately 50% carbon by dry mass.³¹ As sugars are primarily used for energy production, the carbon source for biosynthesis and growth in LB medium originates from the tryptone and yeast extract (see also ref. [32]). *E. coli* has several oligopeptide permeases and peptidases enabling it to recover free catabolizable amino acids from tryptone and yeast extract.³³ The available oxygen in 1 atm of air in the 720 ml headspace of the CERS experiment corresponds to 6 mmol, and the 20 mM glucose in the 250 ml suspension corresponds to 5 mmol glucose. According to Eq. 1, there is therefore an excess of glucose in the experiment and the bacteria are limited by the oxygen available, hence the decrease of O₂ partial pressure down to essentially 0 in the closed system. After about 21 h, all available oxygen in the closed system has been consumed, and aerobic respiration terminates ('D' in Fig. 3). *E. coli* is a facultative anaerobe meaning, upon shifting to anaerobic conditions, the microbes may adapt to the new environment and resume metabolism by anaerobic fermentation of excess glucose. However, we do not see any evidence of further microbial activity such as resuming CO₂ production. The partial pressure of CO₂ was monitored for up to 3 days, not shown in Fig. 3, during which time CO₂ did not increase but rather gradually decreased to a constant value of around 145 mbar. This decrease was not due to a leak as no increase in O₂ was observed. One possible explanation might be provided by the slow conversion of dissolved CO₂ into carbonic acid. Although OD measurements are convenient for indicating the stage of bacterial growth (*i.e.* lag, exponential and stationary phases), the OD cannot determine the point of oxygen depletion as there is no change in OD between phases C and D. The OD measurements also do not indicate that CO₂ production, and thus the overall metabolic activity of *E. coli*, halts under the anaerobic conditions of phase D. For a full characterisation of bacterial growth in changing environments, OD measurements require a complementary method to provide information on changes such as the shift from aerobic to anaerobic conditions.

To make sure that in the isotopically labelled mixed sugar metabolism experiments all CO₂ observed was coming from the sugars and not from the medium, we also performed experiments in M9 minimal medium. Fig. 4 shows a typical time-dependent CERS measurement of oxygen and CO₂ partial pressures with simultaneous OD measurements for the metabolism of *E. coli* in M9 supplemented with 20 mM glucose. As before, the four different phases A to D can be clearly distinguished by the gas analysis while OD is unable to distinguish the stationary phase C from the end of aerobic respiration D. With about 5 h, the lag phase is much longer compared to LB medium. The oxygen uptake rate is constant, as indicated by the almost perfect exponential decay fit of oxygen partial pressure in Fig. 4. The decay extends from the exponential phase to the stationary phase with a rate constant $k = 0.134 \text{ h}^{-1}$ or half-life $t_{1/2} = 5.18 \text{ h}$ which is much slower than in LB. The longer lag phase and the slower oxygen

uptake and growth reflect the limitations of the minimal medium compared to rich LB medium. Similar results were found in three repeat experiments which show a lag phase between 4 – 7 h, onset of stationary phase between 10 – 13 h, and oxygen uptake rates between 0.13 and 0.15 h⁻¹.

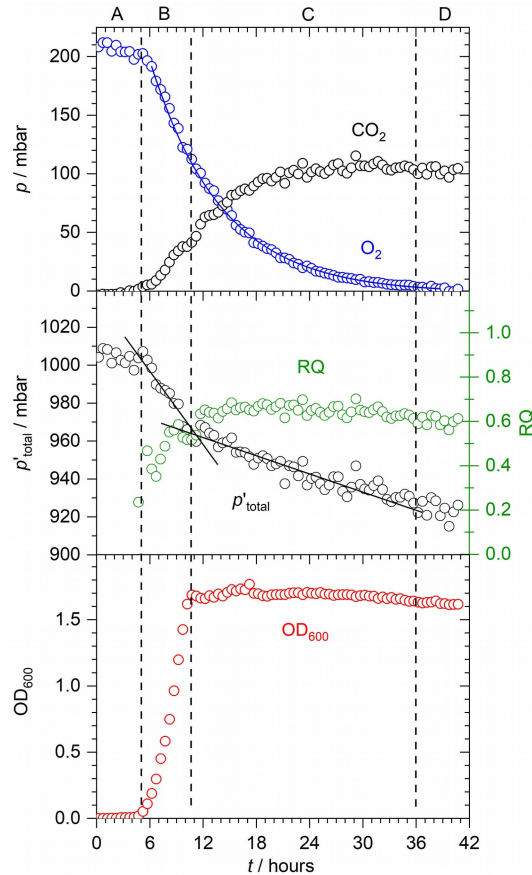


Fig 4. As in Fig. 3, but now monitoring the aerobic *E. coli* metabolism of unlabelled glucose (20 mM) in M9 minimal medium instead of LB medium.

A very distinct different behaviour is exhibited in terms of the total yield of CO₂. There is no 1:1 relationship between oxygen consumed and CO₂ being formed, but rather a considerable amount of CO₂ is missing. The RQ during stationary phase growth of about 0.6 (within 2% in the three repeat experiments) indicates around 40% of CO₂ is missing. This is even clearer in the plot of the total pressure $p_{O_2} + p_{CO_2} + p_{N_2}$ (with correction for dissolved CO₂) also in the middle panel of Fig. 4. The ‘missing’ CO₂ is not due to leaching some dissolved CO₂ *via* carbonic acid into bicarbonate and carbonate ions as determined in a test experiment, as acidifying by injecting HCl into the suspension at the end of growth did not release any noticeable CO₂ over an extended period of time. The imbalance between O₂ consumption and CO₂ production in M9 medium is due to some glucose not being fully oxidised to CO₂, as it is the only available carbon source for biomass synthesis, while O₂ is still

consumed. Tryptone and yeast extract provide amino acids for growth in LB medium, but in minimal medium, *E. coli* must synthesise amino acids, nucleobases and other biomolecules from glucose. In minimal media, *E. coli* has been found to accumulate a high amount of enzymes, which are virtually absent when grown in LB medium, which catalyse the formation of amino acids from glucose, ammonia and sulfate.³⁴ Some formulations of minimal media incorporate casamino acids for biomass synthesis so that sugars are not utilised as building blocks. We did not incorporate casamino acids into M9 medium to be certain that the only available carbon sources for CO₂ production was the supplemented sugars. The need to synthesise essential precursor molecules in M9 medium also contributes to the longer lag phase and slower growth rate. It can be seen from the plot of the total pressure that the rate of decrease is much higher during the exponential growth phase B compared to the stationary phase C. This is consistent with a more significant imbalance between CO₂ and O₂ and a higher requirement for carbon for growth during the exponential phase. About 80 mbar of CO₂ is missing at the end of the experiment which corresponds to approximately 2.5 mmol of carbon atoms. The dry weight of bacteria at the end is about 60 mg. Assuming that about 50% of this is carbon, the bacteria contain about 2.5 mmol carbon atoms in total, in agreement with the missing CO₂.

Experiments were repeated in M9 supplemented with lactose. Fig. 5 shows typical time-dependent traces for the aerobic metabolism of *E. coli* in M9 supplemented with 20 mM lactose, as measured by CERS with simultaneous OD measurements. The results are very similar to M9 supplemented with glucose with a similar lag phase. The exponential decay of oxygen is characterised by an uptake rate of $k = 0.155 \text{ h}^{-1}$ (half-life $t_{1/2} = 4.47 \text{ h}$) with a range of $0.15 - 0.17 \text{ h}^{-1}$ in the three repeats. This is somewhat faster compared to glucose, but probably not different enough to allow the distinction between lactose and glucose metabolism just from a measurement of the uptake rate. Lactose (C₁₂H₂₂O₁₁) is a disaccharide derived from the condensation of glucose and galactose; at complete conversion to CO₂ and H₂O, there is again a 1:1 relationship between oxygen consumed and CO₂ being formed. In M9, however, a considerable amount of CO₂ is missing as in the previous example of glucose in M9. As before, CO₂ is missing because the bacteria need a carbon source for their growth. Since the minimal medium contains no other source of organic carbon, the bacteria must utilise lactose. A noticeable difference concerns the behaviour of the OD curve. As before, the lag phase and exponential growth can be easily seen in the OD curve. In the stationary phase, however, the OD does not remain constant, but first declines a little before increasing again around the point where aerobic respiration terminates, continuing to rise outside the range displayed in Fig. 5. The reason for this behaviour is unclear at present; it might be related to dead cells breaking up, possibly releasing slightly coloured compounds which absorb red light, in addition to scattering losses. In any case it

shows that an OD measurement is a rather indirect determination of cell density and therefore can suffer from interferences not directly related to the density of living cells.

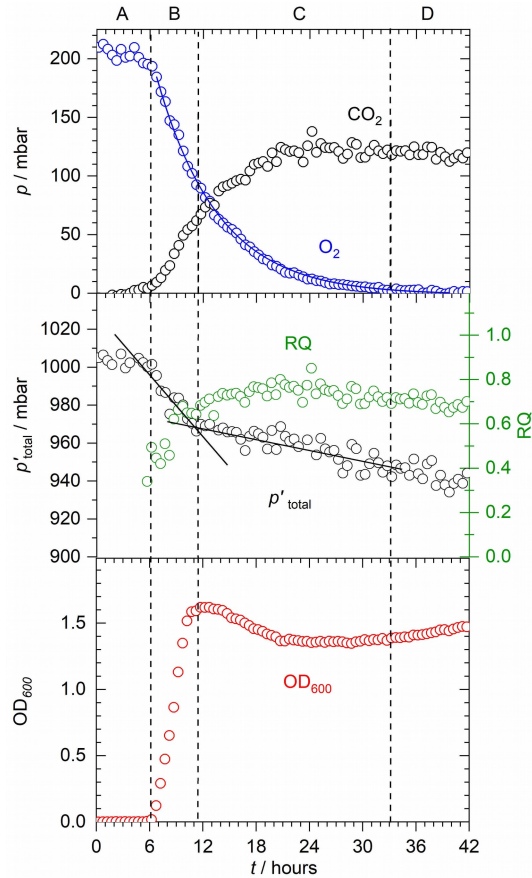


Fig. 5. As in Figures 3 and 4, but now monitoring the aerobic *E. coli* metabolism of unlabelled lactose (20 mM) in minimal M9 medium.

2. Aerobic mixed sugar metabolism of *E. coli*

Experiments were also done using DHR to characterize the metabolism. In the DHR experiments, we used lower sugar concentrations (10 mM), and due to the lower headspace volume, there is also less oxygen available in the closed system. Typical examples of DHR measurements with unlabelled sugars are shown in Fig. 6. The same qualitative behaviour as in the CERS measurement was found, with the exception of the oxygen uptake rate being faster with typically $k = 0.20 - 0.25 \text{ h}^{-1}$ within our repeats. The faster kinetics must be related to the difference in the experimental conditions such as more efficient O_2 mass transfer to the solution or differences in the sugar concentrations. Fig. 6 shows that without isotope labelling, it is not really possible to distinguish the metabolism of different

sugars from the measurements of O₂ and CO₂ partial pressures. In Fig. 6a), M9 was supplemented with 2.5 mM glucose; in this experiment the glucose is limiting, not the oxygen. Fig 6b) shows the metabolism of 10 mM lactose, and finally Fig. 6c) the mixed sugar metabolism of 2.5 mM glucose *and* 10 mM lactose in M9. Even on close inspection of Fig. 6c), no classic diauxic shift lag phase is apparent which would indicate the shift from one sugar to the other; in fact, it would be even unclear whether glucose or lactose is first metabolised, or both simultaneously.

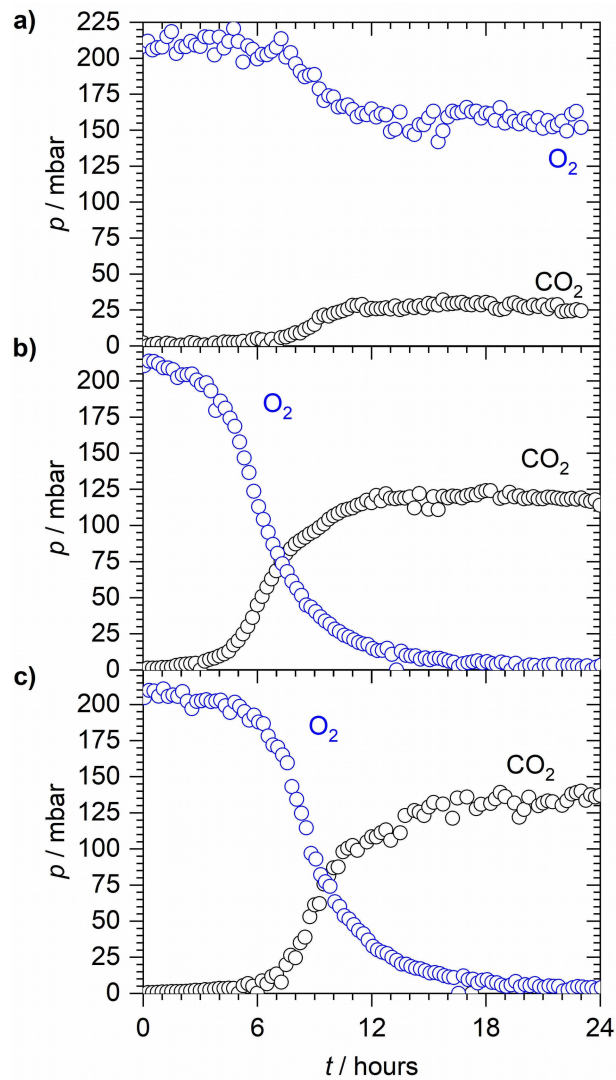


Fig 6. DHR measurement of the headspace in the aerobic *E. coli* metabolism of unlabelled sugars in minimal M9 medium, **a)** supplemented with 2.5 mM glucose; **b)** supplemented with 10 mM lactose; **c)** supplemented with 2.5 mM glucose and 10 mM lactose.

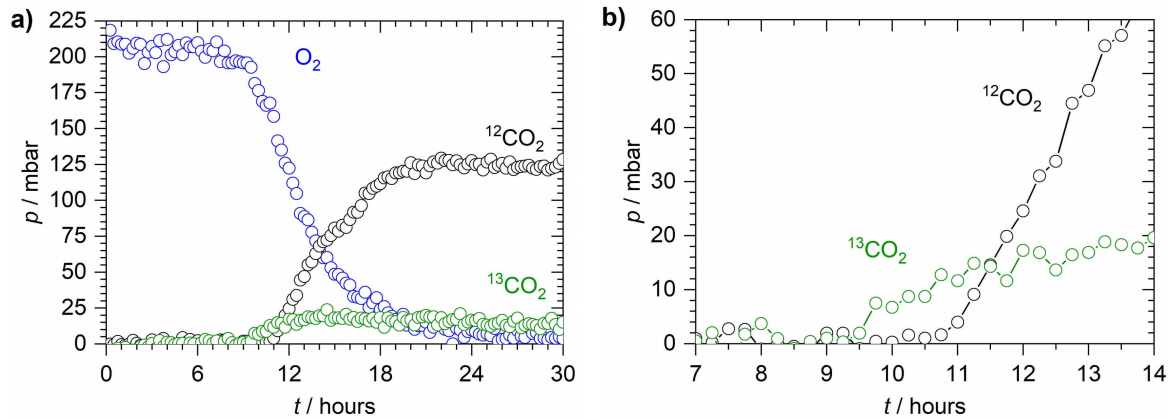


Fig 7. Monitoring mixed sugar metabolism of *E. coli* using DHR photoacoustic spectroscopy with isotopic labelling (2.5 mM ^{13}C -glucose, 10 mM ^{12}C -lactose, in M9). **a)** Overview. **b)** Detail.

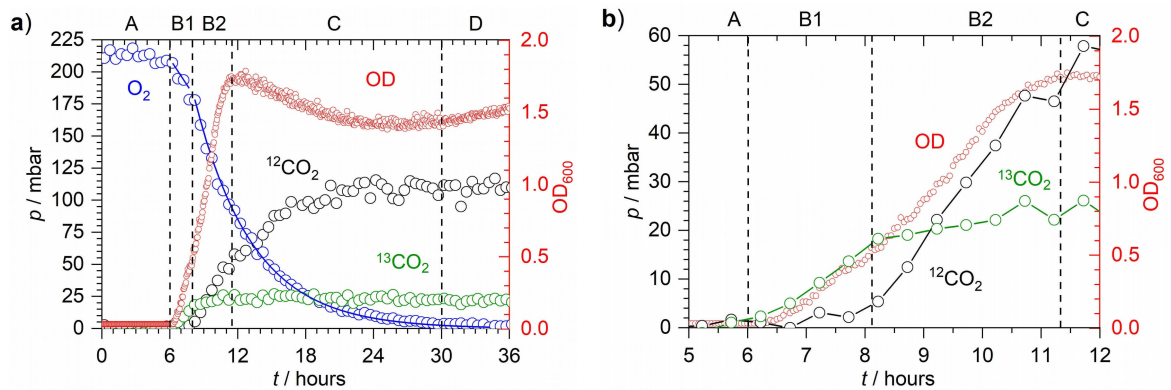


Fig 8. Monitoring mixed sugar metabolism of *E. coli* using CERS spectroscopy with isotopic labelling (3 mM ^{13}C -glucose, 20 mM ^{12}C -lactose, in M9), including an exponential decay fit of p_{O_2} and OD measurements of the culture solution. A to D denote the different phases of bacterial growth, lag phase (A), exponential growth (B1, glucose, B2 lactose), stationary phase (C) and end of aerobic respiration (D). **a)** Overview. **b)** Detail.

The power of spectroscopic detection, however, is the possibility to distinguish isotopes which allows ^{13}C labelling of sugars and detection of $^{13}\text{CO}_2$ in the headspace. Using spectroscopy, this can be easily quantified and distinguished from $^{12}\text{CO}_2$ derived from non-labelled organic compounds. This principle is demonstrated in Fig. 7, showing an experiment with 2.5 mM ^{13}C -glucose and 10 mM ^{12}C -lactose in M9 as measured by DHR, and in Fig. 8, showing an experiment with 3 mM ^{13}C -glucose and 20 mM ^{12}C -lactose in M9 as measured by CERS. Both DHR and CERS are capable of distinguishing $^{13}\text{CO}_2$ arising first from the ^{13}C labelled glucose and $^{12}\text{CO}_2$ arising from the unlabelled lactose. We discuss the mixed sugar metabolism of *E. coli* using the CERS experiment in Fig. 8 as example; the DHR results and all repeats (at least triplicate) have essentially the same qualitative and quantitative behaviour. As before, there is a lag phase of about 6 h ('A' in Fig. 8) after which exponential growth

sets in ('B' in Fig. 8). Exponential growth is characterised by an increase of the OD up to its peak value of about 1.8. After *ca.* 11.5 h, the OD remains more or less stationary indicating the stationary phase ('C' in Fig. 8). During the exponential growth and stationary phase, oxygen is continuously consumed and CO₂ formed, until after about 30 h all oxygen is consumed, indicating the end of aerobic respiration ('D' in Fig. 8). The OD during phases C and D does not remain constant but declines first and then rises again; this behaviour seems to be typical for lactose metabolism and was discussed before. As before, there is some CO₂ missing in the total balance which is attributed to incomplete conversion of the sugars to CO₂ since M9 does not contain an alternative carbon source for bacterial growth.

During the exponential growth phase, there is clearly a shift from glucose metabolism ('B1' in Fig. 8) to lactose metabolism ('B2'). As expected, glucose is metabolised first. When glucose is nearly exhausted, lactose metabolism takes over, without any apparent diauxic lag phase. In addition, there is possibly some overlap between glucose and lactose metabolism. Similar observations were made by Wang *et al.* (2015) that *Saccharomyces cerevisiae* natural isolates growing in mixtures of glucose and galactose would switch to metabolising both sugars before all glucose was exhausted.³⁵ They state that classic diauxic growth with a distinct lag phase is one extreme on a continuum of growth strategies determined by a cost-benefit trade-off. In previous literature, under similar conditions to our experiment, diauxic lag phases of typically up to 1 h have been reported for the diauxic shift from glucose to lactose in *E. coli*, often including OD measurements which showed an increase during glucose metabolism, then a lag phase (stationary OD), followed by a further increase attributed to lactose metabolism.^{1,2,36} In our experiments, no prolonged diauxic lag is apparent in the oxygen consumption/CO₂ production, nor in the OD measurements (see Fig. 8b). All our measurements have a smooth transition from B1 (glucose metabolism) to B2 (lactose metabolism), only the p_{O_2} shows perhaps a slightly different decay slope in B1 compared to B2 (Fig. 8a, blue solid line). Diauxic growth is not always made clear by a prolonged lag phase. Chu and Barnes (2016) proposed a hypothesis that the length of the diauxic lag phase depends on the characteristics of the environment.³⁷ Bacteria growing in rapidly changing environments need to be able to rapidly adapt between two sugars. Our environment is distinct from the majority of previous work studying diauxic shifts as it is oxygen-limited, the effects of rapidly depleting oxygen levels on the glucose-lactose diauxic growth of *E. coli* are as of yet unknown.

In conclusion, without the spectroscopic distinction of the ¹³C labelled and unlabelled sugars, no preference or diauxic shifts of metabolism would be apparent in our CO₂/O₂ or OD measurements.

Despite their widespread use, OD measurements are a very indirect method to characterise bacterial growth and phases and they are prone to interferences, and should only be used in combination with more advanced techniques to supplement more specific measurements such as the spectroscopic measurements in the present study.

CONCLUSIONS

Measuring the headspace above bacterial suspensions by spectroscopy to characterise bacterial growth and metabolism has many advantages compared to more conventional techniques. It is non-intrusive, does not require sampling and thus can be applied to closed systems easily, and it is very sensitive and highly selective due to the spectroscopic fingerprint of headspace gases. The high selectivity allows isotopic distinction which enables isotopic labelling studies. In this contribution, we have introduced two powerful new techniques for headspace monitoring, photoacoustic detection in a differential Helmholtz resonator (DHR) and Raman spectroscopy enhanced in an optical cavity (CERS). Both techniques have been shown to be able to monitor O₂ and CO₂ and its isotopomers with excellent sensitivity and time resolution. Compared to DHR, CERS has the advantage of easier calibration due to the availability of internal standards (N₂, or Si peaks). Without further modifications, the CERS method can also detect other important gases in the metabolism of bacteria, such as H₂, H₂S or N₂. DHR has the advantage of a much simpler setup and being even more cost-effective. The technique can measure O₂, CO₂ and H₂S with high sensitivity and selectivity; extension to the detection of other molecules would require different diode laser sources, however.

OD measurements are a standard, widely used technique to characterise bacterial growth. We have discussed and shown some of its shortcomings if used on its own without supporting complementary measurements. OD measurements are an indirect indicator of bacterial growth. They suffer from interferences and they cannot distinguish living cells from dead cells and debris. OD measurements can therefore not provide sufficient information once the OD becomes constant during the stationary phase of bacterial growth. They also cannot distinguish diauxic growth without a diauxic lag phase present. The spectroscopic measurements, however, can clearly and unambiguously distinguish the different stages of bacterial growth characterising the growth phases in the different media studied, LB and M9. OD measurements can supplement these measurements, but they are not necessary. We have demonstrated how ¹³C isotopic labelling of sugars in the spectroscopic detection allows the study of bacterial mixed sugar metabolism, to establish whether sugars are sequentially or simultaneously

metabolised. For *E. coli*, we have characterised the shift from glucose to lactose metabolism without a classic diauxic lag phase in-between, under oxygen-limited conditions.

DHR and CERS have been proven to be cost-effective, highly specific analytical tools in the biosciences and in biotechnology, complementing and superseding existing, conventional techniques. They also provide new capabilities for mechanistic investigations, in particular due to the possibility to use isotopic labelling easily. In the future, we plan to apply these techniques to further mechanistic studies of bacterial metabolism, monitoring of continuously operating systems and anaerobic bioprocesses.

ACKNOWLEDGEMENTS

We are grateful to Prof. J. Green, Prof. R.K. Poole and Dr J. Reid for help and discussions. We acknowledge the University of Sheffield, the NERC research council (CERS set-up, grant NE/I000844/1), the EPSRC (DTP scholarship to GDM) and the Ministry of Education of Saudi Arabia for financial support of our research.

REFERENCES

- (1) Monod, J. Recherches sur la croissance des cultures bactériennes. (1941, Thesis; Université de Paris, France; Pmid:20784032).
- (2) Monod, J. The Growth of Bacterial Cultures. *Annu. Rev. Microbiol.* **1949**, *3*, 371–394. <https://doi.org/10.1146/annurev.mi.03.100149.002103>.
- (3) Santillán, M.; Mackey, M. C. Quantitative Approaches to the Study of Bistability in the Lac Operon of Escherichia Coli. *J. R. Soc. Interface* **2008**, *5* (SUPPL. 1), S29–S39. <https://doi.org/10.1098/rsif.2008.0086.focus>.
- (4) Görke, B.; Stülke, J. Carbon catabolite repression in bacteria: many ways to make the most out of nutrients. *Nat. Rev. Microbiol.* **2008**, *6*, 613–624. <https://doi.org/10.1038/nrmicro1932>.
- (5) Dien, B. S.; Nichols, N. N.; Bothast, R. J. Fermentation of Sugar Mixtures Using Escherichia Coli Catabolite Repression Mutants Engineered for Production of Lactic Acid. *J. Ind. Microbiol. Biotechnol.* **2002**, *29*, 221–227. <https://doi.org/10.1038/sj.jim.7000299>.
- (6) Ullmann, A. (March 2009) Escherichia coli Lactose Operon. In: Encyclopedia of Life Sciences (ELS). Wiley & Sons, Ltd: Chichester. <https://doi.org/10.1002/9780470015902.a0000849.pub2>
- (7) Solopova, A.; van Gestel, J.; Weissing, F. J.; Bachmann, H.; Teusink, B.; Kok, J.; Kuipers, O. P. Bet-Hedging during Bacterial Diauxic Shift. *PNAS* **2014**, *111*, 7427–7432. <https://doi.org/10.1073/pnas.1320063111>.

- (8) Siegal, M. L. Shifting Sugars and Shifting Paradigms. *PLOS Biol.* **2015**, *13*, e1002068. <https://doi.org/10.1371/journal.pbio.1002068>.
- (9) Aidelberg, G.; Towbin, B. D.; Rothschild, D.; Dekel, E.; Bren, A.; Alon, U. Hierarchy of Non-Glucose Sugars in Escherichia Coli. *BMC Syst. Biol.* **2014**, *8*, 133. <https://doi.org/10.1186/s12918-014-0133-z>.
- (10) Joshua, C. J.; Dahl, R.; Benke, P. I.; Keasling, J. D. Absence of Diauxie during Simultaneous Utilization of Glucose and Xylose by Sulfolobus Acidocaldarius. *J. Bacteriol.* **2011**, *193*, 1293-1301. <https://doi.org/10.1128/JB.01219-10>.
- (11) Desai, T. A.; Rao, C. V. Regulation of Arabinose and Xylose Metabolism in Escherichia Coli. *Appl. Environ. Microbiol.* **2010**, *76*, 1524–1532. <https://doi.org/10.1128/AEM.01970-09>.
- (12) Ammar, E. M.; Wang, X.; Rao, C. V. Regulation of Metabolism in Escherichia Coli during Growth on Mixtures of the Non-Glucose Sugars: Arabinose, Lactose, and Xylose. *Sci. Rep.* **2018**, *8*, 609. <https://doi.org/10.1038/s41598-017-18704-0>.
- (13) Holzberg, T. R.; Watson, V.; Brown, S.; Andar, A.; Ge, X.; Kostov, Y.; Tolosa, L.; Rao, G. Sensors for biomanufacturing process development: facilitating the shift from batch to continuous manufacturing. *Curr. Opp. Biotechnol.* **2018**, *22*, 115-127. <https://doi.org/10.1016/j.coche.2018.09.008>
- (14) Dixon, N. M.; Kell, D. B. The Control and Measurement of ‘CO₂’ during Fermentations. *J. Microbiol. Methods* **1989**, *10*, 155 -176. [https://doi.org/10.1016/0167-7012\(89\)90048-1](https://doi.org/10.1016/0167-7012(89)90048-1).
- (15) Arnoudse, P. B.; Pardue, H. L. Instrumentation for the Breath-by-Breath Determination of Oxygen and Carbon Dioxide Based on Nondispersive Absorption Measurements. *Anal. Chem.* **1992**, *64*, 200-204. <https://doi.org/10.1021/ac00026a020>.
- (16) Gianfrani L.; Sasso, A.; Tino, G. M. Monitoring of O₂ and NO₂ using tunable diode lasers in the near-infrared region. *Sens. Actuat. B Chem.* **1997**, *39*, 283-285. [https://doi.org/10.1016/S0925-4005\(97\)80219-5](https://doi.org/10.1016/S0925-4005(97)80219-5).
- (17) Busse, G.; Herboeck, D. Differential Helmholtz resonator as an optoacoustic detector. *Appl. Optics* **1979**, *18*, 3959-3961. <https://doi.org/10.1364/AO.18.003959>.
- (18) Zeninari, V.; Courtois, D.; Parvitte, B.; Kapitanov, V. A.; Ponomarev, Y. N. Methane detection on the sub-ppm level with a near-infrared diode laser photoacoustic sensor. *Infrared Phy. & Tech.* **2003**, *44*, 253. [https://doi.org/10.1016/S1350-4495\(03\)00135-X](https://doi.org/10.1016/S1350-4495(03)00135-X).
- (19) Rouxel, J.; Coutard, J. G.; Gidon, S.; Lartigue, O.; Nicoletti, S.; Parvitte, B.; Vallon, R.; Zéninari, V.; Glière, A. Miniaturized differential Helmholtz resonators for photoacoustic trace gas detection. *Sensors and Actuators B* **2016**, *236*, 1104–1110. <https://doi.org/10.1016/j.snb.2016.06.074>.
- (20) Alahmari, S.; Kang, X.-W.; Hippler, M. Diode Laser Photoacoustic Spectroscopy of CO₂, H₂S and O₂ in a Differential Helmholtz Resonator for Trace Gas Analysis in the Biosciences and Petrochemistry. *Anal. Bioanal. Chem.* **2019**, *411*, 3777–3787. <https://doi.org/10.1007/s00216-019-01877-0>.
- (21) Salter, R.; Chu, J.; Hippler, M. Cavity-enhanced Raman spectroscopy with optical feedback cw diode lasers for gas phase analysis and spectroscopy. *Analyst* **2012**, *137*, 4669-4676. <https://doi.org/10.1039/C2AN35722D>.

- (22) Keiner, R.; Frosch, T.; Massad, T.; Trumbore, S.; Popp, J. Enhanced Raman multigas sensing – a novel tool for control and analysis of $^{13}\text{CO}_2$ labeling experiments in environmental research. *Analyst* **2014**, *139*, 3879-3884. <https://doi.org/10.1039/c3an01971c>.
- (23) Hippler, M. Cavity-Enhanced Raman Spectroscopy of Natural Gas with Optical Feedback cw-Diode Lasers. *Anal. Chem.* **2015**, *87*, 7803-7809. <https://doi.org/10.1021/acs.analchem.5b01462>.
- (24) Smith, T. W.; Hippler, M. Cavity-Enhanced Raman Spectroscopy in the Biosciences: In Situ, Multicomponent and Isotope Selective Gas Measurements To Study Hydrogen Production and Consumption by *Escherichia coli*. *Anal. Chem.* **2017**, *89*, 2147-2154. <https://doi.org/10.1021/acs.analchem.6b04924>.
- (25) Jochum, T.; Fastnacht, A.; Trumbore, S.; Popp, J.; Frosch, T. Direct Raman Spectroscopic Measurements of Biological Nitrogen Fixation under Natural Conditions: An Analytical Approach for Studying Nitrogenase Activity. *Anal. Chem.* **2017**, *89*, 1117-1122. <https://doi.org/10.1021/acs.analchem.6b03101>.
- (26) Gordon, I. E.; Rothman, L. S.; Hill, C.; Kochanov, R. V.; Tan, Y.; Bernath, P. F.; Birk, M.; Boudon, V.; Campargue, A.; Chance, K. V.; Drouin, B. J.; Flaud, J.-M.; Gamache, R. R.; Hodges, J. T.; Jacquemart, D.; Perevalov, V. I.; Perrin, A.; Shine, K. P.; Smith, M.-A. H.; Tennyson, J.; Toon, G. C.; Tran, H.; Tyuterev, V. G.; Barbe, A.; Császár, A. G.; Devi, V.M.; Furtenbacher, T.; Harrison, J. J.; Hartmann, J.-M.; Jolly, A.; Johnson, T. J.; Karman, T.; Kleiner, I.; Kyuberis, A. A.; Loos, J.; Lyulin, O. M.; Massie, S. T.; Mikhailenko, S. N.; Moazzen-Ahmadi, N.; Müller, H. S. P.; Naumenko, O. V.; Nikitin, A. V.; Polyansky, O. L.; Rey, M.; Rotger, M.; Sharpe, S. W.; Sung, K.; Starikova, E.; Tashkun, S. A.; Vander Auwera, J.; Wagner, G.; Wilzewski, J.; Wcisło, P.; Yu, S.; Zak, E. J. The HITRAN2016 Molecular Spectroscopic Database. *J. Quant. Spectrosc. Radiat. Transf.* **2017**, *203*, 3-69. <https://doi.org/10.1016/j.jqsrt.2017.06.038>.
- (27) www.webbook.nist.gov/chemistry; accessed 16/10/2018.
- (28) Loomis, W.F. Jr; Magasanik, B. Glucose-lactose diauxie in *Escherichia coli*. *J Bacteriol.* **1967**, *93*, 1397-1401. <https://jlb.asm.org/content/93/4/1397>
- (29) Inada, T.; Kimata, K.; Aiba, H. Mechanism responsible for glucose-lactose diauxie in *Escherichia coli*: challenge to the cAMP model. *Genes Cells* **1996**, *1*, 293-301. <https://doi.org/10.1046/j.1365-2443.1996.24025.x>
- (30) Mostovenko, E.; Deelder, A. M.; Palmblad, M. Protein expression dynamics during *Escherichia Coli* glucose-lactose diauxie. *BMC Microbiology* **2011**, *11*:126. <https://doi.org/10.1186/1471-2180-11-126>.
- (31) Grosz, R.; Stephanopoulos, G. Statistical Mechanical Estimation of the Free Energy of Formation of *E. coli* Biomass for Use with Macroscopic Bioreactor Balances. *Biotechn. Bioeng.* **1983**, *25*, 2149-2163. <https://doi.org/10.1002/bit.260250904>.
- (32) Sezonov, G.; Joseleau-Petit, D.; D'Ari, R. *Escherichia coli* physiology in Luria-Bertani broth. *J. Bacteriol.* **2007**, *189*, 8746-8749. <https://www.ncbi.nlm.nih.gov/pmc/articles/PMC2168924/>.
- (33) Miller, C. G. Protein degradation and proteolytic modification, pp. 938-954. In: *Escherichia coli and Salmonella: Cellular and Molecular Biology*, 2nd edn. (edited by Neidhardt, F. C.; Curtiss, R.; Ingraham, J. I.; Lin, E. C. C.; Low, K. B.; Magasanik, B.; Reznikoff, W.; Riley, M.; Schaechter, M.; Umberger, H. E. **1996**, ASM Press, Washington, D.C., USA).

- (34) Li, Z.; Nimtz, M.; Rinas, U. The metabolic potential of *Escherichia coli* BL21 in defined and rich medium. *Microb. Cell Fact.* **2014**, *13*, 45. <https://doi.org/10.1186/1475-2859-13-45>.
- (35) Wang, J.; Atolia, E.; Hua, B.; Savir, Y.; Escalante-Chong, R.; Springer, M. Natural Variation in Preparation for Nutrient Depletion Reveals a Cost-Benefit Tradeoff. *PLoS Biol.* **2015**, *13*, e1002041. <https://doi.org/10.1371/journal.pbio.1002041>.
- (36) Fernández-Coll, L.; Cashel, M. Contributions of SpoT Hydrolase, SpoT Synthetase, and ReIA Synthetase to Carbon Source Diauxic Growth Transitions in *Escherichia coli*. *Front. Microbiol.* **2018**, *9*, 1802. <http://dx.doi.org/10.3389/fmicb.2018.01802>.
- (37) Chu, D.; Barnes, D. J. The lag-phase during diauxic growth is a trade-off between fast adaption and high growth rate. *Sci. Rep.* **2016**, *6*, 25191. <https://doi.org/10.1038/srep25191>.